Analysis of Preliminary Data at the CERN NA62 Experiment

Thesis submitted in accordance with the requirements of
the University of Liverpool for the degree of Doctor in Philosophy
by

Liam David Joseph Fulton

August 2016

Abstract

This Thesis describes three topics in which I was engaged namely: Completion of the mechanical construction of KTAG; A Monte Carlo study to identify the optimal CEDAR Cherenkov radiator gas; Physics analysis using the preliminary NA62 data produced in 2014 and 2015.

The work undertaken to complete the mechanical construction of the kaon identification system (KTAG) and the installation procedure as was performed in 2013 is outlined. The completion of the final five light guides which house the KTAG PMTs is detailed. The work undertaken to align the optical components of the KTAG detector and the instalation on the NA62 beamline in 2013 is described.

A detailed Monte Carlo driven study is presented investigated the downstream effects of using either hydrogen or nitrogen in the upstream differential Cherenkov detector, KTAG. The results of this study alongside the relative kaon identification performance for both gases lead to the conclusion that nitrogen be used as the Cherenkov radiator.

A selection of the $K^+ \to \pi^+\pi^0$, $K^+ \to \pi^+\pi^0\pi^0$ and $K^+ \to e^+\pi^0\nu$ decays is performed using primarily the NA62 LKr electromagnetic calorimeter and the 2014 minimum bias run data. An attempt is then made at calculating the relative branching fractions between the channels showing deviations of around 20% with respect to the expected values for relative branching fractions involving the $K^+ \to \pi^+\pi^0\pi^0$ channel. The analysis was repeated using a 2015 data set and the problem was shown to persist. The downstream spectrometer tracking information was used in order to perform a data driven study of both hadronic and electromagnetic cluster response in the calorimeter. The study identified a differing response in data and Monte Carlo when modelling hadronic clusters. Hadronic clusters were removed from the data sample using Straw Spectrometer information and the anticipated branching fractions were recovered within statistical uncertainties. Finally a discussion is presented of what is necessary to produce the correct response in Monte Carlo.

Declaration

The analysis of data from the 2014 and 2015 data in Chapters 6 and 7 was primarily my own work. Where results from other studies were used they are explicitly mentioned. The Monte Carlo analysis regarding the optimal Cherenkov gas was also my own work unless otherwise stated. I was not involved in the design of the NA62 detector described in Chapter 4 but I took part in the final stages of the mechanical completion of the detector. I was involved with the installation of the KTAG detector described later in Chapter 4. No other qualifications have been achieved with the work reported in this thesis.

Acknowledgements

First I would like to thank John Dainton and John Fry for countless long and interesting discussions surrounding the analysis and whos supervision made this thesis possible. Great thanks also to Bozydar Wrona and Emilie Maurice whom I enjoyed working with thoroughly whilst at the University. I am also very grateful to Giuseppe Ruggiero whose approach to analysis, especially during 2014 data taking, was a pleasure to be a part of and is something I will take with me going forward. Thank you to all at Liverpool, the NA62 collaboration and the wider CERN community for such an enjoyable experience. Finally thank you to the European Research Council whose funding made my studies possible.

It is often said that no man stands alone. Im not sure if that is true or not but fortunately I am lucky enough that I have never had to find out. To Mum, Dad, Claire, Martin, Josh and Alex thank you, always.

Contents

List of Figures

Chapter 1

Introduction

The study of kaons has been central to formulation of the Standard Model of Particle Physics in the second half of the 20th century. The kaon was first discovered when it was realised that parity is not a conserved symmetry of nature and two previously identified particles θ^+ and τ^+ were in fact the same particle, the positively charged kaon, K^+. Soon after it was discovered that the weak interaction violates the symmetries of parity and charge conjugation simultaneously. That revelation came from the study of neutral kaon decays of K^0 and $\overline{K}^0$. In addition to the discovery of CP violation, studies of the kaon and it's decay modes yielded insight in the following areas: the first evidence of strangeness; postulation of the charm quark in the GIM mechanism to explain the suppression of flavour changing neutral current decays; many elements of the CKM matrix were also measured through the study of (semi-)leptonic decays.

Kaon physics now offers a unique window in the search for New Physics beyond the Standard Model through the measurement of very rare kaon decays. The absence of flavour changing neutral currents in the Standard Model at tree level and the effect of the GIM mechanism make the $K^+ \to \pi^+\nu\overline{\nu}$ decay of particular interest as will be described in detail in this thesis. The branching ratio of $K^+ \to \pi^+\nu\overline{\nu}$ is predicted to be of the order of 10^{-10} in the Standard Model. New heavy particles from physics beyond the Standard Model could allow for tree level interactions resulting in a measurable enhancement of the $K^+ \to \pi^+\nu\overline{\nu}$ Standard Model branching ratio. The analysis presented throughout this thesis is based on data from the NA62 experiment, the latest of a long history of fixed target kaon experiments at the CERN North Area (NA) served by the Super Proton Synchotron (SPS) accelerator. Today, NA62 aims to study the ultra-rare decay $K^+ \to \pi^+\nu\overline{\nu}$ to provide a precision test of the Standard Model.

The NA62 experiment began taking data in 2015 but a data sample was also collected in 2014 during an initial commissioning run with an incomplete detector. This thesis presents the work that was undertaken prior to initial data taking in 2014 in order to produce a full report on the relative merits of using hydrogen

and nitrogen as a Cherenkov radiator, performing a comparison of the simulation with data. The latter half of this thesis is involved with reproducing three of the common kaon decay modes with the largest branching fractions using the experiment's primary electromagnetic calorimeter, focussing on the observed differences in the 2014 and 2015 data sets with respect to Monte Carlo simulations.

This thesis is organised as follows, Chapter 2 gives the theoretical motivation for the NA62 experiment's aim of studying the ultra-rare decay $K^+ \to \pi^+ \nu\overline{\nu}$ along with the current state of the art values from previous experiments. Chapter 3 details the entire NA62 detector system, including the beamline set up and the various sub-detector components. Chapter 4 provides further detail regarding the KTAG Cherenkov detector including details of hardware construction in Liverpool and installation at CERN and the performance as evaluated in 2015 data. Chapter 5 presents the methodology and results of a detailed Monte Carlo study into the consequences of choosing either hydrogen or nitrogen as the CEDAR Cherenkov radiator on the downstream spectrometer along with how each gas affects the KTAG performance. A comparison with data is also given. Chapter 6 uses the 2014 minimum bias data to extract three of the largest kaon decay modes using primarily the electromagntic calorimeter, the relative branching ratios are calculated and discrepancies between data and Monte Carlo discussed in detail. Chapter 7 uses the 2015 minimum bias data to test the findings in the 2014 data set and to use additional detectors in order to understand and explain the observed discrepancies. Finally Chapter 8 summarises the findings regarding the optimal Cherenkov gas study and the analysis using the LKr electromagnetic calorimeter using 2014 and 2015 data.

Chapter 2

Theoretical Motivation

2.1 Overview

Within the Standard Model (SM) two very rare kaon decays that are of particular interest for probing high mass scales are the $K^+ \to \pi^+\nu\overline{\nu}$ and $K^0 \to \pi^0\nu\overline{\nu}$ decays. Both of these involve flavour changing neutral currents (FCNCs) at tree level which is expressly forbidden in the SM. These decays are possible in the SM through one loop diagrams which are GIM Suppressed. The lack of leading order contributions from SM physics means that mass scales at higher order than can currently be probed directly are therefore accessible. The presence of New Physics at such energies will enhance the well understood SM branching ratio.

A major advantage in studying this particular rare kaon decay is that the associated theoretically uncertainties are precisely predicted, as will be shown in Section 2.3. Section 2.4 gives more detail on the reasons why the $K \to \pi\nu\overline{\nu}$ decays present such a unique and interesting window into New Physics in the flavour sector. Finally some time is spent discussing the state of the art experimental measurement of the $K^+ \to \pi^+\nu\overline{\nu}$ branching ratio. The experimental challenges of previous experiments and what will be required for an NA62 branching ratio measurement is highlighted in Section 2.5.

2.2 The CKM Framework and Flavour Changing Neutral Currents

The $K \to \pi\nu\overline{\nu}$ decays have such small predicted SM branching fractions due to the absence of flavour changing neutral currents at tree level in the SM. The lack of FCNCs is best understood by first considering the CKM matrix which is present in the SM as the Yukawa mass matrices cannot be simultaneously diagonalized for up and down type quarks, that is that it is not possible to make the non leading

diagonal elements zero. The flavour representation of quarks is not diagonal. This means the flavour eigenstates are not equivalent to the mass eigenstates. The transitions in quark flavour observed as the physical mass states are therefore possible via the mixing of quark flavour states. If we diagonalise the basis of the up type quarks, $u_L^{(m)} = u_l$, such that Y^u is diagonal it is possible to interpret the CKM matrix , V_{CKM}, as the rate of mixing between the physical mass states of down type and up type states for which the charged current interactions are diagonal, such that:

$$\begin{pmatrix} d \\ s \\ b \end{pmatrix} = V_{\text{CKM}} \begin{pmatrix} d^{(m)} \\ s^{(m)} \\ b^{(m)} \end{pmatrix}, V_{\text{CKM}} = \begin{pmatrix} V_{ud} & V_{us} & V_{ub} \\ V_{cd} & V_{cs} & V_{cb} \\ V_{td} & V_{ts} & V_{tb} \end{pmatrix} \tag{2.1}$$

where d, s, b are weak eigenstates of the down type quarks which interact with the up type states, u, c, d, in the charged current weak interactions and $d^{(m)}, s^{(m)}, b^{(m)}$ are the mass eigenstates for the down type quarks. The elements of the CKM matrix represent the amplitude for transitions between quark flavours, the square of which represents the transition probability between the two states. As an example of how the CKM matrix affects the rate of interactions between quarks the V_{tb}/V_{ts} ratio determines the ratio of amplitudes for a top quark to decay into a bottom or a strange quark mass state. Experimentally it is observed that $V_{ts} \ll V_{tb}$, and decays involving $t \to s$ are said to be Cabbibo suppressed. Indeed all the amplitudes involving off diagonal elements in the CKM matrix, corresponding to mixing between quark generations are suppressed. The neutral current, J^{μ}_{NC}, which couple to the neutral boson, Z_0, does not mix up and down type quarks in the weak basis.

The neutral current remains diagonal in the mass basis which explains the absence of FCNCs at tree level [1]. There are explicitly no cross terms coupling different flavours for neutral current interactions. Furthermore, in the Standard Model, FCNCs are mediated at higher order perturbation theory by box diagrams exchanging virtual W bosons and quarks. Before the discovery of the charm quark Glashow, Iliopoulos and Maiani realized that the contribution from the up quark exchange is suppressed by the contribution by the postulated charm quark exchange. The charm contribution has opposite sign to the up contribution and if the charm and up quarks had equal mass the contributions would cancel completely and the decay would not be observed. The process is then proportional to the mass difference of the charm and up quarks. This suppression can be generalised to three quark generations and is the basis of the GIM mechanism [1].

2.2.1 CKM Unitarity

In general a square matrix of size n has $2n^2$ free parameters. As will be explained in this Section however the CKM matrix has fewer free parameters. Firstly, from

the unitarity condition,

$$V_{ji}^{*}V_{jk} = \delta_{ik}, \tag{2.2}$$

n^2 constraints are imposed. The number of remaining free parameters is then n^2. The definitions of the quark mass states require a number of residual arbitrary phases. The transformations,

$$u^{(m)f} \rightarrow e^{i\phi_f^u}u^{(m)f}, \quad d^{(m)f} \rightarrow e^{i\phi_f^d}d^{(m)f}, \tag{2.3}$$

transform the CKM matrix such that,

$$V_{CKM} \rightarrow U_{\phi^u}V_{CKM}U_{\phi^d}, \tag{2.4}$$

where U_{ϕ^u} and U_{ϕ^d} are complex diagonal matrices of $2n$ total phases. Note that this transformation has no physical significance [2]. The invariance to the choice of complex phases allows us to eliminate (2n - 1) relative phases from V_{CKM}, leaving one remaining phase which is significant. The resulting number of free parameters is $n^2 - (2n-1) = (n-1)^2$. Unitary matrices are also orthogonal so $n(n-1)/2$ of the parameters can be identified as rotation angles between n independent bases. The remaining $\frac{1}{2}(n-1)(n-2)$ parameters correspond to complex phases. For the three dimensional CKM matrix, this means 3 rotation angles and 1 complex phase. Note that there would be no complex phase in the scenario in which there were only two generations.

2.2.2 CP Violation

The CKM matrix contains a complex phase and therefore CP violation is possible in the quark sector. We will show in this section the effect of parity, P, and charge conjugation, C, transformations on fermion fields and therefore how CP violation arises.

Parity, P, inverts the sign of the spatial coordinates through the transformation,

$$\overrightarrow{x} \rightarrow P\overrightarrow{x} = -\overrightarrow{x}, \tag{2.5}$$

a parity transformed quantum state should be identical to the original state except the spatial components will be inverted. A state of definite momentum $\overrightarrow{p}$, spin s, and charge q, would transform as,

$$P|\overrightarrow{p}, s, q\rangle = \eta_p|\overrightarrow{-p}, s, q\rangle \tag{2.6}$$

where $\eta_p = \pm 1$. The Dirac spinors, which describe fermion fields, must transform as,

$$P\psi(t, \overrightarrow{x}) = \eta_p \gamma_0 \psi(t, \overrightarrow{-x}), \tag{2.7}$$

if the Dirac equation is to be invariant under parity transformations.

Charge conjugation, C, inverts the sign of all quantum charges associated with a field. For a fermion field the transformation acts as,

$$C\psi(t, \overrightarrow{x}) = \eta_C \gamma_0 \psi^*(t, \overrightarrow{x}) = \eta_C \widehat{\psi}(t, \overrightarrow{x}), \tag{2.8}$$

where η_C is a complex phase, and C is an antisymmetric matrix defined as,

$$C^{-1}\gamma_\mu C = \gamma_\mu^T. \tag{2.9}$$

The exact form depends on the chosen representation of the Dirac γ matrices.

Charge and Parity are maximally violated by the weak interaction. For example, in the weak decay $\pi^+ \to \mu^+ \nu_L$ the net helicity polarisation of muons is always left-handed. The parity reversed process $\pi^+ \to \mu^+ \nu_R$ which would produce muons with net right-handed helicity, is not observed (because the $W^\pm$ do not couple to left-chiral anti-neutrinos). Similarly the charge conjugated process $\pi^- \to \mu^- \overline{\nu}_L$ is not observed. On the other hand, the CP conjugated process $\pi^- \to \mu^- \overline{\nu}_R$ decay does occur with net right-handed polarisation .The Charge and Parity breaking then leads to a conservation of Charge and Parity simultaneously (CP) in the weak interactions. CP violation however was discovered in the neutral kaon mixing [3], and later in B mesons in the interference between mixing and decay [4]. CP violation does not arise from the structure of the weak interaction itself but instead enters through the CKM matrix and the presence of three quark generations.

The charged current interaction term in the SM Lagrangian is,

$$\mathcal{L}_{CC} = -\frac{g_2}{\sqrt{2}} \left(\overline{u}_L \gamma^\mu W_\mu^+ V_{CKM} d_L + \overline{d}_L \gamma^\mu W_\mu^- V_{CKM}^\dagger u_L \right). \tag{2.10}$$

Applying the the Charge conjugation and Parity transformations yields,

$$\mathcal{L}_{CC}^{CP} = -\frac{g_2}{\sqrt{2}} \left(\overline{d}_L \gamma^\mu W_\mu^- V_{CKM}^T u_L + \overline{u}_L \gamma^\mu W_\mu^+ V_{CKM}^* d_L \right). \tag{2.11}$$

CP is therefore only conserved in the charged current interaction if $V_{CKM} = V_{CKM}^*$. The presence of a non zero irreducible complex phase in the CKM matrix as described leads to CP violation as 2.10 and 2.11 cannot be made equivalent.

2.2.3 CKM Parametrization

The CKM matrix is most commonly defined in terms of the three rotation angles θ_{12}, θ_{23}, θ_{13}, and the single complex phase δ_{CP} [6].

$$V_{CKM} = \begin{pmatrix} c_{12}c_{13} & s_{12}c_{13} & s_{13}e^{-i\delta_{CP}} \\ -s_{12}c_{23} - c_{12}s_{23}s_{13}e^{-i\delta_{CP}} & -c_{12}c_{23} - s_{12}s_{23}s_{13}e^{-i\delta_{CP}} & s_{23}c_{13} \\ s_{12}s_{23} - c_{12}c_{23}s_{13}e^{-i\delta_{CP}} & -c_{12}s_{23} - s_{12}c_{23}s_{13}e^{-i\delta_{CP}} & c_{23}c_{13} \end{pmatrix} \tag{2.12}$$

where $c_x \equiv \cos\theta_x$ and $s_x \equiv \sin\theta_x$.

The presence of Cabibbo suppression reduces the absolute magnitudes of these numbers in the off diagonal elements. A hierarchical structure is clearly present where the diagonal elements are approximately unity and the off-diagonal elements are increasingly suppressed as more generations are skipped. The following are the current world averages [7] of the magnitude of each of the CKM components,

$$V_{CKM} = \begin{pmatrix} 0.97425 \pm 0.00022 & 0.2253 \pm 0.0008 & 0.00413 \pm 0.00049 \\ 0.225 \pm 0.008 & 0.986 \pm 0.016 & 0.0410 \pm 0.0013 \\ 0.0084 \pm 0.0006 & 0.040 \pm 0.0027 & 1.021 \pm 0.032 \end{pmatrix} \tag{2.13}$$

It is clear that $|\theta_{12}| \gg |\theta_{23}| \gg |\theta_{13}|$. A useful alternative parametrisation is the Wolfenstein parametrisation which represents the CKM matrix as follows,

$$V_{CKM} = \begin{pmatrix} 1 - \frac{1}{2}\lambda^2 & \lambda & A\lambda^3\left[\rho - i\eta\right] \\ -\lambda & 1 - \frac{1}{2}\lambda^2 & A\lambda^2 \\ A\lambda^3\left(1 - \rho - i\eta\right) & -A\lambda^2 & 1 \end{pmatrix} + \mathcal{O}(\lambda^4). \tag{2.14}$$

This parametrisation is based on the following,

$$s_{12} = \lambda = \frac{|V_{us}|}{\sqrt{|V_{ud}|^2 + |V_{us}|^2}} \tag{2.15}$$

$$s_{23} = A\lambda^2 = \lambda \left|\frac{V_{cb}}{V_{us}}\right| \tag{2.16}$$

$$s_{13}e^{i\delta_{CP}} = A\lambda^3(\rho + i\eta) = V_{ub}^* \tag{2.17}$$

As alluded to earlier the complex phase can be placed anywhere in the parametrization without affecting the physics of the CKM matrix. CP violation only depends on the presence of a complex phase which is irreducible.

2.2.4 Unitarity Triangles

The level of CP violation in the quark sector can be represented in the visually interesting unitarity triangles. If we first consider the unitarity condition of the CKM matrix,

$$(V^{\dagger}V)_{ij} = \sum_k V_{ik}^{\dagger} V_{kj} = \sum_k V_{ki}^{*} V_{kj} = \delta_{ij} \tag{2.18}$$

The three diagonal terms relate as,

$$\sum_i |V_{ij}|^2 = 1 \tag{2.19}$$

which have no impact on CP violation as they are solely real numbers. The off-diagonal elements however produce a sum of three complex phases which must total zero as the matrix is unitary.

$$\sum_k V_{ki}^{*} V_{kj} = 0; i \neq j \tag{2.20}$$

These six relations produce triangles in the complex plane. As several of the CKM matrix elements differ by orders of magnitude most of the triangles produced have sides with very different lengths and therefore angles close to 0, $\pi/2$ or π. Two of the triangles however do have sides with similar lengths and correspondingly sensible angles, they are,

$$V_{td}^{*} V_{ud} + V_{ts}^{*} V_{us} + V_{tb}^{*} V_{ub} = 0, \tag{2.21}$$

$$V_{ub}^{*} V_{ud} + V_{cb}^{*} V_{cd} + V_{tb}^{*} V_{td} = 0. \tag{2.22}$$

For both of these triangles the sides lengths are $\mathcal{O}(\lambda^3)$. The second triangle is commonly used to present constraints on the CKM matrix coming from experiment and will be the one considered here. Normalizing one side to unit length, the relation is,

$$\frac{V_{ub}^{*} V_{ud}}{V_{cb}^{*} V_{cd}} + 1 + \frac{V_{tb}^{*} V_{td}}{V_{cb}^{*} V_{cd}} = 0, \tag{2.23}$$

Parameters $\overline{\rho}$ and $\overline{\eta}$ are defined which are not dependent on any phase convention such that,

$$\overline{\rho} + i\overline{\eta} = -\frac{V_{ub} V_{ud}^{*}}{V_{cb}^{*} V_{cd}}. \tag{2.24}$$

$\overline{\rho}$ and $\overline{\eta}$ are related to the Wolfenstein parameters ρ and η. Figure 2.1 shows how the unitarity triangle described by 2.23 is represented in $\overline{\rho}$ and $\overline{\eta}$ space.

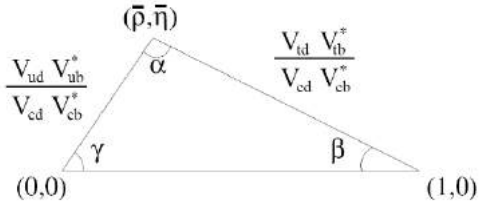

Figure 2.1: One of the common CKM unitary triangles, related to equation 2.23.

The study of this triangle has and continues to be a major part of experimental flavour physics. A measurement which shows deviation from unitarity will be a clear sign of beyond the SM physics. Furthermore if two measurements are made of $\overline{\rho}$ and $\overline{\eta}$ using different experimental methodologies this would also indicate a version of CP violation in the CKM framework which is not predicted in the SM.

The current experimental status of the unitarity triangle is summarised in figure 2.2 as aggregated by the CKM fitter collaboration. The angles α, β, and γ are defined as,

$$\alpha = \arg\left(-\frac{V_{td}V_{tb}^*}{V_{ud}V_{ub}^*}\right) \tag{2.25}$$

$$\beta = \arg\left(-\frac{V_{cd}V_{cb}^*}{V_{td}V_{tb}^*}\right) \tag{2.26}$$

$$\gamma = \arg\left(-\frac{V_{ud}V_{ub}^*}{V_{cd}V_{cb}^*}\right) \tag{2.27}$$

2.3 $K \to \pi\nu\overline{\nu}$ Theoretical Predictions

In this Section we will look in more detail at why the predicted Standard Model branching fractions for the $K \to \pi\nu\overline{\nu}$ decays are so small and illustrate how a measurement of this branching fraction constrains the CKM parameters discussed in the previous section. In the kaon sector the $K^+ \to \pi^+\nu\overline{\nu}$ and $K^0 \to \pi^0\nu\overline{\nu}$ decays play an especially important role in studying the CKM matrix. Their branching ratios are very low ($\mathcal{O}(10^{-10})$) and, crucially, they can be predicted theoretically very accurately in the Standard Model, providing clean measurements of the $\overline{\rho}$ and $\overline{\eta}$ parameters.

2.3.1 Standard Model Predictions

Both $K \to \pi\nu\overline{\nu}$ decays involve flavour changing neutral currents and therefore cannot occur at tree level through $Z^0/W^\pm$ boson exchange. Figure 2.3 shows the

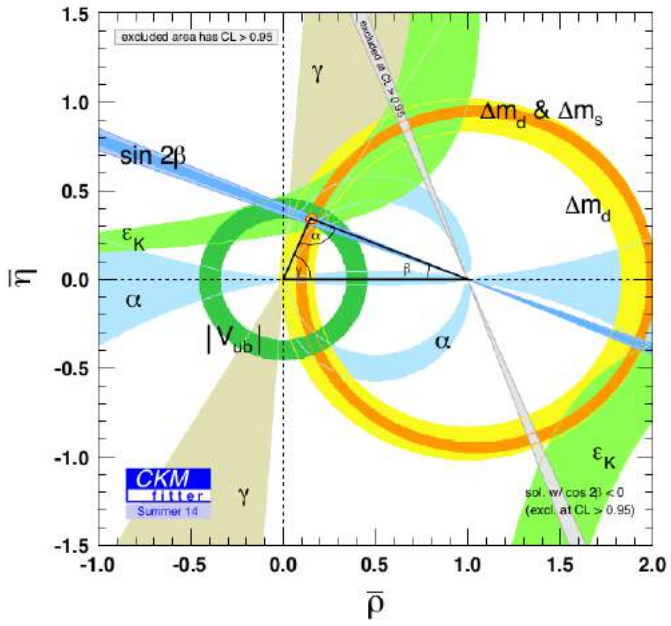

Figure 2.2: Experimental constraints on the unitarity triangle of the CKM matrix. [7]

loop induced processes by which the decay can proceed. All three include as the 'loop' in the processes an exchange between W bosons and quarks and either a lepton on Z^0 boson[8].

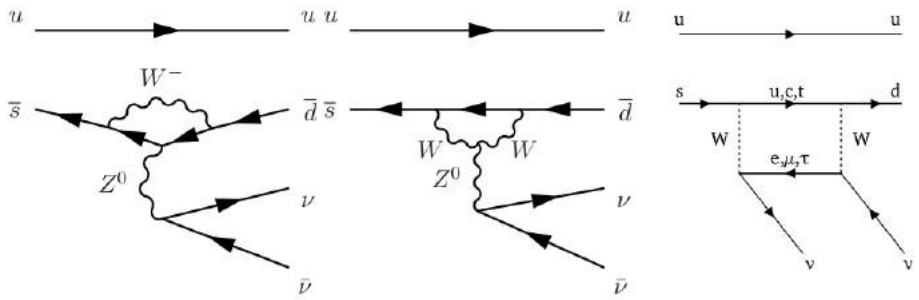

Figure 2.3: Feynman diagrams for the 1 loop processes by which the $K^+ \to \pi^+\nu\overline{\nu}$ decay can proceed.

In any loop diagram the amplitude is suppressed with respect to the tree level process by a factor of G_F^2, where G_F is the Fermi constant defined as $G_F = \frac{\sqrt{2}}{8}\frac{g^2}{m_W^2}$, g is the weak coupling constant. The GIM mechanism however further suppresses these decays as the quark states are not mass degenerate. Summing over all the quarks in the loop the amplitudes, $A(K \to \pi\nu\overline{\nu})$ have the form [9],

$$A(K \to \pi\nu\overline{\nu}) \sim \sum_{e,\mu,\tau} \sum_{f=u,c,t} X_f V_{fd} V_{fs}^* \tag{2.28}$$

where V_{ij} are the elements of the CKM matrix and X_f is a function of quark masses, for quark f. The unitarity of the CKM matrix requires that the amplitude is zero in the case that the quarks are mass degenerate. The amplitude does not vanish because X_f is a function of quark mass. It can be shown that $X_f \propto m_f^2/m_X^2$, the power-like GIM mechanism, hence the amplitude is dominated by the top quark exchange contribution. These decays are therefore excellent candidates for studying the V_{td} element of the CKM matrix.

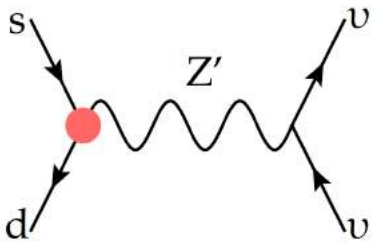

Figure 2.4: Feynman diagram by which a beyond the Standard Model process involving a hypothetical Z' boson allows for tree level contributions to the $K^+ \to \pi^+\nu\overline{\nu}$ decay.

Figure 2.4 illustrates an example of a beyond the Standard Model process where tree level interactions involving new particles act as the propagator. Specifically shown here is a common Standard Model extension where a new heavy boson Z' acts as a propagator. The contribution to the $K^+ \to \pi^+\nu\overline{\nu}$ branching fraction, $K_{\pi\nu\nu}$ is $K_{\pi\nu\nu} \propto |g_{Z'}|^2 M_{Z'}^{-4}$, where $M_{Z'}$ is the mass of the Z' boson and $|g_{Z'}|$ is the magnitude of the coupling constant associated with the hypothetical boson.

Long distance contributions from hadronic degrees of freedom and photon exchange have been shown to be small [10,11,12]. From the low-energy effective Hamiltonian for the K^+ decay[13,14] it is possible to extract the branching ratio[15] for $K^+ \to \pi^+\nu\overline{\nu}$,

$$\mathcal{B}(K^+ \to \pi^+\nu\overline{\nu}) = \kappa_+(1+\Delta_{EM}) \left[\left(\frac{\mathcal{I}m\lambda_t}{\lambda^5} X_t \right)^2 + \left(\frac{\mathcal{R}e\lambda_c}{\lambda}(P_c + \delta P_{c,u}) + \frac{\mathcal{R}e\lambda_t}{\lambda^5} X_t \right) \right] \tag{2.29}$$

The terms listed in 2.28 are defined as,

- λ, the Wolfenstein parameter.
- $P_c = \frac{1}{\lambda^4}\left(\frac{2}{3}X_c^e + \frac{1}{3}X_c^\tau\right)$. Containing the contribution from short distance charm exchange. P_c has been computed at NLO [14] and partially at NNLO [16] and with one loop electroweak corrections [17].
- $\delta P_{c,u}$ is the correction for long distance contributions to the charm quark exchange, $\delta P_{c,u} = 0.04 \pm 0.02$ [18].

- $\Delta_{EM} = -0.003$ is the long distance QED correction. [19]
- X_t, the contribution from top quark exchange, has been evaluated with QCD NLO corrections [13] and two loop electroweak corrections [15]. The associated error is $\sim$1% and is dominated by uncertainties in the QCD corrections.
  $\kappa_+ = r_{K^+} \frac{3\alpha^2 \mathcal{B}(K^+ \to \pi^0 l^+ \nu)}{2\pi^2 \sin^4 \theta_W} \lambda^8$, where $r_{K^+} = 0.901$ [20] accounts for isospin breaking corrections.
- κ_+ contains the hadronic matrix element along with electroweak corrections. The hadronic matrix element can be found by considering the well measured semi-leptonic decays $K^+ \to \pi^0 l^+ \nu$ [20].

The Standard Model theoretical prediction using current experimental knowledge is [15] [16],

$$\mathcal{B}(K^+ \to \pi^+ \nu\overline{\nu}) = (9.11 \pm 0.71) \times 10^{-11}, \tag{2.30}$$

where the first error relates to uncertainties in the input parameters and the second comes is the purely theoretical error.

The current theoretical prediction of $K^0 \to \pi^0 \nu\overline{\nu}$ decay can similarly be quantified as,

$$\mathcal{B}(K^0 \to \pi^0 \nu\overline{\nu}) = \kappa_L \left(\frac{\mathcal{I}m\lambda_t}{\lambda^5} X_t \right)^2, \tag{2.31}$$

where κ_L is extracted by considering the decay $K_L \to \pi^\pm e^\mp \nu$. The SM prediction for this branching ratio is,

$$\mathcal{B}(K^0 \to \pi^0 \nu\overline{\nu}) = (2.43^{+0.80}_{-0.37} \pm 0.06) \times 10^{-11} \tag{2.32}$$

Here the first error is dominated by V_{cb} experimental uncertainty and the theoretical uncertainty is dominated by QCD contributions. Also note that as this decay is dependent on only imaginary components of the CKM matrix the theoretical uncertainty for the neutral mode is much smaller than for the charged mode.

2.3.2 $K \to \pi\nu\overline{\nu}$ and Unitarity Triangles

Measured values of the $K \to \pi\nu\overline{\nu}$ branching ratios can be used to constrain the CKM matrix and uncertainty triangle. This also provides independent measurements of the Wolfenstein parameters to compare with those extracted from B meson decay measurements. In the Wolfenstein parametrization, the $K^+ \to \pi^+ \nu\overline{\nu}$

decay mode branching ratio can be expressed in terms of the $\overline{\rho}$ and $\overline{\eta}$ parameters producing an ellipse in ($\overline{\rho}$,$\overline{\eta}$) space. Specifically the measurement is free from the hadronic uncertainties which cancel [29]. A measurement of sin2β using the rare kaon decays gives an interesting test of the SM and minimal flavour violation models [21], Such models would still have CKM present from the CKM matrix but the amount of violation could vary between the processes. sin2β has already been measured with ∼5% precision at LHCb [22]. A kaon sector measurement could yield ∼10% precision with the current generation of experiments and ∼5% precision in the longer term [8].

The only observations of $K^+ \to \pi^+\nu\overline{\nu}$ so far come from the E747 and E949 experiments at Brookhaven National Laboratory. The experiments are described in the Section 2.4 and the final result was [23],

$$\mathcal{B}(K^+ \to \pi^+\nu\overline{\nu}) = (1.73^{+1.15}_{-1.05}) \times 10^{-10}. \tag{2.33}$$

So far there have been no observations of the $K^0 \to \pi^0\nu\overline{\nu}$ decay. An upper limit was set by the E931a experiment at KEK of [24],

$$\mathcal{B}(K^0 \to \pi^0\nu\overline{\nu}) < 2.6 \times 10^{-8}. \quad (90\%\text{C.L}). \tag{2.34}$$

The current generation of rare kaon decay experiments are expected to set limits on the branching ratios of $K^+ \to \pi^+\nu\overline{\nu}$ and $K^0 \to \pi^0\nu\overline{\nu}$ which are comparable with the theoretical uncertainty. NA62 expects to measure $\mathcal{B}(K^+ \to \pi^+\nu\overline{\nu})$ with 10% precision [25] KOTO aims to measure $\mathcal{B}(K^0 \to \pi^0\nu\overline{\nu})$ to within a few percent [26].

2.4 $K \to \pi\nu\overline{\nu}$ Experimental observations

In 1969 the first searches for the $K^+ \to \pi^+\nu\overline{\nu}$ decay were undertaken. The first experiments used stopped kaon beams. The first result was published by a heavy-liquid bubble chamber experiment [27]. Pions were identified by looking for the $\pi \to \mu \to e$ decay chain in the chamber, photon vetoing was done by looking for gamma-ray conversion into e^+e^-. No $K^+ \to \pi^+\nu\overline{\nu}$ events were observed and an upper limit on the branching ratio of 5.7×10^{-5} was set at 90% confidence level [28]. The next results came from the Berkeley Bevatron, which tracked the decay products of stopped kaons in a stack of spark chambers. Again no events were observed and the upper limit was extended to 5.6×10^{-7} [29].

The E787 [30] and E949 [31] experiments recorded the only observed $K^+ \to \pi^+\nu\overline{\nu}$ candidate events and as such provide the current experimental value for the branching ratio of $K^+ \to \pi^+\nu\overline{\nu}$. Both experiments span several data taking

runs with the experimental apparatus undergoing several upgrades. These experiments used stopped kaons impinging on a target at the centre of a cylindrical detector apparatus at the Brookhaven National Laboratory (BNL) beginning in the early 1980s. The E949 experiment is shown in its final form in figure 2.5. The E787 experiment used a 710 MeV/c kaon beam which was unseparated and included a pion and proton component, extracted from the Alternating Gradient Synchrotron, providing 24 GeV/c primary protons. This beam slowed using an 11 cm thick BeO degrader before eventually being stopped in a scintillating fibre target with a typical instantaneous kaon rate of typically 2 MHz. Cherenkov counters where used to identify kaons and the timing was done in the scintillating counters. Wire chambers were used to monitor the beam profile and identify multiple incoming particles.

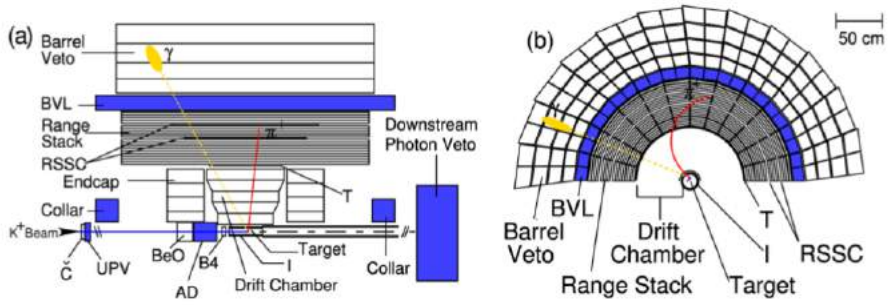

Figure 2.5: A Schematic of the E949 final detector configuration.

The key features of the E787 and E949 experiments are as follows. The entire detector was contained within a 1T solenoid magnet, required for momentum determination from charged tracks. A cylindrical drift chamber, filled with a mixture of argon and ethane at atmospheric pressure, surrounded the target provided 2.5% momentum resolution. The drift chamber was surrounded by the Ranged Stack, which contained stacked layers of scintillator counters (20 in total) and two multi-wire chambers in order to provide information on the energy, range and decay sequence of charged particles. The outer region of the detector was a layered lead-scintillator Shashlyk electromagnetic calorimeter used as a photon veto, crucial for suppression of photons from the $K^+ \to \pi^+\pi^0$ decay. The remainder of the detector was formed from several calorimeters with average thickness of 10 radiation lengths, X_0, and two upstream and downstream end caps. The overall π^0 detection inefficiency for the experiment was around 1×10^{-6}. The first run of E787 placed a limit of 1.7×10^{-8} [32] on the $K^+ \to \pi^+\nu\overline{\nu}$ branching ratio. After a significant upgrade of the detector [33] the E787 recorded the first ever $K^+ \to \pi^+\nu\overline{\nu}$ candidate with an expected background of 0.08 events this corresponded to a branching ratio of $(4.2^{+9.7}_{-3.5}) \times 10^{-10}$ [34]. Further data yielded two more candidates and the branching ratio measurement was improved to $(1.57^{+1.75}_{-0.82}) \times 10^{-10}$ [35]. In 2001 significant upgrades were done on the E787 experiment which vastly improved the number of kaons on target and detector efficiency. The new E949 collaboration obtained 4 more signal events. The

combined branching ratio is currently $(1.73^{+1.15}_{-1.05}) \times 10^{-10}$ [23], this is consistent with the Standard Model prediction given in equation 2.30 of $(9.11 \pm 0.71) \times 10^{-11}$.

The NA62 experiment uses a decay in flight technique and as such it is not possible to use a compact detector design as was used for E747 and E949. Instead the high momentum boosted kaons require a much larger experimental set up with a decidedly different geometry. The advantages and challenges of such a system will be detailed in the next Chapter which details the full NA62 experimental set up. Certain challenges do persist however for detecting the candidate events. Two of the most prescient issues will be investigated in this thesis, the first will be the ability to remove the background from scattered beam pions using upstream detectors to identify the kaons. Another background that must be controlled by the downstream detectors is the ability to suppress the $K^+ \to \pi^+\pi^0$ background by first rejecting photons at the detector level and then using the known kinematics of the decay which are dependent on the momentum resolution of the detected decay products.

Chapter 3

The NA62 Detector

Previous experiments aimed at measuring the $K^+ \to \pi^+\nu\overline{\nu}$ involved a mixed hadron beam containing kaons being stopped in a target and surrounding that target with sufficient detection apparatus. The NA62 experiment is a decay-in-flight kaon decay experiment which aims to collect and analyse O(10^{13}) K^+ decays in 3 years of data taking. There are distinct advantages that come from performing an in-flight high energy kaon decay experiment such as NA62 compared with the stopped, lower energy experiments that measured the $K^+ \to \pi^+\nu\overline{\nu}$ branching ratio previously. A K^+ of momentum p_K is produced by impinging a proton beam of momentum, P_p, on a fixed target. The production rate increases as p_K^2 and hence p_p^2. The rate of K^+ production increases quadratically with energy, meaning higher energy K^+ are produced at larger rates which is a distinct advantage. Furthermore the acceptance, resolution and efficiency of common sub-detector systems increases at higher energies as will be detailed throughout this Chapter. The principal difficulty in performing an experiment at higher energies than previously done for kaons lies in identifying the K^+ in the unseparated hadron beam which also contained π^+ and protons, overcoming this challenge will be addressed in this Chapter.

The three main principles of the detector are as follows.

1. Identify and track the K^+ from a positively charged mixed hadron beam.
2. Identify and track the K^+ decay products downstream of a 60m fiducial decay volume. For the $K^+ \to \pi^+\nu\overline{\nu}$ decay this is the π^+ only.
3. Make use of a series of photon and muon veto detectors to reject kinematically irreducible background decays. For the $K^+ \to \pi^+\nu\overline{\nu}$ decay all events with downstream detector information not corresponding to the π^+ are vetoed.

Detection of the $K^+ \to \pi^+\nu\overline{\nu}$ decay requires a positive identification of a K^+ upstream, a candidate π^+ as identified by the downstream tracking detectors with the additional requirement of no muon or photon candidates in any of the photon or muon veto detectors in order to suppress the background channels.

Background rejection is the key to NA62. The performance of the sub-detector systems are driven by the need to constrain the kinematically reducible backgrounds as shown in figure 3.1. The discriminatory kinematic variable is the so called 'missing mass squared' variable defined as the square of the difference in the measured π^+ and K^+ 4-momenta. Measurements of the upstream K^+ and downstream π^+ momenta must provide sufficient resolution in this variable, specifically on the $K^+ \to \pi^+\pi^0$ peak, to isolate decays outside of the two signal regions which are defined in the missing mass squared distribution as shown in figure 3.1. The resoloution on the $K^+ \to \pi^+\pi^0$ peak which lies between the two signal regions is vital in order to prevent events in the tail of this decay distribution from providing fake $K^+ \to \pi^+\nu\overline{\nu}$ candidates. The non kinematically constrained backgrounds must be controlled by sufficient detection of all the decay products of such decays. Distributions for some non kinematically constrained decays are shown in figure 3.1. These decays cannot be isolated from signal the signal regions and as such vetoing events with photons and/or muons in the downstream detector is vital.

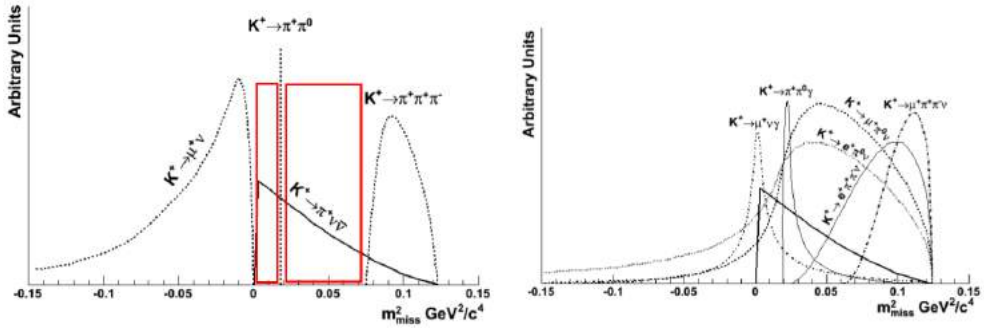

Figure 3.1: Left: The kinematically constrained K^+ decays with the $K^+ \to \pi^+\nu\overline{\nu}$ distribution overlayed. Note that the frequency of the $K^+ \to \pi^+\nu\overline{\nu}$ distribution has been exaggerated here in both distributions for illustrative purposes. Highlighted in red are the areas which are defined as the signal regions for the $K^+ \to \pi^+\nu\overline{\nu}$ decay. Right: The non kinematically reducible decays which must be removed from the $K^+ \to \pi^+\nu\overline{\nu}$ using the veto detector systems.

The NA62 experiment[37] is situated at the CERN North Area and uses the same extraction line used previously by the NA48 experiment. A schematic of the CERN accelerator complex with the North Area highlighted is shown in figure 3.2. The mixed hadron beam is produced by impinging 400 GeV/c protons from the SPS [38] on a beryllium target to produce a beam consisting of protons, pions and kaons. A series of collimators and magnets are placed between the target and the first sub-detector. The collimators and magnets remove muons from the beam and provide a 750 MHz hadron beam with momentum, p, of 75 GeV/c with $\delta p/p$ of 1%. The fluxes of particles at the beginning of the fiducial decay volume are summarised in table 3.1 along with the beam size.

Flux at Beginning of Fiducial Decay region	p	173 MHz
	K^+	45 MHz
	π^+	525 MHz
	e^+	0.3 MHz
	μ^+	6 MHz
Beam Size (rms)	x	$\pm$27.5 mm
	y	$\pm$11.4 mm

Table 3.1: Fluxes at the beginning of the fiducial region, $\sim$100 m downstream of the target. Also given are the r.m.s of the beam [38].

From the first sub-detector to the beam dump the experiment is over 200m long. A two dimensional schematic of the NA62 experimental design is shown in figure 3.3. A 60m long fiducial decay region is situated after the KTAG and GigaTracker sub-detectors which are designed to identify the K^+ in the beam and measure it's position and momentum prior to entering the decay volume, Section 3.1. After the decay volume come the detectors which are designed to identify the kaon decay products and measure their momentum, Section 3.2. In addition to these detectors there are several muon and photon veto detectors which are designed to veto events which are part of the irreducible background for the $K^+ \to \pi^+\nu\overline{\nu}$ decay, Section 3.3. The high rate nature of the experiment requires high performance triggering and data acquisition, Section 3.4. Throughout this Chapter all figures, design specifications and performance requirements are taken from the NA62 Technical Design Report (TDR) [37] unless otherwise stated.

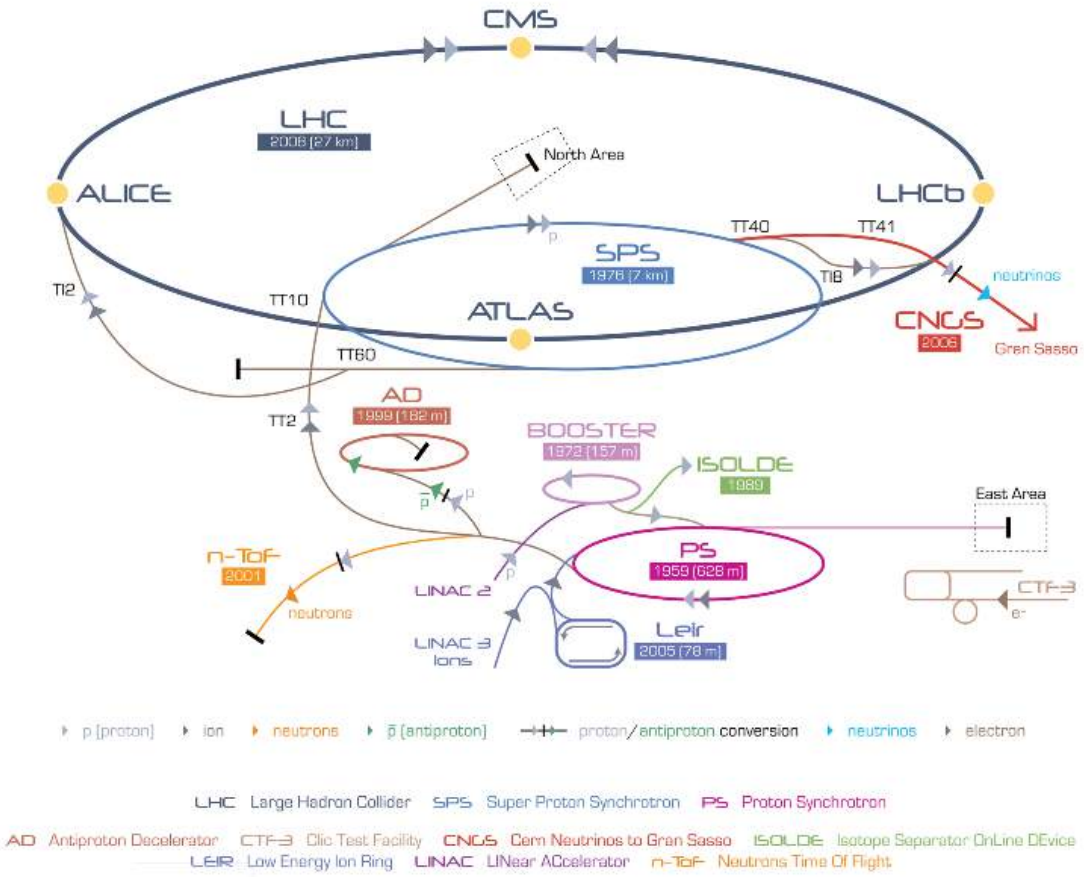

Figure 3.2: A schematic view of the CERN accelerator complex. The NA62 experiment is located at the north area SPS extraction line. Note that the image is not to scale.

3.1 Kaon Identification and tracking

Two sub-detectors which are responsible for identifying the K^+ and measuring it's position and momentum in the beam are the KTAG and the GigaTracker. The KTAG detector is responsible for positively identifying the K^+ whilst the GigaTracker measures the position and momentum of the K^+ within the beam.

3.1.1 KTAG

The KTAG detector is an upgrade of an old CEDAR (ChErenkov Differential counter with Achromatic Ring focus) west differential Cherenkov detector. It is the first subdetector of the beam line and is situated ∼70 m downstream of the target. It is required to positively identify the 6% K^+ component of the 750 MHz mixed hadron beam. A more detailed discussion of the construction and installation of the KTAG PMT housing is given in Chapter 4. The CEDAR vessel is a differential Cherenkov detector designed to run with nitrogen which has the

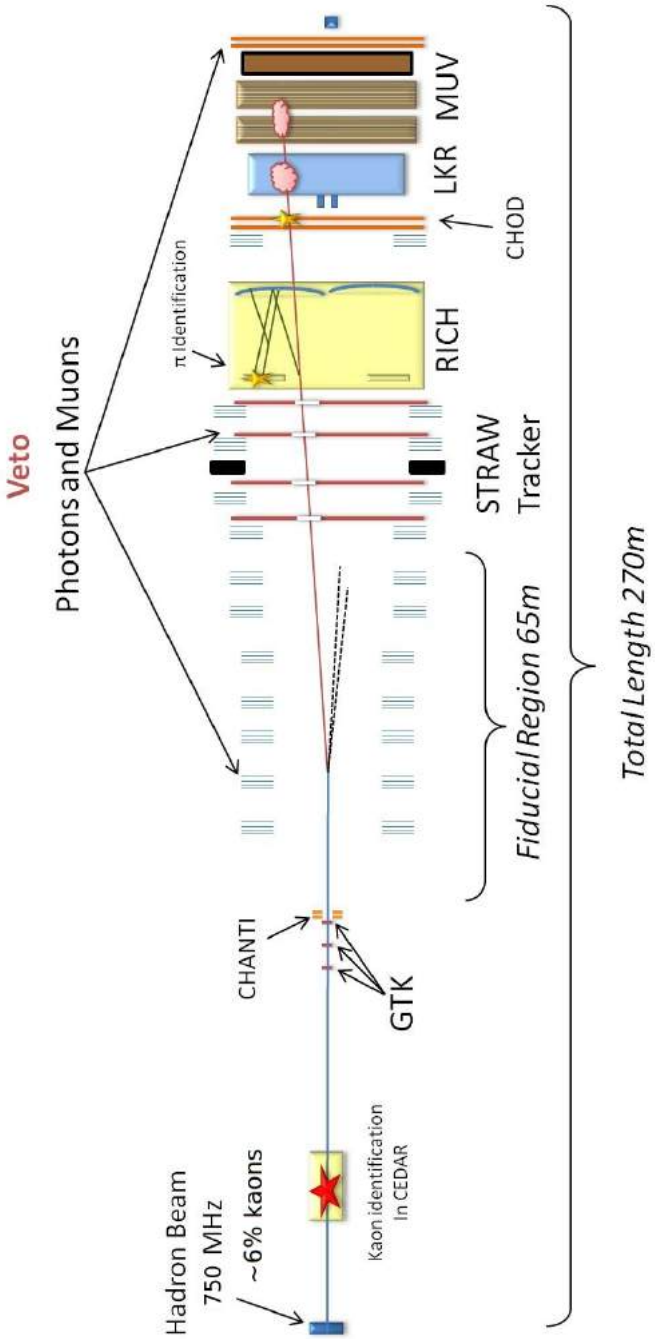

Figure 3.3: Layout of the NA62 experiment as viewed in the y-z plane. (not to scale)

ability to operate with either hydrogen or nitrogen as the Cherenkov medium. A study of the advantages and disadvantages of using hydrogen or nitrogen in the detector is given in Chapter 5. A schematic of the CEDAR vessel is shown in figure 3.4. The principle of the detector is as follows, beam particles entering the gas volume emit a cone of Cherenkov light, the angle of the emitted light, θ, is

given by,

$$\cos\theta = \frac{1}{n\beta}, \tag{3.1}$$

where β is the velocity of light in units of c and n is the refractive index of the radiator gas. How this is dependent on the mass of the incident particle is given in the next Chapter which is dedicated to the CEDAR KTAG detector. For a given beam momentum the pion, proton and kaon components will produce light cones of varying radius. The light is then reflected by a spherical mirror onto an adjustable diaphragm at the entrance of the vessel. A chromatic corrector lens designed to correct for the dispersion in the gas is placed before the diaphragm. By adjusting the diaphragm aperture we can remove light originating from unwanted pions and protons.

The KTAG extension to CEDAR is necessary in order to identify kaons at an incoming rate of 45 MHz and provide time resolution for each K^+ of at least 100 ps. This time widow is required in order to reduce the background introduced by incorrect association of the K^+ with downstream decay products and to assure that the detected K^+ is the only particle in the time window given the 750 MHz total beam rate. To achieve this Cherenkov light exiting the CEDAR through one of the eight quartz windows is reflected through 90 degrees by a spherical mirror which disperses the light over an array of Photomultiplier Tubes (PMTs) held in 8 light guides. This increased number of PMTs is aimed at dealing with the large K^+ rate of 45 MHz and can provide a K^+ tagging efficiency of over 95%. Each light guide itself is a spherically curved aluminium segment containing 64 conical holes which will each house a PMT. These PMTs generate heat which is removed using a re-circulating chiller. The KTAG front end system is based on 8 ultra fast NINO[37] amplifier/discriminator chips, which pass the analogue signal to the TEL62 readout boards which are common to most of the detector. The TEL62[37] boards, digitise the signal and read out the detector if an event is triggered. A more detailed description of the NINO chip and TEL62 board will be given in Chapter 4 which focuses on the operation of the KTAG detector in much more detail.

3.1.2 GigaTracker

The next sub-detector on the beam line is the GigaTracker (GTK) [37] and is situated approximately 30 m downstream of KTAG and immediately before the fiducial decay region. The GTK is a central detector of the NA62 set up as it measures the position and momentum of the K^+ in the beam which is needed for the kinematic based rejection of major decay modes.

The GigaTracker must satisfy the following requirements which are evaluated

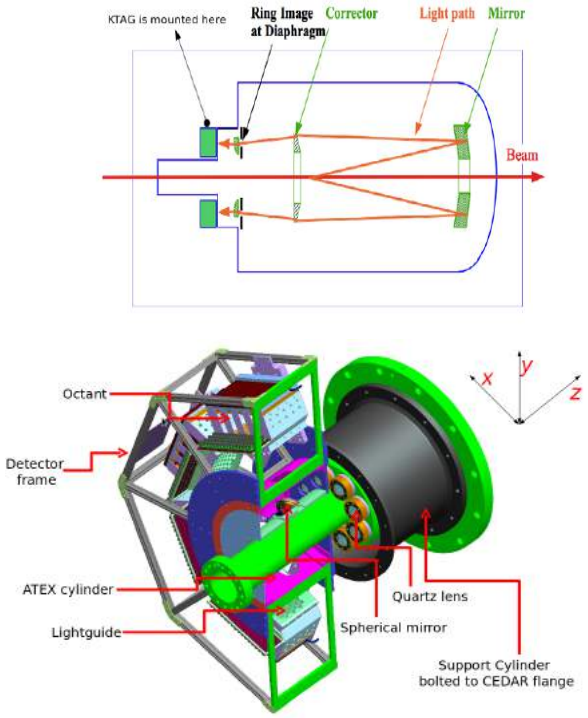

Figure 3.4: Top: A schematic layout of the CEDAR detector. Bottom: A cutaway schematic of the KTAG detector with important components labelled. The axes given are for the spherical mirror shown.

from the expected beam intensity and extensive Monte Carlo simulation,

- The sensor must be able to withstand a rate of 1.4 MHz/mm^2 from the beam, in order observe to the entire flux of the beam.
- The GigaTracker must have time resolution of better than 150 ps due to the high rate environment. This is to provide a positive correlation both with the KTAG identification and with the various downstream components.
- The GigaTracker must be able to measure the momentum with resolution, $\sigma(p)/p \sim 0.2\%$ and direction with a resolution of 16 μrad. These values in conjunction with the downstream spectrometer measurements allow the measurement of the kinematic peak (figure 3.1) produced by the $K^+ \to \pi^+\pi^0$ decay to be sufficiently constrained from the $K^+ \to \pi^+\nu\overline{\nu}$ signal regions.

The GigaTracker is a silicon spectrometer consisting of three stations, the second of which is offset by 60mm and sits between two magnetic fields in order to provide a measurement of the beam particle's momentum, as can be seen in the schematic layout, figure 3.5. Each GTK station is a hybrid silicon pixel detector measuring 63.1 mm $\times$ 29.3 mm, each station consists of 18000 pixels arranged 90 $\times$ 200. A single pixel is $(330 \times 300)\mu m^2$ and has a thickness of 200 μm. The total material budget for one station, including Sensor, readout chip, bump bonding

and cooling is less than 0.5% X_0, where X_0 denotes radiation length. A station is composed of 10 bump bonded TDC based readout ASICs [37], called TDCPix, as can be seen in figure 3.6 [37]. Each TDCPix delivers a time resolution of 200 ps for each pixel hit and is capable of withstanding 210 MHits/s.

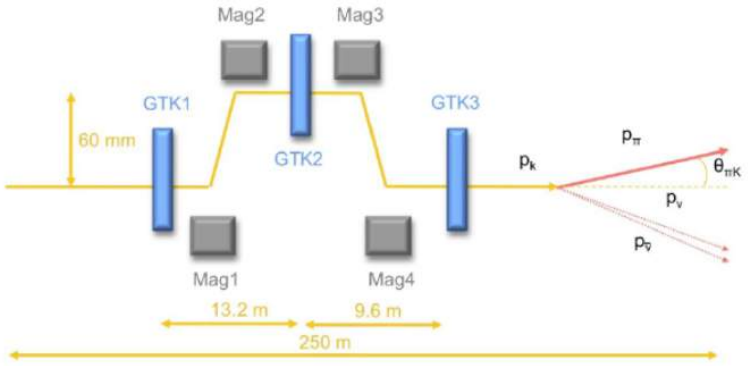

Figure 3.5: Schematic of the GigaTracker stations layout.

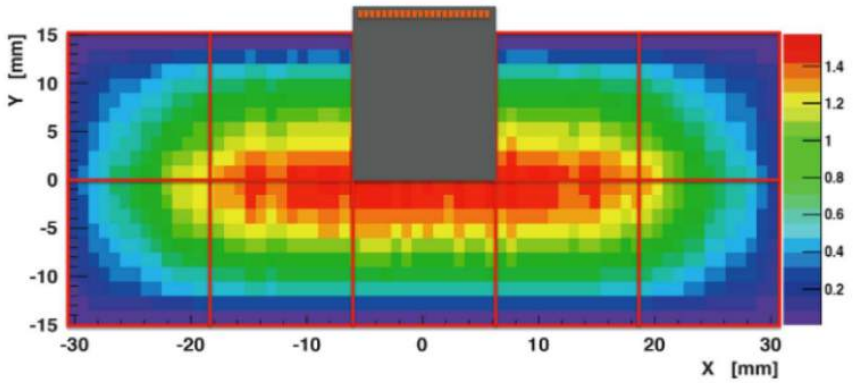

Figure 3.6: Beam intensity distribution for the third GTK station (MHz/mm^2). Each station is divided into 10 (2×5) readout chips with. A schematic of one of the chips overlayed.

3.2 Pion Identification and tracking

Downstream of the fiducial decay volume there are a series of detectors whose aim is to measure the position and momentum of the K^+ decay products and identify the decay particles accordingly. The measurement of the position and momentum of the decay products is primarily performed by the Straw spectrometer. The Charged Hodoscope can also be used to provide information regarding tracks which may enter into the level 0 trigger. The Ring Imaging Cherenkov detector (RICH) is placed downstream of the straw spectrometer and is designed

to provide particle identification of the decay products. For the $K^+ \to \pi^+\nu\overline{\nu}$ decay the decay product of interest is the π^+.

3.2.1 Straw Spectrometer

The straw magnetic spectrometer is designed to measure the direction and momentum of the secondary charged particles coming from the decay region. It will also be used in the higher level trigger to discriminate between single and multi track events. The required performance of the detector is a momentum resolution of $\sigma(p)/p \sim 1\%$ and a spatial resolution of 130 μm in order to correctly reconstruct the decay vertex with low track reconstruction inefficiency [37]. This resolution when combined with the measurement of the upstream K^+ corresponding values provides the design resolution on the peak $(P_K - P_\pi)^2$ variable such that the major background arrising from $K^+ \to \pi^+\pi^0$ is kinematically constrained from the $K^+ \to \pi^+\nu\overline{\nu}$ signal regions. The nominal electron drift time in the straws is approximately 150 ns and as such the timing of each track is provided by a geometrical matching of the propagated track with the downstream RICH and CHOD detectors.

The schematic layout of the four straw chambers along with the MNP33 magnet [37] is shown in figure 3.7. Each straw chamber contains 1792 straws spread across 16 layers of 122 straws. There are 4 orientations of layers named x, y, u, and v views as outlined in figure 3.8. The distance between the straws in each layer is 17.6 mm.

The individual straws are 2.1m long with a diameter of 9.8mm. The tubes are made from 36 μm thin PET foils. The inside is coated with two metal layers, 0.05 μm of copper and 0.02 μm of gold to provide conductance on the cathode. The anode wire is made from gold-plated tungsten and is 30 μm in diameter. The use of the very thin materials in the straws minimizes the amount of Coulomb scattering in the material, the total thickness of one full chamber is less than 0.5% X_0.

The MNP33 magnet lies between the third and fourth chambers. It is 1.3m long and has an integrated field off 0.858 Tm producing a transverse momentum kick of 257.4 MeV/c. The presence of the magnetic field allows a determination of the momentum to the required 1% as well as giving a clear indication of the charge of the track. The straw spectrometer front end electronics is the 8-channel CARIOCA chip which was developed for LHCb [37]. It is not read out with the common TEL62 system but with dedicated straw readout boards.

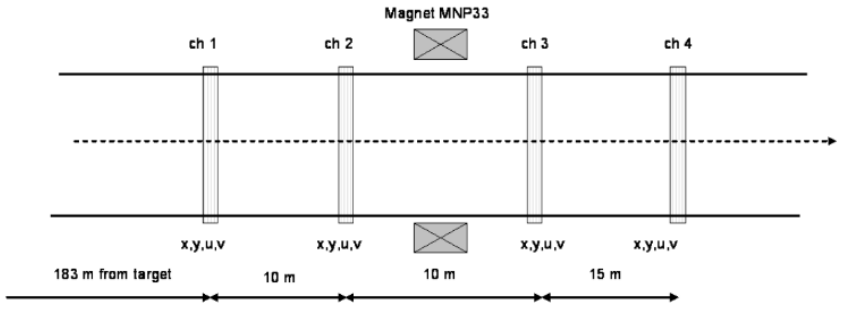

Figure 3.7: A schematic view of the four straw planes as viewed in the y-z plane.

3.2.2 CHOD

The Charged Hodoscope (CHOD) currently being used for the NA62 experiment [37] is the same detector that was used for NA48. It is placed immediately after the RICH vessel and before the LKr electromagnetic calorimeter. The CHOD has two main functions for the NA62 experiment. Firstly it must detect photonuclear interactions which can occur in the RICH mirror and secondly it provides a complementary level zero trigger for charged tracks, alongside the RICH.

The RICH mirrors correspond to around $0.2X_0$ for photons. High energy photons from π^0 decay can therefore undergo photonuclear interactions in the RICH mirrors and produce low energy hadrons. The LKr as a subsequent photon veto detector (Section 3.3.2) can lose sensitivity. Detailed Monte Carlo simulations show that the photon veto capability of the LKr can be fulfilled if events with photon interactions in the RICH are identified as additional tracks in the CHOD.

The CHOD is composed of two planes of BC408 plastic scintillator slabs offset by 30 cm oriented vertically and horizontally as can be seen in figure 3.9. Each plane contains 64 slabs which vary in length from 60 cm to 121 cm. The width of each slab also varies from 6.5 cm close to the beam to 9.9 cm in the outer regions. Each slab is 2 cm thick which corresponds to $0.05X_0$. The central hole of the CHOD is 21.6 cm in diameter in order to allow the beam to pass through.

The scintillation light produced in each slab is collected at the edge of the slab by a Plexiglas fishtail shaped lightguide connected to a PMT. The timing difference in the front and back planes of the CHOD can be used to identify coincidences from genuine charged tracks as opposed to accidental coincidences, for example from the backsplash of electromagnetic showers coming from the LKr surface.

The CHOD can achieve a timing resolution of around 200 ps. This is necessary to time align any CHOD hits with the RICH to provide sufficient vetoing of the intended photonuclear reactions in the RICH mirror. The information produced by the CHOD on the timing of charged tracks complements well the information

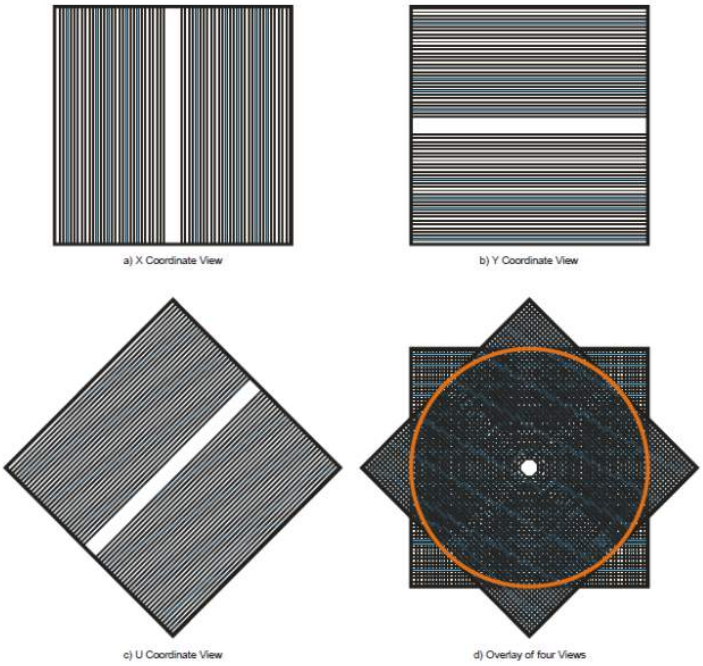

Figure 3.8: Drawing illustrating the four different straw tube layouts. a) is the x-coordinate layout with vertically arranged straws. b) is the y-coordinate layout with horizontally arranged straws. c) is the u-coordinate layout with the straws oriented at 45°, note the v-coordinate view is the reflection of c). An overlay of all four views is shown in d).

produced by the RICH for selecting single track events at the level 0 trigger. The CHOD uses the LAV front end electronics and is read out using the common TEL62 system.

3.2.3 RICH

The Ring Imaging Cherenkov detector (RICH) [37] is the primary particle identification detector for the K^+ decay products. It is situated immediately after the fourth straw chamber and before the charge hodoscope. The detector requirements are as follows:

- Identify π^+ and μ^+ in the 15 to 35 GeV/c momentum range with a muon suppression factor of at least 10^{-2}. The lower bound here is determined by requiring sufficient photon vetoing efficiency in subsequent detectors whilst the upper bound is the region in which π^+/μ^+ separation becomes inefficient in this detector.

- Measure the π^+ time to resolution of at least 100 ps. This allows for timing association with the upstream K^+ to reduce background from accidentals and sufficiently measure the kinematic variable of $(P_K - P_\pi)^2$.

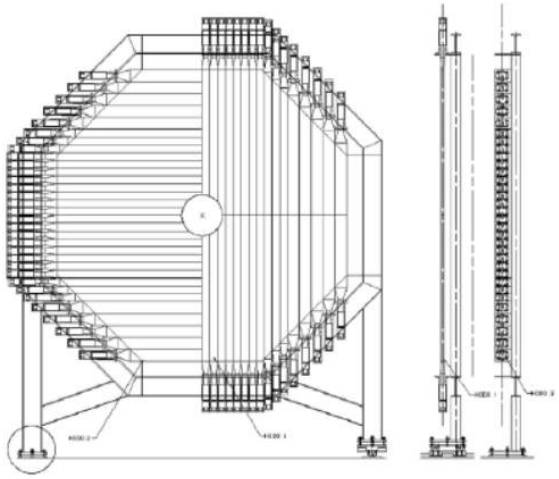

Figure 3.9: A sketch of the two CHOD planes as viewed on the left looking down the beam and on the right side on.

- Provide a L0 trigger to discriminate single and multi charged track events.

The RICH vessel is a 17m long cylindrical tank with neon acting as the Cherenkov radiator. The volume of neon corresponds to 0.056 X_0. An aluminium beam pipe composed of three interlocking segments of 20 cm, 22 cm and 24 cm diameter allow the undecayed component of the beam to pass through the volume without interacting with the neon. A schematic view of the detector is shown in figure 3.10.

As was the case for the upstream KTAG Cherenkov detector, for a known momentum of a passing particle the radius of the emitted light cone is dependent only on the mass of the particle. The choice of neon at atmospheric pressure as the radiator is motivated by requirement to separate π^+ and μ^+ in the 15 to 35 GeV/c momentum range. The number of emitted photons through a radiator per unit of photon energy is given by, $\frac{d^2N}{dxdE} \propto \sin^2\theta_c$ and the momentum threshold, $p_t = m/\sqrt{n^2-1}$ below which no light is emitted. If we assume a momentum threshold of 12.5 GeV/c for pions, so that rings produced at 15 GeV/c can be efficiently detected and reconstructed by the RICH, then this corresponds to a choice of neon at atmospheric pressure such that $(n-1) = 62 \times 10^{-6}$.

The produced Cherenkov light is reflected by an array of 18 hexagonal mirrors and two semi hexagonal mirrors (to allow for the beam hole) placed at the downstream end of the tank and arranged as can be seen in figure 3.11. The mirrors are designed such that the focal length corresponds to the length of the RICH vessel. The light from each half of the mirror array is then focussed upstream on two separate PMT arrays. The use of two separate PMT arrays is to prevent any absorption of reflected Cherenkov light by the beam pipe. The centre of each PMT array is 1.2 m either side of the beam pipe and contains 960 PMTs and

image of one of the PMT arrays can be seen in figure 3.11. Each PMT has an active area with diameter 8 mm and a Winston cone is used to collect light from an area of 18 mm in diameter. The front end electronics is much the same as for the KTAG read out where the PMT signals are processed by a NINO chip [37]. The readout of the 1920 channels is then done using the common TEL62 system.

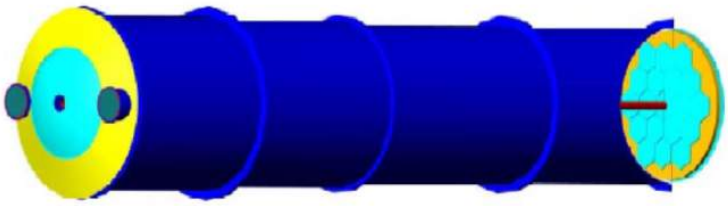

Figure 3.10: A schematic view of the RICH vessel with a cutaway the the right hand end showing the hexagonal mirror array.

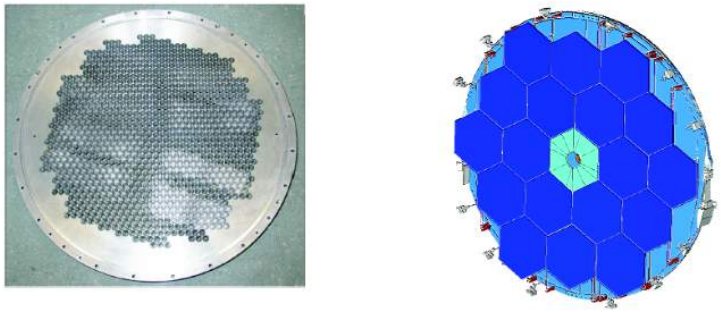

Figure 3.11: Left: One of the PMT flanges which house the PMTs. On the right a drawing of the RICH mirror array.

3.3 Veto system

The veto detectors for NA62 can be separated into three specific categories. The first is the CHANTI detector designed to veto inelastic interactions in the Giga-Tracker. The second are the photon vetoes which are four different detectors that when combined give photon veto coverage in the 0 to 50 mrad region. Finally we have the muon vetoes which are used to suppress events containing muons at trigger level and also provide further separation between μ^+ and π^+.

3.3.1 CHANTI

Inelastic interactions can occur in the upstream material, be it the CEDAR gas or the three silicon GTK stations [37]. The majority of the inelastic events are

removed due to the presence of a collimator between the second and third GTK stations. The third GTK station however is immediately exposed to the decay volume. A non negligible background to the $K^+ \to \pi^+\nu\overline{\nu}$ analysis is when a beam K^+ interacts inelastically with the third GTK station. If a π^+ is produced and detected in the downstream detectors whilst the other particles produced in the interaction remain undetected then these events will have a $K^+ \to \pi^+\nu\overline{\nu}$ like signature. The CHANTI is required to detect such events as can be seen in the schematic shown in figure 3.12.

The probability of a K^+ inelastically scattering in GTK3 is 10^{-3}. The purpose of the CHANTI is to detect events with inelastic interactions in the third GTK station. The CHANTI detector consists of 6 stations placed at 27, 77, 177, 377, 777, and 1577 mm from GTK3. Each station is a rectangular formation of scintallator bars with square outer sides of length 300 mm and a rectangular inner hole of 50 mm in y and 90 mm in x to allow for the beam. The angular coverage for particles originating at the centre of GTK 3 is between 34 mrad and 1.38 rad.

Each station is composed of two layers of 22 and 24 triangular prism scintillator bars in the x and y directions. Wavelength shifting fibres in each bar transport the scintillation light to a silicon PMT. The CHANTI will be exposed to both the inelastic rate and also the muon halo rate which is present near the beam. A timing resolution below 2 ns is required in order to cope with the expected 2 MHz rate.

The CHANTI is able to veto 95% of K^+ inelastic interactions. If we consider only the events which would be signal like, namely where the kaon does not survive the interaction or does not decay the overall vetoing efficiency for signal like events increases to 99%. A time over threshold output is produced by the LAV front end electronics which is then sent to the TEL62 readout system.

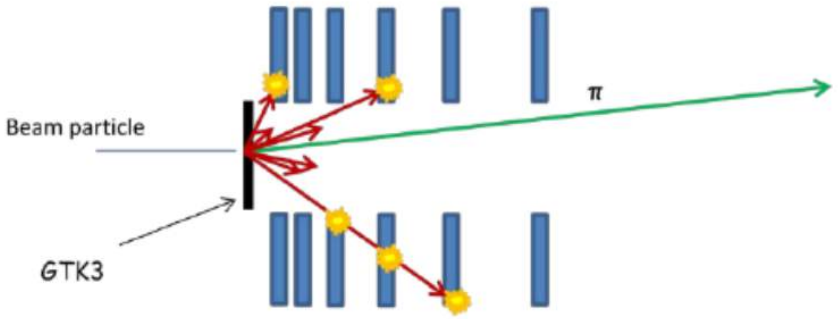

Figure 3.12: A sketch highlighting the purpose of the CHANTI. The CHANTI stations (blue) are intersected by inelastic interaction products (red) whilst a pion continues downstream (green).

3.3.2 Photon Vetoes

The photon veto system is composed of four subdetector systems. The required performance of the detector is driven by the background $K^+ \to \pi^+\pi^0$ decay, requiring a total π^0 inefficiency of the order 10^{-8}. The angular coverage and required efficiency of each subdetector system is as follows. The Large Angle Veto(LAV) system covers the region from 8.5 to 50 mrad, providing photon inefficiencies of 10^{-4} for photon energies greater than 0.5 GeV. The Liquid Krypton electromagnetic calorimeter (LKr) covers from 1 mrad to 8.5 mrad and provides photon detection inefficiency of 10^{-5}. The remaining small angle coverage from 0 to 1 mrad is provided by the IRC and SAC detectors and also provides a photon inefficiency of 10^{-5} due to the high energy nature of photons in this region. The combination of these three detectors reduces the kinematically constrained decays where photons are detected such as $K^+ \to \pi^+\pi^0$ whilst also providing a crucial veto on the non kinematically constrained decays such as $K^+ \to \pi^+\pi^0\gamma$. What follows is a description of each of the three photon veto systems along with the required associated performance to achieve the above inefficiencies for photon detection.

LAV

The Large Angle Vetoes (LAVs) are a series of 12 circular photon veto detectors placed at various points along the beam line which give an angular coverage from 8.5 to 50 mrad to provide a veto against K^+ decays with photons at large angles.

The LAV stations use the lead glass blocks recycled from the OPAL electromagnetic calorimeter barrel [39]. The lead glass blocks are around 75% lead oxide by weight and have a density of $\rho = 5.5$ gcm^{-3} with a radiation length of 1.50 cm. The index of refraction for the material varies from 1.85 to 1.91 in the wavelength range 550 to 400 nm. The electromagnetic showers in the glass produce Cherenkov light. On average minimum ionising particles produce 0.34 photoelectrons per MeV of deposited energy.

Each block is 37 cm long and is 10×10 cm^2 at the front face increasing to 11×11 cm^2 at the rear face. The dimensions of a single block are superimposed on the image shown in figure 3.13. Each block is read out by a PMT coupled at the rear face by a 4cm long light guide.

A LAV station is composed of rings of lead glass blocks aligned radially along a segment of the vacuum tank to form a ring, see figure 3.13. Of the 12 LAV stations the first 8 contain five layers of blocks whilst the remaining 4 contain only 4. The rings in each station are staggered in azimuth to ensure full coverage. As a result of the staggering the majority of incident particles traverse at least 4 blocks (27 X_0). The length of the first 8 stations is 1.55 m, the last 4 stations

are 1.43 m long. The diameter of the stations increases the further downstream they are placed. A summary of the LAV station geometry is given in table 3.2.

Figure 3.13: Left: One of the lead glass modules with dimensions overlayed. Right: The completed first LAV station with all 5 layers of lead glass visible.

Station	Diameter(mm) Outer Wall	Layers	Blocks
1-5	2168	5	160
6-8	2662	5	240
9-11	3060	4	240
12	3250	4	256

Table 3.2: Geometrical parameters for all LAV stations.

The LAVs provide time and energy measurements by using a time over threshold readout technique. A front end discriminator board converts the analogue signals to low voltage differential signals. The TEL62 system is again used for the readout. Results from a test beam using the LAV stations showed a single block time resolution of 140 ps, and an energy resolution of 2.5% [40].

LKr

The photon veto in the intermediate range 1 mrad to 8.5 mrad is performed by the Liquid Krypton electromagnetic calorimeter (LKr). The LKr is placed immediately after the CHOD and is 1.27 m in length corresponding to about 27 radiation lengths and as such fully contains electromagnetic showers coming from photons.

The NA48 experiment required an electromagnetic calorimeter with excellent energy, position and time resolution which was also capable of accurate charge calibration and was stable in the long term [40]. The NA62 experiment reuses this calorimeter as the main photon veto of the experiment. The LKr is an almost homogeneous ionisation chamber. Photons and electrons entering the chamber produce electromagnetic showers via repeat Bremsstrahlung and pair production processes until the energy is below critical. The shower particles then ionise the krypton atoms to generate electron-ion pairs proportional to the deposited energy. The electrons are then accelerated toward the anode before they can recombine but do not have enough energy to produce secondary ionization. The choice of liquid krypton ensures a linearity of response in energy along with good resolution. A relatively short radiation length allows a compact design without the need for heavy passive parts. The radioactivity of the krypton is negligible when compared with the electronic noise. The boiling point of krypton is 120 K and as such the whole detector must be kept in a cryostat where temperature variations must be kept small due to the electron drift velocity being proportional to the temperature ($\delta v_d/v_d \propto \delta T/T$).

The LKr is octagonal in shape, inscribed by a circle of radius 128 cm and is 127 cm deep. The volume of the LKr is divided into 13,248 cells which are 18 mm wide, 40 μm thick copper-beryllium ribbons each separated by 1 cm with no longitudinal segmentation. Each ribbon is an electrode which collects the ionisation signal. A cell contains a central anode with an applied voltage of 3 kV, two cathodes are placed such that each cathode has two cells in common. The separation between layers is 2 mm. The cells are not straight but rather are arranged in a zig-zag shape in order to avoid response variations depending on the lateral distance between shower core and anode. The structure of the LKr electrode is shown in figure 3.14. The energy resolution of the LKr was measured by using an electron beam of fixed momenta and can be parametrised as,

$$\frac{\sigma(E)}{E} = \frac{3.2\%}{\sqrt{E(GeV)}} \oplus \frac{9\%}{E(GeV)} \oplus 0.42\%,$$

where the first term is from stochastic fluctuations, the second due to electronic noise and the last from the uncertainty of inter cell calibration. For a typical 20 GeV shower the energy resolution is around 1%. The resolution on the spatial position of the shower is measured to be,

$$\sigma_x, y = \frac{0.42cm}{\sqrt{E(GeV)}} \oplus 0.06cm.$$

For a typical 20 GeV energy shower the spatial resolution is around 1.1 mm in x and y. The time resolution for a single shower is around 500 ps. The LKr readout utilises a current sensitive mode taking the initial induced current proportional to the ionisation generated by the LKr. The sampling and digitization of the signal

is performed every 25 ns by a flash ADC based calorimeter readout (CREAM). A zero suppression is applied in the data to only read out cells above a certain energy. A detailed discussion of zero suppression is given in Chapter 6.

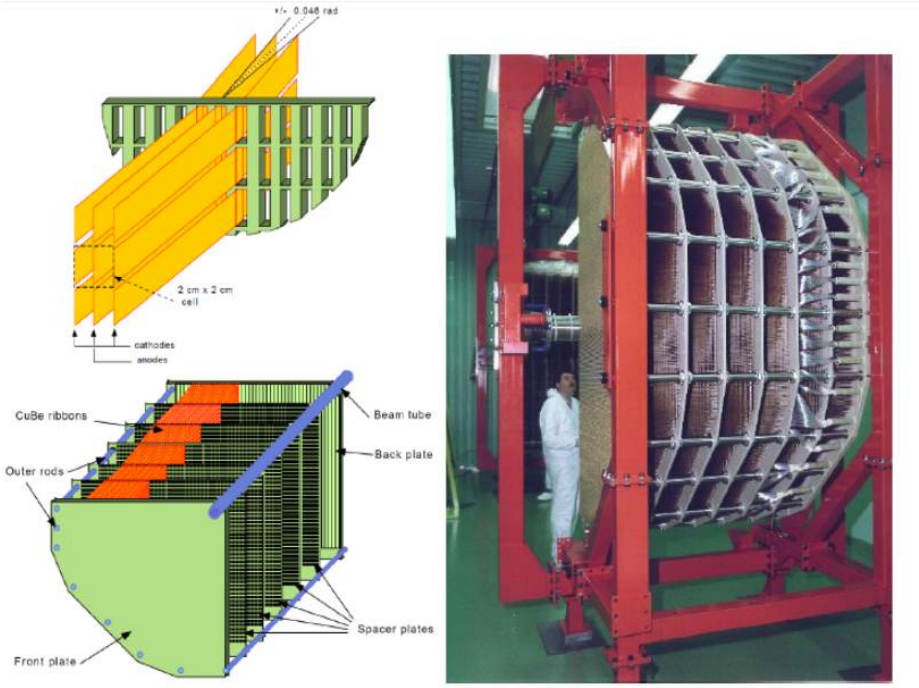

Figure 3.14: Left: Structure of the LKr electrodes showing the formation of LKr cells. Right: A picture of the completed LKr detector.

IRC and SAC

The Inner Ring Calorimeter (IRC) [37] and Small Angle Calorimeter (SAC) [37] are the two small angle veto detectors which cover the region less than 1 mrad not covered by the LAVs and LKr. Both detectors must provide detection inefficiency of the order 10^{-5}. The timing of the detctors is required to be similar to that of the timing for showers in the LKr of around 500 ps. Both detectors are Shashlyk calorimeters such that they are composed of consecutive layers of lead and plastic scintillator as shown in figures 3.15 and 3.16. When photons enter the lead layers they begin to shower and the electromagnetic products produce scintillation light in the next layer. Wavelength shifting fibres take the scintillation light out of the material to a photomultiplier. The PMTs of both detectors are read out by the GANDALF board [37] equipped with ADC based mezzanines.

IRC

The IRC [37] lies between the CHOD and LKr detectors. It is ring shaped as can be seen in figure 3.15 and is placed close enough to the beam that it covers a central region which the LKr does not, but is also far enough away from the

beam that the total rate does not exceed 6 MHz. Of this 6 MHz only around 100 KHz comes from photons with the majority being muons originating from the beam halo.

The cylindrical tube structure of the IRC has two active regions, the first with 25 layers and the second with 45. Each region is separated into 4 quadrants as can be seen in figure 3.15. The outer radius of the detector is centred on the z axis, whilst the inner radius is centred on the beam axis which is displaced by 1cm in the x direction at the IRC.

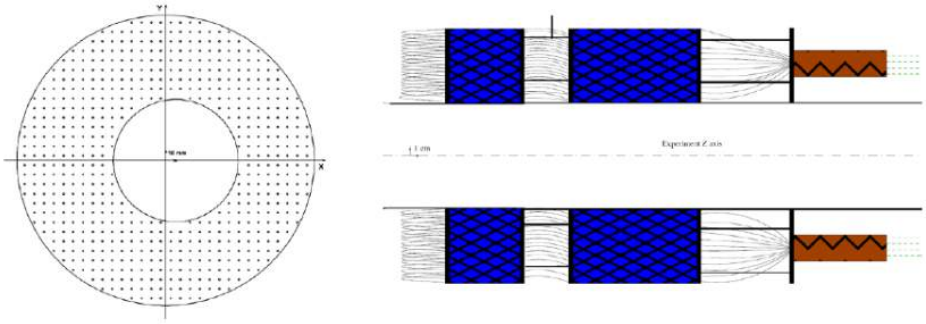

Figure 3.15: Left: Layout of the IRC detector as viewed looking down the beam line. Right: Side on sketch of the IRC.

SAC
The SAC [37] is the last detector of NA62 and is situated at the end of the experimental hall, around 20 m downstream of the IRC. It covers the remaining angular region corresponding to the central hole of the IRC. Between the SAC and the IRC there is a sweeping magnet to displace the beam. The SAC detects the undeflected photon component at the end of the hall and is exposed to rates of around 100 KHz. The SAC is composed of 70 1.5 mm lead plates with 1.5 mm scintillator between. The total length of the SAC is 21 cm corresponding to around 17 radiation lengths. This ensures a punch through probability below 10^{-5}. The 480 wavelength shifting fibres are divided into four channels read by 4 PMTs.

3.3.3 Muon Vetoes

The Muon Veto (MUV) system performs two key roles for the NA62 experiment. The first is to utilise the hadronic calorimeters MUV1 and MUV2 detectors to provide separation between π^+ and μ^+. When this information is used in conjunction with the the LKr electromagnetic shower information the muon detection inefficiency should be below 10^{-5}. This is in addition to the 10^{-2} muon detection inefficiency present from the upstream RICH detector. This is crucial in reducing

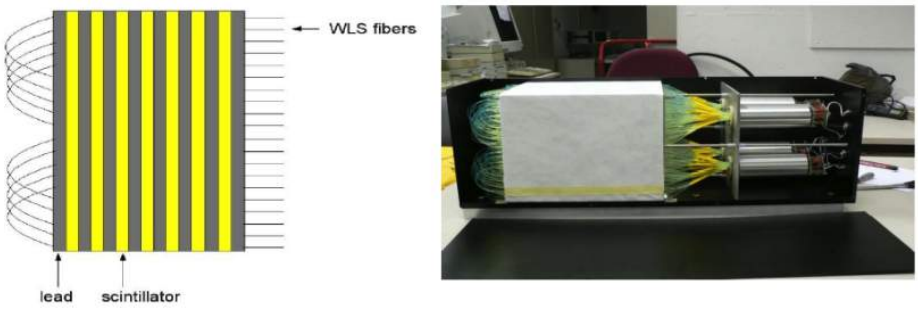

Figure 3.16: Left: General layout of a Shashlyk calorimeter. Right: picture of the SAC prototype.

non kinematically constrained decays such as $K^+ \to \mu^+\nu\gamma$. The MUV3 detector provides a fast response to allow muon suppression at the trigger level. The timing of this detector system should be less than 1 ns in order to provide a positive coincidence with the upstream KTAG measurement of the K^+ time and reject those events.

MUV1 and MUV2

The MUV1 and MUV2 detectors [37] are a pair of hadronic calorimeters which aim to discriminate between pions and muons via the shower shapes of the incident particles. The MUV1 and 2 detectors aim to provide muon reduction of 10^{-5} independent of the straw and RICH detectors.

The main rejection comes from requiring that only a small amount of energy is released when the muons traverse both the MUV1 and MUV2 detectors, however events in which muons undergo catastrophic Bremsstrahlung or pair production in the calorimeter deposit significant amounts of energy and to assure the 10^{-5} muon rejection power these events must be discriminated from pions via the shower shape.

The MUV1 and MUV2 module schematics are shown in figure 3.17, both detectors are typical iron-scintillator hadronic calorimeters. The MUV1 has 24 layers whilst the MUV2 has 22 which are alternatively arranged horizontally then vertically. The MUV1 is a new detector whilst the MUV2 is the NA48 hadronic calorimeter repositioned and rotated by 180°. Both the MUV1 and 2 detectors have a central hole of 212 mm diameter to allow the beam to pass through. The MUV1 detector has steel layers of $2700 \times 2600 \times 25$ mm^3 spaced out by 12 mm whilst the MUV2 has $2600 \times 2600 \times 25$ mm^3 which are also separated by 12 mm.

The scintillator strips in MUV1 are 6 cm wide and there are 48 strips per layer, as shown in figure 3.18. The readout is made by two wavelength shifting fibres per

scintillator strip. All fibres in one longitudinal row are bunched together to feed one PMT and so no longitudinal separation exists. The MUV2 planes consist of 44 wider 11 cm strips, with each one spanning half of the detector, as shown in figure 3.18. Consecutive strips with identical x(y) coordinate are coupled to the same PMT using Plexiglas light guides. MUV1 and MUV2 detectors are read out using the same ADC-based CREAM module used by the LKr calorimeter.

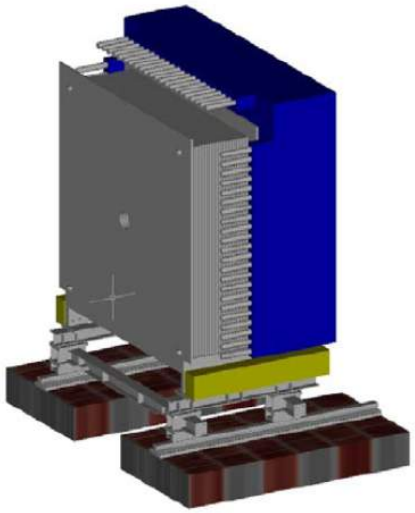

Figure 3.17: 3D Drawing of the MUV1 and MUV2 detectors shown in grey and blue respectively.

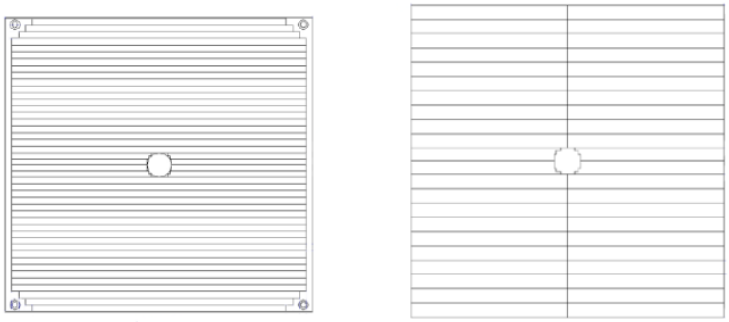

Figure 3.18: Layout of one (horizontal) layer of scintillators on the left for MUV1 and the right for MUV2.

MUV3

The third muon veto detector (MUV3) is located downstream of the first two stations and is behind an 80 cm iron wall in order to detect non showering muons. The MUV3 is also an important part of the level zero trigger system as over 60%

of all kaon decays produce final state muons.

The detector consists of an array of (12 × 12) 5 cm thick scintillator tiles, corresponding to an area of 22 × 22 cm^2. The PMTs are situated around 20 cm downstream allowing for a time resolution of 250 ps. The timing can be effected by Cherenkov light which reaches the PMTs earlier than the photons produced by the scintillator. In order to remove signals from Cherenkov light which spoil the time resolution, two PMTS are used per tile with the average time of the coincidence of the PMTs used.

A schematic diagram of MUV3 is shown in figure 3.19, along with a drawing of the dimensions and PMT set up for one tile. In order to better cope with the higher rate caused by the muon halo near the beam eight smaller tiles replace the 4 standard tiles that would have been in the very centre of the array. The MUV3 PMT outputs are sent to constant fraction discriminators which then pass the signal to the common TEL62 readout. Analysis from test beam data has shown the MUV3 design is capable of time resolution below 500 ps [41] which is what is required for this detector to be time aligned with the upstream detectors.

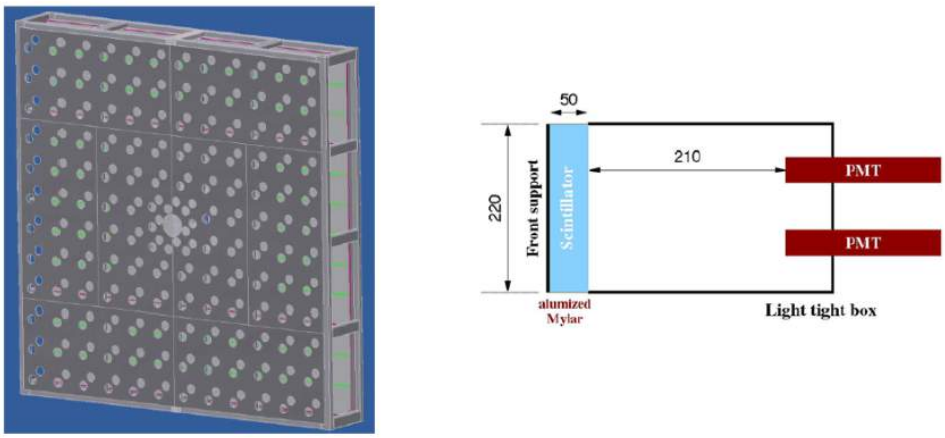

Figure 3.19: Left: The layout of scintillator tiles for MUV3 with two holes shown in each to house PMTs. Right: Side view of a single scintillator tile with associated PMTs, note particles would be incident from the left.

3.4 Trigger and DAQ System

The high fluxes required in order to operate a rare kaon decay experiment such as NA62 require high performance triggering and data acquisition. The number of channels and typical rate for the 12 sub-detector systems are summarised in table 3.3. The NA62 trigger system operates with a three tiered trigger system in

order to reduce the amount of data recorded to a manageable level. The trigger system is as follows;

- Level 0 - A hardware based trigger with input from some sub-detectors. The data is then readout to the PC farm.
- Level 1 - A software based trigger which takes the data sent to the PC farm and applies software based triggers from sub detectors independently.
- Level 2 - A second software based trigger which is capable of triggering on information from several sub-detectors at once.

The result of the trigger system is to reduce an input of around 10MHz to around 10KHz to be stored [42] [43]. An outline of the NA62 TDAQ system, as defined detector by detector in this Chapter, is shown in figure 3.20 as well as the effect of the various triggers. A more detailed description of the TEL62 system will be given in the next Chapter which is dedicated to the KTAG design, construction and performance.

Detector	Total Channels	Hit Rate (MHz)
CEDAR	384	50
GigaTracker	54000	2700
CHANTI	276	2
LAV	4992	11
STRAW	7168	240
RICH	1920	11
CHOD	128	12
IRC	4	6
LKr	13248	40
MUV	576	30
SAC	4	2

Table 3.3: The Total number of channels per subdetector and the rate expected on the whole detector.

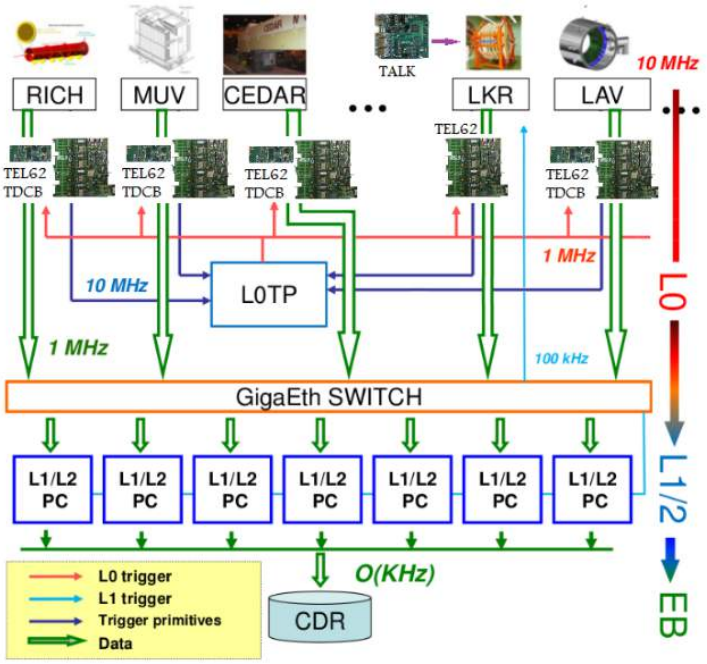

Figure 3.20: Scematic view of the NA62 TDAQ system with data entering the system via the subdetectors at the top to being stored on the CDR at the bottom.

Chapter 4

The KTAG Detector

The NA62 experiment is a high precision experiment that takes advantage of a high intensity beam rate of 750 MHz in order to fulfil its primary aim of measuring the $K^+ \to \pi^+\nu\overline{\nu}$ branching ratio to around 10% accuracy.

As outlined in Chapter 3 the incoming mixed hadron beam is 6% K^+, 70% π^+ with the remainder being protons. One kinematically irreducible background is when a beam pion is scattered before the downstream spectrometer and mimics the $K^+ \to \pi^+\nu\overline{\nu}$ decay signal of one π^+ in the downstream detectors with no photon or muon signal in additional detectors. To remove this background we must positively identify K^+ in the beam upstream of the decay volume.

Assuming an expected standard model branching fraction of the $K^+ \to \pi^+\nu\overline{\nu}$ of $O(10^{-10})$ the required efficiency of detecting kaons upstream is at least 95% with a π^+ contamination no larger than 10^{-4}. The timing resolution of each K^+ must be no greater than 100 ps. To fulfil these requirements the KTAG [45] detector is used on the NA62 beam line.

The environmental limitations in which the KTAG must be able to perform in are as follows,

- nominal instantaneous rate of 45 MHz,
- radiation level of 1 Gy/year.

The KTAG detector comprises two distinct systems, the CEDAR Cherenkov vessel and the KTAG photon detector, shown together on the beamline in figure 4.1. Section 4.1 details the physics behind the operation of the CEDAR detector along with a discussion of the required set up of the detector. Section 4.2 states the case for the KTAG extension of the CEDAR detector detailing the design. Detailed discussion is given in Sections 4.2.2 and 4.2.3 regarding the aspects of the detector construction which I was involved in. Finally Section 4.3 is a summary of the installation of the full detector which was performed in June 2013.

Figure 4.1: A picture of the CEDAR vessel and KTAG Detector in situ on the beam line.

4.1 The CEDAR Detector

The CEDAR differential Cherenkov detector is a 7m long, 60cm diameter gas vessel which acts as the Cherenkov radiator for passing particles [44, 46]. The CEDAR vessel is filled with N_2 at room temperature, although the option exists to run the detector with H_2 as the Cherenkov radiator. A study of the relative performance of running the KTAG with H_2 or N_2 and the effects of the wider NA62 experiment are given in Chapter 5. The emitted Cherenkov light is reflected back upstream via the CEDAR internal optics and an annular diaphragm then absorbs all light which does not correspond to light from K^+.

4.1.1 CEDAR Operational Physics

When charged particles pass through the gas radiator in the CEDAR Cherenkov photons are emitted to form a ring of radius $r = f \tan\theta_c$, where f is the focal length of the internal optics (3.24 m) and θ_c is the angle at which the Cherenkov light is emitted. The CEDAR detector is designed to only allow light cones of a given radius to pass through a diaphragm of radius 100 mm with an annular hole, w_{dia}, with an adjustable aperture width of 0 to 20 mm. The angular range selected from a given diaphragm aperture is given by,

$$(V_c^0 - 0.5w_{dia}/f, V_c^0 + 0.5w_{dia}/f), \text{ where } V_c^0 = 30.9mrad.$$

For a given monochromatic beam of momentum p, a particle of mass m_1 can be selected by tuning the pressure of the gas which changes the refractive index, n, as,

$$\cos\theta_c = \frac{1}{n\beta} = \frac{1}{n}\sqrt{1 + \frac{m_1^2}{p^2}}, \tag{4.1}$$

where β is the velocity of the particle in units of the speed of light, c. Tuning the diaphragm aperture for a given particle mass makes the CEDAR detector well suited to tagging minority particles in a high rate environment. The difference between the radius of the rings given by two distinct mass particles, m_1, m_2 is given by,

$$\delta R_C = f\delta\theta_c = \frac{f}{\tan\theta_c}\frac{\delta\beta}{\beta} \approx \frac{f^2}{R_{Dia}}\frac{|m_2 - m_1|^2}{2p^2}. \tag{4.2}$$

Assuming a beam momentum of 75 GeV/c with nominal π^+ and K^+ masses, it can be seen that $\delta R_C \approx 2$ mm. This is the idealised situation and in fact several effects that contribute to the broadening of the light cones must be considered when choosing the diaphragm aperture.

4.1.2 CEDAR Diaphragm Aperture

The choice of the diaphragm aperture is dependent on the broadening of the light ring. Broadening is caused by three main effects, beam divergence, chromatic dispersion, and multiple scattering.

Beam Divergence

The effect of each particle not travelling exactly parallel to one another has the effect of broadening the light cone. The estimated beam divergence $\Delta\theta_{x,y} = 80$ μrad (RMS) increases the RMS of the Cherenkov light cone by $\Delta R_{div} = f\Delta\theta_{x,y} \approx$ 0.26mm. This effect is coherent due to the fact that we are averaging over multiple particles.

Chromatic Dispersion

Chromatic dispersion occurs in the Cherenkov vessel due to the fact that the refractive index, n, of the material is dependent on the wavelength of the light, λ . The contribution to the broadening of the ring radius is given as follows,

$$\Delta R \approx \frac{R_{Dia}}{2\nu},$$

where ν is the Abbe number, which characterises the reciprocal dispersion of materials. $\nu = \frac{(n_D-1)}{(n_F-n_C)}$, where, n_D, n_F, n_C correspond to the wavelengths at 589.3 mm, 486.1 mm and 656.3 mm respectively. Nitrogen at an absolute pressure of 1.7bar [47] has an Abbe number of 35 corresponding to an increase in the ring RMS of $\Delta R \approx 1.4$ mm. The original design of the CEDAR contains a chromatic corrector lens which reduces the dispersion by a factor of 11 [46] resulting in an increase in the RMS of the ring of only $\Delta R \approx 0.13$ mm.

Multiple Scattering

If a particle changes direction inside the gas radiator the resulting Cherenkov rings will be non concentric and lead to a broadening of the ring at the diaphragm. The angular deflection (RMS) due to a particle travelling through $\frac{x}{X_0}$ radiation lengths(X_0) is described as follows,

$$\theta_{sc}(p) = \frac{1}{\sqrt{(3)}} \frac{13.6MeV}{\beta cp} \sqrt{\frac{x}{X_0}} \left[1 + 0.038ln\left(\frac{x}{X_0}\right)\right]. \tag{4.3}$$

The 75 GeV/c beam particles traversing the N_2 gas radiator are passing through $0.3X_0$ of material. The increase in the RMS of the ring from multiple scattering can then be calculated to be $\Delta R = f\theta_{sc} \approx 0.05$ mm.

The quadratic sum of the three contributions corresponds to a total ring RMS of $\Delta R_{Tot} = 0.3$ mm. A diaphragm aperture of width 1.5 mm then is sufficient to accommodate at least 99 % of the Cherenkov light produced by kaons and is greater than 3 standard deviations from the pion peak as shown in figure 4.2.

4.1.3 CEDAR Internal Optics and Alignment

Vessel Alignment

In order for the internal optics of the CEDAR vessel to function correctly and for the diaphragm aperture opening in the previous section to be valid the misalignment of the CEDAR vessel with respect to the beam axis must be as small as possible.

The total increase of the RMS of the ring due to the broadening effects outlined in Section 4.1.2 is quantified as 0.3 mm. The alignment of the CEDAR vessel must therefore be aligned to much better than 0.3 mm in both the x and y directions. To achieve this the CEDAR vessel has an alignment system that is made by moving two chariots downstream of the CEDAR vessel. Together

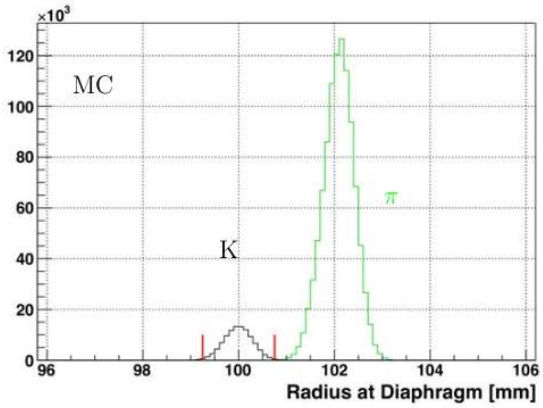

Figure 4.2: Expected ring radius for Cherenkov photons at the diaphragm for K^+ (black) and π^+ (green). The CEDAR is simulated containing nitrogen at 1.71 bar. The diaphragm opening for K^+ is overlayed. Extracted from MC simulations.

with these downstream chariots an additional pivot is fixed 4.35 m upstream on the CEDAR vessel forming a V-shape. The adjustable downstream pivots are attached to two motors with step resolution of 0.01 mm providing an angular resolution of 2μrad. A misalignment in Δx and Δy translates to an average ring displacement of $\Delta R_{al} = f\sqrt{\Delta x^2 + \Delta y^2}/l$.

CEDAR Optics

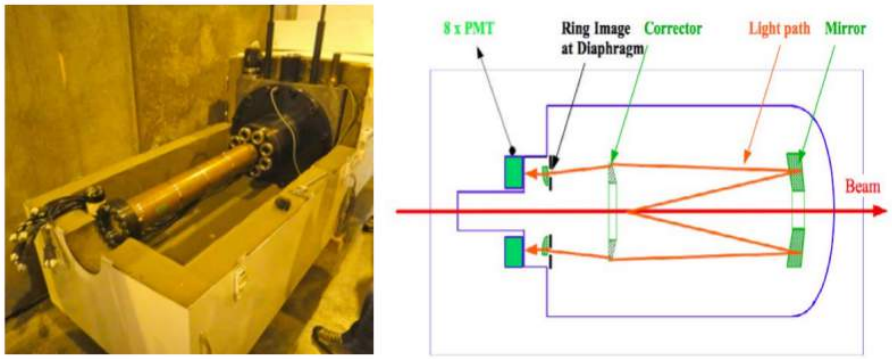

Figure 4.3: (a) A cut away picture of the CEDAR vessel with the nose and quartz windows visible. (b) 2D schematic of the CEDAR optical compenents with the light path for Cherenkov photons shown in orange.

The CEDAR vessel is 4.5 m long and made of steel with a 55.8 cm external diameter (53.4cm internal). The downstream end has a spherical head. The upstream end is closed by a 1 m long nose with two aluminium windows of 150 and 200 μm, which corresponds to 0.004 radiation lengths. Upstream of the diaphragm are eight quartz windows which allow the Cherenkov light which passes the diaphragm to enter the KTAG detector (Section 4.2). The vessel is filled with N_2

gas at room temperature and a photograph of half of the vessel is shown in figure 4.3.

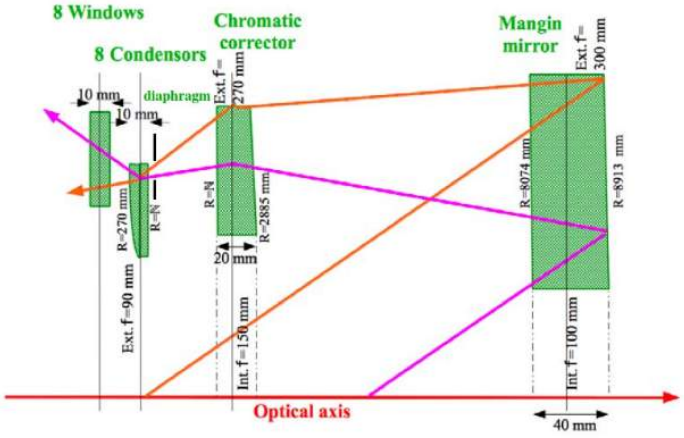

Figure 4.4: Schematic of the light path of Cherenkov photons through the optical components in the hall of the detector above the optical axis (beamline).

The internal optics of the detector can be see in figure 4.3 where Cherenkov light is reflected by a mangin mirror at the downstream end of the detector before passing the chromatic corrector lens and then the diaphragm. Figure 4.4 illustrates in more detail the light path taken through the various optical elements. It can also be seen that a hole is present in the centre of all the optical elements to allow the beam particles to pass undisturbed. The hole in the diaphragm is 100 mm in radius and increases to 150 mm for the corrector lens to allow Cherenkov photons that have already been emitted to pass. The mangin mirror at the end of the vessel also has a 100 mm hole.

As mentioned in the previous Section the chromatic corrector lens is used to reduce the effect of the chromatic dispersion which would otherwise increase the width of the Cherenkov light ring. After passing the corrector lens and through the annular hole in the diaphragm the Cherenkov light is then focussed by a condenser lens in the azimuthal angle onto eight quartz windows. The original CEDAR vessel had eight PMTs in place of the current quartz windows but as will be seen Section 4.2 this will be insufficient for the requirements of NA62 and therefore the KTAG extension to the CEDAR is required.

4.2 KTAG

The mean number of photons, N_γ, emitted at an angle θ_c travelling along a radiator of length L is given by the Frank-Tamm formula [48],

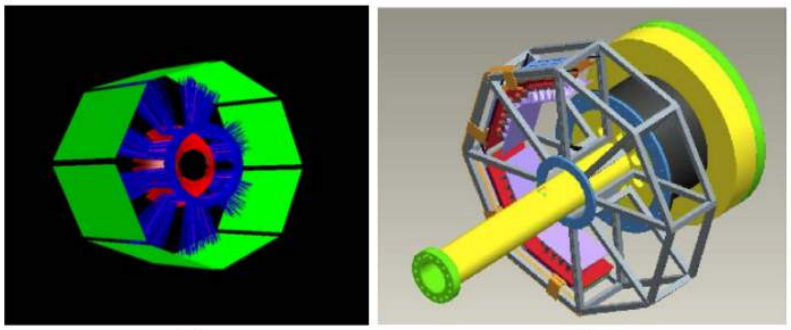

(a) (b)

Figure 4.5: (a) Simulation of the light path of photons (blue) through the KTAG. phtons emerging from the quartz windows reflect off the spherical mirrors (red) and on to the PMT arrays (green). (b) Mechanical design of the new KTAG support structure (grey) with four of the eight light boxes shown (red).

$$N_\gamma = 2\pi\alpha L \sin^2\theta_c \int \frac{d\lambda}{\lambda^2}, \tag{4.4}$$

where α is the fine structure constant and λ is the photon wavelength. Using the CEDAR parameters of length $L = 4.5$ mm, $\theta_c = 30.9$ mrad and taking into account the spectral range of λ = (200 - 600)nm [44], then $N_\gamma \approx 660$ however the CEDAR optics select only a fraction of these photons due to the size and placement of the quartz windows. The number of photons entering the quartz windows $N_\gamma^{qw} \approx 230$ [49].

For this number of mean photons we find an average of about 4 photoelectrons per particle (N_{pe}) for each one of the 8 original PMTs associated with each of the 8 quartz windows. The PMT gain G $\sim 2 \times 10^7$ (Section 4.2.4) and the average current drawn per PMT must be $i_{max} \simeq 0.1mA$ [44]. The maximum affordable beam rate, f_{max} for such technology is given by,

$$f_{max} = \frac{i_{max}}{eGN_{pe}} \approx 8\text{MHz}. \tag{4.5}$$

It is obvious then that the original 8 PMT set up from the original beam design will not be sufficient for a K^+ beam rate of 45 MHz. The time resolution of these PMTs is $\sigma_t \approx 2ns$, assuming a 100% PMT efficiency for the 8 PMTs the resulting kaon crossing time $\sigma_K = \sigma_t/\sqrt{8} \simeq 700$ ps which is larger than the required 100 ps resolution.

In order to be able to cope with a 45 MHz kaon rate and deliver the required 100 ps time resolution the original 8 PMTs were replaced by 8 arrays of single

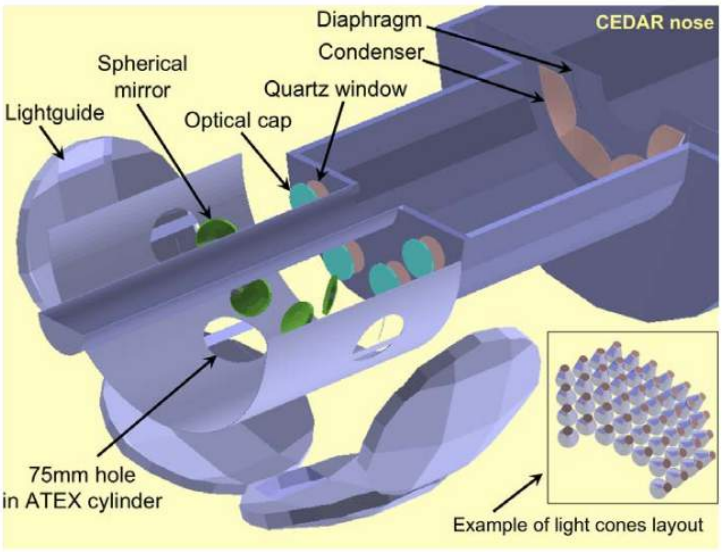

Figure 4.6: Schematic of half of the KTAG detector with optical components labelled.

photon counting PMTs. The minimum number of PMTs (N_{PMTs}) required for the CEDAR requirements listed previously in order to have a maximum rate per PMT (f_{PMT}^{max}) on a single channel can be evaluated as,

$$N_{PMT} = N_{\gamma}^{qw} \epsilon_{qe} \varepsilon \frac{f_K}{f_{PMT}^{max}}, \tag{4.6}$$

where ϵ_{qe} is the quantum efficiency of the photo-detector technology and ε is the overall efficiency of the system. The quantum efficiency is the fraction of charge carriers (electrons) detected per incident photon. If we take some realistic values of $\epsilon_{qe} = 0.25$ and $\varepsilon = 0.7$, it follows that a mean PMT output rate below $f_{PMT}^{max} = 5$ MHZ can be achieved by distributing the Cherenkov photons over $N_{PMT} \simeq 360$ PMTs, which corresponds to $\simeq 45$ PMTs in place of each of the original 8 PMTs.

4.2.1 KTAG Design and construction

To handle the instantaneous kaon rate of ∼50 MHz the new KTAG detector was designed to house the 512 (64x8) PMTs. This arrangement was the result of several MC simulations to determine the optimal set up [49, 50] The concept is illustrated in figure 4.5. The required size of a 64 PMT array dictates that the 8 octants must be placed radially around the beam line. The radial distance from the beam line was chosen in order to minimise the expected radiation from muons and neutrons and is between 30 and 50 cm from the beam line. To focus Cherenkov light emerging from the quartz windows onto the radially displaced light boxes the Cherenkov light which passes through the quartz windows (blue

in figure 4.5) is reflected radially off eight spherical mirrors through 90 degrees and on to one of the eight PMT arrays which house the 45 PMTs. The PMT arrays are held in place mechanically by an atex [37] frame which is mounted upstream of the CEDAR vessel on the existing CEDAR flange. The frame is surrounded by an enclosure to insulate the detector thermally and electrically as well as preventing any light leaks. The enclosure is continually flushed with nitrogen to ensure the optical components are free of any dust or corrosion. The enclosure is separated in two mirror symmetric halves to allow it to be removed if necessary to access the KTAG components.

As illustrated in the cut away of the detector shown in figure 4.6 the enclosure contains the following components,

- 8 focussing lenses
  - 8 corrector lenses located in front of the quartz windows to compensate for the additional divergence of the Cherenkov light.
- 8 spherical mirrors
  - Designed to radially reflect the Cherenkov light onto the PMT arrays. Each mirror can be moved along the beam line with adjustable positioning in the x and z directions in order to align the reflected Cherenkov light with the centre of the PMT array. A more detailed explanation of the spherical mirror mount is given in Section 4.2.2.
- 8 'light guides'
  - Each light guide is an aluminium spherically machined surface which contains 64 conical holes which focus the incoming Cherenkov light on to the active area of the PMTs. Each hole contains a mylar insert to increase the reflectivity of the surface, see Section 4.2.3.
- 8 'light boxes'
  - The light box houses the front end electronics going from the PMTs to the front end board which is mounted at the back of the light box, see Section 4.2.4.
- Gas and cooling systems with relevant monitoring.

Simulations were performed in order to identify the optimum set up of the KTAG apparatus for the NA62 design. The optimum design includes 48 PMTs with a spherical mirror with radius of curvature of 64.6 mm. This allows kaon tagging efficiency of over 95% to be achieved with kaon crossing time of 100 ps. The light distribution across the PMTs as evaluated by the MC simulations is shown in figure 4.7.

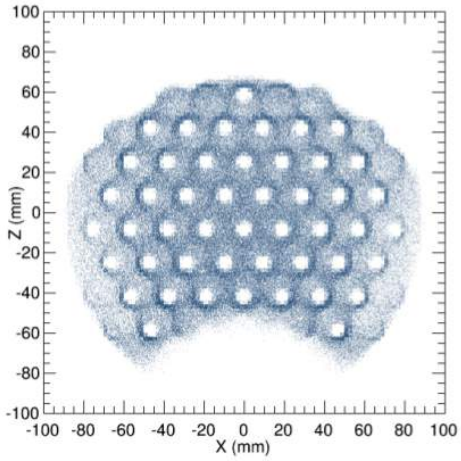

Figure 4.7: Expected photon distribution on one of the light guides. The conical holes which house the PMTs are clearly visible.

4.2.2 Designing and Calibrating the Spherical Mirror Stages

The eight spherical mirrors mentioned previously must be mounted on an Atex cylinder. The centre of each mirror must correspond to the centre of a given PMT array. Although NA62 currently runs with a 48 PMT matrix it is possible in future to change the size of the array and correspondingly the centre. In order to hold the spherical mirrors in place and allow the position of each mirror to be altered in situ on the beam line an adjustable stage was designed and fabricated at Liverpool before fixing each stage in place before shipping the detector to CERN.

Verifying the Current Radial Offset

In order to have the spherical mirrors mounted at the correct position we would need to measure the current radial (y) offset of each mirror[1]. This was done before designing the new stage as any discrepancies could be compensated for in the new stage design. The distance between the centre of opposing mirror mounts was measured, halving this value and accounting for 6.364 mm from the known mirror thickness of 9 mm orientated at 45 degrees we were able to deduce that with the old stage design we had a radial offset of 107.375 mm from the centre of the beampipe. This meant that the new stage design must incorporate a 1.375 mm reduction in height in order to bring the mirrors to the optimal radial offset of 106 mm.

[1]This measurement was undertaken by Kevin McCormick of the Liverpool University physics workshop

Prototype Stage Design

A prototype design was produced[2] which allowed us to move the spherical mirror in the z direction by ±20mm from the nominal position of 701mm by releasing four screws and sliding to the desired position as can be seen in figures 4.8 and 4.9. This prototype also allowed movement in the x direction, this is achieved by loosening a screw at the back of the stage and turning the screw at the side of the stage either clockwise or anti-clockwise to produce an offset of ±8mm. This can be seen in figure 4.9.

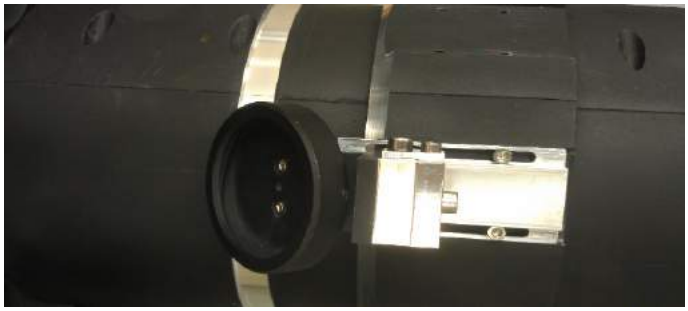

Figure 4.8: Above view of the prototype spherical mirror stage design showing two of the four screws which when loosened allow the z position to be varied.

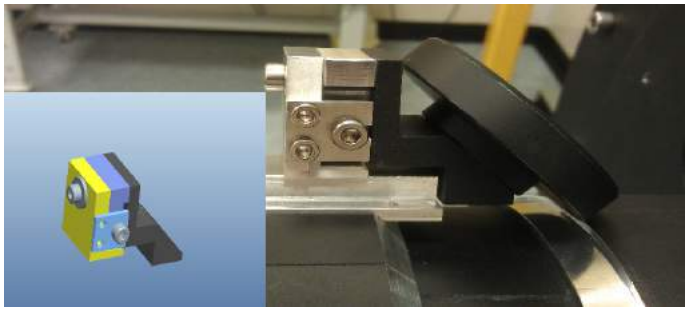

Figure 4.9: Side view of the prototype spherical mirror stage design and a 3D model showing the back screw attached to the yellow block which when loosened allows the side screw attached to the blue block to move the stage to introduce a x offset.

To test this we used a helium laser in the laboratory in order to verify that this design produces a movement of the stage that we can control down to the 0.25 mm scale. This was done by taking the helium laser and mounting it inside a cylindrical container which is shown in figure 4.10. This was then inserted into the hole where the Quartz window would usually be in order to assure that we had a laser which was travelling parallel to the beampipe and striking the centre of the mirror. Using calculations[3] for where we would expect to see the reflected

[2]by Peter Sutcliffe based on a conceptual design by John Fry

[3]produced by Evgueni Goudzovski

laser spot on the atex cylinder. We also tested if it was possible to move the stage whilst all the other components where in situ at CERN, by attempting to move the stages whilst the KTAG frame was attached. It was found that this is possible but that it is simplified greatly if only two screws are used to attach the base to the mirror cylinder.

Figure 4.10: A 3D model of the component used to hold a helium laser pointer. It is made so that it fits into the atex cylinder so that we can calibrate the spherical mirror positions.

An updated stage design was then produced. [4] Due to the desire to secure the stage to the mirror cylinder with only two screws a reduced base length of the stage was required. This meant we had to reduce our range of motion in z and x. The final design would have only a range in the x direction of ±3mm and a range in z of ±10mm. These values are smaller than those given previously for moving the light pattern one row and one column but this would still be sufficient as we only need to be able to move by half a row and half a column to switch between the 48 and 32 PMT set-ups.

The Final Stage Calibration

The final stage is shown in figure 4.11. The only modification to the specified design was that the range in x motion had reduced from ± 3mm to ±2.5 mm in the manufacturing process.

Upon receipt of these components we calibrated them using the helium laser and technique described earlier. We first of all moved each mirror upstream of the old nominal z position by 0.7 mm in order to compensate for the increased thickness of the new spherical mirrors. We also confirmed that the stages were in the correct position by comparing the reflected laser spot from each mirror on the atex cylinder. A summary of the final stage design parameters is shown in table 4.1. We also spray painted the new components matt black in order to minimise reflections within the detector. After this was completed we assembled the detector and shipped it out to CERN in June 2013.

[4] by the Liverpool workshop which was based on the prototype design

Figure 4.11: The Final stage design installed on the mirror cylinder at Liverpool, calibrated and ready to be shipped to CERN.

Coordinate	x	y	z
nominal position (mm)	0	106	700.3
required range of motion (mm)	± 2.5	0	+ 10.7 − 9.3

Table 4.1: A summary of the parameters the new spherical mirror stage. Note that the z nominal position has changed as the new lens has an increased thickness of 1 mm increasing the z position of the mirror centre by 0.7 mm which needs to be accounted for.

4.2.3 Completing the Light Boxes

The 8 light boxes, one of which is shown below in figure 4.12, are a pivotal component of the KTAG detector. Each light box contains a light guide necessary for gathering the incoming Cherenkov photons and then delivering them to the attached PMTs in the most efficient way possible. At Liverpool we were responsible for the manufacture of each of these light boxes, delivering them to a point when the PMTs and associated electronics can be installed. During the technical run of November 2012 4 of the 8 light guides were implemented. Each of these was fully equipped with 32 of the 64 possible PMTs. The Liverpool group were responsible for completing the remaining 4 light guides (plus one for testing purposes) by gluing the aluminised Mylar inserts and making sure that all 8 light guides where at a stage here they were ready to house up to 64 PMTs by assembling the light boxes.

A key process that was involved in achieving 8 fully equipped light guides was the gluing of aluminised Mylar cones into each of the 64 holes on the 5 new boxes. This aluminised Mylar is necessary in order to increase the reflectivity of the surface to 90%, from 75% without the aluminised Mylar inserts [51], to give us the best transmission of light to the PMTs possible.

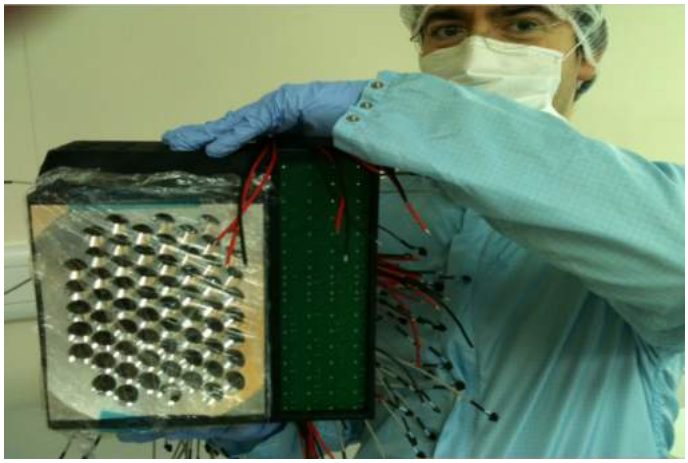

Figure 4.12: A front on view of one of the 8 light guides. The 64 PMT matrix can be seen here.

Gluing the Aluminised Mylar Cones

The procedure for attaching the Mylar inserts into the cones is as follows. Firstly the aluminised Mylar was pre-cut into the desired cone shapes and then covered in a protective plastic. For each cone an Araldite glue was mixed and this was applied to the non plastic covered side. This was then placed in the hole and moved to the optimal position. A metal stopper was then used in order to keep the aluminised Mylar in the correct place whilst the glue dried. 24 hours was allowed for curing. After the glue had cured the stopper was carefully removed. After all the cones have undergone this procedure the protective plastic layer is removed from all of them and the surface of each light guide is covered with a perspex slab in order to protect it during transportation. I was responsible for applying this procedure to over 100 light guide cones.

Assembling the Light Boxes

After the light guides have had the aluminised Mylar cones glued into position all that remains in the mechanical construction process is to complete the assembly of each light box. This involves attaching the 4 sides of anodised aluminium to each light guide and attaching a shelf and heat sink to the bottom of each light guide which will hold the electronics and PMTs which were inserted by our colleagues in Birmingham. The result of this procedure is that we had 5 mechanically complete light boxes which are shown in figures 4.12 and 4.13. The boxes were then shipped to Birmingham at the end of April 2013 for installation of the PMTs and associated electronics.

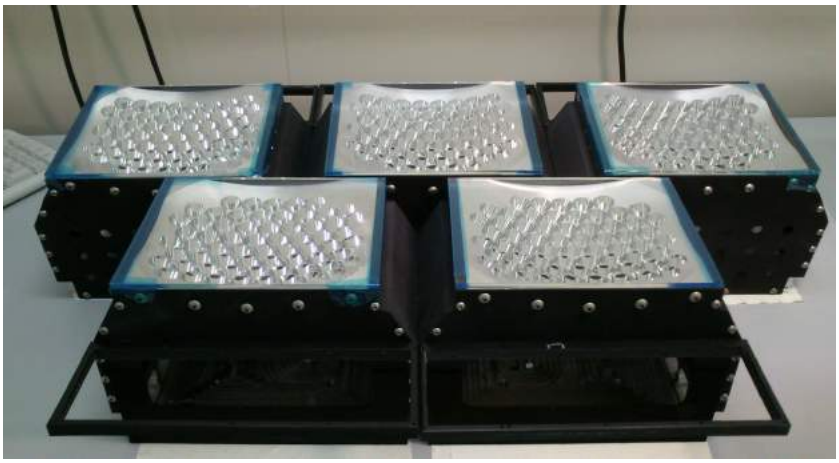

Figure 4.13: The 5 completed light guides ready to be shipped to Birmingham to have electronics fitted then join the 4 fully functioning boxes at CERN. Note that including the 4 that where used in the technical run we have 9 light guides in total, one of which will be used at CERN for electronics testing and development.

4.2.4 KTAG PMTs and Electronics

KTAG PMTs

The PMTs used in the KTAG must be able to identify individual photo-electrons produced at the cathode and separate them in time. This is known as single photon counting. Two types of PMTs are used in the KTAG detector, the Hamamatsu R7400U [52] series 03 PMT and the R9880U [53] series 210 PMT. Both PMTs were selected for their size and compactness as can be seen in table 4.2.

PMT	Series	Diameter × length	Quantum Efficiency	Gain (@ 900V)
R7400U	03	16 × 12mm	$\sim 20\%$	1×10^6
R9880U	210	16 × 12mm	$\sim 40\%$	2×10^6

Table 4.2: Overview of the characteristics of the two types of Hammamatsu PMTs used in the KTAG detector.

Both PMTs have a time resolution of ∼300 ps on single photon detection, have a good resistance to radiation, a low dark count rate of a few Hz, and are sensitive to visible and near-UV wavelengths.

The light guides have 64 cylindrical holes capable of housing as many PMTs but currently the detector requirements are met by equipping only 48 of these with PMTs. Figure 4.14 shows the arrangement of each type of PMT within the light guide. The reasoning behind having two types of PMT is historical. The R7400U PMTs were used in a technical run in 2012. The R9880U were then chosen with

the closest possible specification due to the original PMT type no longer being in production. The main difference between the two PMTs is the quantum efficiency (QE), being ∼20% for the first type of PMT and ∼40% for the newer version. Considering the expected rate on the PMT matrices as evaluated using the MC simulations the average and peak rates are found to be 3.5 MHz and 5.5 MHz respectively. This can be seen in figure 4.14 which shows the PMT layout along with the expected rate per channel.

The second difference between the PMTs is the gain: the R7400U PMTs have an 8-dynode electron multiplier system with a typical gain of 1×10^6 at $V = 900$V; the R9880U PMTs have an 9-dynode electron multiplier system with a typical gain of 2×10^6 at $V = 900$V.

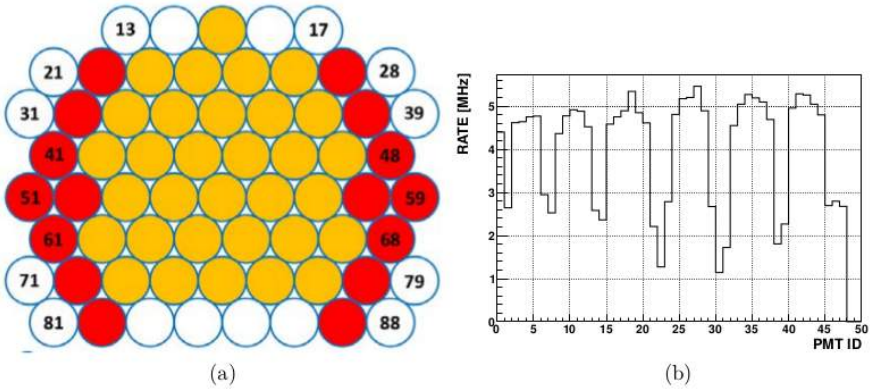

Figure 4.14: (a) Arrangement of the 48 PMTs within the 64 hole light guide. Type R7400U PMTs are shown in red and type R9880U PMTs are shown in yellow. (b) Expected PMT rate per channel for nominal beam rate paramaters with the CEDAR filled with N_2 at 1.71 bar.

Front End and Read Out

The front end system that interfaces the PMTs with the read out system relies on NINO ASIC [54] mezzanine chips with 8 channels. The standard Hammamatsu high voltage (HV) divider is replaced with a customised printed circuit board with differential anode output in order to accommodate the differential input of the NINO mezzanine.

Each light box contains a board housing 8 NINO mezzanine chips, used to shape and discriminate the output signals from the PMTs. A front end board with the NINO mezzanines is shown in figure 4.15. Communication with the Detector Control System (DCS) is achieved via Control Area Network (CAN) bus connectors at the right hand side of the board which are connected through the Embedded Local Monitoring Board (ELMB). Also on the right hand side the central connector is for the low voltage supply. The readout system is connected

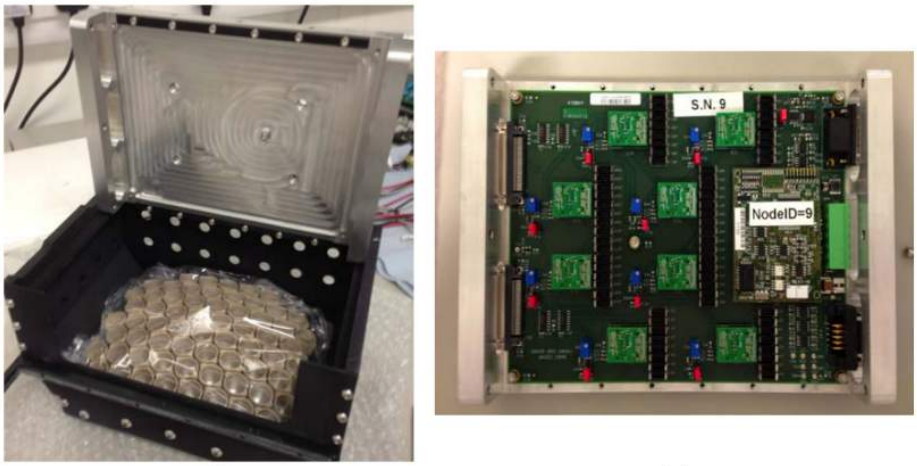

(a) (b)

Figure 4.15: (a) An open light guide in the laboratory. The metalic lid is raised and the holders for the PMTs which are attached to the light cones are visible. (b) A NINO board with CAN bus and central voltage connector mounted to the right hand side and two LDVS connectors to the left. The NINO boards are attached to the inside of the metal slide shown in (a).

to the front-end board via two connectors situated on the left side of the board. The NINO board is attached to the inside of the metallic lid of the light box, shown in figure 4.15.

The NINO chip threshold can be set remotely and independently for each NINO mezzanine via the DCS and all chips operate in Time-Over-Threshold (TOT) mode. The NINO Low Voltage Differential Signaling (LVDS) output is sent to 128-channel Time to Digital Converter (TDC) modules which work in trigger matching mode. The signal from the KTAG front-end is distributed by passive splitter boards (figure 4.16) over readout channels which are arranged non consecutively. The splitting of the signal occurs before the signal reaches the TDC boards. This splitting is needed to minimise the readout inefficiency at the expected rate that occurs due to groups of eight consecutive readout channels sharing a latency buffer. The limited buffer size implies a 10% readout inefficiency for rates above 5 MHz per channel, if more than one channel shares the same buffer [55]. With the split channel configuration, one single channel is sent to each latency buffer, allowing to an inefficiency below 4% for the maximum expected rate of 5.5 MHz (Section 4.2.1).

Precise time tagging of the electronic signals is achieved via four High Performance Time to Digital Converter (HPTDC) chips [55] contained in each TDC module. The leading and trailing edges of the LVDS output are recorded to provide information regarding the width of the NINO output signal. Information on the width is needed in order to compensate the rising time differences between signals with different amplitudes (slewing corrections). Each TDC board

is hosted by a TEL62 motherboard shown in figure 4.16. The TEL62 boards are integrated with trigger and data acquisition boards developed by the NA62 collaboration.

The TEL62 board [56, 46] is an upgrade of a FPGA-based readout board inherited from the LHCb readout system [58]. It can host up to four TDC boards and is formed from the following components:

- 4 Altera Stratix III FPGAs with each with a 2 GByte DDR2 memory buffer, for handling data from the TDC boards;
- 1 central Altera Stratix III FPGA, for processing triggers to synchronise the data;
- a Quad GbE card with four 1 Gbit Ethernet channels, for data and trigger handling;
- a commercial Credit-Card PC (CCPC) and a custom card for the board slow control.

To minimise the readout inefficiency , 8 readout channels are required per KTAG PMT (7 of them left empty due to the inefficiency discussed above). Therefore, in order to reach the required number of channels the KTAG requires six TEL62 equipped with four TDC boards.
(6 TEL62 $\times$ 4 TDC boards $\times$ 128 channels = 8 $\times$ 8 sectors $\times$ 48 PMTs).

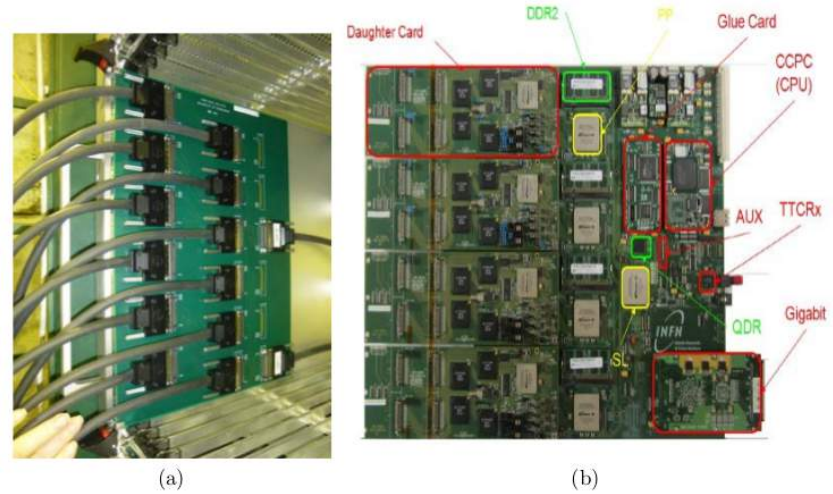

(a) (b)

Figure 4.16: (a) A splitter board used for distributing the KTAG signals from one sector among TEL62 boards. The 2 input LDVS cables shown to the right and the 12 LDVS cables shown to the left. (b) A TEL62 FPGA-based board with components labelled.

4.3 KTAG Installation at CERN

With the completion of the adaptation to the spherical mirror stages, and after the light guides were shipped to Birmingham for the fitting of PMTs and readout electronics, the mechanical components of the KTAG were completed. This meant that a full mechanical installation of the KTAG detector was possible in early June 2013. This installation allowed the detector to be tested at the sub detector testing phases without beam (dry runs) in July and September of 2013 when the installation of the accompanying electronics took place. As part of the installation of the KTAG, the installation of an insulating enclosure for the section between the CEDAR and the KTAG was also undertaken.

4.3.1 Re-installation of KTAG

After the new mirror stages had been installed and calibrated in Liverpool, the mirror and atex cylinders were dismantled and shipped out to CERN. Upon arrival at CERN eight new lenses that cover the quartz windows were installed which allow the Cherenkov light to pass from the CEDAR to the KTAG. The mirror cylinder was then mounted and the new spherical mirrors where fixed in place, each covered with a protective cap in order to protect from dust between the time of installation and when tests are required. The atex cylinder was then attached in order to provide protection for the newly installed mirrors whilst the two halves of KTAG where installed. Using the crane available in the experimental area each half of KTAG was raised onto the cylinder and attached one at a time. After this was completed optical fibres were threaded through the new optical fibre ring[5] and the mirror cylinder was then sealed before each half of the KTAG was sealed using the insulating panels. An overview of this process is shown below in figure 4.17.

4.3.2 Installing the New Insulating Enclosure

In order to make the whole of the CEDAR KTAG detector electrically and thermally insulating enclosure was placed around the gap between the original CEDAR vessel and the KTAG. As well as being insulating and fire retardant in the event that the CEDAR was ever operated with hydrogen the enclosure needs a provision for extracting hydrogen from this space should a leak occur where the CEDAR gas inlet and outlet pipes are attached as shown in figure 4.18. In order to allow any hydrogen to escape the enclosure two chimneys were placed over the inlet and outlet pipes, these were sealed in place using silicon sealant shown in figure 4.18. The stainless steel panels insulated by fire retardant Rohacell 51S were then attached by clamping onto the existing cedar clamps and butting up

[5]designed by Bozydar Wrona

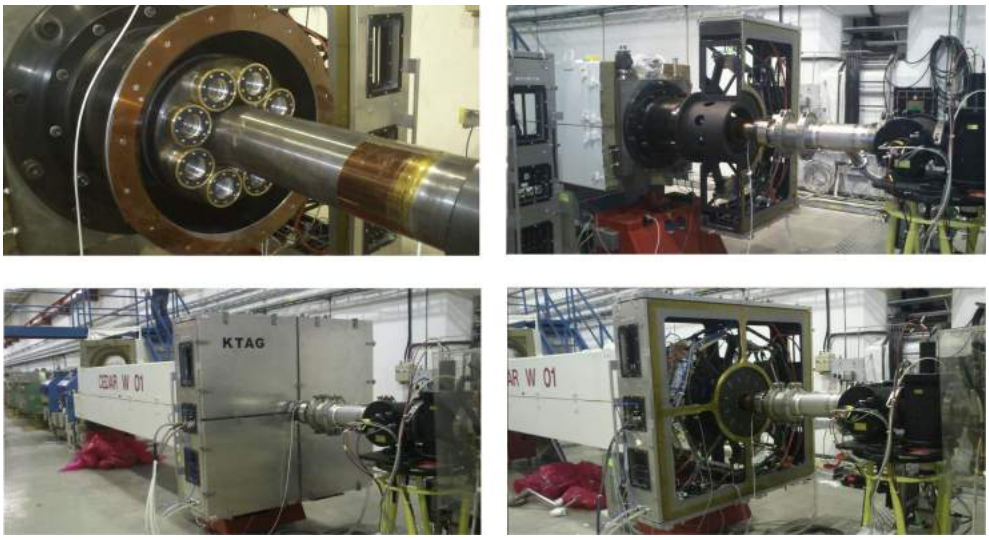

Figure 4.17: The installation procedure for KTAG. Clockwise from top left, the new quartz window lenses and bare beam pipe. KTAG with one half installed and mirror and atex cylinders installed as visible. KTAG with both sides mounted and the back plates of the Atex cylinder attached. KTAG fully assembled.

against KTAG. This design assures that the parts of CEDAR and KTAG that may need to be accessed in future are easily reachable as the whole enclosure is easily removed by two people.

4.4 KTAG Performance in 2015

The performance of the KTAG was evaluated during 2015 data taking. A description of the data taking conditions will be given in detail in Chapter 7. The main features relating to the KTAG however are that the vessel was filled with nitrogen at nominal pressure and whilst the beam intensity varied it was never greater than 10% (75 MHz) for any of the analysed runs in 2015. The results quoted here are taken from the upcoming NA62 detector paper which will be published around the time of submission of this Thesis.

Alignment of the CEDAR vessel with the optical axis was achieved by measuring the light yield distribution in each box and varying the horizontal and vertical position of the vessel in order to equalise the left-right and up-down distributions within each light box. The ability of KTAG to disriminate between particle types is clearly seen in figure 4.19, where the frequency of coincidences between boxes is shown as a function of nitrogen gas pressure. The three peaks corresponding to the kaon, pion and proton are clearly visible. At the kaon nominal pressure the mean number of photomultiplier signals per kaon is 20.

Figure 4.18: Clockwise from the top left. One of the inlet/outlet pipes that need to be covered. One of the two chimneys used to cover the inlet and outlet pipes. One half of the enclosure lined with Rohacell 51S. The full enclosure assembled between CEDAR and KTAG.

The kaon time resolution was assessed by calculating the difference in hit times and average time produced by all signals produced by a beam particle. In this way there is no reliance on any external timing. Time offset and slewing corrections were evaluated and the time resolution of a single channel was found to be 300 ps, figure 4.20. With 20 channels per kaon this leads to a timing resolution per kaon of around 70 ps, well below the required 100 ps of the design specification.

In order to assess the efficiency of the KTAG detector a sample of $K^+ \to \pi^+\pi^0$ was selected using the downstream detectors. Chapter 6 will discuss in great detail how such a selection is achieved. Using this sample the kaon detection efficiency was found to be above 98% when requiring Cherenkov light coincident in at least five of the eight light boxes. Using the pressure scan data the pion misidentification rate was estimated to be of the order 10^{-4} when using a 5-fold octant coincidence condition. Figure 4.21 shows the kaon detection efficiency of the KTAG as a function of the number of coincident sectors required.

4.5 Summary

At the beginning of my studies in Liverpool I had the opportunity to perform some of the final hardware tasks involved with producing the eight mechanical light boxes. Later after the electronics had been installed in Birmingham I was involved with the installation of the KTAG detector on the beamline at CERN. The remaining Chapters detail the analysis tasks I was involved with beginning

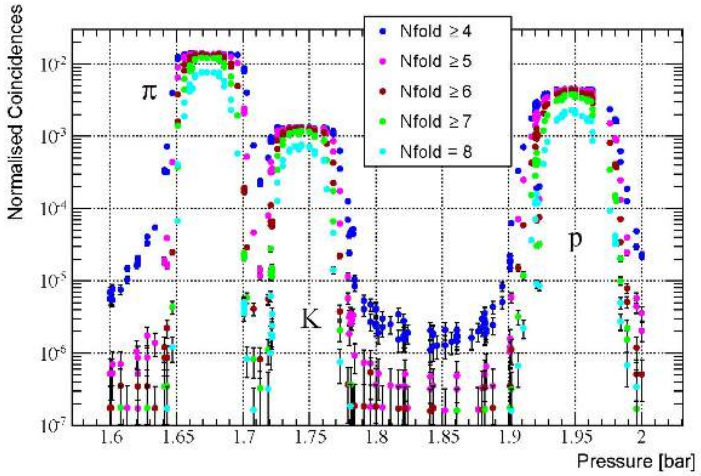

Figure 4.19: Results of a CEDAR pressure scan (for nitrogen) taken with the nominal diaphragm aperture of 1.5 mm. For each of the KTAG sector coincidences (ranging from 4 to 8), the normalised number of events satisfying the requirement is plotted versus the N2 gas pressure. [From the upcoming NA62 detector paper].

with a Monte Carlo based study of the optimal gas for the CEDAR vessel. Chapter 6 and 7 then outline selection criteria for kaon decays were the KTAG timing is used to remove accidental activity.

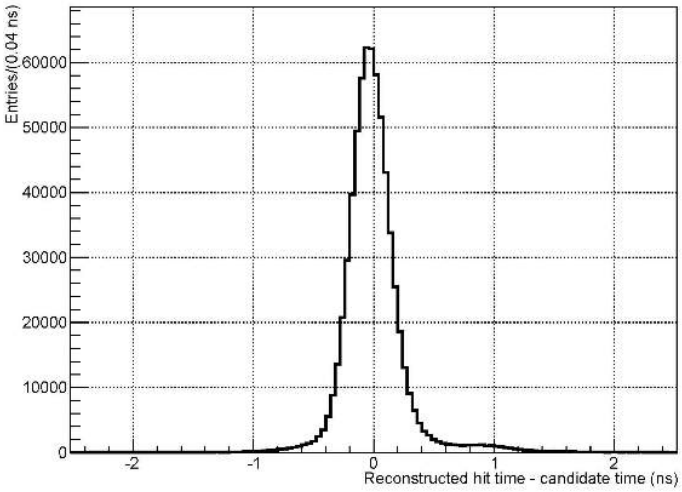

Figure 4.20: KTAG hit time resolution measured with the 2015 data (using nitrogen in the CEDAR). The hit time resolution is 300 ps rms, while the width of the peak is 160 ps. [From the upcoming NA62 detector paper].

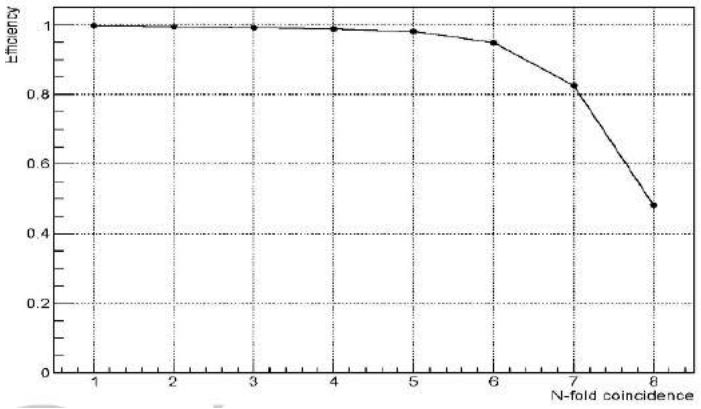

Figure 4.21: Kaon identification efficiency with KTAG (using nitrogen in the CEDAR) measured with the 2015 data as a function of the minimum number of octants required in coincidence. [From the upcoming NA62 detector paper].

Chapter 5

The Choice of Cherenkov Gas in the CEDAR Vessel

5.1 Introduction

The NA62 experiment has the option to use either hydrogen or nitrogen as the Cherenkov radiator gas in the CEDAR vessel. A key consideration in the design of the experiment is to minimize the background seen by the Straw tubes which comprise the downstream spectrometer, and hence the risk of inefficient operation arising from pile-up. The preliminary Monte Carlo (MC) calculations presented in the TDR [37] indicate that for the baseline detector KTAG, with hydrogen gas as the active Cherenkov radiator, the background originating from the muon halo dominates while that from interactions in the gas is small by comparison. A very good reason for using nitrogen is that the optics of the CEDAR were optimised to remove the effects of chromatic aberration with nitrogen as the Cherenkov radiator. Since additional chromatic aberration is present with a hydrogen radiator this degrades the performance of KTAG, resulting in worse efficiency for detecting a kaon and poorer time resolution. Clearly, the better the time resolution of the RICH and KTAG detectors, the smaller the overlap of unassociated particles with the charged kaon and candidate decay particles. The argument against using nitrogen is based on the increased background in other detectors that scattering in the nitrogen will produce.

In this Chapter we quantify the additional rate of charged particles on the first and last planes of the straw-chamber spectrometer, which comes from scattering in the nitrogen gas, and compare it with a revised calculation of the hit rate arising from all other upstream interactions and from decay particles. In this way we assess the significance of the nitrogen as a source of background hits on the straw chambers. We also attempt to quantify the difference in performance of KTAG when operating with hydrogen and with nitrogen. The experiment clearly benefits from minimal background in the Straw spectrometer tubes (and other downstream detectors) to ensure their efficient operation and also from optimal

performance of KTAG in efficiently detecting charged kaons and time-stamping them with as small a time resolution as possible. The aim is therefore to present the advantages and disadvantages of using nitrogen, rather than hydrogen, in the CEDAR vessel. The background rates are calculated in two steps. One part arises from the difference in scattering of the muon halo in the gas [1][70], while the second part is due to the different behaviour of the multiple Coulomb scattering, elastic and inelastic scattering in the two gases.

The organisation of the Chapter is as follows. In Sections 5.2-5.8 we discuss the disadvantages of the nitrogen filling, while in Section 5.9 we discuss the advantages, summarising our conclusions in Section 5.10. In Section 5.2 we present an analytical calculation of the increased background at Straw chamber 1 arising from using nitrogen. Sections 5.3-5.6 we present more detailed Monte Carlo comparisons of the backgrounds to be expected in straw chambers 1 and 4 from hydrogen and nitrogen CEDAR fillings, using the NA62MC Framework. In section 5.7 we present the results of the simulations of the beam muon halo, showing the difference in illumination of the downstream chambers when hydrogen is replaced by nitrogen in the CEDAR. Section 5.8 will outline some first experimental evidence obtained from the physics commissioning run of 2014. In section 5.9 we discuss the advantages of using nitrogen in the CEDAR arising from the cleaner separation of kaon and pion Cherenkov light due to the better correction of chromatic aberration for nitrogen. The conclusions of this study are summarised in Section 5.10.

5.2 Analytical Calculation

An analytical calculation[2] [70] was used with the aim of determining the scale of the increased background in the Straw chambers in order to see whether the use of nitrogen as the Cherenkov radiator could be immediately ruled out. In the event that the background from nitrogen was found to be small compared with other sources of background, as was indeed found, then a more sophisticated Monte Carlo simulation with the NA62 GEANT4 framework would be performed to make a more realistic assessment.

The analytical calculation starts with the known spatial and angular profile of the beam at the beginning of CEDAR, convolutes these distributions with analytical formulations of the physical scattering processes to produce revised angular distributions, and then propagates the beam at each transverse position to the appropriate Straw plane through collimators 6 and 7 located around 20 m downstream of the KTAG, which serve to clean the beam of the larger-angle products

[1] calculated by Niels Doble (CERN)

[2] The analytical calculation was performed by John Fry, University of Liverpool

of upstream interactions. All types of interactions within nitrogen are considered, namely Multiple Coulomb Scattering (MCS), (quasi-)elastic and inelastic scattering. As a template for better appreciating the effects of interactions in nitrogen, the elastic and inelastic interactions in the three GigaTracker planes (GTK1, GTK2 and GTK3) were also calculated, although the effect of MCS in these planes was ignored. In all cases the material properties of the different media were taken from the TDR and are summarised in table 5.1. Analytical parameterizations of the elastic and inelastic-scattering distributions were taken from the Particle Data Group (PDG)[60], while the MCS parameterization is described in terms of three Gaussian distributions of different widths taken from the careful study of data by the DIRAC collaboration[61]. No account was taken of the magnetic fields between the planes of the GigaTracker in sweeping low-momentum particles into or out of the beam; interactions in the collimators, which would produce a halo of scattered particles, were ignored; no account was taken of the interactions of secondary particles as they traversed the walls of the beam pipe en route to the downstream detectors. The calculations of these additional rate are discussed in later sections of this chapter using MC simulations.

	Hydrogen	Nitrogen
Aluminium Window [X_0%]	0.39	0.22
Gas Thickness [X_0%]	0.32	3.5
All 3 GigaTracker Planes [X_0%]	0.99	0.99
Total Thickness [X_0%]	1.7	4.7

Table 5.1: The material budget of the the CEDAR and GigaTracker stations as a percentage of radiation length X_0.

Calculations were made of the rate and angular distribution of hits in Straw plane 1, and the innermost tubes of the Straw detector, for the interactions described above. In view of the approximations made, it is to be expected that the analytical calculation should be accurate within a factor of about 2. The calculated background rate for the Straw plane due to interactions in nitrogen is not expected to be sensitive to any unforeseen tails in the beam distribution, while that in the innermost tubes, where the steep MCS angular distribution dominates, is expected to be sensitive.

The results for the hit rates on Straw plane 1 are summarized in table 5.2.

	Rate (kHz)		Rate (kHz)		Rate (kHz)
MCS Nitrogen	30	Elastic GTK1	10	Inelastic GTK1	2
Elastic Nitrogen	30	Elastic GTK2	25	Inelastic GTK2	5
Inelastic Nitrogen	30	Elastic GTK3	100	Inelastic GTK3	400

Table 5.2: Rates derived from analytical calculation of scattering processes in the upstream detectors. The total elastic scattering due to GigaTracker stations 1, 2, and 3 is 135 kHz. The sum of these rates is 632 kHz.

The conclusions from these calculations are clear:

1. Inelastic scattering in nitrogen plays no significant role in illuminating the Straw tubes, while inelastic scattering from GTK3 dominates;

2. The illumination of the Straw plane arising from elastic scattering in nitrogen is small compared with that from GTK1-3 and insignificant compared with the 10 MHz illumination from the beam halo;

3. The contribution to each inner Straw tube has been calculated to be 5-10 kHz and arises from MCS in the nitrogen gas. This is very small compared with the estimated rate of 400-500 kHz arising from beam halo. This rate is, however, sensitive to tails in the description of the beam profile.

Within the limitations of the analytical approach, this suggests that additional backgrounds at the Straw detector arising from using nitrogen as the Cherenkov radiator are extremely small. A more careful MC simulation of all effects due to the nitrogen that are potentially harmful to the experiment has therefore been carried out to study the effects.

5.3 Monte Carlo Simulation

5.3.1 NA62MC Set-up

Following the analytical calculation, a full NA62 Monte Carlo study was performed to quantify the additional rate on the first and fourth straw planes due to scattering in the upstream detectors. The simulation used the NA62MC framework (rev. 277)[62]. Beam particles were generated using the TURTLE program[63] and then passed to Geant 4[64] for simulation through the detector. The sub-detectors that were enabled for these simulations were the CEDAR, GigaTracker, CHANTI and Straw spectrometer modules. In order to study the rates on the Straw spectrometer coming from scattering in the upstream detectors, an alteration was made to the physics implementation in Geant 4 in order to disable decays of all particles. The Cherenkov process was also disabled to

reduce simulation time. With decays disabled, kaons and pions interact similarly with material on the beamline and therefore there was no need to simulate both.

As a particle is propagated through the simulation, each step made by Geant 4 is saved to the output root[64] file. With all steps of each particle saved, tracks can be reconstructed for particles which interact with the straw spectrometer. An advantage of saving each step in the case of inelastic scattering is that the location of the scatter can be determined. For example, rates coming from inelastic scatters in the CEDAR and inelastic scatters originating in the third GigaTracker plane can be separated. 1,000,000 K^+ and 500,000 protons were simulated in this manner for three different CEDAR configurations:

- CEDAR evacuated (vacuum),
- CEDAR filled with hydrogen,
- CEDAR filled with nitrogen.

5.3.2 Straw Plane Geometry

After the simulation was performed, hits on the first Straw plane were defined as coming from any steps which belong to a charged particle intercepting the region of space which corresponds to the first Straw plane. Two geometries were defined for the first straw plane, named here as the square and circular geometries summarised in table 5.3. Hits were also recorded for the fourth straw plane using the circular geometry also given in table 5.3.

Straw Plane	Geometry	z Range	Detector Boundary	Inner Aperture	Inner Aperture Centre (x,y)
1	Square	183.316 - 183.353 m	$\|L\|$ <1.05m	$\|l\|$ <63.8mm	(101.2mm,0)
1	Circular	183.316 - 183.353 m	$\|R\|$ <1.05m	$\|r\|$ <63.8mm	(101.2mm,0)
4	Circular	218.983 - 219.020 m	$\|R\|$ <1.05m	$\|r\|$ <63.8mm	(52.8mm,0)

Table 5.3: An outline of the geometries used to define the first and fourth straw planes. Note that for the given inner aperture the edge of the square/circle corresponds to the position at which the centre of the innermost straw is placed.

In reality the physical geometry is that shown in figure 5.1. The physical straw material corresponds to the overlap of the 4 views of which the circle of diameter

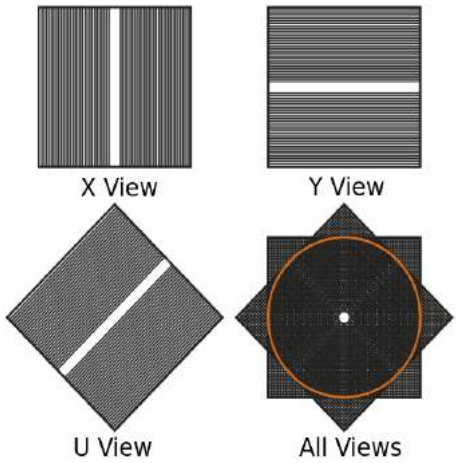

Figure 5.1: An outline of the four straw views, x,y,u,v (view v corresponds to view u rotated 90 degrees.) The overlapping of these views corresponds to one of the four straw chambers[37]. The instrumented area is the circle highlighted and an octagonal hole is present in each of the straw planes to allow the beam to pass through.

2.1 m is instrumented. The central beam hole will be an octagon corresponding to the 4 overlapping views and as such the inner boundary will be described somewhere between the two geometries used for the first straw plane, outlined in Table 5.3. The two geometries defined here (square and circular) enabled step by step comparison with the analytical calculations described earlier. As will become clear, the results of this study do not depend significantly on the choice of the two geometries.

5.3.3 Extracting Raw Hits

In all geometries, particles intercepting the defined volume are recorded as hits. For each hit the series of steps upstream of the hit are reconstructed as a track of the particle through the detector. This track then contains all the information of the charged particle's path through the detectors. These hits can be further decomposed into two categories depending on what type of scattering produced the hit, namely elastic or inelastic scattering.

Hits from elastic scattering: Hits from elastic scatters are defined as hits which maintain the identity of the beam particle and where it has lost only a small amount of energy; the minimum amount of energy a particle must have to be considered to have scattered elastically is 70 GeV. This number was set by considering the energy spectrum of hits coming from 20,000 incident protons at the fourth straw plane shown in figure 5.2. Elastic scatters will therefore cover all scattering processes in which energy losses are small, namely elastic scattering off a nucleus, elastic scattering off a nucleon, and multiple coulomb scattering. The

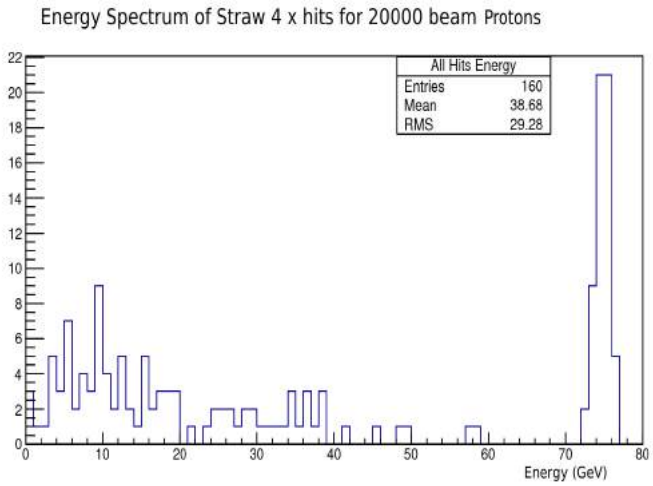

Figure 5.2: The energy spectrum of all hits on the fourth straw plane which occur due to scattering in the upstream detectors.

hits arising from elastic-type interactions have no discernible location of scatter, because the particle type does not change, and therefore a total elastic scatter rate for all processes will be quoted for each simulation, without reference to the origin of the scatter.

Hits from inelastic scattering: Hits from inelastic scatters are those where the beam particle changes identity in the interaction and where the resulting particle has much less energy than for an elastic scatter, as can be seen in figure 5.2. Hits from inelastic scatters appear typically at larger angles on the straw plane. Each track from an inelastic scatter can be traced back to a location at which the inelastic scatter occurred; for example an inelastic scatter in the third GigaTracker station is distinguishable from an inelastic scatter in the CEDAR gas volume.

5.4 Results - Raw Hits

Raw hits were extracted for the first and fourth Straw planes and each hit was categorised as elastic or inelastic. Hits from inelastic scatters were further categorised by their origin. Inelastic scatters are categorised as originating in the CEDAR gas volume, or in one of the three GigaTracker planes. Hits from inelastic scatters elsewhere in the detector are termed 'other' inelastics. The Monte Carlo simulation shows that over 90% of the hits being categorised as 'other' inelastics are due to scattering in collimators 6 and 7.

Section 5.4 of this chapter is organised as follows, Sections 5.4.1 and 5.4.2 document the raw hits that were extracted for the first straw plane, along with a summary of the hits on the straw closest to the beam in the positive x direction

(Jura side). In Section 5.4.3 the ratio of elastic scatters from kaons and protons are computed along with the ratio between kaons and protons for inelastic scatters which are used as a physics check. In Sections 5.4.4 and 5.4.5 the raw hits for the fourth straw plane and its corresponding closest straw are given. As stated in Section 5.3.1, 1 million kaons have been simulated along with 500,000 protons, for the raw hits shown in Section 5.4 the raw hits for the protons have been scaled by a factor of two to allow for direct comparison. Note that the error on the number of raw hits shown in tables 5.4-5.9 is $\sqrt{N}$ for kaons and $2\sqrt{N}$ for protons, where N is the number shown in the table. This takes into account the scaling by a factor of 2 for protons.

5.4.1 Raw Hits on the First Straw Plane

The number of hits, divided into hit type, on the first straw plane using the square geometry is shown in table 5.4 for kaons and protons; the numbers for the circular definition are shown in table 5.5. Each table contains the number of each hit type that is present when the CEDAR vessel is filled with vacuum, hydrogen or nitrogen. It can be seen that as we go from vacuum to hydrogen to nitrogen the number of total elastic hits increases, as would be expected. The number of CEDAR, GTK1 and GTK2 inelastics is small compared with GTK3 inelastics; this is because collimators 6 and 7, situated between GTK2 and GTK3, remove large angle inelastic scatters. As expected, the number of GTK3 inelastic scatters is independent of the CEDAR gas. An increase in the number of other inelastics is clearly visible as we go from vacuum to nitrogen.

	Kaons			Protons		
Hit Type	Vacuum	H_2	N_2	Vacuum	H_2	N_2
All Elastic	263	285	405	820	776	1332
CEDAR Gas Inelastic	0	1	23	0	8	28
GTK1 Inelastic	1	1	0	2	2	0
GTK2 Inelastic	1	2	6	2	12	0
GTK3 Inelastic	179	177	198	258	312	278
Other Inelastic	21	16	66	34	52	106

Table 5.4: Raw hits at the first straw plane for 1 million K^+ and 1 million protons using the square geometry.

Hit Type	Kaons			Protons		
	Vacuum	H_2	N_2	Vacuum	H_2	N_2
All Elastic	287	312	455	876	864	1554
CEDAR Gas Inelastic	0	2	24	0	8	28
GTK1 Inelastic	1	1	0	2	2	0
GTK2 Inelastic	1	1	6	2	10	2
GTK3 Inelastic	150	146	153	234	258	214
Other Inelastic	20	11	53	30	40	84

Table 5.5: Raw hits at the first straw plane for 1 million K^+ and 1 million protons using the circular geometry.

A comparison of hits for the square and circular geometries, in tables 5.4 and 5.5, shows two prominent differences. Firstly the number of elastic scatters is greater for the circular geometry than for the square geometry. This is because elastic scatters are typically at small angles and the circular geometry has more acceptance close to the beam. The opposite is true for inelastic scatters since they occur typically at larger angles than elastic scatters. As the square geometry covers a larger area we see more inelastic scatters in the square geometry than we do in the circular. These two effects are similar in size so that the total number of hits is almost the same for both geometries. The elastic scatters which typically occur at smaller angles tend to hit the straw plane around the innermost straws where the rate is highest. As there is a limit on the rate that individual straws can tolerate, as discussed in Sections 5.5.2 and 5.5.4 only the circular geometry was used to extract the raw hits for sections 5.4.2, 5.4.4 and 5.4.5.

5.4.2 Raw Hits on the Innermost Straw at the First Straw Plane

Raw hits were also extracted from the region corresponding to the first straw in the positive x direction (Jura side), This straw was chosen as it is known to have the highest rate from the muon halo. This was done using exactly the same procedure as for extracting hits for the whole of the straw plane, but requiring the hits to fall within the geometry of the first straw. Because of MCS, the straws closest to the beam hole are expected to have the largest rates and it is important to assess whether the additional scattering caused by nitrogen is concentrated on the innermost straws.

The same definitions of hits from elastic and inelastic scatters were used for the single straw simulations. The square and circular geometries provide similar results; as such only the number of hits from the square geometry is given. For both kaons and protons the hits on the innermost straws are dominated by elastic scattering, with a small contribution from inelastic scattering amounting to less

than 2 hits. For 1 million kaons the total number of hits on the innermost straw are 9±4, 25±5, 28±5 for vacuum, hydrogen, and nitrogen respectively. For 1 million protons the total number of hits on the innermost straw are 18±6, 24±7, 54±10 for vacuum, hydrogen, and nitrogen respectively. The number of hits is small on the innermost straw when compared with the total number of hits on the plane as shown in Table 5.5.

5.4.3 Physics Checks

To validate these simulations two physics checks were undertaken using the raw hit results. For both these checks the raw hits extracted using the square geometry is used. The proton:K^+ ratio of GTK3 inelastic scatters is expected to be 1.5 as the cross section for inelastic scattering is 50% larger for protons than K^+. Similarly the proton:K^+ ratio for all elastic scatters is expected to be 1.5.

The ratio between GTK3 inelastic hits for the three CEDAR gas configurations is shown in table 5.6 and can be seen to be consistent with a factor of 1.5.

	Hit Type	Vacuum	H_2	N_2
K^+	GTK3 Inelastic	179±13	177±13	198±14
Protons	GTK3 Inelastic	258±23	312±25	278±24
Protons /K^+	GTK3 Inelastic	1.4±0.2	1.7±0.2	1.4±0.2

Table 5.6: The ratio of GTK3 Inelastic scatters from 1 million protons to 1 million K^+.

The results for elastic scattering can be seen below in table 5.7.

	Hit Type	Vacuum	H_2	N_2
K^+	All Elastic	263±16	285±17	405±20
Protons	All Elastic	820±40	776±40	1332±52
Protons /K^+	All Elastic	3.1±0.2	2.7±0.2	3.3±0.2

Table 5.7: The ratio of elastic scatters from 1 million protons to 1 million K^+.

We can see that we have a ratio larger than 1.5 for the number of elastic hits. The ratio of 1.5 is expected for elastic scatters off an individual nucleon, the other two contributing factors to the definition of elastic hits, elastic scattering from a

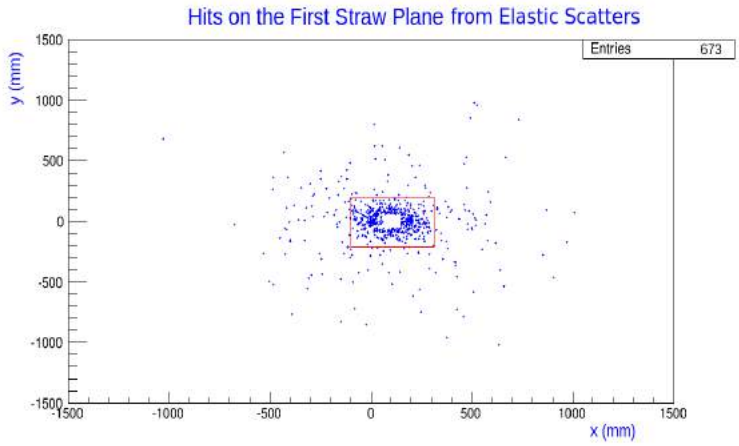

Figure 5.3: A scatter plot of the x-y position of elastic hits on the first straw plane with the boundary chosen to seperate small angle and large angle scatters shown.

recoil nucleus and multiple coulomb scattering are not known to scale by a factor of 1.5. Elastic scattering from an individual nucleon will typically occur at larger angle than the other two processes. To see if a factor of 1.5 was true for larger angle scatters, hits were considered outside an area corresponding to ±150 mm in the x and y directions from the edge of the beam hole, illustrated in figure 5.3. The results of the proton:K^+ ratio for large angle scatters are summarised in table 5.8, and agree with expectation.

	Hit Type	Vacuum	H_2	N_2
K^+	Large Angle Elastic	97±10	89±9	99±10
Protons	Large Angle Elastic	144±17	140±17	144±17
Protons $/K^+$	Large Angle Elastic	1.5±0.3	1.6±0.3	1.5±0.3

Table 5.8: The ratio of large angle elastic scatters from 1 million protons to 1 million K^+.

5.4.4 Raw Hits on the Fourth Straw Plane

The same procedure for extracting raw hits at the fourth straw plane was followed as for the first. For the fourth straw plane only the circular geometry was used. Table 5.9 shows the raw hit rates for kaons and protons. In general, the same trend of increasing numbers of hits from elastic scattering was observed when going from vacuum to nitrogen. We also appear to have increasing numbers of hits coming from other inelastic scatters for nitrogen compared with vacuum and hydrogen. When compared with Straw plane 1 results for the circular geometry, shown in table 5.5, there is an increase in the number of hits from elastic scatter-

ing and a decrease in the number of hits from inelastic scattering (mainly from GTK3). This is to be expected when we consider that straw plane four is 35 m downstream of straw plane one and, as such, small angle hits from elastic scatters will register on straw plane four which were unable to hit straw plane one, while conversely large angle hits from elastic scatters will have left the detector by the time they propagate from straw plane one to straw plane four.

	Kaons			Protons		
Hit Type	Vacuum	H_2	N_2	Vacuum	H_2	N_2
All Elastic	347	422	654	880	1050	2032
CEDAR Gas Inelastic	0	3	26	0	8	24
GTK1 Inelastic	1	1	1	2	2	0
GTK2 Inelastic	1	1	6	2	10	2
GTK3 Inelastic	67	69	86	152	148	124
Other Inelastic	13	5	20	44	46	96

Table 5.9: Raw hits at the fourth straw plane for 1 million K^+ and 1 million protons using the circular geometry.

5.4.5 Raw Hits on the Innermost Straw at the Fourth Straw Plane

In the same way as for the first straw plane, raw hits for the straw tube closest to the beam in the positive x direction were extracted for the fourth straw plane. For both kaons and protons the hits on the innermost straws are dominated by elastic scattering, with a small contribution from inelastic scattering amounting to less than 2 hits. For 1 million kaons the total number of hits on the innermost straw are 29±4, 21±5, 39±6 for vacuum, hydrogen, and nitrogen respectively. For 1 million protons the total number of hits on the innermost straw are 38±9, 50±10, 102±14 for vacuum, hydrogen, and nitrogen respectively. The number of hits is small on the innermost straw when compared with the total number of hits on the plane as shown in table 5.9.

5.5 Results - Hit Rates

Having extracted a raw number of hits for 1 million kaons and protons, it was necessary to scale and combine these numbers to represent the expected beam flux. The following beam properties were taken from the NA62 Technical Design Report (TDR)[37]

- Beam rate of 743 MHz.

- 570 MHz K^+ and π^+ combined.
- 173 MHz protons.

The number of hits were then scaled and combined to give the following scaled hit rates for the first and fourth straw planes along with the rate for the straw tube closest to the beam in the positive x direction for both cases.

5.5.1 Hit Rates on the First Straw Plane

For the first straw plane, the following scaled total beam rates were deduced for the square geometry and the circular geometry in table 5.10.

	Square			Circular		
Hit Type	Vacuum	H_2	N_2	Vacuum	H_2	N_2
Elastic	293±16	296±16	461±20	315±17	327±17	528±22
CEDAR Gas Inelastic	0	2±1	18±4	0	3±1	19±4
GTK1 Inelastic	1±1	1±1	0±1	1±1	1±1	0±1
GTK2 Inelastic	1±1	3±1	3±1	1±1	2±1	4±2
GTK3 Inelastic	147±12	155±12	161±12	126±11	128±11	124±11
Other Inelastic	18±4	18±4	56±7	17±4	13±3	45±6
Rate from scattering	460±20	475±20	699±25	460±21	474±21	720±26

Table 5.10: Scaled hit rates (kHz) at the first straw plane using the square and circular geometries.

Note that as the rates calculated for the square and circular geometries in table 5.10 used the same Monte Carlo sample, the errors for the two are correlated. For both the square and circular geometry the following is observed:

- There is little difference in the rates between vacuum and hydrogen in the CEDAR.
- An increased rate coming from elastic scatters is present with nitrogen in the CEDAR.
- Inelastic hits upstream of GTK3 are suppressed due to the presence of collimators 6 and 7 between GTK2 and GTK3.
- The rate of GTK3 hits from inelastic scattering is independent of the gas in the CEDAR as would be expected.
- The rate of 'other' hits from inelastic scattering is greater with nitrogen in the CEDAR.

'Other' hits from inelastic scattering are inelastic scatters that occur at a point in the simulation not corresponding to the CEDAR gas volume or the three GTK planes. They arise mostly from interactions in collimators 6 and 7. It is thought that the increase in 'other' inelastics arises because the beam distribution is larger after passing through nitrogen compared with hydrogen. This in turn means that more particles hit the jaws of collimators 6 and 7.

5.5.2 Hit Rates on the Innermost Straw at the First Straw Plane

Rates were also extracted for the straw tube closest to the beam in the positive x direction, using the same procedure as for extracting rates in the first straw plane. The extracted rates are 16±4, 19±4, 25±5 kHz for vacuum, hydrogen, and nitrogen respectively.

Out of a total hit rate on the plane of 720 kHz, only 25 kHz on the innermost tube occurs when running with nitrogen. This number can be compared with the maximum rate which an individual straw can tolerate, given in the TDR as 500 kHz on an individual straw.

5.5.3 Hit Rates on the Fourth Straw Plane

Hit rates were also calculated for the fourth Straw plane. This was done in the same way as for the first Straw plane. The circular geometry, only, was used when extracting hits and as such the rates given in table 5.11 are to be compared with the rates when using the circular geometry for Straw plane one in table 5.10.

Hit Type	Vacuum	H_2	N_2
Elastic	350±18	420±20	724±25
CEDAR Gas Inelastic	0	3±2	19±4
GTK1 Inelastic	1±1	1±1	1±1
GTK2 Inelastic	1±1	2±1	4±2
GTK3 Inelastic	64±8	65±8	70±8
Other Inelastic	15±4	11±3	28±5
Rate from scattering	431±20	504±22	846±28

Table 5.11: Scaled hit rates (kHz) at the fourth straw plane using the circular geometry.

It can be seen that when compared with straw plane one the rate is larger for the whole plane by about 100 kHz. This is mainly due to an increase in the number

of elastic scatters, while there is a reduction in the number of GTK3 inelastic scatters.

5.5.4 Hit Rates on the Innermost Straw at the Fourth Straw Plane

It is again necessary to extract the rate on the straw tube closest to the beam in order to check if a significant rate arises. The extracted rates are are 23±5, 21±4, 40±6 kHz for vacuum, hydrogen, and nitrogen respectively.

As with the closest straw in the first straw plane the majority of the rate comes from elastic scatters. The rate due to nitrogen has increased to 40 kHz, compared with 25 kHz for Straw chamber 1, this is still small compared with the maximum allowable rate of 500 kHz.

5.5.5 Hit Rates Due to Nitrogen

Three sources of excess rates in the straw spectrometer due to nitrogen were identified.

1. Inelastic scatters in the nitrogen.
2. Elastic scatters in the nitrogen.
3. Additional "other" inelastic scatters.

The rates for each of these scatters was then extracted in the following way, for the hit rates in tables 5.10 and 5.11.

1. The number of nitrogen inelastic scatters is known directly from the simulations with nitrogen in the CEDAR.
2. The rate of elastic scatters due to nitrogen is calculated by subtracting the number of elastic scatters with the CEDAR evacuated from the total number of elastic scatters occurring with nitrogen in the CEDAR.
3. The additional inelastic scattering was calculated by subtracting the number of other inelastic scatters with the CEDAR evacuated, from the number of other inelastic scatters when the CEDAR was filled with nitrogen.

When the three contributing factors are combined they comprise the hit rate due to nitrogen, summarised in table 5.12.

Region	Total Rate (kHz)	Rate due to Nitrogen (kHz)
Plane 1 Square Geometry	699±25	224±27
Plane 1 Circular Geometry	720±26	260±29
Plane 1 Innermost Straw	25±5	8±7
Plane 4 Circular Geometry	846±28	406±32
Plane 4 Innermost Straw	40±6	16±8

Table 5.12: Summary of the total rates (including nitrogen) and the rate due to nitrogen for straw plane 1 and straw plane 4 regions.

For the simulations involving hydrogen in the CEDAR the total rates on the planes along with the rates on the innermost straw are as follows. For the first straw chamber we observe 9±25 kHz on the plane and 2±7 kHz on the innermost straw due to hydrogen. Similarly for chamber 4 we find 69±27 kHz on the plane and -3±7 kHz on the innermost straw due to hydrogen.

The total rate of elastic and inelastic scatters, and the rate due to nitrogen, are larger on both the plane and the closest straw for Straw 4 than Straw 1. For Straw 4, approximately half the total rate on both the plane and the closest straw is due to nitrogen. This corresponds to a rate due to nitrogen at the fourth plane of 406±20 kHz of which 16±8 kHz is concentrated on the straw closest to the beam in the positive x direction. The distribution from upstream scattering is symmetric in x and y and therefore the rate for one of the closest straws given here corresponds to the expected rate on the other three innermost straws.

5.6 Summary of Hit Rates due to scattering

The hit rates outlined in Section 5.5 are summarised below in table 5.13. The rates due to each gas are found by subtracting the rates which were calculated for when the Cedar vessel contained vacuum from hydrogen and nitrogen calculated rates.

Straw Chamber	CEDAR Gas	**Total Rate(kHz)** Chamber	Innermost Straw	**Rate due to gas(kHz)** Chamber	Innermost Straw
1	H_2	474±21	19±4	9±25	2±7
1	N_2	720±26	25±5	260±29	8±7
4	H_2	**504±22**	**21±4**	69±27	-3±7
4	N_2	**846±28**	**40±6**	406±32	16±8

Table 5.13: Summary rates on the first and fourth straw chambers when the CEDAR vessel is filled with either hydrogen or nitrogen. All rates here are with respect to the rates calculated when there is vacuum in the CEDAR.

We can see then that having nitrogen in the CEDAR increases the rate on the first Straw chamber to 720±26 kHz from 474±21 kHz which is an increase of 246±33 kHz. On the fourth straw chamber the rate increases to 846±28 kHz from 504±22 kHz, an increase of 342±35 kHz.

The innermost straw on the first straw chamber has a rate of 25±5 kHz for nitrogen and 19±4 kHz for hydrogen, 8±7 kHz comes from having nitrogen in the CEDAR. For the innermost straw on the fourth straw chamber the rate with nitrogen is 40±6 kHz compared to 21±4 kHz with hydrogen, 16±8 kHz is from scattering in the nitrogen.

We can compare now the results in table 5.13 with the the results of the analytical calculation, shown in table 5.2. The expected rate due to nitrogen on the first straw plane from table 5.2 is 90 kHz and it was stated in Section 5.2 that this calculation is expected to be accurate to within a factor of 2. The rate on the first straw plane due to nitrogen shown in table 5.13 is 260±29 kHz. The difference in these two figures is slightly larger than the expected factor of 2 but this is believed to be because the Monte Carlo simulation includes sources of increased rate which are due to the presence of nitrogen but not directly from scatters in the gas volume. An example of this is that a larger beam profile, due to passing through nitrogen, causes a greater number of particles to inelastically scatter off collimators 6 and 7.

As was stated in Section 5.5 the increase in rates on individual straws are small compared with the maximum operating rates for the straws of 500 kHz. It will also be outlined in Section 5.7 that the rates on the planes coming from additional scattering in the nitrogen are small compared with the the rates on the straw planes coming from kaon and pion decay products which are around 10 MHz.

5.7 Expected Hit Rates from Decays

The rates given so far are only concerned with the scattering of the beam hadrons, in particular the additional rate on the first and fourth planes of the straw detector. In order to put these rates into context it is important to quote the expected rate on the first and fourth straw planes which comes from decays of the beam particles. This rate can be separated into two distinct rates.

1. The rate coming from the muon halo produced by beam particle decays into muons.

2. The rate coming from K^+ decay products which are not muons.

The muon halo rate for the first straw plane has been previously simulated for the CEDAR filled with hydrogen and is 6700 kHz[37]. The rates for the muon halo at the fourth straw plane and at the closest straws in x and y are given in table 5.14. The rates for nitrogen in the CEDAR also given for comparison in table 5.14[3]. The overall scattering rate on the plane does not increase and nor does the rate on the innermost straw in the x direction, where the physics is most sensitive. However, a 50 kHz increase in muon halo rate on the innermost straws in the y direction is observed.

Source	Gas in CEDAR	Fourth Straw Plane	Innermost Straw x Direction	Innermost Straw y Direction
Muon Halo (kHz)	H_2	8000	500	400
	N_2	8000	500	450
Non-Muon Halo (kHz)	H_2	2500	90	90
	N_2	2500	90	90

Table 5.14: Muon and non-muon halo rates at the fourth straw plane and for the innermost straws in both the x and y directions, when CEDAR is filled with hydrogen and nitrogen.

The other source of rate on the straws comes from charged decay products other than muons; this is termed the non-muon halo in table 5.14. The expected rate from these charged decay products is estimated to be 2500 kHz on the fourth straw plane, with an uncertainty of 500 kHz[4]. These decays will also increase the hit rate in the innermost straws, In order to quantify this increase a Monte Carlo simulation was performed with 300,000 K^+ decays. 100,000 K^+ decays were simulated for the K^+ decays without muons in the final state with the 3 largest branching fractions. The three decays correspond to around 95% of K^+

[3]Calculated by Niels Doble.

[4]This estimate was reached after discussion with Giuseppe Ruggiero(CERN) and Evgueni Goudzovski (Birmingham) and is consistent with their current trigger studies, as discussed privately.

decays which produce charged particles which are not muons. The total increase in rate on the innermost straw, corresponding to 2500 kHz on the plane, is then calculated to be 90±20 kHz, as shown in Table 5.14.

The total rate on Straw chamber 4 is approximately 11 MHz, of which 0.4 MHz arises from filling the CEDAR with nitrogen. The effect of nitrogen on the innermost tubes is to increase the hit rate from 490 to 540 kHz in y direction.

5.8 Experimental Evidence

In December 2014 CEDAR was evacuated towards the end of the scheduled Physics Commissioning Run. A small amount of data (200,000 events) was recorded in run number 1543 using a minimum bias trigger. A full discussion of the 2014 data taking and minimum bias trigger will be given in Chapter 6. This data has been compared with a sample of 9,000,000 events from run number 1520, recorded with the same trigger and similar beam conditions, when the CEDAR was filled with nitrogen at the nominal pressure of 1.71 bar.

During both runs there were intermittent problems with the Straw chamber electronics readout which caused straw planes and sections of the straw tubes to have no data. As such it was necessary to restrict the data analysis to events with good straw data. Because of significant out-of-time backgrounds from the beam halo, the particle flux, defined as the number of straw hits per event at a single straw or over a plane of straws, was dependent on the beam intensity and did not give a true measure of activity. As such, the ratio of fluxes does not give a true estimation of the effects of the nitrogen radiator. Thus, the measured fluxes, where flux is parametrised by number of hits per event, over straw plane 1 were: 11.7 ± 0.1 (vacuum) and 10.9 ± 0.1 (nitrogen), indicating an apparent, but false, decrease in activity due to the nitrogen. This effect was further investigated by using the out-of-time hits in MUV3 as a proxy for the beam intensity and observing a linear dependence with the flux over the straw plane. Correcting for the effect of the varying beam intensity with the necessary precision has not proved possible, however, since the variation within each of the runs 1520 and 1543, separately, was rather small.

From the Monte Carlo simulation and, particularly, the analytical calculations described in Sections 5.2-5.6, it is clear that scattering in the material in the CEDAR gas volume produces much greater effects in the innermost straws than elsewhere in the Straw plane. This results from the tails of the multiple Coulomb scattering distribution. A sensitive measure of the effect of the radiator material, which is rather independent of the relatively small (10%) variations in beam intensity, is then the ratio of the flux (per event) in the innermost and outermost

straws on a plane. This ratio is shown in table 5.15 for Straw chamber 1, where all 20 innermost and 20 outermost straws from all straw planes were used.

Chamber	Vacuum	Nitrogen	Ratio Vacuum/Nitrogen
1	3.60 ± 0.03	4.79 ± 0.01	0.75 ± 0.01
4	3.82 ± 0.04	4.95 ± 0.03	0.77 ± 0.01

Table 5.15: Ratio of fluxes on the 20 innermost and 20 outermost straws of chambers 1 and 4 for data when CEDAR is evacuated(vacuum) and filled with nitrogen gas at 1.74 bar(nitrogen).

An increased activity in the innermost straws with nitrogen is to be expected, but any interpretation requires quantitative comparison with the Monte Carlo simulation. This comparison is given in table 5.16, where a software trigger equivalent to the one applied in data was implemented, resulting in 10,000 kaon decays, dominantly to $\pi^+\pi^0$.

Chamber	Vacuum	Nitrogen	Ratio Vacuum/Nitrogen
1	3.44 ± 0.07	4.51 ± 0.09	0.076 ± 0.02
4	3.54 ± 0.08	4.63 ± 0.09	0.076 ± 0.02

Table 5.16: Ratio of fluxes on the 20 innermost and 20 outermost straws of chambers 1 and 4 for Monte Carlo when CEDAR is evacuated(vacuum) and filled with nitrogen gas at 1.74 bar(nitrogen).

A comparison of tables 5.15 and 5.16 indicates that the effect of the additional scattering in nitrogen gas, compared with CEDAR being evacuated, is well reproduced by the Monte Carlo simulation.

5.8.1 Conclusions from 2014 Data

Using data from runs 1520 and 1543, where the CEDAR volume was filled with nitrogen gas at 1.74 bar and evacuated, respectively, has enabled us to assess the effects of scattering in the nitrogen on the particle flux illuminating the Straw chambers. In particular, the ratio of flux per event in the innermost and outermost 20 straw tubes of Straw chamber 1 gave a sensitive measure of this effect, which was well reproduced by the Monte Carlo simulation using a software trigger similar to that used for the data. With this validation of the MC simulation our confidence in the results discussed in Section 5.6 has been confirmed. We therefore conclude that filling the CEDAR with nitrogen introduces no significant increase in background on the straw chambers, including the innermost straw tubes, compared with the CEDAR being evacuated or filled with hydrogen. As will be discussed in Section 5.9, there are significant advantages in the performance of

KTAG, and particularly in its expected efficiency in tagging kaons, when CEDAR is filled with nitrogen.

5.9 Advantages of using Nitrogen in the CEDAR

KTAG detects the Cherenkov photons radiated by the passage of a beam particle through the gas in the CEDAR and is designed to operate with high efficiency at beam intensities of 50 MHz, corresponding to the rate for the minority kaon particles in the NA62 beam. The CEDAR optics was designed to fully correct the chromatic aberration of nitrogen gas when used as the Cherenkov radiator, but this is no longer true when hydrogen is used. Beam particles produce a cone of Cherenkov light that is reflected and focused onto a backplane in which a circular diaphragm of fixed radius, but variable aperture is situated, figure 5.4[65]. The pressure, and hence refractive index, of the gas is varied until the angle of the cone matches the radius of the aperture. The nominal pressures for the nitrogen and hydrogen are 1.71 and 3.67 bar respectively, where pressure changes with refractive index, n, as $p \sim (n-1)$. Particles of different mass travel at different speeds and hence generate cones of different angles, but in order to ensure that photons from the different cones do not overlap the particles must travel parallel to the axis of CEDAR. This is achieved by designing the beam to be parallel with minimal divergence as it traverses the CEDAR and by aligning the CEDAR to be parallel to the beam. Under this circumstance, and with full correction for the effects of chromatic aberration, the Cherenkov ring produced by kaons is well separated from that of pions, figure 5.5 (a). We have verified during test runs in October 2011 and November 2012[66], along with data analysis done with 2015 data as explained in Chapter 4, using nitrogen gas as the radiator that the CEDAR diaphragm can be opened sufficiently to accept all the light from kaons while being blind to that from pions, thereby providing excellent discrimination between kaons and pions.

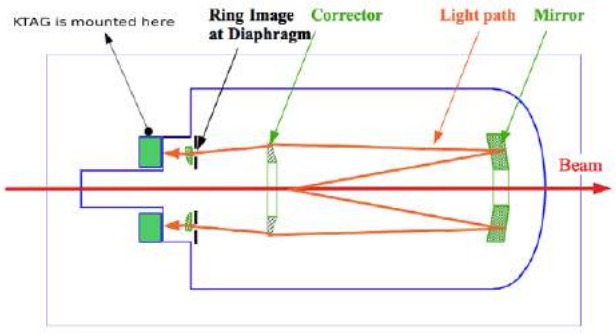

Figure 5.4: Schematic of the optical systems involved in focusing Cherenkov light onto the PMTs in the CEDAR vessel.

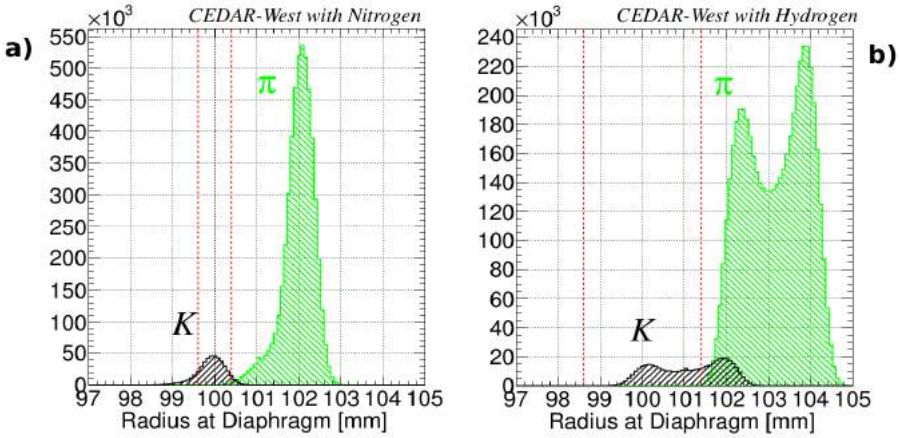

Figure 5.5: Plot showing the separation of photons coming from kaons and pions when using a) nitrogen, b) hydrogen in the CEDAR as evaluated in MC.

During the November 2012 Technical Run (TR), when nitrogen was used as the Cherenkov radiator, an attempt was made to align CEDAR with the particle beam using the available 4 active octants out of the final 8, each populated with 32 PMTs of type R7400U. Technically, the alignment was difficult to achieve and subsequent analysis of the data has revealed a misalignment of the order of 1 mm, which has resulted in somewhat reduced efficiency for detecting kaons. In 2014 KTAG operated with 8 octants, each populated with 48 PMTS, of which 32 are the new R9880U-110 PMTS, which will be surrounded by 16 of the old R7400U PMTs used in previous runs. Spherical mirrors of revised radius have been implemented to produce a light spot to match this geometry and the signal-processing electronics has been modified to enable the higher rate capability to be accepted. The time resolution of a single PMT was measured during the December 2014 run to be 300 ps. KTAG has been shown in 2015 to detect an average number of 20 photo-electrons per kaon for nitrogen, however during the run of December 2014 the diaphragm aperture was only 1mm, 0.5mm below the design aperture, as such the average number of photo-electrons detected was only 14. The measured kaon tagging efficiency in 2014 was still above 95% when requiring at least 5 coincident octant photo-detections and the time resolution per kaon was ∼90 ps [68]. Later analysis of 2015 data with the correct diaphragm aperture found an efficiency of over 98% and time resolution of 70 ps.

When hydrogen is used as the Cherenkov radiator the residual, uncorrected chromatic aberration broadens the Cherenkov rings from pions and kaons, figure 5.5 (b), which then overlap with the danger of giving false kaon identification. The reason for this is understood from figure 5.6, where the effect of chromatic aberration gives rise to a variation in Cherenkov angle, and hence radial position at the diaphragm, with wavelength. In principle, the separation of light from pions and kaons can be recovered, albeit at the expense of an estimated 30% loss in the number of photons[67], by reducing the diaphragm aperture. Some work has been done to assess whether it is possible to recover at least part of this light loss

by changing the 8 spherical mirrors in KTAG for ones with a larger radius of curvature and re-optimising the focal length of the focusing lenses, Chapter 4. This does not currently look to be possible, but a new set of mirrors of larger radius of curvature have been produced in the event that measurements in 2016 indicate otherwise. Using hydrogen as the Cherenkov radiator is then an uncomfortable situation as a loss of 30% in the number of photons reduces the kaon tagging efficiency as shown in figure 5.7, where the measured mean number of detected photons is 20 for nitrogen, a 5-fold coincidence gives 98% efficiency as was the case in 2015.

In addition to the predicted loss of light from a narrower diaphragm aperture, if KTAG were to ever run with hydrogen as the Cherenkov radiator the sensitivity to the alignment of the detector is greater as the kaon and pion peaks are less well separated than for nitrogen. Alignment studies have been performed[5] which highlight the challenges of aligning with a smaller diaphragm radius which is required for hydrogen[69].

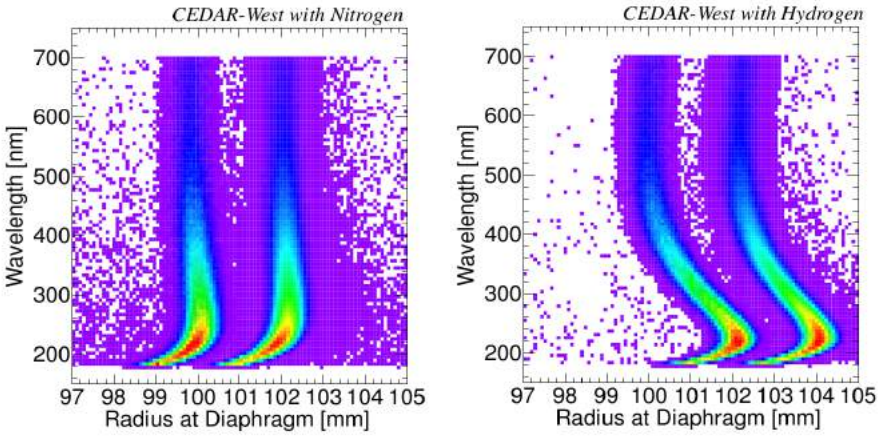

Figure 5.6: The variation in radius on the diaphragm plane of Cherenkov light of different wavelengths arising from chromatic aberration in hydrogen.

Given our previous experience of running with nitrogen as the Cherenkov radiator we can be fairly sure that KTAG will continue to fulfil its design brief: its efficiency will be close to 100% and the kaon will be time-stamped with a resolution of less than 100 ps, which in combination with the excellent timing of the RICH will help to reduce the background to rare decays arising from multiple combinations of beam and decay particles. In contrast, the alignment of the CEDAR to the precision required for hydrogen is non-trivial. Indeed, the very design of the KTAG optics, with a lens and spherical mirror spreading the light rather uniformly over the array of PMTs in each octant, means that we are rather insensitive to the precise alignment of the CEDAR. This is of little consequence for nitrogen, where the kaon and pion peaks are well separated and we can be sure of selecting all photons only from kaons. For hydrogen that certainty is lost.

[5]by Francis Newson

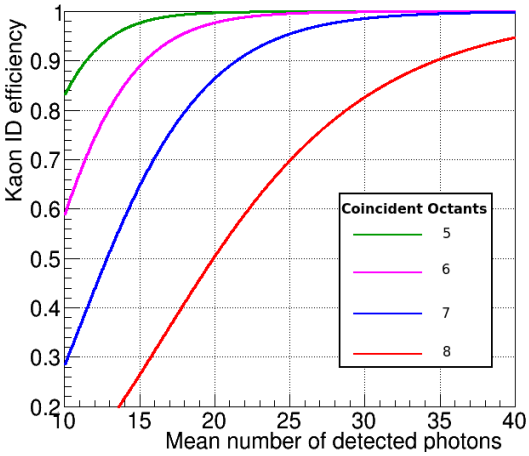

Figure 5.7: The efficiency for detecting a kaon as a function of the number of detected photons for 4 different requirements on the number of octants in coincidence.

Without precise alignment and a clear separation of the kaon and pion peaks we are in danger of operating at reduced efficiency, with a worsened time resolution and with a mixture of photons from a pion overlapping with those from the desired kaon beam particle. The initial time to set up and calibrate the detector is likely to be longer than for nitrogen which was used as the cherenkov radiator both in the 2014 and 2015 runs.

Even if the alignment and other concerns can be addressed the loss of light that arises as a result of using hydrogen as the Cherenkov radiator is unavoidable. With nitrogen it was demonstrated in 2015 that we observe on average 20 photoelectrons per kaon and requiring at least a five fold coincidence of octants produces an efficiency of over 98% which is in line with what we expect from Monte Carlo, figure 5.7. It is estimated that there would be around a 30% light loss from using hydrogen and hence we would expect 14 photoelectrons per kaon, we would expect then a degraded efficiency of around 95% when using hydrogen, figure 5.7. We must consider however that any additional contamination from pions that may need to be controlled by requiring a stricter six fold coincidence would reduce the kaon efficiency for hydrogen to around 80% which leads to a direct reduction in the size of data samples with positively identified kaons that can be used for physics analysis.

5.10 Summary and Conclusion

The rate on the Straws due to decays and scattering from the upstream detectors has been studied here for the first and fourth Straw planes and was summarised in Section 5.6 for hydrogen and nitrogen Cherenkov media in table 5.13. Table

5.17 here shows a summary of the expected rates due to scattering, which has been studied in detail in this Chapter, and for the expected rate from decays (muon halo and non-muon halo), outlined in Section 5.7.

	Total Rates (kHz)		
CEDAR Gas	Fourth Straw Plane	Innermost Straw x Direction	Innermost Straw y Direction
H_2	11000	610	510
N_2	11300	630	580

Table 5.17: Summary of the total rates including expected rates from decays, combination of bold entries in Table 5.13 and all of Table 5.14. The Rates for the fourth straw plane.

In table 5.17 the rates on the plane are rounded to the nearest 100 kHz for the plane, the largest uncertainty on this number comes from 500 kHz of uncertainty from decay products which are not muons, see Section 5.7. The rates on the closest straws in x and y are rounded to the nearest 10 kHz with the dominant uncertainty of 20 kHz coming from additional rate due to K^+ decay products which are not muons, Section 5.7.

From table 5.17 we see that the increase in rate on the fourth straw plane when using nitrogen is about 300 kHz compared with a total rate of 11 MHz. For the innermost straw in the x and y directions the increase of the total rate is 20 and 70 kHz, respectively.

During the 2014 NA62 Physics Commissioning Run a limited data set was taken with the CEDAR vessel evacuated. Due to the limitations in size and data quality, data was considered for a grouping of the 20 straws in the innermost region of straw plane 1 along with the outermost 20 straws in straw plane 1. Comparison with Monte Carlo shows the observed ratio of rates in these regions for CEDAR evacuated and CEDAR filled with nitrogen is entirely consistent between data and Monte Carlo.

Providing that CEDAR can be very precisely aligned and a clear separation established between light from pions and kaons, the performance of KTAG with hydrogen will be degraded. However, there are considerable concerns over achieving the required level of alignment and the penalty in performance if we are unable to do so will be severe. With nitrogen, KTAG currently identifies kaons with 98% efficiency and $\sim$70 ps time resolution.

In conclusion, given the information from both the MC simulations and 2014 data analysis presented here, nitrogen is the preferred Cherenkov radiator for the NA62 experiment as a whole. The increased rate on the downstream Straw

spectrometer chambers from the MC simulations is less than 3% on any given chamber and the increase in rate for the individual straws located closest to the beam is less than 15%. These results are supported indirectly from analysis of data by assessing the ratio of hits in the inner and outer straws for CEDAR filled with nitrogen and CEDAR evacuated. This analysis shows agreement between data and MC. The light loss in the KTAG detector when running with hydrogen, assuming perfect alignment, is conservatively estimated at 30% when compared with nitrogen. This translates to at least a 5% loss in efficiency for positive kaon detection. This 5% loss in efficiency is assuming we can use the 5-fold coincidence condition between octants. If instead a 6-fold coincidence is required the loss in efficiency due to hydrogen is around 15%. The benefit of running with nitrogen is evident when contrasting this modest increase in downstream rate with a light loss in the KTAG detector which translates directly to the size of any NA62 data set.

Chapter 6

$K^+ \to \pi^+\pi^0$, $K^+ \to e^+\pi^0\nu$, and $K^+ \to \pi^+\pi^0\pi^0$ in the 2014 Physics Commissioning Run

6.1 Introduction

The NA62 experiment underwent a physics commissioning run from 6th October to 15th December 2014. The aims of this run were to incorporate and commission the sub-detector systems, described in Chapter 3, on the NA62 beamline under data taking conditions. One of the first detectors to be successfully installed and read out on the beamline was the Liquid Krypton (LKr) electromagnetic calorimeter. Data was available within the first week of the run and many of the commissioning efforts of other sub detector systems involved in some part K^+ decays reconstructed using the LKr calorimeter [72]. An example of this already used in this Thesis is the study of the KTAG K^+ identification efficiency as presented in Chapter 4 which was performed by selecting a pure sample of $K^+ \to \pi^+\pi^0$ decays where both photons from the $\pi^0 \to \gamma\gamma$ decay were within the LKr calorimeter acceptance.

The LKr calorimeter volume itself was already present on the beamline after being used in the previous NA48 experimental set up as well as in the technical runs of the NA62 detector before the 2014 run. Whilst the physical volume remained the same the electronic readout system for the detector was replaced with a new detector readout system. A study of the LKr performance then is motivated firstly by the availability of LKr data in the 2014 run and also from the fact that a new electronic readout system was present for the first time.

The main aim of this chapter is to investigate the performance of the LKr detector during the 2014 physics commissioning run. To do this a selection of the $K^+ \to \pi^+\pi^0$, $K^+ \to \pi^+\pi^0\pi^0$, and $K^+ \to e^+\pi^0\nu$ are presented in Section 6.3,

and a detailed comparison with Monte Carlo (MC) simulations is performed in Section 6.4. The three decays $K^+ \to \pi^+\pi^0$, $K^+ \to \pi^+\pi^0\pi^0$, and $K^+ \to e^+\pi^0\nu$ will commonly be referred to throughout the rest of this Thesis as the K2π, K3π0 and Ke3 respectively. These three channels were chosen as out of the six K^+ decay channels with the largest branching fraction, see table 6.1, they all have at least one π^0 in the final state which makes selection with an electromagnetic calorimeter possible. Furthermore for all three channels all but one of the final state particles are identifiable via the presence of electromagnetic clusters in the LKr calorimeter, π^0s leaving two photon cluster deposits from π^0 decay ($\pi^0 \to \gamma\gamma$) and the e^+ from the $K^+ \to e^+\pi^0\nu$ decay leaving a single cluster.

Decay Mode	Abbreviation	Branching Fraction (%)
$K^+ \to \mu^+\nu$	$K\mu2$	63.55
$K^+ \to \pi^+\pi^0$	$K2\pi$	20.66
$K^+ \to \pi^+\pi^+\pi^-$	$K3\pi$	5.59
$K^+ \to e^+\pi^0\nu$	$Ke3$	5.07
$K^+ \to \mu^+\pi^0\nu$	$K\mu3$	3.35
$K^+ \to \pi^+\pi^0\pi^0$	$K3\pi0$	1.76

Table 6.1: List of the six K^+ decay modes with the largest branching fractions [60]. Highlighted are the decays selected in this analysis. These six decays account for $> 99\%$ of all K^+ decays.

A discussion of the trigger used for this data is outlined in Section 6.2. A data driven study using the geometry of the experiment to motivate a global energy scaling correction is presented in Section 6.3. A cut based selection in data of the $K^+ \to \pi^+\pi^0$, $K^+ \to \pi^+\pi^0\pi^0$, and $K^+ \to e^+\pi^0\nu$ channels is also presented in Section 6.3. A description of the Monte Carlo samples generated for this study along with the necessary selection criteria to make them compatible with data is given in Section 6.4. A full data-MC comparison for the selection criteria of each channel is then given with any areas of tension between the two discussed.

After the selection of the channels in data a background estimation is calculated using MC. Using the data and MC selections to extract signal and background estimations relative branching fractions are calculated for the three channels. At this stage the well established Particle Data Group (PDG) value [60] for these ratios is used as a benchmark to probe the understanding of the LKr detector. We observe reasonable agreement in the data-MC matching of section 6.4 but a significant deviation of the calculated relative branching fractions in Section 6.5. A hypothesis is posited that insufficient modelling of the LKr environment is responsible for the observed discrepancy with the PDG relative branching fractions. There is also significant evidence from the 2014 data analysis that the Zero Suppression (ZS) of clusters in MC is not simulated correctly.

6.2 The 2014 Minimum Bias Data

The data used in this Chapter was all collected in the 2014 minimum bias run which took place on 14th December 2014 and lasted approximately 8 hours. The beam intensity was 5% of the experimental design intensity and approximately 26.5 million triggers were collected in all trigger streams. The data was reconstructed centrally by the collaboration and data is only used if the reconstruction was possible for all read out sub detectors.

During the 2014 minimum bias run all detectors outlined in Chapter 2 were physically present on the beamline, with the exception of the second muon veto system (MUV2). For what concerns this analysis the KTAG, CHOD, LKr and MUV3 detectors were read out for the entirety of the run. The data quality for these sub detectors was generally good, however some discrepancies exist and are discussed in this Chapter. Of the remaining detectors the upstream GigaTracker was not read out for this run and as such nominal assumptions regarding the decaying kaon are made, namely the the momentum is 75 GeV/c and it's position is on the nominal beam axis. The downstream Straw spectrometer tracker was read out during this run, however the read out was done independently of the broader NA62 readout framework. This separate readout meant that a significant amount of time elapsed before the independently read out tracking information was trigger matched and suitable for use, as such this analysis contains no straw tracking information. The RICH detector information is available but due to significant misalignment of the two innermost mirrors there is a significant reduction in geometrical acceptance, as such the RICH data is not used. The remaining muon and photon veto systems contain several detectors which were in various states, non of these detectors were used in this analysis.

The triggers that were implemented during the run were the Q1 trigger (at least one charged track) and the Q1*!MUV3 trigger (at least one non muon charged track). For this analysis only the Q1*!MUV3 trigger was used, primarily because this corresponds to around 95% of the collected data and preferentially rejects the $K^+ \to \mu^+\nu$ channel which has no final state π^0 and a branching fraction of 63.55%. A detailed description of the two trigger conditions follows in Section 6.2.1

6.2.1 Trigger

Q1

The Q1 trigger condition aims to provide an 'at least one' track data sample. As discussed in Chapter 2 Section 2.2.2 the CHOD consists of two planes of plastic scintillator oriented vertically and horizontally. Each plane is divided into quad-

rants with a hole in the centre of the detector to allow the undecayed components of the beam to pass through. The Q1 trigger condition is a coincidence of hits in the same quadrant in the horizontal and vertical planes of the CHOD plastic scintillator slabs. Applying this trigger ensures that we have at least one charged particle reaching the CHOD.

!MUV3

The !MUV3 (not MUV3) trigger condition is based on having no hits, coincident with a positive Q1 trigger condition, above threshold in the MUV3 fast muon veto detector. The MUV3 consists of tiles of scintallator placed downstream of the first two muon veto detectors and an 80cm iron wall. !MUV3 requires that there are no hits in the MUV3 detector and consequently decays in which muons are in the final state are preferentially vetoed. The end result is that predominantly $K2\pi$, $K3\pi0$, $K3\pi$, and $Ke3$ decays are selected. The Q1*!MUV3 triggers were taken by 95% of the readout bandwidth. The Q1*!MUV3 triggered data set is the one used in the analysis in this Chapter.

6.3 LKr based Data Analysis

This Section highlights the data selection and correction techniques that have been utilised in this analysis. The data selection can be categorised as follows.

1. **K^+ Identification for subdetector timing and trigger implementation**
   Needed to remove any background non K^+ decays and to define a suitable time window in the downstream detectors to implement a software version of the trigger described in Section 6.2 and look for in-time data in the LKr calorimeter.

2. **LKr Energy Scaling**
   Applying the two data driven techniques for correcting for any global offset in LKr cluster energies and corrections for the way in which the ∼13,000 channel calorimeter is read out.

3. **Cluster Selection and π^0 Reconstruction**
   Defining cuts based on cluster energy and position variables in order to preselect a sample of photon cluster candidates. Candidates are then combined in pairs to reconstruct candidate π^0's these steps are common to all three final state selections.

4. **Selection of the three decay channels using the kinematics of each decay.**

6.3.1 K^+ Identification, Timing, and Trigger Simulation

In order to select events in downstream sub-detectors which correspond to only the decay products of an identified upstream K^+ it is necessary to identify a time window in various sub detectors with respect to the time of the candidate K^+ identified in the KTAG. In the analysis presented in this Chapter this timing is necessary in the data and MC in order to apply an offline version of the trigger Q1*!MUV3 and also to remove out-of-time clusters in the LKr calorimeter which are due to accidental activity.

K^+ Identification

K^+ identification in the KTAG is achieved by requiring photons hitting PMTs in at least 5 of the 8 octants. Figure 6.1a shows the number of sectors hit per KTAG candidate with the K^+ candidates highlighted. Previous studies have shown [45] that for this method K^+ identification efficiency is greater than 98% with π^+ misidentification probability of less than 0.01%. The main difference between this run and the design specification of the KTAG is that the CEDAR diaphragm was opened to 1 mm, 0.5 mm smaller than design. The result of the smaller diaphragm can clearly be seen in figure 6.1b were the total number of hits across all octants is shown. The data has around 30% fewer hits, this is primarily due to the the smaller diaphragm opening. The consequences of a smaller diaphragm opening, fewer detected photons, is a broadening of the time resolution per kaon. The kaon detection efficiency will also be lower than the design efficiency. The efficiency for identifying a kaon in this run is found to be greater than 95% [73]. As this data set was taken with 5% of nominal intensity, the poorer time resolution is not a factor for this analysis. The only observable effect of a 1mm diaphragm opening in this analysis is that data is lost by the reduction in kaon detection efficiency which simply has the effect of reducing the size of the data set.

Timing and Trigger Simulation

In order to remove any accidental activity and correctly simulate the trigger logic at the analysis level it is necessary to define a time widow for each detector with respect to the K^+ candidate time. The K^+ candidate time is shown in figure 6.2a. The KTAG time resolution here is of the order of 10 ns as the time needs to be corrected with respect to the fine time of the each trigger, this was not readily available for this data but it will be corrected for in the 2015 data shown in Chapter 7. Figure 6.2b shows a strong correlation between the KTAG and CHOD timings as expected. The allowed region for a KTAG-CHOD in-time matching is -22 to 18 ns. As can be seen in figure 6.2c the KTAG-MUV3 time coincidence shows no strong correlation between the two sub-detectors. In order to simulate the !MUV3 trigger any event with a MUV3 hit is rejected. This is

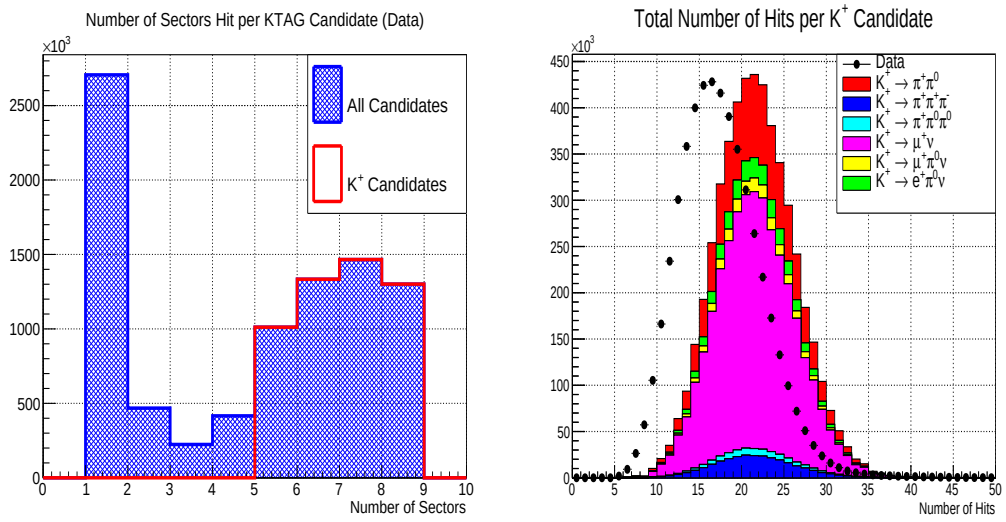

(a) (b)

Figure 6.1: a) Number of sectors per kaon candidate for the data sample, overlayed are the candidates positively identified as K^+. b) Total hits per K^+ candidate. The offset in the data and MC distributions comes from the data diaphragm opening being 1mm compared with the design value of 1.5mm in MC.

not the optimal case as events will be lost where an out of time muon vetoes the event. Any MUV3 channels above threshold due to noisy channels will also cause events to be vetoed. The result of poor time alignment between the KTAG and MUV3 is to reduce the size of the data sample we are considering. The effect on the background estimation from Kμ2 and Kμ3 affecting the total background computation is minimal as for all three of the final states we are concerned with selecting the background from events with final state muons is small, as such a large uncertainty in the rate of Kμ2 and Kμ3 propagates into a much smaller uncertainty of the total background in the K2π, K3π0, and Ke3 selections. Finally a window of 105 to 140 ns is applied to the KTAG-LKr cluster times as can be seen in figure 6.2d. This removes any out of time clusters from consideration of the analysis discussed in Section 6.4.

6.3.2 LKr Detector, Zero Suppression, and Clustering

After applying timing cuts and the trigger logic at the software level the remainder of the analysis is primarily concerned with identifying clusters in the LKr corresponding to energy deposits from incident photons. Some time will be spent in this section detailing the LKr detector and how it is read out along with a discussion on how below threshold channels are zero suppressed. Finally a description of the clustering algorithm will be given to highlight how clusters are formed in the reconstruction from individual LKr cells. The active volume of the electromagnetic calorimeter consists of almost 10m^3 of liquid krypton held inside a cryostat at 120 K. The volume is segmented into 13,248 cells by copper-

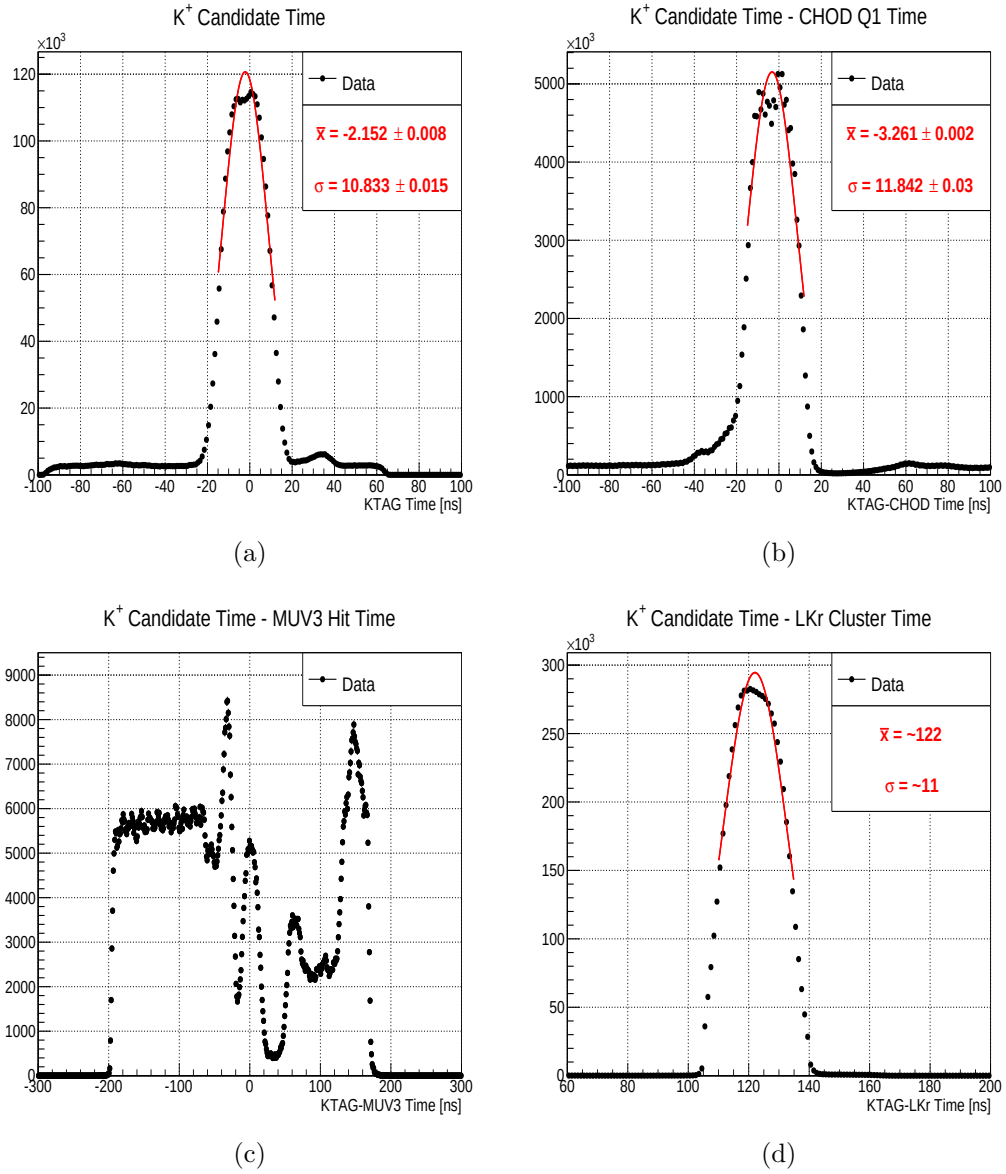

Figure 6.2: a) KTAG K^+ candidate time, show in red are the mean and sigma values of the gaussian fit in the peak region. b) The difference between the KTAG candidate time and the Q1 time, in red are the parameters of the gaussian fit. c) The difference between the KTAG time and the time of every MUV3 hit, no fit is performed as there is no strong correlation between detectors. d) The time difference between the KTAG time and all LKr clusters, again parameters of the gaussian fit are given in red.

beryllium electrodes running through the entire length of the detector as shown in figure 6.3. The resultant active cell of the LKr is a square of side approximately 2 cm. No segmentation along the length axis of the detector is possible due to each electrode passing through the full detector length.

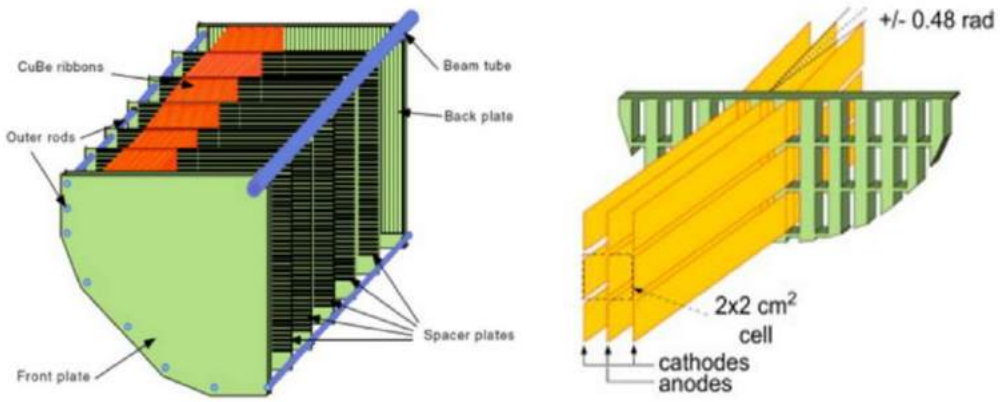

Figure 6.3: Left: One quadrant scematic of the LKr layout, Right: LKr Cell geometry.

Preamplifiers mounted inside of the cryostat directly attached to the electrodes collect the signal produced in the detector by passing particles. The output signal is then fed out of the cryostat via coaxial cables to the readout system. The typical signal shape produced by the detector is a triangular pulse with rise time of $\sim$20 ns and a total length of $\sim$2.7 μs. A uniform response through the detector is produced by using 2000 pulse generators each serving 8 channels. The constant pulse height is then used to calibrate each channel.

LKr Readout Modules

The Calorimeter REAdout Module (CREAM) Module [37] is the new readout system developed to serve the LKr detector. Each CREAM module contains a daughter board which digitises the analogue input signal and a motherboard where the data is processed and sent out if a trigger condition is met. Each board reads out 32 channels. A total of 448 CREAMs read out the full detector.

Each CREAM receives an optical signal encoded using a 40 MHz clock, producing 25 ns time slots, and transmitted at a rate of 160 MHz. Each signal is shaped into a 70 ns wide Gaussian and digitised via the daughter card on each board. The data is then sent to an FPGA mounted on the motherboard where the data enters a circular buffer to be read out if trigger conditions are met. Upon receiving a L0 trigger signal, data is extracted and fed into a secondary buffer. Here the data waits for higher level trigger signals. It is while waiting in the secondary buffer that zero suppression may be applied to the data. If all trigger flags are met the data is read out to the NA62 PC farm. A schematic of the data flow of the CREAM modules is given in figure 6.4.

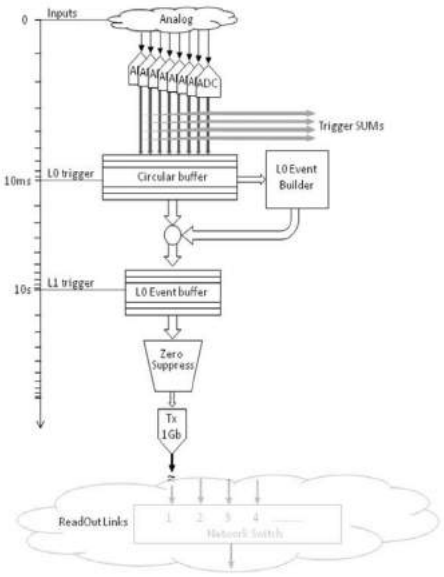

Figure 6.4: Data flow through the LKr CREAM readout module.

Zero Suppression Implementation in the CREAMS

The data that is read out of the LKr calorimeter needs to be compressed due to the ∼13,000 active channels in the detector. This compression is achieved by zero suppressing the data. Zero Suppression (ZS) aims to only read out those cells which have a signal that is appreciably above the noise in a given cell. Further to this suppression of cells in which their is no signal the zero suppression algorithm also removes cells which belong to a genuine shower. A typical electromagnetic shower in the LKr calorimeter will spread it's energy across around 100 cells and therefore the zero suppression threshold is set such that an appreciable number of these cells are not read out. The zero suppression algorithm is based on the difference between the maximum count ($maxCount$) and minimum count ($minCount$) in the read out of a cell for a given event. The features of a typical LKr signal are given in figure 6.5. The readout time window is eight time slots totalling 200 ns. This is more than sufficient to contain the ∼70 ns Gaussian pulse that is produced from an incident particle. The algorithm that was used to provide the 2014 zero suppression was,

$$\text{Channel is suppressed if } (maxCount - ped) < 20, \tag{6.1}$$

where ped is the pedestal value of ADC counts and 20 refers to an ADC count within the detector electronics. The disadvantage of this 2014 method is that the pedestals are regularly recalculated in data taking and this requires the zero suppression to be modified in a time depeneant manner. The 2015 zero suppression scheme was as follows,

$$\text{Channel is suppressed if } (maxCount - minCount) < 20. \tag{6.2}$$

This zero suppression removes any cells below a threshold of ADC counts which translates into a minimum energy per cell cut. This cut does not translate to a uniform minimum cell energy however as cells have varying baselines of noise. This suppression of cells removes the vast majority of cells without signal however when the LKr reconstruction is implemented to group cells into clusters genuine signal cells which are below threshold can be suppressed and as such an energy dependent zero suppression energy correction for cells is required. This correction will be discussed for this data set in Section 6.3.3 and for the MC samples in Section 6.4.

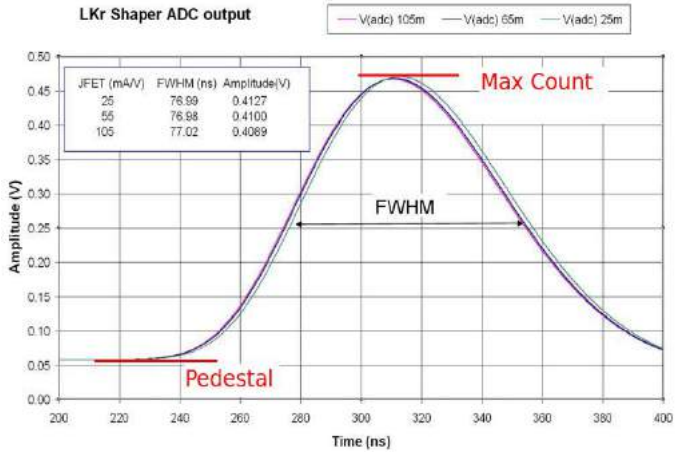

Figure 6.5: Idealised shape of the LKr signal for an incident particle. The voltage increase here is analogous to an increase in ADC counts. The maximum count and pedestal value is shown. For this idealised case the pedestal value is equivalent to the minimum number of counts. [37]

LKr Clustering

The LKr electromagnetic calorimeter is comprised of over 13,000 individual cells which must be combined in such a way as to reproduce clusters that are indicative of the incident particles. The key features of a signal are summarised in figure 6.5 which is an idealised representation of an LKr signal shape in a cell. the important features here are the pedestal which is recalculated periodically and is indicative of the noise in a given cell. The pulse has a width of ∼70 ns [37]. In order to form clusters the following steps are invoked in the LKr Reconstruction software:

- the pedestal of each cell is subtracted to evaluate the cell energy;
- a seed is defined if a cell has an energy larger than 250 MeV;
- a loop on all seeds is performed to identify a cluster, which is defined by a cell with more energy than the eight surrounding ones and such that:

$E_{Seed} > 0.18GeV + 1.8E_{av}$, where E_{av} is the average energy of the eight surrounding cells;

- to determine the cluster energy another loop on the LKr cells is performed: for each cell the number of clusters within 11 cm and 20 ns is evaluated and if only one is found, then the cell energy is added to the cluster energy;
- when a cell belongs to more than one cluster according to the above procedure, then the cell energy is shared among the clusters according to the expected (simulated) energy profile distribution;
- the cluster position is evaluated as the centre of gravity of the energy deposition in a box of 3×3 cells around the seed position;
- the cluster time is defined as the average time between cells in a box 5×5 cells centred on the seed position;
- the shower width (i.e. the cluster size) is evaluated separately in x and y as the r.m.s. of the energy distribution in a box of 5×5 cells centred on the seed position.

This algorithm is tuned to specifically detect electromagnetic showers. It is applied at the reconstruction level to data and MC after ZS. A study in the next Chapter using a data driven technique to select hadronic and electromagnetic clusters will show that the detection efficiency of hadronic clusters is small when compared with electromagnetic cluster detection efficiency.

6.3.3 LKr Energy Corrections

Two energy corrections must be applied to the LKr clusters before performing energy selection cuts. The corrections are as follows,

- Zero suppression energy correction
- Global energy scaling correction

Zero Suppression Energy Correction

Zero suppression is applied to the LKr data in the 2014 minimum bias run. Zero suppression involves suppressing the readout of cells which are below a given threshold, as described in the previous Section. A previous study [74] was performed in order to evaluate the necessary correction to cluster energy for zero suppressed data. The results of this study are shown in figure 6.6. The study took a small non zero suppressed data sample and applied the zero suppression algorithm to this data at the reconstruction phase in order to compare the energies of clusters with and without zero suppression. The result is the energy

dependent correction for zero suppressed clusters as parametrised by the red line in figure 6.6. Later in this Chapter MC samples will be studied where the zero suppression is applied to MC clusters at a software level.

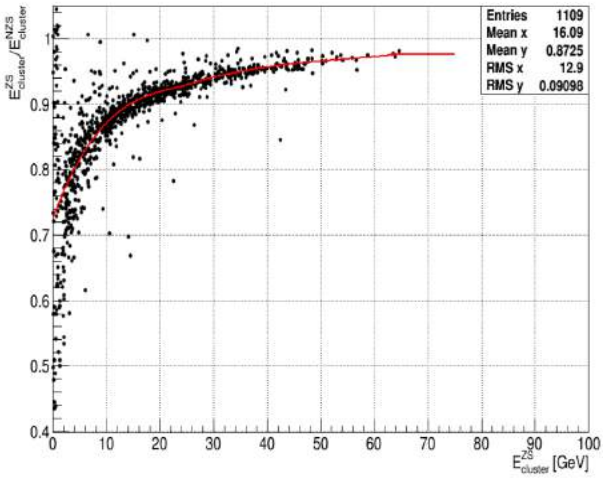

Figure 6.6: Ratio of zero suppressed cluster energy to non zero suppressed cluster energy as a function of the zero suppressed cluster energy. The zero suppression energy correction for data is parametrised by the red curve shown.

It is clearly evident from figure 6.6 that an energy dependent correction due to the presence of zero suppression must be appliedf to the zero suppressed data in order to produce the correct cluster energy. The red curve in figure 6.6 is parametrised in three regions 0 to 25 GeV, 25 to 65 GeV, and greater than 65 GeV. The correction is larger at smaller energies. The divergent behaviour of clusters at very low energies will be excluded from further studies when a minimum cluster energy cut of 3 GeV is applied to the data.

Global Energy Scaling

The global energy scaling is applied to the data only. It takes into account any energy loss in the LKr energy depositions not simulated in MC. This correction must be identified by a data driven technique. To find the global scaling correction, first the zero suppression energy correction is applied. The clusters are then passed through the analysis steps that will be described in Sections 6.3.4 and 6.3.5 of this Chapter where candidate photon clusters are selected and then combined to produce candidate π^0s. The decay vertex position of the candidate π^0 is then found. The final collimators before the decay volume are 1m in length and are present in the z region of 100.255 m to 101.255 m. We would therefore only expect to observe a substantial increase in the detected decays after this point. As will be shown in Section 6.3.5, the calculated π^0 decay vertex z position is proportional to the candidate photon cluster energies, as such we can

apply a global scaling to the LKr clusters such that the π^0 decay vertices are calculated in accordance with the collimator position. As indicated in figure 6.7 a global scaling to cluster energies of 3% was found by earlier studies within the collaboration and is applied to all data to account for the perceived shift in the start point of the decay volume caused by an underestimation of cluster energies.

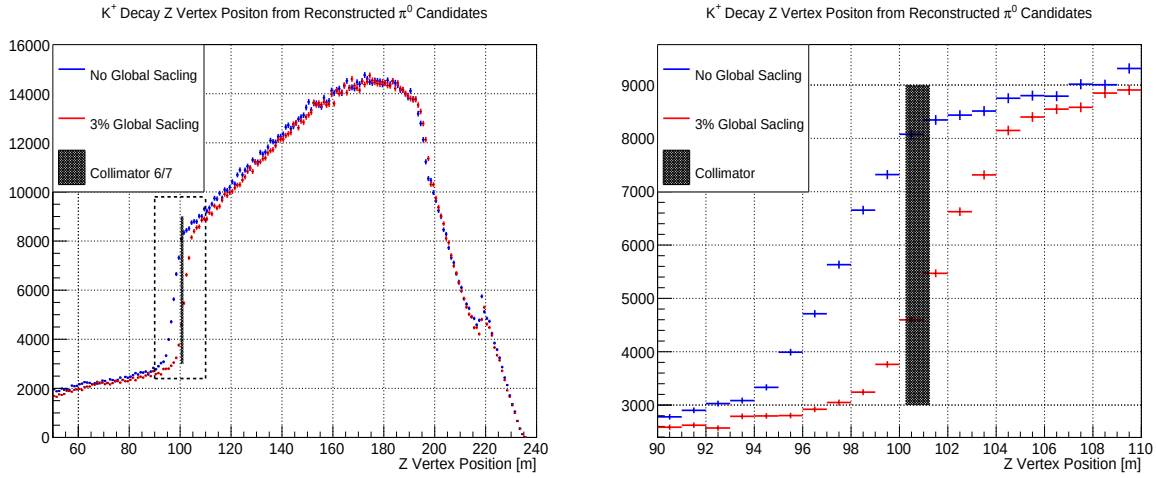

(a) (b)

Figure 6.7: a) Two distributions of the z coordinate of the K^+ decay vertex as inferred from reconstructed π^0 candidates. In blue is the distribution before any global scaling is applied and in red the same distribution with a 3% global energy correction applied. b) The same distribution but zoomed around the region where the final collimator is located. The collimator position is overlayed on both.

6.3.4 LKr Cluster Selection

The cut based analysis to select all the final state π^0s (and in the case of the Ke3 decay the e^+) uses a minimal set of cuts which are well motivated by the expected response of the LKr detector to minimum ionising particles and the LKr sub-detector geometry. This selection of clusters can be broken up into two sections, minimum cluster energy and cluster separation.

Minimum Cluster Energy

The first cut rejects clusters coming from minimum ionising particles (MIPs) which can be vetoed as candidate photon clusters using a minimum energy cut. The response of the LKr detector to MIPs is well understood and is best illustrated by considering the Monte Carlo (MC) response of the detector. Two MC samples generated for the distributions in figure 6.8 are 100,000 $K^+ \to \pi^+\pi^0$

decays and 100,000 $K^+ \to \mu^+\nu$ decays. No triggering or timing was applied to these samples, they are used only to get a representative sample of μ^+ (MIP), π^+ (hadronic), and e^+ (electromagnetic) responses in the detector. Figure 6.8a shows μ^+ clusters which are MIP particles in the LKr detector. MIPs produce a Landau distribution with a strong peak at approximately 500 MeV/c. It can also be noted that π^+, figure 6.8b, will not shower in the LKr around 30% of the time and as such π^+ can produce a MIP response in the detector. A cut requiring cluster energy greater than 3 GeV/c is therefore sufficient to remove greater than 99% of clusters coming from MIPs, whilst preserving the majority of photon clusters, figure 6.8c. In figure 6.9a we see the energy of all in-time data clusters with a MIP peak clearly visible.

Cluster Separation

After applying a minimum energy cut we only accept events which are well separated both from each other and from any dead cells. Firstly we require that the centre of a cluster is greater than 2 cm from any known dead cell. This is to prevent any large energy loss in the cluster due to dead cells as 2 cm is approximately the size of one square LKr cell. There are currently less than 100 known dead cells out of 13,248 total.

We must also ask that any two clusters be well separated from one another to prevent overlap of clusters. Clusters which share common cells share the energy of those cells as part of the clustering algorithm however we would like to remove the dependence of this response from this analysis and use only clusters which have no overlap. By requiring cluster separation to be greater than 20 cm we isolate the clusters sufficiently, due to a typical cluster radius of around 10 cm. In figure 6.9b we see the distribution of the separation between all in-time clusters, there is a minimum present at around 20 cm corresponding to a typical cluster radius. Clusters with a separation of less than 20 cm are present due to the fact that the LKr clustering procedure described in Section 6.3.2 allows for clusters to be formed within 20 cm of one another if the criteria on the central seed cell and surrounding eight cells are satisfied.

Summary of LKr Cluster Selection Cuts

The following are a summary of the sequential cuts applied to LKr clusters in data.

- $E_{\text{Cluster}} > 3\text{GeV}$
- $D_{\text{Dead Cell}} > 2\text{cm}$
- $D_{\text{Cluster}} > 20\text{cm}$

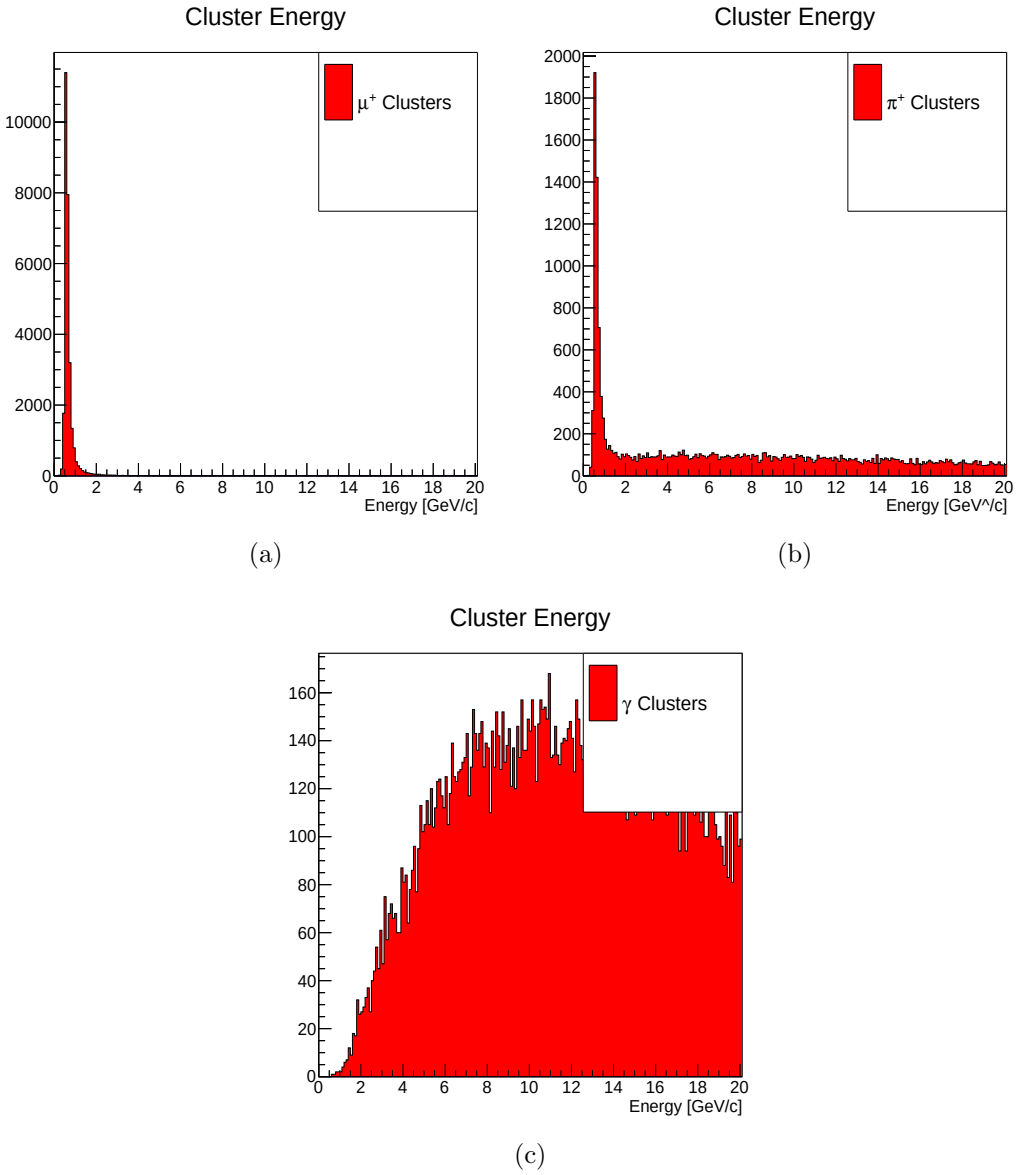

Figure 6.8: a) μ^+ (MIP) cluster energy deposits simulated using Monte Carlo. b) π^+ (hadronic) clusters simulated using Monte Carlo. c) γ (electromagnetic) clusters simulated using Monte Carlo.

It is worth noting at this point that whilst a discussion was given of how MIP clusters are rejected from this sample no attempt has been made to remove hadronic clusters from π^+ which shower. Any cut which wishes to discriminate between hadronic and electromagnetic showers using LKr information only requires a study be performed in data and MC in order to compare the effectiveness of the cut in both. This was attempted using a data driven technique for 2015 data in the next Chapter. The decision not to include a hadronic-electromagnetic discriminatory cut at this stage will become clear at the end of this Chapter when it becomes evident that, primarily for hadronic clusters, the data and MC response under zero suppression is not the same. Any attempt to include a hadronic-

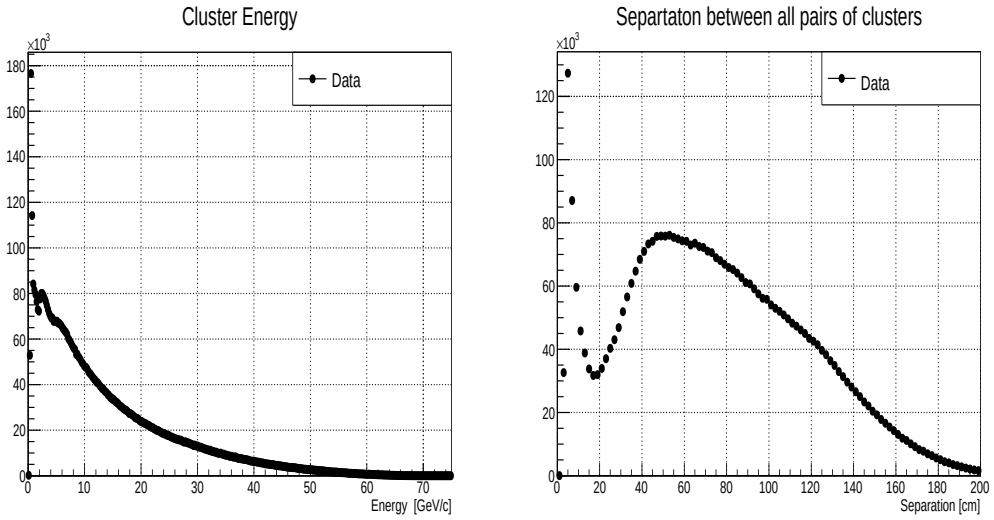

(a) (b)

Figure 6.9: a) Energy of all in-time LKr clusters. b) The distance between all pairs of in-time LKr clusters.

electromagnetic discriminatory cut which was tuned on MC which is not entirely representative of the data would introduce further uncertainty.

6.3.5 π^0 Reconstruction

After we have pre selected clusters we then reconstruct candidate π^0s. This is done using all possible pairs of candidate photon clusters. The correct number of final state π^0's for the three final state channels can then be selected appropriately.

π^0 Decay Vertex

The first step is to calculate the position in z, the axis running parallel to the beam, of the π^0 decay vertex. It is possible to do so using only the positions and energies of the two clusters at the LKr if we assume that both clusters are photons coming from $\pi^0 \to \gamma\gamma$. The formula for calculating the z coordinate of the vertex is,

$$Z_{\text{Vertex}} = Z_{\text{LKr}} - \frac{\sqrt{E_1 E_2 d_{12}^2}}{m_{\pi^0}}, \tag{6.3}$$

where $Z_{\text{LKr}} = 241.495$ m is the position of the LKr. E_1, E_2 are the energies of the two candidate clusters, and d_{12} is the distance between the two clusters. The calculated decay vertex z spectrum is shown in figure 6.10a. In figure 6.10a we

can see a distribution which begins as expected after the final collimator position, indeed this was a variable that was used to tune the global energy scaling correction in Section 6.3.3. Decays before this point represent non physical vertex positions which are found from selecting a cluster which was not formed from a photon as a candidate cluster. At around 220 m we can see the effect of the mirror for the RICH detector which is the largest object between the decay volume and the LKr at $0.2X_0$. We then cut on the vertex such that the reconstructed vertex is within the decay volume of 110 m $< Z_{\text{Vertex}} <$ 165 m.

After we have found the z position it is possible to find the x and y coordinates of the vertex by assuming the decayed K^+ had nominal beam parameters, that is to say it is originally at (0,0) in the x-y plane and receives no deviation in y and a 1.2 mRad deflection in x from the trim 5 magnet located immediately before GTK3 at z=102 m. The trim 5 magnet provides an initial angular deviation to the beam such the MNP33 magnet located in the middle of the four spectrometer planes brings the undecayed beam component back to the beam dump position at the end of the experimental hall. The (x,y,z) position of the K^+ decay vertex is then given by,

$$((Z_{\text{Vertex}} - Z_{\text{T5}}) \tan\theta_{\text{T5}}, 0, Z_{\text{Vertex}}), \tag{6.4}$$

were Z_{Vertex} is the z coordinate of the vertex calculated using (6.3). Z_{T5} is the z coordinate of the trim 5 magnet, 102 m. θ_{T5} is the angle of deflection of a 75 GeV K^+ due to the trim magnet, 1.2 mRad.

π^0 4-momentum

After finding the position of the decay vertex and selecting accordingly we then reconstruct the π^0 4-momentum, P_{π^0}, by summing the 4-momenta of the two candidate photons, $P_{\gamma i}$,

$$P_{\pi^0} = P_{\gamma_1} + P_{\gamma_2}. \tag{6.5}$$

The energy component of the photon 4-momenta is known already from the cluster energy, while the direction of the 3-momentum for each photon is found from the positions of the clusters relative to the decay vertex. The magnitude of the three vector is then found by taking into account the energy of the photon from the cluster energy.

An additional cut on the energy of the π^0 such that it is between 10 and 65 GeV is imposed, figure 6.10b. This cut was introduced in order to reduce the dependence of the analysis on any low energy final state particles, either sub 10 GeV π^0s or sub 10 GeV π^+ corresponding to a 65 GeV π^0. We see in figure 6.10 all candidate π^0s which have passed all selection criteria. The next stage in the analysis methodology will involve either selecting one final state π^0 in

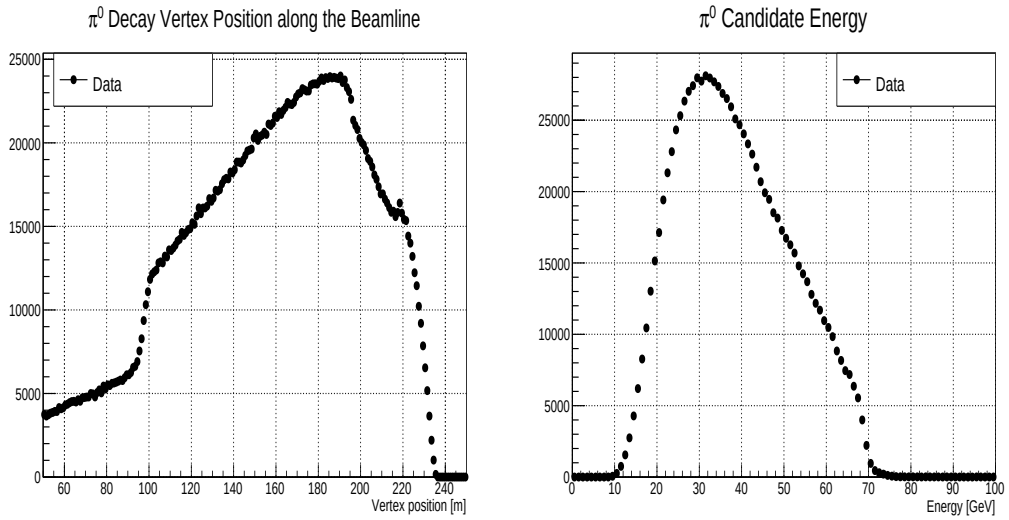

(a) (b)

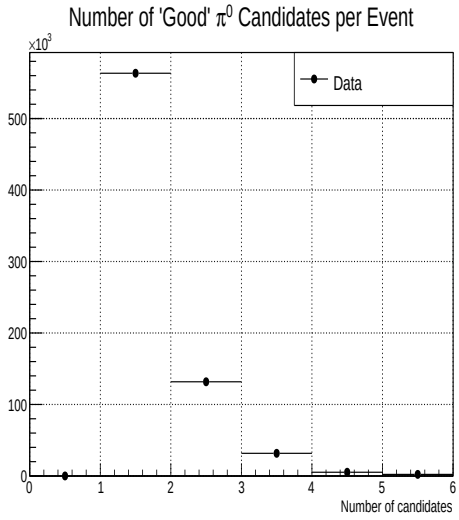

(c)

Figure 6.10: a) Z Coordinate of the vertex for all possible π^0 candidates. b) Energy of all π^0 candidates with Vertex position in the fiducial decay volume. c) The number of candidate π^0s per event which satisfy all previous selection criteria.

the case of $K^+ \to \pi^+\pi^0$ and $K^+ \to e^+\pi^0\nu$ or two independent π^0s as is the case for $K^+ \to \pi^+\pi^0\pi^0$. It is at this stage then where the common selection criteria diverge and it will be necessary to deal with each of the final states separately.

Summary of π^0 Reconstruction Cuts

The following are the nominal set of parameters for defining a good π^0 candidate. These cuts are common to all three final states.

- $110 < Z_{\text{Vertex}} < 165$ m
- $10 < E_{\pi^0} < 65$ GeV

6.3.6 Decay Channels

$K^+ \to \pi^+\pi^0$

The first final state channel investigated was the $K^+ \to \pi^+\pi^0$ two body decay. The procedure for reconstructing the π^+ 4-momentum is relatively straightforward. Firstly any events with more than a single final state π^0, as can be seen from figure 6.10c, are rejected. When we have isolated the sample of events with only one final state π^0 we must compute the π^+ 4-momentum under assumption of nominal beam parameters. This is due to the fact that no upstream information is available for this data set. The π^+ 4-momentum, P_{π^+}, is computed by,

$$P_{\pi^+} = P_{K^+} - P_{\pi^0}, \tag{6.6}$$

if we have correctly identified the π^0 such that both photons have been successfully identified to form the π^0 we should see a peak in the $(P_{K^+} - P_{\pi^0})^2$ spectrum centred on the mass of the π^+, $(0.0195\ \text{GeV}^2/c^4)$. Hereinafter $(P_{K^+} - P_{\pi^0})^2$ will be referred to as the $K^+ \to \pi^+\pi^0$ missing mass squared.

The $K^+ \to \pi^+\pi^0$ missing mass squared spectrum for the full data set is shown in figure 6.11. A peak is clearly visible and fitting this peak with a Gaussian distribution shows this is centred at $0.0189 \pm 0.0045\ \text{GeV}^2/c^4$ showing we are able to select $K^+ \to \pi^+\pi^0$. Background is clearly visible away from the $K^+ \to \pi^+\pi^0$ peak in the large missing mass region of the distribution. This will be studied in much greater detail in Section 6.4 when we perform comparisons with Monte Carlo.

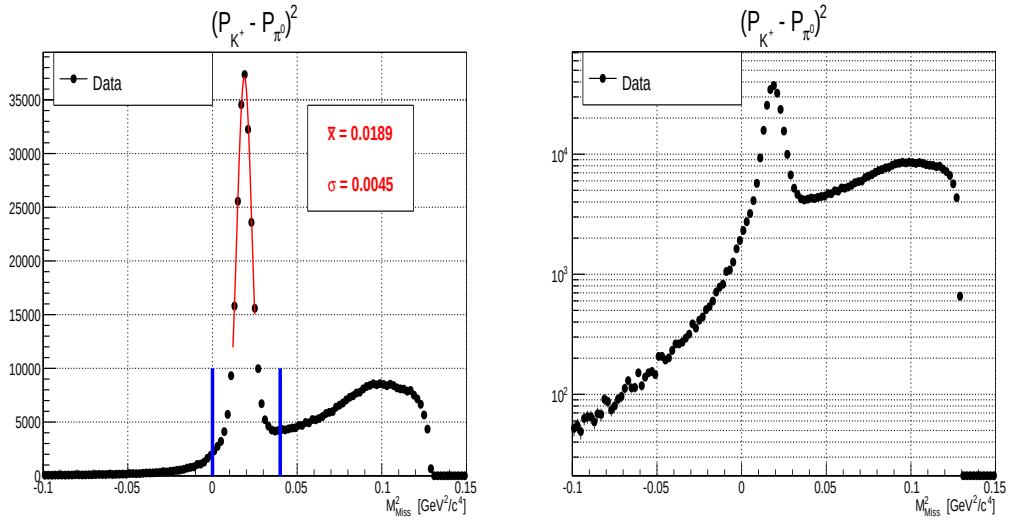

(a) (b)

Figure 6.11: a) The missing mass squared of the $K^+ \to \pi^+\pi^0$ process with a main peak fitted using a Gaussian distribution. Overlayed in blue are the boundaries for the region which will be used to extract signal $K^+ \to \pi^+\pi^0$ events. b) The same distribution but on a logarithmic scale.

$K^+ \to e^+\pi^0\nu$

In order to reconstruct the $K^+ \to e^+\pi^0\nu$ using only the LKr an unconventional approach must be taken. Firstly the analysis steps are repeated as listed previously for selecting $K^+ \to \pi^+\pi^0$. In order to then remove the now background K2π decays we select events in the $K^+ \to \pi^+\pi^0$ missing mass squared region of $0.035 < (P_{K^+} - P_{\pi^0})^2 < 0.055$ GeV^2/c^4, away from the K2π peak. We then reconstruct the e^+ 4-momentum by looking for a third good cluster in the LKr which was not used to reconstruct the π^0. Once a third cluster is identified the e^+ 4-momentum is found by taking advantage of the fact that we know the decay vertex position from the previous π^0 reconstruction. Using the candidate e^+ cluster position, the vertex π^0 position, and taking into account the effect of the MNP33 magnet, which gives a transverse momentum kick of -270 MeV/c in x and is situated between straw planes 2 and 3 at z position 196.955 m corresponding to the centre of the magnet, it is possible to reconstruct the e^+ 4-momentum. The ν 4-momentum, P_ν, is computed by,

$$P_\nu = P_{K^+} - P_{\pi^0} - P_{e^+}. \tag{6.7}$$

If we have correctly identified the $K^+ \to e^+\pi^0\nu$ decay so that both photons have been successfully combined to form the π^0 and the e^+ cluster correctly identified we should see a peak in the $(P_{K^+} - P_{\pi^0} - P_{e^+})^2$ spectrum centred on 0, the approximate mass of the neutrino. Hereinafter the $(P_{K^+} - P_{\pi^0} - P_{e^+})^2$ variable will be referred to as the $K^+ \to e^+\pi^0\nu$ missing mass squared variable.

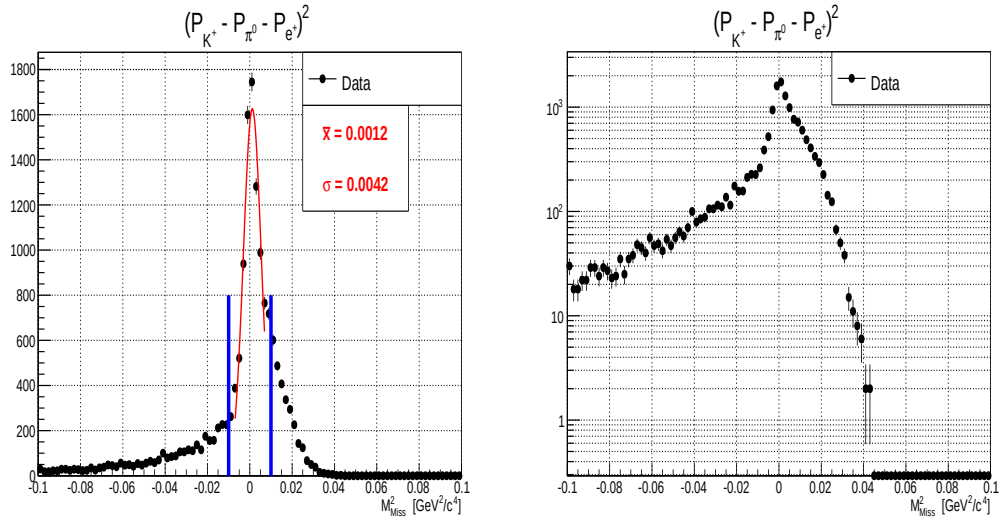

(a) (b)

Figure 6.12: a) The missing mass squared of the $K^+ \to e^+\pi^0\nu$ process with a main peak fitted using a Gaussian distribution. Overlayed on the left in blue are the boundaries for the region which will be used to extract signal $K^+ \to e^+\pi^0\nu$ events. b) The same distribution but on a logarithmic scale.

If we consider the $K^+ \to e^+\pi^0\nu$ missing mass squared spectrum in figure 6.12 we can see that there is a peak in the distribution centred on zero as we would expect. The distribution around this peak is not uniform however due to the kinematic distribution of the remaining $K^+ \to \pi^+\pi^0$ background. This will be discussed when performing data-MC comparisons in Section 6.4.

$K^+ \to \pi^+\pi^0\pi^0$

In the $K^+ \to \pi^+\pi^0\pi^0$ selection we initially select only events with at least two π^0 candidates, figure 6.10c. We then require that only one unique pair of π^0s in the event originate from vertices separated by no more than 5m, the separation between all possible pairs of π^0s is shown in figure 6.13. It is important to note that in order to eliminate the non-physical combinatorial background arising from all possible combinations of π^0s, only pairs of π^0s with no repeated clusters are considered. The reconstruction of the π^+ 4-momentum P_{π^+} is much the same as the $K^+ \to \pi^+\pi^0$ selection, with a small modification due to the second neutral pion such that,

$$P_{\pi^+} = P_{K^+} - P_{\pi^0} - P_{\pi^0}. \tag{6.8}$$

Again if we have correctly selected the four photon clusters in the LKr and paired them appropriately we would expected see a peak in the $(P_{K^+} - P_{\pi^0} - P_{\pi^0})^2$ spectrum centred on the mass of the π^+ (0.0195 GeV$^2/c^4$). If we consult figure 6.14

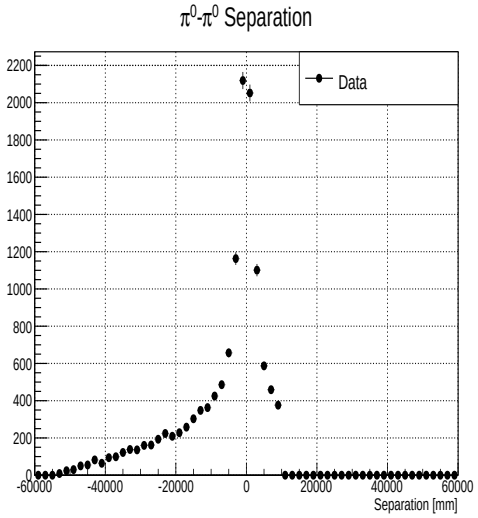

Figure 6.13: Separation of all π^0-π^0 pairs in mm.

we can see that this peak is clearly visible and is much narrower than it was in the case of $K^+ \to \pi^+\pi^0$. This much cleaner selection for $K^+ \to \pi^+\pi^0\pi^0$ is largely due to the fact that the condition that we have four unique LKr clusters forming two good π^0 candidates which share a common decay vertex is indeed a very powerful suppressant of any background. Consequently we observe far fewer events for the $K^+ \to \pi^+\pi^0\pi^0$ decay.

Decay Channel Signal Regions

The amount of data in the signal regions for the three decay channels is given in table 6.2 along with the signal region definition in the missing mass squared variable for each decay. These values will be used in Section 6.5 to calculate the relative branching fractions between the channels. These values contain both the signal events in data as well as background events which need to be modelled by Monte Carlo which will be done in Section 6.4.

Decay Mode	Missing mass squared (MMS) signal region	Events in Signal Region
$K^+ \to \pi^+\pi^0$	$0 < \text{MMS} < 0.04$	251235
$K^+ \to \pi^+\pi^0\pi^0$	$-0.012 < \text{MMS} < 0.05$	6649
$K^+ \to e^+\pi^0\nu$	$-0.01 < \text{MMS} < 0.01$	9208

Table 6.2: The definition of the signal region in the missing mass squared variable for each of the three decay modes. Also given is the number of data events in the given signal region.

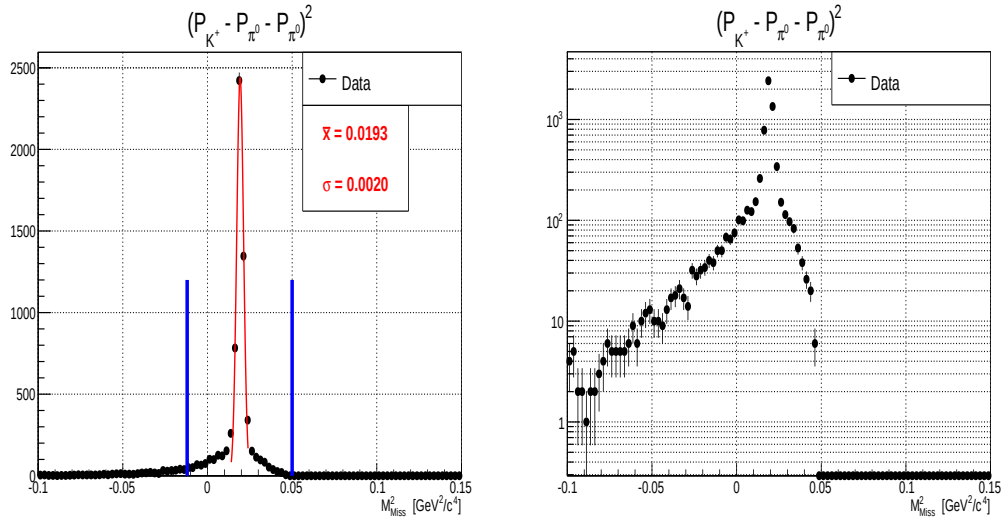

(a) (b)

Figure 6.14: a) The missing mass squared of the $K^+ \to \pi^+\pi^0\pi^0$ process with a main peak fitted using a Gaussian distribution. Overlayed on the left in blue are the boundaries for the region which will be used to extract signal $K^+ \to \pi^+\pi^0\pi^0$ events. b) The same distribution but on a logarithmic scale.

6.3.7 Understanding the Data

In order to study in more detail the data sample we consider some further analysis of the $K^+ \to \pi^+\pi^0$ final state in order to investigate the behaviour of our selected data as a function of the computed candidate π^+ variables. For this analysis all events are accepted which have a single candidate π^0. No restrictions are placed on the vertex position or energy of the candidate π^0 in the distributions shown in figure 6.15. The K2π missing mass squared spectrum is then investigated with respect to the following two quantities,

1. Candidate π^+ Momentum - calculated using the reconstructed π^0 momentum and assuming nominal values for the parent K^+.

2. K^+ Decay Vertex - Found by combining the LKr clusters under the π^0 mass hypothesis outlined in equation 6.3.

We can see from figure 6.15a that we observe a strong peak in the expected region of the π^+ mass squared. As was the case in Section 6.3.6. we also see considerable background for larger missing mass squared, when we expand this distribution as a function of the π^+ momentum, figure 6.15b, we see that the central peak is distributed evenly as a function of momentum. The large missing mass squared shoulder is correlated to the incorrect π^+ momentum. When we expand the missing mass squared as a function of candidate z vertex we observe a reasonably uniform distribution across the decay region, figure 6.15c. An interesting feature of this distribution is the band corresponding to the decay vertex

at ∼100 m which is the position of the final GigaTracker station and interactions with the material are being observed. When we look at the z vertex as a function of candidate π^+ momentum we see a sensible distribution in the region of the decay volume of 100 to 165m however as the decay vertex is calculated to be closer to the LKr position at 240m this becomes strongly correlated with momentum as the π^0 must be low momentum in order for both photons to be within the LKr acceptance, consequentially we observe high momentum reconstructed π^+ candidates in figure 6.15d.

6.4 Data and Monte Carlo Comparisons

6.4.1 Monte Carlo Samples

In order to perform meaningful data-MC comparisons it is necessary to generate MC samples which are representative of the data set. The MC samples generated force the K^+ to decay in the z range of 105 m to 240 m. The initial boundary of 105 m is dictated by the position of the vacuum decay volume. The upper bound of 240 m is the position of the front of the LKr detector. Samples were generated for the six largest decay modes only as the presence of a positive K^+ identification in the KTAG removes the additional beam components. 200,000 events were simulated for the six K^+ decay modes with the largest branching fractions using the NA62 MC framework [62].

The generated Monte Carlo files were then reconstructed using the NA62 reconstruction package, version 516, the same version was used to reconstruct the minimum bias data set. All simulated detectors were reconstructed. The main difference between data and MC, for what concerns this analysis, is that a zero suppression was not applied to the MC for reasons that will be detailed in Section 6.4.2.

After the MC samples had been reconstructed two differences remain between the data set and the MC samples which must be accounted for. Firstly the MC has no trigger applied whilst the data is intrinsically triggered, as discussed in Section 6.2. The same offline triggering conditions were applied to MC as they were for data. Secondly the sub-detector systems in MC are, by definition, time aligned and do not take into account any accidental activity which is present in the data set. The same timing cuts were imposed as were used for data, outlined in Section 6.3 The MC is perfectly time aligned and therefore timing cuts have the effect of accepting almost 100% of events. As the data sample was only gathered at 5% of the nominal intensity accidental activity present in the data set not simulated in MC should be minimal. No global scaling is required in the MC as this scaling was applied to data to correct for energy losses not simulated by the MC. Finally a zero suppression energy correction should, in principle, be applied

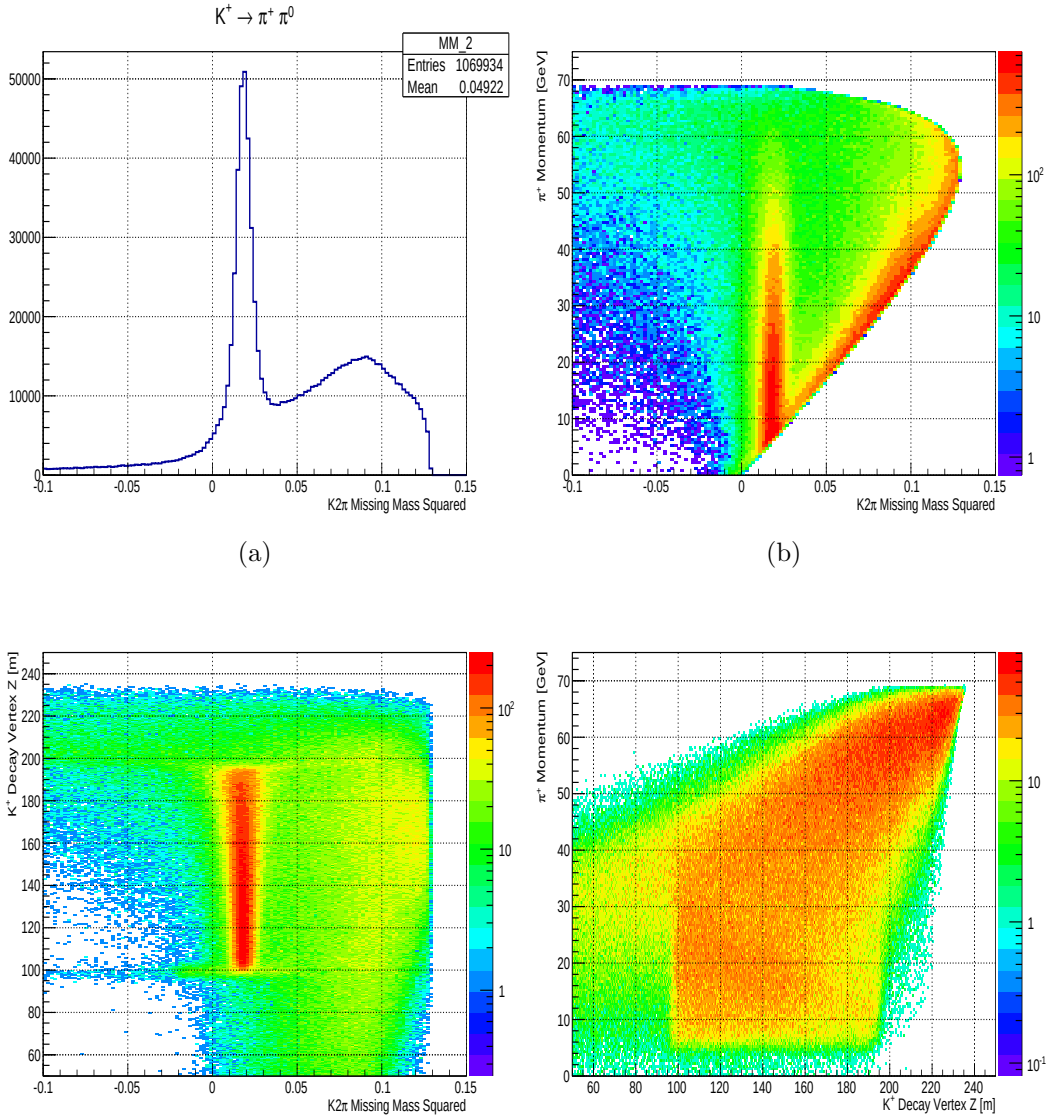

(a) (b)

(c) (d)

Figure 6.15: a) The K2π missing mass squared spectrum. b) The K2π missing mass squared as a function of reconstructed candidate π^+ momentum. c) The K2π missing mass squared as a function of the reconstructed K^+ decay vertex. d) The K^+ decay vertex as a function of candidate π^+ momentum.

to MC. The next Section addresses the issue of ZS in MC.

6.4.2 Zero Suppression in Monte Carlo

If necessary, zero suppression (ZS) is applied to the MC at the LKr reconstruction phase. The algorithm used is the same which was implemented in the CREAM firmware detailed in Section 6.3.2. In principle this ZS energy correction should be the same as it was for data providing that a) the pre-ZS LKr environment is correctly modelled by the MC and b) the ZS algorithm being applied to MC performs in the same way as is done for data. A study was performed that compared the energies of identical clusters in MC with and without zero suppression applied for a sample of 10,000 $K^+ \to \pi^+\pi^0$ decays. The results of this study are shown in figure 6.16. Figure 6.16 shows that a ZS energy correction is required at low energies. However when we compare this distribution to what was found for data in figure 6.6, clearly the level of zero suppression is different between data and MC. In principle as long as these two energy corrections are correctly implemented then this difference should not effect the data-MC comparisons, however there is no way to be sure that a different implementation of ZS in data and MC will produce exactly the same distribution of reconstructed clusters for identical events simply with different energies, the number of clusters per event is liable to change. The study to extract the MC ZS energy correction shown in figure 6.16 involved comparing clusters in identical MC events and using the MC truth parameters stored by the MC generation in order to compare the energy of identical clusters with and without the zero suppression algorithm implemented. Whilst we are considering MC it is possible to separate the clusters in MC into clusters of hadronic origin and electromagnetic clusters. The zero suppression energy corrections for hadronic and electromagnetic clusters in MC are shown in figure 6.17. It becomes immediately apparent that the electromagnetic clusters do not require any energy correction, figure 6.17b. This is an unusual situation as any degree of zero suppression should reduce the energy of any cluster. When we consider the hadronic clusters the zero suppression appears to have been applied and the energy reduced accordingly, figure 6.17a. As we will be concerned in the following analysis with correctly identifying electromagnetic clusters no ZS energy correction is applied to MC. This will cause tension in the data-MC comparisons that follow in the initial cluster selections which should be mitigated when further cuts in the analysis preferentially remove hadronic clusters. The issue of zero suppression in data and MC will be referenced throughout this Chapter and the next. The problem of implementing ZS in MC as outlined here is why it will not be used for the remainder of this Chapter and is an issue of active investigation by the NA62 collaboration.

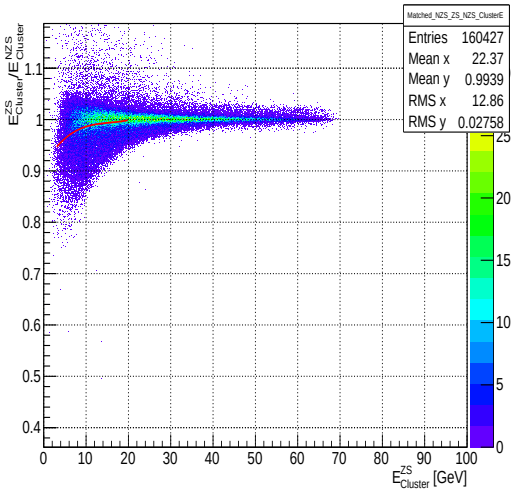

Figure 6.16: Ratio of zero suppressed cluster energies to non zero suppressed cluster energies as a function of the zero suppressed cluster energy for all clusters

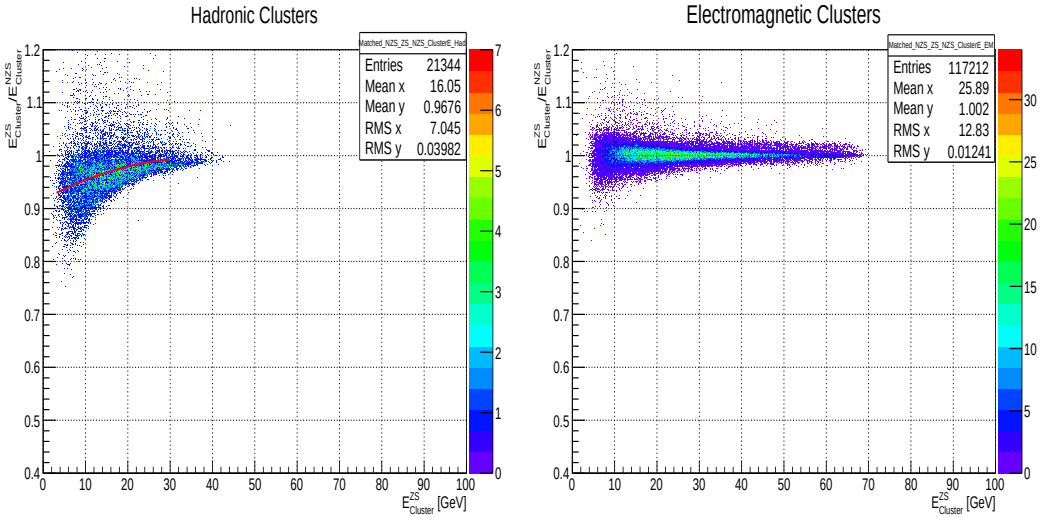

(a) (b)

Figure 6.17: Ratio of zero suppressed cluster energies to non zero suppressed cluster energies as a function of the zero suppressed cluster energy a) for hadronic clusters and b) for electromagnetic clusters.

6.4.3 Monte Carlo and Data Comparisons

In order to understand the purity of the data selections outlined in Section 6.3 the MC samples generated for this analysis were subjected to the same selection criteria as those used for data in Section 6.3, namely,

- $E_{\text{Cluster}} > 3\text{GeV}$,
- $D_{\text{Dead Cell}} > 2\text{cm}$,

- $D_{\text{Cluster}} > 20\text{cm}$,
- $110 < Z_{\text{Vertex}} < 165$ m,
- $10 < E_{\pi^0} < 65$ GeV.

Each of these cuts are applied sequentially. To perform the data-MC matching the total number of MC events was scaled to the total number of data events, N_{Data}. Each channel, $K^+ \to i$ (K_i), was scaled according to the known branching fraction [60], BF_i and the acceptance for each decay channel into each distribution A_i, where this acceptance is defined as the ratio of the number of entries in any given distribution to the number of simulated MC events. The number of scaled events per channel, S_i, in any given distribution is then,

$$S_i = N_{Data} * \frac{BF_i A_i}{\sum_{j=1}^{6} BF_j A_j}. \tag{6.9}$$

The Data-MC comparisons for the minimum cluster energy are shown in figure 6.18a. It can be seen that the energy distributions for the clusters are not well matched across the spectrum. This is in part expected for the MIP particles located at ∼500 MeV as previous studies have shown known inefficiencies for MIP detection in the LKr using the standard clustering algorithm [73]. After the cut is applied at 3 GeV and the MIPs removed from the sample we would expect to see much better agreement between data and MC. After the minimum energy cut is applied and the MC rescaled in figure 6.18b the agreement does improve but is still not well matched. At low cluster energies, typically below 15 GeV/c we see a mismatch between data and MC suggesting that there is a problem in finding the correct cluster energy at low energies for data and/or MC. We can compare with figure 6.17a and see that the MC ZS is also only noticeable in the sub 15 GeV region were we have a significant amount of hadronic clusters. It is likely then that the data-MC discrepancy in cluster energy can at least partially be explained by the effect of ZS in MC on hadronic clusters which has not been corrected for. The comparisons between data and MC not shown here for separation between clusters and separation of clusters from dead cells is reasonable.

Figure 6.19a shows the data-MC comparison for the candidate π^0s decay vertex. There is a notable discrepancy in the region of around 90 to 110m for the decay vertex position, figure 6.19a. The deficiency of MC is well understood here as the MC samples only begin to be generated at 105m whilst the final collimator which removes upstream decays is situated at around 100m. The condition that we scale the total number of MC to the total number of data forces the slight excess in MC elsewhere in the data. After the cut has been applied and the scaling recalculated we see good agreement between data and MC. An interesting feature to note here is the increase in events coming at around 220m where the RICH mirror is situated and the interactions in that material are visible. figure 6.19b shows the π^0 candidate energy after we have selected in the fiducial decay

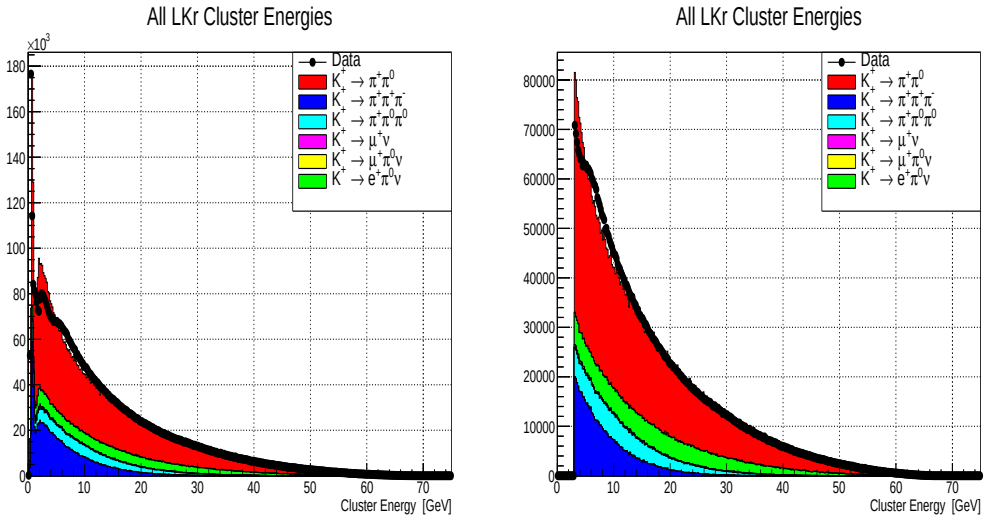

(a) (b)

Figure 6.18: a) Data-MC comparison for all in-time LKr cluster energies. b) Data-MC comparison for all in-time LKr cluster energies after imposing a 3GeV cut.

region were we see good agreement between data and MC. figure 6.19c shows the number of π^0 candidates which pass the previous selection criteria. Although we saw good agreement for the π^0 decay vertex and energy distributions there is a visible difference in the number of candidate π^0 per event between data and MC.

The selection cuts discussed are applied sequentially. We initially see a mismatch in the data-MC comparison for low cluster energies and it was noted that this is where we would expect a significant number of hadronic clusters to be present. As further cuts are applied we see improving data-MC agreement with the π^0 candidate energy distribution showing no obvious error. This may be due to the fact that as we impose cuts on the LKr clusters and the π^0 candidates we are preferentially rejecting hadronic clusters from the sample which we believe are insufficiently modelled in MC at least in terms of the energy response to ZS. When we look at the number of π^0 candidates per event however we see a disagreement in the expected number of single π^0 events of 4%. The distribution shown in figure 6.19c shows that MC predicts on average a larger number of π^0 candidates per event compared with data, which implies a larger initial LKr in-time cluster population in MC. We will return to this in Chapter 7 when we investigate the LKr response in terms of cluster energy distribution and the cluster population for electromagnetic and hadronic clusters separately. At the end of this Chapter when we come to compute relative branching fractions it will be stated how our reliance on MC to estimate the total acceptance for each signal decay into a defined signal region will directly affect the measured relative branching fractions.

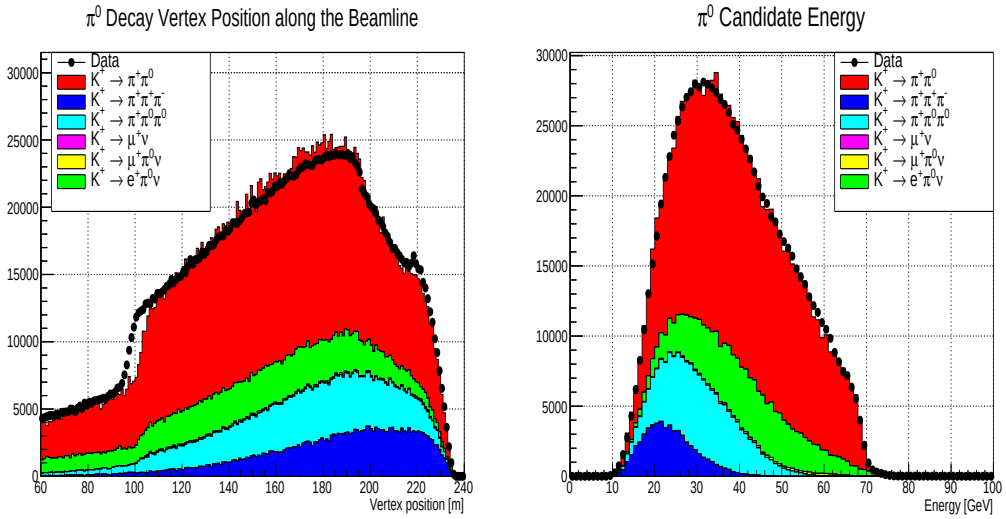

(a) (b)

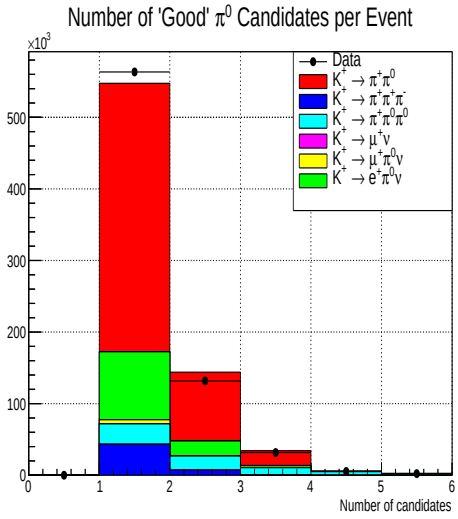

(c)

Figure 6.19: a) Reconstructed π^0 vertex position for all candidate π^0s. b) π^0 candidate energy for all π^0s with decay vertex in the fiducial decay volume, c) Number of candidate π^0s passing all previous cuts per event.

6.4.4 Decay Channels

This section takes the selected π^0 candidates and performs selection of the $K^+ \to \pi^+\pi^0$, $K^+ \to \pi^+\pi^0\pi^0$ and $K^+ \to e^+\pi^0\nu$ channels as was done in section 6.3.6 and scales the MC samples to data in order to extract the expected background in each of the three final state decays. Throughout this Section the data and Monte Carlo selections will be detailed for each of the three channels of interest. The associated statistical error is related to $\sqrt{N_{Data}}$ for each selection in data. The errors on the expected number of background events is related to $\sqrt{N_{MC}}$ for each channel in MC and the measured error from the current PDG[60] value, combined appropriately according to equation 6.9. The full statistical error associated with the branching fractions is no greater than 5% as will be shown in Section 6.5. This same technique will be detailed both in the remainder of this Chapter and in Chapter 7.

$K^+ \to \pi^+\pi^0$

The $K^+ \to \pi^+\pi^0$ decay is selected in exactly the same way as was described in Section 6.3.6. The data-MC comparison for the total number of good final state π^0s is given in figure 6.20. We can see here that we have reasonable agreement in the shapes of the distributions compared with MC.

The background in the signal region of K2π then is calculated as 42633, when considering the Data-MC comparisons. Table 6.3 shows the total amount of data in this signal region was 251235. This corresponds to a background estimation of 17.0%. The agreement both in the positions of the peak and the background distribution across the whole missing mass squared distribution agrees well with data. It should be noted that genuine K2π events will appear in the high missing mass squared shoulder of the distribution when a π^+ cluster fakes a photon cluster in the π^0 reconstruction.

$K^+ \to e^+\pi^0\nu$

The Ke3 sample performs the same analysis steps outlined in Section 6.3.6 and scales the MC to the data to perform a background estimation as shown in figure 6.21 and summarised in table 6.4.

When applying these selection criteria the background estimated in this signal region is 33.7% of the 9208 data events. The data-MC comparison shows good agreement, figure 6.21, as was the case for the K2π selection. It must also be noted at this point that we have reduced statistics for the Ke3 selection compared with the K2π selection due to the following three factors. Firstly the branching

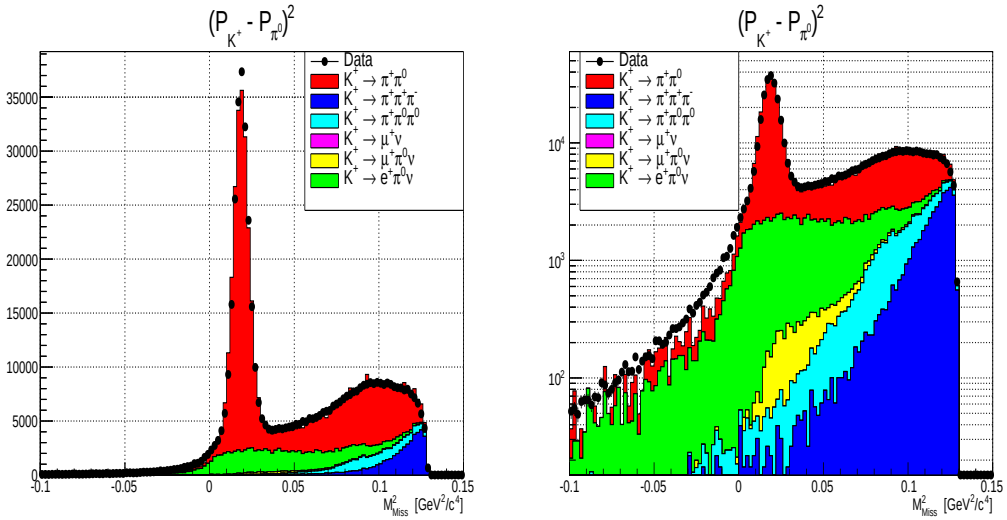

(a) (b)

Figure 6.20: Data-MC comparison of $(P_{K^+} - P_{\pi^0})^2$, on the right is the same plot on a logarithmic axis. The signal region for this distribution is chosen to be $0 <$ K2π MMS $< 0.04\ GeV^2/c^4$.

Decay Mode	Total Events	Signal Region Events	MC Acceptance %
Data	562009	251235	
$K^+ \to \pi^+\pi^0$	385436	211080	6.55
$K^+ \to e^+\pi^0\nu$	96939	39189	4.95
$K^+ \to \pi^+\pi^0\pi^0$	29289	745	0.27
$K^+ \to \mu^+\pi^0\nu$	5877	2149	0.41
$K^+ \to \pi^+\pi^+\pi^-$	44469	550	0.06
$K^+ \to \mu^+\nu$	0	0	0.0
Total Background	176574	42633	

Table 6.3: The total number of events and number of events in the signal region $0 <$ K2π MMS $< 0.04\ GeV^2/c^4$ for the data sample and the individual MC channels where the sum of the MC channels is scaled to the total number of events in data. Also shown are the MC acceptances of events into the signal region.

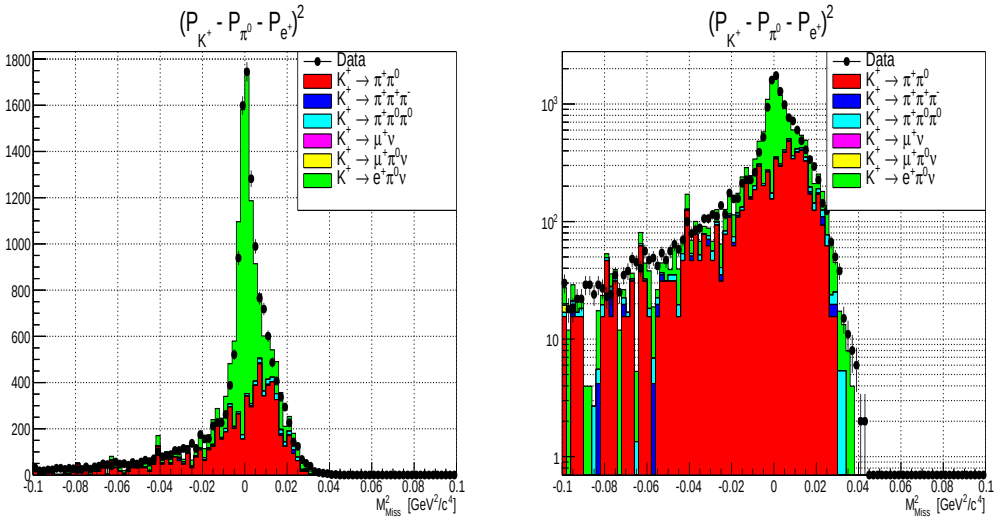

(a) (b)

Figure 6.21: Data-MC comparison of $(P_{K^+} - P_{\pi^0} - P_{e^+})^2$, on the right is the same plot on a logarithmic axis. The signal region for this distribution is chosen to be -0.01 < Ke3 MMS < 0.01 GeV^2/c^4.

Decay Mode	Total Events	Signal Region Events	MC Acceptance %
Data	15325	9208	
$K^+ \to e^+\pi^0\nu$	8025	6200	0.82
$K^+ \to \pi^+\pi^0$	6723	2950	0.10
$K^+ \to \pi^+\pi^0\pi^0$	453	139	0.00
$K^+ \to \mu^+\pi^0\nu$	8	3	0.00
$K^+ \to \pi^+\pi^+\pi^-$	117	8	0.001
$K^+ \to \mu^+\nu$	0	0	0.00
Total Background	7301	3100	

Table 6.4: The total number of events and number of events in the signal region -0.01 < Ke3 MMS < 0.01 GeV^2/c^4 for the data sample and the individual MC channels where the sum of the MC channels is scaled to the total number of events in data. Also shown are the MC acceptances of events into the signal region.

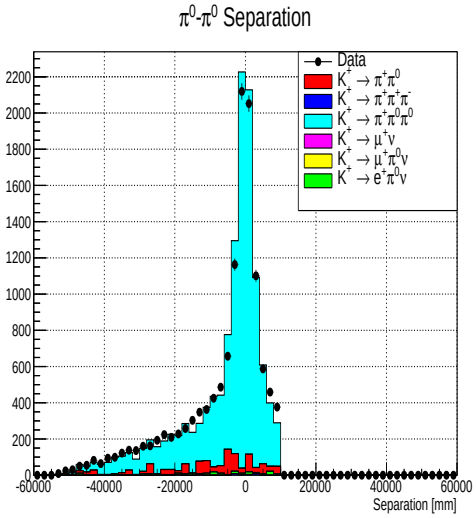

Figure 6.22: Separation of all π^0-π^0 pairs in mm for data and scaled MC.

ratio for Ke3 is around a quarter the size of the branching ratio of K2π. Secondly, as part of the Ke3 selection we selected in the tail of the distribution of missing mass squared from K2π, which still further reduces the number of Ke3 decays we select. Finally we require that the e^+ is in the acceptance of the LKr in order to identify a third electromagnetic cluster which introduces an additional acceptance condition.

$K^+ \to \pi^+\pi^0\pi^0$

The selection of K3π0 follows the same selection criteria in data as it did for MC, Section 6.3.6. The separation between all possible π^0 pairs is shown for data and MC in figure 6.22. Shown in figure 6.23 is the data-MC matching for the K3π0 channel along with background estimation summarised in table 6.5.

The K3π0 sample shows excellent agreement between data and MC. The key thing to note here with respect to the previous channels is that the estimated number of background events in the K3π0 data sample is only 3.1% which is much smaller than for the previous two decay channels. This reduction in estimated background is in large part due to the requirement that we have four separate clusters capable of forming two unique π^0s with a coincident vertex which strongly rejects any sources of background for this decay channel.

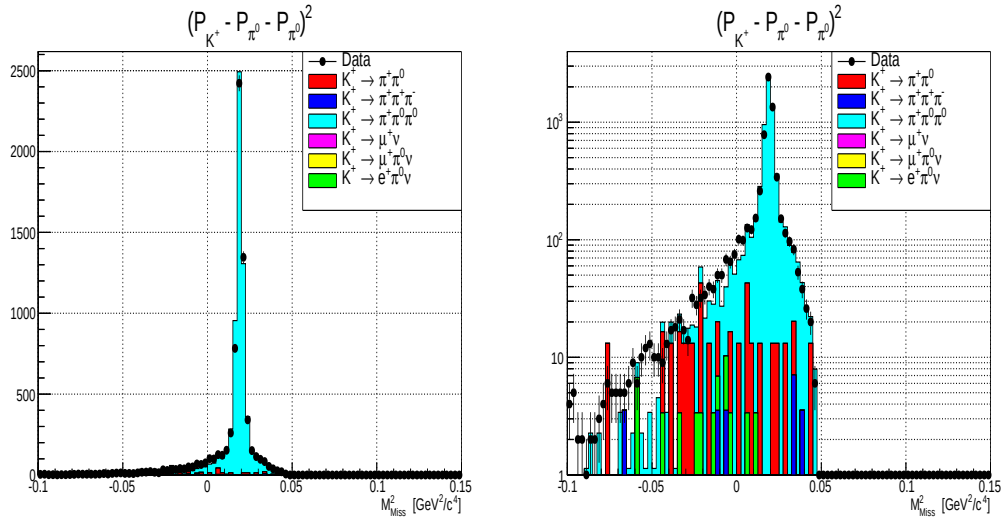

(a) (b)

Figure 6.23: Data-MC comparison of $(P_{K^+} - P_{\pi^0} - P_{\pi^0})^2$, on the right is the same plot on a logarithmic axis. The signal region for this distribution is chosen to be -0.012 < K3π0 MMS < 0.05 GeV^2/c^4.

Decay Mode	Total Events	Signal Region Events	MC Acceptance %
Data	7089	6649	
$K^+ \to \pi^+\pi^0\pi^0$	6709	6551	2.94
$K^+ \to \pi^+\pi^0$	315	171	0.006
$K^+ \to e^+\pi^0\nu$	44	20	0.003
$K^+ \to \mu^+\pi^0\nu$	0	0	0.000
$K^+ \to \pi^+\pi^+\pi^-$	21	18	0.002
$K^+ \to \mu^+\nu$	0	0	0.000
Total Background	380	209	

Table 6.5: The total number of events and number of events in the signal region -0.012 < K3π0 MMS < 0.05 GeV^2/c^4 for the data sample and the individual MC channels where the sum of the MC channels is scaled to the total number of events in data. Also shown are the MC acceptances of events into the signal region.

6.5 Relative Branching Ratios

Section 6.4.4 detailed the individual selections of $K^+ \to \pi^+\pi^0$, $K^+ \to \pi^+\pi^0\pi^0$, and $K^+ \to e^+\pi^0\nu$ showing good agreement between data and MC in the final state kinematic variable of missing mass squared for each channel. After selecting the three channels described in Section 6.4.4 it is useful to compute the relative branching ratios of the three channels. This is a useful piece of analysis as it allows for further probing of both the LKr detector performance during the 2014 run as well as investigating whether the LKr response and environment is sufficiently modelled. Any discrepancies will be indicative of a subtle difference between data and MC. Subtle because as can be seen in figures 6.20 to 6.23 the data-MC agreement is good for each individual channel. All errors given in this Chapter and in the subsequent Chapter 7 using 2015 data are purely statistical. For the values of data and MC the error on a given number in the final state signal region, N, is $\sqrt{N}$. These errors are combined accordingly to calculate the scale factors for scaling each MC channel to the total value of data and also when evaluating the total acceptance in MC.

For a given K^+ decay $K^+ \to i$ (K_i) where i represents the K^+ decay products the total number of kaon decays into final state i, $N(K_i)$, which enter into the signal regions is as follows,

$$N(K_i) = T(K) \times BF(K_i) \times A(K_i), \tag{6.10}$$

where $T(K)$ is the total number of K^+, $BF(K_i)$ is the branching fraction of the given channel, and $A(K_i)$ is the acceptance for a decay K_i into the signal region. Note that $A(K_i)$ is the total acceptance and includes geometrical detector acceptances, trigger acceptances, and the acceptance into the final state via passing the analysis cuts described in Section 6.3 and is evaluated entirely from MC in this analysis.

In this analysis the number of K^+ decays into a final state $N(K_i)$ is found by first identifying the amount of data in the final state signal region as the signal and background from the analysis, $SB_{Data}(K_i)$, and then removing the estimated background evaluated using MC, $B_{MC}(K_i)$, such that,

$$N(K_i) = SB_{Data}(K_i) - B_{MC}(K_i). \tag{6.11}$$

If we then wish to find the relative branching fractions of two channels K_i and K_j the combining (6.10) and (6.11) we get,

$$\frac{BF(K_i)}{BF(K_j)} = \frac{SB_{Data}(K_i) - B_{MC}(K_i)}{SB_{Data}(Ki) - B_{MC}(Kj)} \times \frac{A(K_j)}{A(K_i)}. \tag{6.12}$$

The parameters outlined in (6.12) for the three kaon decays K2π K3π0 and Ke3 are summarised below in table 6.6.

Decay Mode	Data in Signal region SB_{Data}	MC Background B_{MC}	MC Acceptance (%) A
$K^+ \to \pi^+\pi^0$	251235	42633	6.55
$K^+ \to e^+\pi^0\nu$	9208	3100	0.82
$K^+ \to \pi^+\pi^0\pi^0$	6649	209	2.94

Table 6.6: The Data and MC parameters used to calculate the relative branching fractions between the three given channels an the associated statistical error.

The branching fractions for the three channels along with the current Particle Data Group (PDG) value and difference with respect to that are given in table 6.7.

Decay Modes	Relative Branching Fraction	PDG Value	Variation from PDG(%)
$\frac{K^+\to e^+\pi^0\nu}{K^+\to\pi^+\pi^0}$	0.233±0.012	0.245±0.002	(-4.90±5.21)
$\frac{K^+\to\pi^+\pi^0\pi^0}{K^+\to\pi^+\pi^0}$	0.069±0.002	0.085±0.001	(-18.82±3.13)
$\frac{K^+\to\pi^+\pi^0\pi^0}{K^+\to e^+\pi^0\nu}$	0.294±0.016	0.347±0.005	(-15.27±5.63)

Table 6.7: The relative branching fractions for the three selected K^+ decay channels. Also given is the current PDG values and the difference between the two.

As can be seen from table 6.7 a $\sim 20\%$ difference is observed in the branching ratios which contain $K^+ \to \pi^+\pi^0\pi^0$. Whilst the relative branching fraction of $\frac{K^+\to e^+\pi^0\nu}{K^+\to\pi^+\pi^0}$ is in agreement with the PDG value, given the large statistical errors. An investigation was performed in order to evaluate any bias introduced at the analysis level which would cause such discrepancies with the well understood PDG values.

The first way the mismatch in branching ratios was investigated was by varying the thresholds for the various cuts used in this analysis. The cuts were varied and the new branching ratio computed. The result of this analysis was that with the exception of the minimum cluster energy cut, which will be discussed separately, varying the remaining cuts by a sensible amount yields no more than 3% variation in the calculated relative branching fraction and as such would not be sufficient to explain a variation of almost 20% in the $\frac{K^+\to\pi^+\pi^0\pi^0}{K^+\to\pi^+\pi^0}$ relative branching fraction, for example.

As mentioned varying the minimum cluster energy cut and repeating the analysis changes the relative branching fraction by up to 15% for $\frac{K^+\to\pi^+\pi^0\pi^0}{K^+\to\pi^+\pi^0}$ and up to 6% for $\frac{K^+\to e^+\pi^0\nu}{K^+\to\pi^+\pi^0}$. This is shown in figure 6.24. The errors shown in figure 6.24 are not the full statistical error which was calculated for the nominal values in

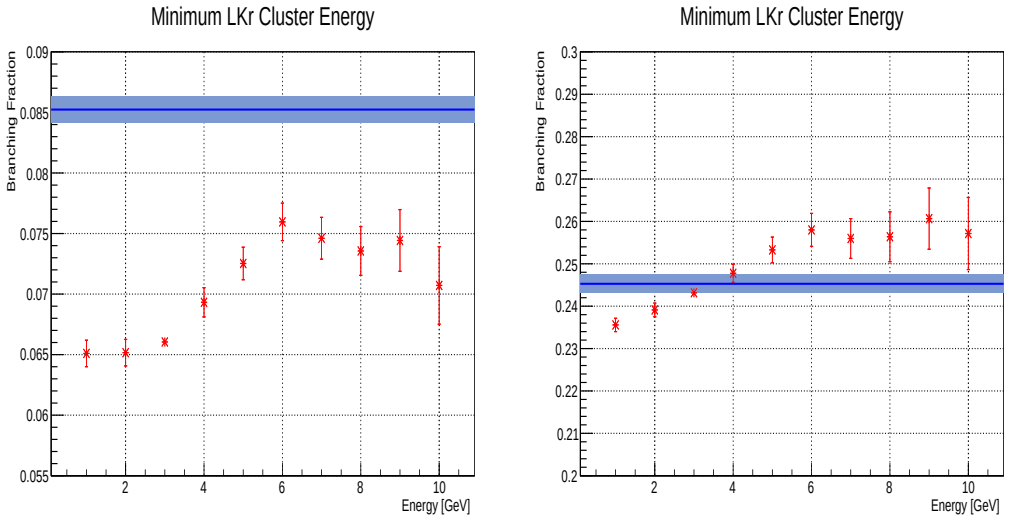

(a) (b)

Figure 6.24: Relative branching fraction of a) $\frac{K^+\to\pi^+\pi^0\pi^0}{K^+\to\pi^+\pi^0}$ b) $\frac{K^+\to e^+\pi^0\nu}{K^+\to\pi^+\pi^0}$ as a function of the minimum cluster energy threshold. The nominal value at 3 GeV has no given error and the errors are the statistical error relative to the nominal value.

table 6.7 but rather the relative statistical error such that for any value N where the statistical error is considered $\sqrt{N}$, the relative statistical error is defined as $\sqrt{abs(N_i - N_{Nom})}$, where N_i is the number of events for a minimum cluster energy i and N_{Nom} is the number of clusters using the nominal minimum cluster energy cut of 3 GeV/c. As we go to an increasing cluster energy cut the relative error becomes large as we are removing significant numbers of events from data and MC. Whilst it is difficult to draw a clear trend from figure 6.24 it is clear that both relative branching fractions are sensitive to the minimum energy cut giving further evidence for poor modelling of cluster response in MC.

6.5.1 LKr Environment in Data and Monte Carlo

So far in this chapter we have observed the following,

1. The data-MC comparisons for all three final states are in good agreement.
2. Despite the above the relative branching fraction of $\frac{K^+\to\pi^+\pi^0\pi^0}{K^+\to\pi^+\pi^0}$ is around 20% below the expected value. $\frac{K^+\to e^+\pi^0\nu}{K^+\to\pi^+\pi^0}$ is in agreement with the PDG value but with large statistical errors.
3. Variation of the cuts in this analysis show that we are sensitive to the minimum cluster energy threshold.
4. After applying a 3 GeV/c minimum energy cut we observe poor agreement

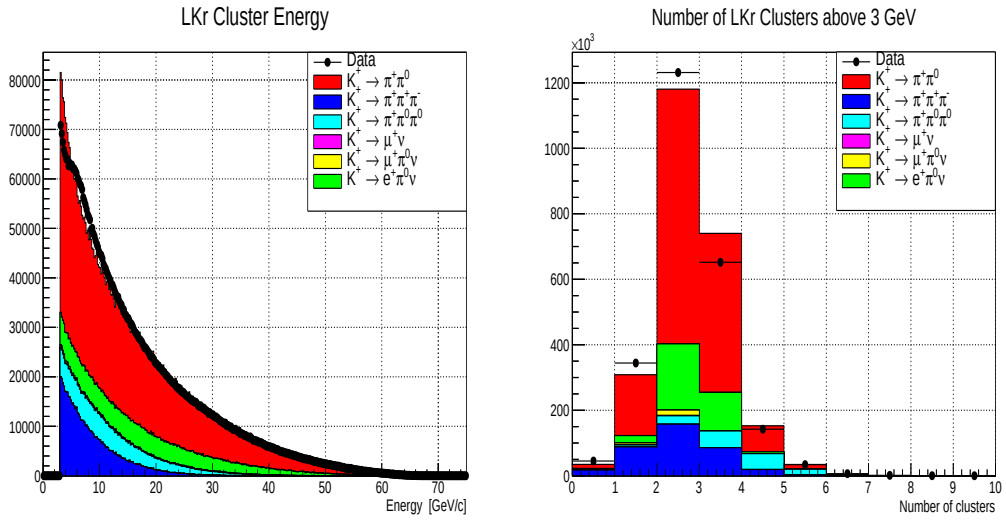

(a) (b)

Figure 6.25: a) Data-MC comparison for all in-time LKr cluster energies after imposing a 3GeV cut. b) Total number of LKr clusters with energy greater than 3 GeV/c in-time with a K^+ candidate for data and MC

between data and MC both in the LKr cluster energy, figure 6.25a, and in the number of in-time clusters per event above 3 GeV/c, figure 6.25b.

The response of the LKr detector is described by the two distributions shown in figure 6.25. For both these distributions we require only in-time clusters in order to eliminate additional clusters in data from accidental activity and a minimum cluster energy threshold of 3 GeV/c to remove MIP clusters which are known to be poorly modelled [74]. The LKr response is clearly not well modelled for these selection criteria and it is vital we understand the origin of this disagreement. In order to assure good agreement between data and MC the following must be considered:

- The pre-zero suppressed LKr environment must be correctly modelled.
- The zero suppression algorithm must be implemented on MC at the software level to replicate what is done in hardware for data.
- The LKr clustering algorithm must have the same efficiency for data and MC at producing clusters from both electromagnetic and hadronic showers.

We have already seen in this Chapter evidence that ZS applied to MC does not correctly replicate data, as the ZS is applied at different stages for data and MC however it is difficult to disentangle the effect of ZS from any inefficiencies in the clustering algorithm. For the sake of clarity both the extent to which ZS is implemented and the LKr clustering algorithm will both be referred to as the LKr clustering efficiency from here on. The effect of clustering efficiency will be

studied in much greater detail in the next Chapter where the Straw spectrometer will be used to identify clusters as either electromagnetic or hadronic in data and assess the responses separately. Validating the electromagnetic response is well modelled in MC is of great interest for the LKr as it's main function is as an electromagnetic calorimeter. The next Chapter then will repeat the analysis presented here for 2014 data on 2015 to see if this problem persists. A separate Straw spectrometer only analysis will then be performed in order to verify that the problem is indeed with the LKr and not symptomatic of the wider data set. Finally studies will be performed using the Straw spectrometer to assess the LKr clustering efficiency for electromagnetic and hadronic clusters separately for data and MC.

6.6 Conclusions

In this Chapter an analysis was presented which selected the $K^+ \to \pi^+\pi^0$, $K^+ \to e^+\pi^0\nu$, and $K^+ \to \pi^+\pi^0\pi^0$ decays in the 2014 minimum bias data set. We were able to identify around 250,000 $K^+ \to \pi^+\pi^0$ decays in data with an expected background of around 17%, 9,000 $K^+ \to e^+\pi^0\nu$ decays in data with an expected background of around 34%, and 6,500 $K^+ \to \pi^+\pi^0\pi^0$ decays in data with an expected background of around 3%. An attempt was then made to calculate the relative branching fractions for the three channels. The $\frac{K^+ \to e^+\pi^0\nu}{K^+ \to \pi^+\pi^0}$ relative branching fraction was found to agree with the current PDG value within the statistical uncertainty. The $\frac{K^+ \to \pi^+\pi^0\pi^0}{K^+ \to \pi^+\pi^0}$ relative branching fraction was found to be around 20% below the PDG value with a statistical uncertainty of 3%. The behaviour of zero suppression in MC along with the average cluster energy distributions and the number of clusters per event was found to be different between data and MC. Using the LKr only selection criteria detailed in this Chapter does not replicate the LKr environment adequately in MC. A plan was outlined for investigating the discrepancy in the measured $\frac{K^+ \to \pi^+\pi^0\pi^0}{K^+ \to \pi^+\pi^0}$ relative branching fraction and more generally the modelling of the LKr environment in the more complete 2015 data set. This will be done in the next Chapter beginning with a repeat of the 2014 analysis on 2015 data to check the effect persists, followed by using Straw spectrometer tracking information to verify the problem is isolated to the LKr and then establish whether the poor modelling arises from electromagnetic clusters, hadronic clusters, or indeed some combination of the two.

Chapter 7

The LKr Calorimeter and Straw Spectrometer Data in the 2015 Minimum Bias Run

7.1 Introduction

Beginning on the 23rd June 2015 and lasting for almost 22 weeks the NA62 experiment entered a second data taking phase increasing significantly on the data sample size from 2014 with an increased number of detectors on the beam line being successfully read out. The aim of this Chapter is to use the 2015 data set to investigate the hypothesis that insufficient modelling of the LKr environment leads to incorrect relative branching fractions when we select the the $K^+ \to \pi^+\pi^0$, $K^+ \to \pi^+\pi^0\pi^0$, and $K^+ \to e^+\pi^0\nu$ decay channels using the LKr as the primary detector. This is done in three distinct ways,

- Firstly, repeat the 2014 data analysis done in Chapter 6 on the 2015 data set to see if the same behaviour persists.

- Then, use information from the Straw Spectrometer to perform a parallel analysis of the three relative branching fractions, independently of the LKr, in order to show that the problem is indeed confined to the LKr.

- Finally, the Straw Spectrometer data was used in order to investigate the LKr response for electromagnetic and hadronic clusters for data, zero suppressed MC, and non zero suppressed MC.

It is important to stress at this point that the deviation between the measured and PDG values of the relative branching fraction of $K^+ \to \pi^+\pi^0\pi^0$ and $K^+ \to \pi^+\pi^0$ was around 20%. As such the whole of this Chapter uses the PDG values [60] as

a benchmark in order to investigate the large discrepancy between the two.

In order to establish that the problems identified in the 2014 data still persist in the 2015 data set it is necessary to apply an LKr based $K^+ \to \pi^+\pi^0$, $K^+ \to \pi^+\pi^0\pi^0$, and $K^+ \to e^+\pi^0\nu$ K^+ selection to the 2015 data. This selection follows as closely as is possible the 2014 analysis, the most notable exception is that the 2015 zero suppression algorithm for data changed slightly with respect to 2014. Section 7.2 contains the global NA62 detector changes in 2015 compared with 2014 and how they will affect this analysis. Data-MC comparisons akin to those done in Chapter 6 are presented and the updated relative branching fractions between the three channels are given in Section 7.3. Section 7.3 will show that whilst the size of the disagreement with the PDG has changed slightly the effect persists.

An analysis which does not use the LKr is performed in Section 7.4 to assess whether this problem is indeed isolated to the LKr and not symptomatic of the data sets as a whole. The analysis uses the Straw spectrometer to select single charged track events. It is then possible to use the known kinematics of single charged track K^+ decays to isolate the $K^+ \to \pi^+\pi^0$, $K^+ \to \pi^+\pi^0\pi^0$, and $K^+ \to e^+\pi^0\nu$ channels. This approach shows agreement between the PDG values of the relative branching fractions within the statistical errors. The problem then appears to be confined to the LKr and not to the data set as a whole.

After showing that this is a problem which is present in the 2015 LKr data set but not persistent in the Straw only data, the next step is to use the Straw spectrometer to study in detail the cluster response of the LKr for both electromagnetic and hadronic clusters. This is performed in Section 7.5 where a non zero suppressed MC sample is also considered in an attempt to understand the LKr environment and response to zero suppression. It will be shown that the LKr detector response in data is poorly modelled by MC for hadronic clusters. The modelling of electromagnetic clusters however appears to be good. In order to see if the poor modelling of hadronic clusters is indeed responsible for the observed discrepancies in relative branching fractions the LKr only analysis is repeated but with the inclusion of Straw spectrometer tracking information used in order to veto hadronic clusters. Using this method agreement with the PDG values is recovered.

7.2 The 2015 Minimum Bias Data

Several minimum bias runs were taken during the 2015 data taking period. This analysis makes use of 200 bursts of run number 3821 corresponding to approximately 8.5 million triggers. The triggering system was the same as it was in the

2014 minimum bias runs, described in Chapter 6. Namely a combination of Q1 and Q1*!MUV3 triggers in combination. Around 95% of all triggers in the data sample correspond to a Q1*!MUV3 condition. The remaining 5% satisfy only the Q1 condition and are not used in this analysis.

The NA62 detector was in the same overall detector conditions as for 2014 with the following major exceptions.

1. Beam intensity changes from 5 to 1 %.
2. GigaTracker thickness is 0.35% radiation lengths from the previous 0.5%.
3. The second muon veto chamber, MUV2, was present on the beamline in 2015.

We would not expect to observe any effects of these three detector wide differences between the data sets as we required sufficient timing windows in all subdetectors which mitigates the difference in beam intensity along with rejecting events decaying in the region of the GigaTracker. The MUV2 is downstream of the LKr and as such will only affect the !MUV3 condition in this analysis. In any case the changes in the detector set up were included in the 2015 MC samples and as such will have a negligible effect on the analysis shown here.

7.3 LKr based Analysis

The aim of this Section is to establish whether the issues raised surrounding the LKr only analysis in the 2014 data persist in 2015. The Section begins with a detailed discussion of the differences between the 2014 and 2015 data sets. The remainder of the section is dedicated to repeating the LKr based analysis steps of Chapter 6 on the 2015 data.

7.3.1 2014 and 2015 Detector Differences

As highlighted in Section 7.2 there are several differences with the experimental conditions of NA62 during the 2015 minimum bias runs compared with the 2014 data which we would expect to provide negligible differences between the 2014 and 2015 analyses. The analysis of the 2014 data took advantage of the LKr electromagnetic calorimeter as the main detector for the analysis. The key difference concerning the LKr is that in 2015 the zero suppression algorithm was changed slightly from what was in place in 2014. Instead of placing a threshold on the difference between the maximum count and the baseline of noise in a channel, also known as the pedestal, the cut was placed between the minimum and maximum

number of ADC counts in each cell. If we consider the idealised signal shape shown in Chapter 6 (figure 6.5) then the pedestal value and the minimum count would be equivalent, however in reality these values may differ slightly depending on the noise of any given channel. The threshold was kept at 20 ADC counts and the new zero suppression algorithm was applied to the Monte Carlo data sets.

Monte Carlo samples of the six main decay channels were generated for the 2015 data reconstructed with software version 834, the number of events generated per decay channel varied and is summarised in table 7.1. A fundamental difference between the 2014 and 2015 MC samples is that the 2015 MC samples were not allowed to decay outside of the region 102.5 to 180m. The reasoning for this is that these MC samples were generated in order to allow efficient analysis to be done with the straw spectrometer which begins at 180m. This difference will have a minimal effect on the LKr selection as we have imposed a cut which requires that reconstructed π^0s must be located in the region 105 to 165m.

The remainder of this section follows as closely as possible the selection that was performed in Chapter 6. The aim is to establish if the same observations regarding the relative branching fractions of the $K^+ \to \pi^+\pi^0$, $K^+ \to \pi^+\pi^0\pi^0$, and $K^+ \to e^+\pi^0\nu$ persist in the 2015 data set.

Decay Mode	Total Generated MC
$K^+ \to \pi^+\pi^0$	964414
$K^+ \to \pi^+\pi^0\pi^0$	967527
$K^+ \to e^+\pi^0\nu$	956135
$K^+ \to \pi^+\pi^+\pi^-$	90997
$K^+ \to \mu^+\pi^0\nu$	794163
$K^+ \to \mu^+\nu$	50147

Table 7.1: Number of MC events for each of the six largest K^+ decays. Used for all 2015 based analyses. Note that for decay modes with no final state π^0s a much smaller number of events were generated.

7.3.2 K^+ Identification, Timing, and Trigger Simulation

The analysis procedure begins in the same way as for 2014 with the K^+ positive identification in data and MC in order to look for in-time activity in the LKr and provide the Q1*!MUV3 trigger at the software level in data and MC. Turning first to the KTAG performance, we can see in figure 7.1a that we observe improved behaviour in 2015 with regard to K^+ tagging as the CEDAR diaphragm was opened a further 0.5 mm to 1.5 mm. The increased diaphragm opening allows a larger number of photons per kaon to reach the KTAG photomultipliers compared with

2014. Figure 7.1b shows that the average number of photons per kaon candidate distribution agrees well with simulation. figure 7.1c shows the distribution of KTAG times which have not been corrected for the fine trigger time and as such are displaced from zero with a resolution of over 10 ns. Correcting for the fine time of the trigger yields the expected behaviour from the KTAG in that we observe a distribution which is centred close to zero with a time resolution of around 1.5 ns per candidate. Note at this stage that the timing resolution is driven by the fine timing resolution of the trigger and not by the independent KTAG timing resolution which is measured to be around 70 ps, as detailed in Chapter 4. This was not required as this run was taken with only 1% nominal beam intensity.

After selecting a K^+ candidate a time window was selected in the CHOD and LKr subdetectors to look for the Q1 trigger condition and candidate LKr clusters respectively. The time distribution of CHOD Q1 conditions with respect to the K^+ candidate time is shown in figure 7.2a and with a resolution of 2.3ns, as such a time window to be defined as within coincidence with the KTAG was chosen from [-6,7]ns. LKr Cluster times with respect to K^+ candidate time is shown in figure 7.2b, a time window of [-6,7]ns was also used for the LKr clusters. We can see from figure 7.2c that it would be possible now to search in a defined time window in the MUV3 in order to require no hits for the !MUV3 condition however as this was not possible for the 2014 data this was not attempted here with the 2015 sample. Also of note in figure 7.2c is the secondary peak offset by around 10 ns, this secondary peak is present in data and MC and is under investigation currently by the collaboration.

7.3.3 LKr Energy Scaling

The global scaling for the 2015 data was 3% as it was for the 2014 data. A change to the zero suppression algorithm was implemented in 2015 and as such the analysis of the zero suppression energy correction in data was repeated which yielded an energy correction which is slightly different than for 2015. Figure 7.3 shows the 2014 ZS energy correction curve and some benchmark cluster energies and the corrected cluster energy after the two different ZS energy corrections are applied. As is made clear from the benchmark values the difference in the correction between 2014 and 2015 is small. A repeat of the investigation into the effect on cluster energy as a result of zero suppression applied to MC was performed. As can be seen in figure 7.4 the result is much the same as for 2014 in that we observe that when we use the knowledge of the true cluster origin gleaned from MC we see that for electromagnetic clusters, figure 7.4b, no correction is needed however for typically lower energy hadronic clusters, figure 7.5a, zero suppression reduces the cluster energy from the non zero suppressed case. No zero suppression energy correction was applied to the 2015 MC.

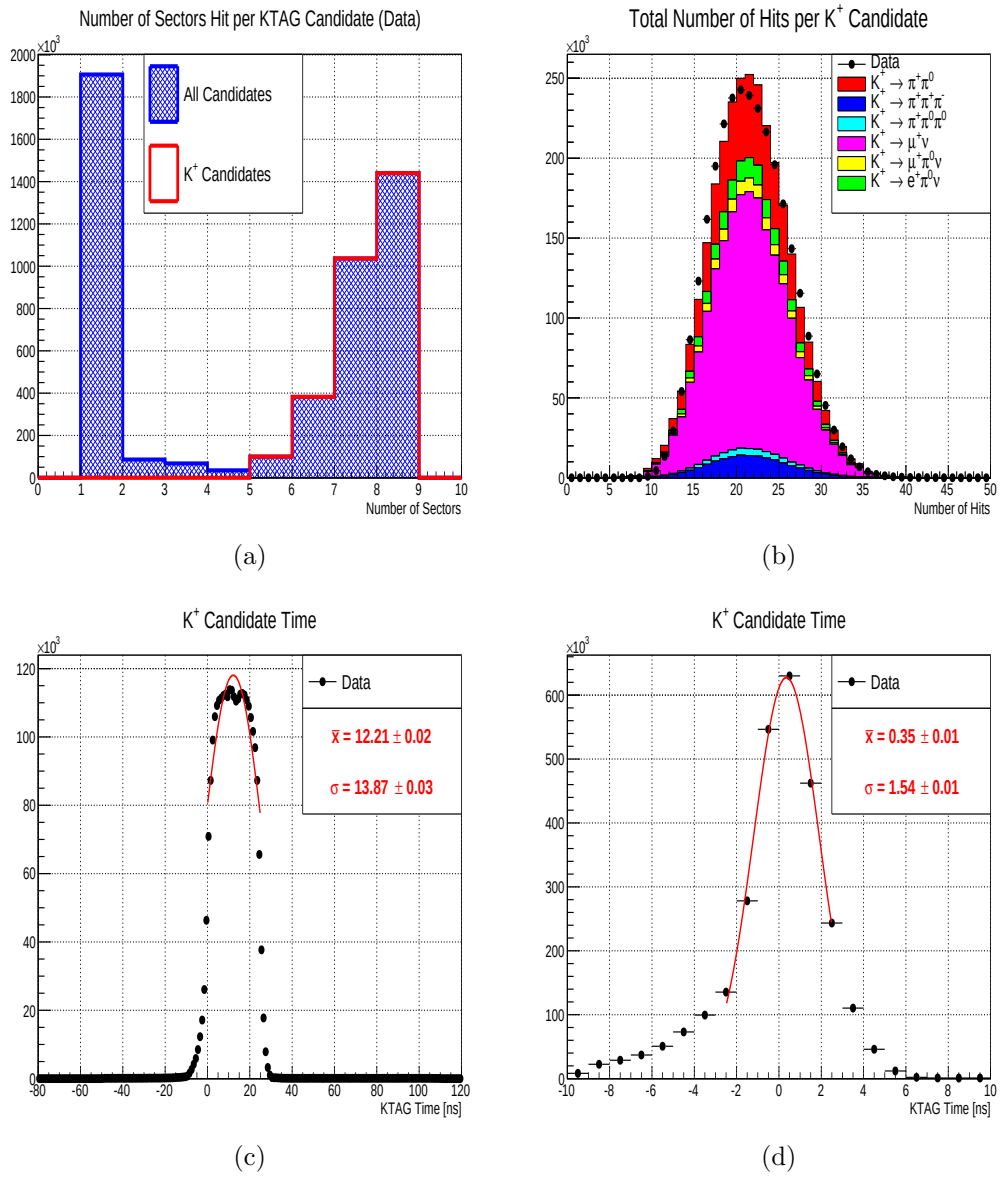

Figure 7.1: a) Number of sectors per kaon candidate for the data sample, overlayed are the candidates positively identified as K^+. b) Total photomultiplier hits per K^+ candidate. c) Kaon Time for each selected K^+ candidate before correcting for the trigger time. d) Kaon Time for each selected K^+ candidate after correcting for the trigger time.

7.3.4 Cut Comparison

After selecting events which satisfy a Q1*!MUV3 trigger condition in-time with a K^+ candidate the same selection cuts are applied to select candidate LKr photon clusters and combine them into π^0s. The selection cuts applied to clusters are identical to those used for the 2014 data and are as follows,

1. Clusters have a minimum energy of 3 GeV.

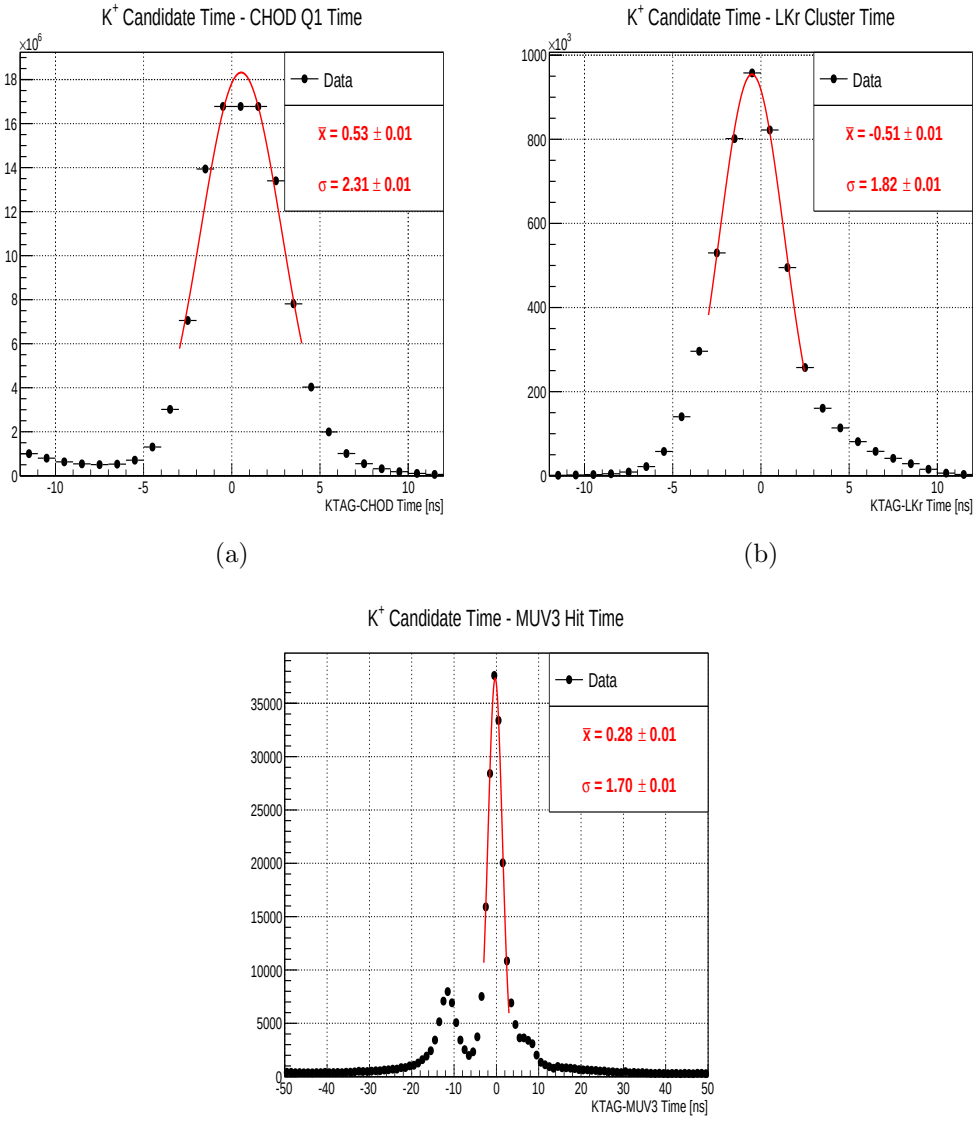

Figure 7.2: a) The difference between the KTAG candidate time and all Q1 candidate times. no fit is performed as there is no strong correlation between detectors. b) The time difference between the KTAG time and all LKr clusters. c) The difference between the KTAG time and the time of every MUV3 hit. In all three distribution a Gaussian fit is made to the primary peak with the mean and σ values of the fit shown.

2. Clusters are separated from all dead cells by at least 2cm.

3. Clusters are separated from each other by at least 20cm.

Figure 7.5a shows the energy distribution of all in-time clusters before any cuts are applied for data and MC. As with the 2014 data and for the rest of the data-MC comparisons in this section the MC was scaled to the data taking into

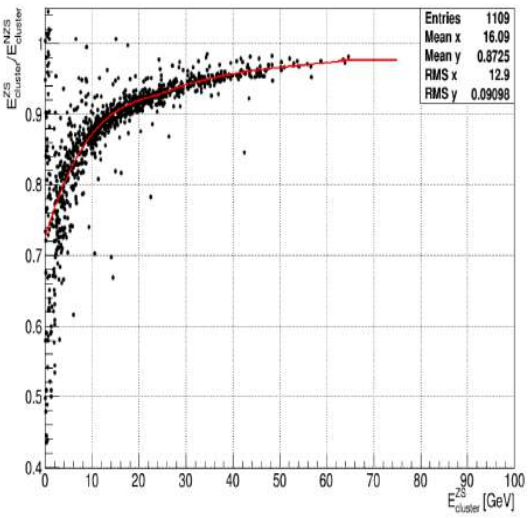

Comparison of the 2014 and 2015 zero suppression energy corrections. All energies given in GeV

Uncorrected Energy	2014 Correction	2015 Correction
3	3.83	3.61
5	6.14	5.82
10	11.48	11.13
25	26.91	26.37
50	50.78	50.35

Figure 7.3: Left: Ratio of ZS Cluster energies to NZS Cluster energies as a function of ZS Cluster energy for 2014 data. Overlayed in red is the zero suppression energy correction. Right: comparison of the zero suppression energy correction at some given cluster energies.

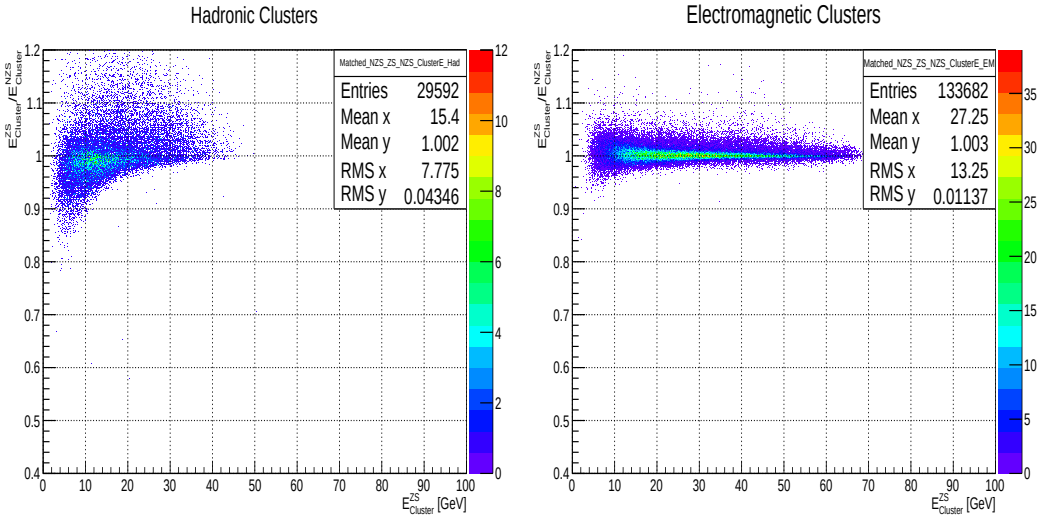

(a) (b)

Figure 7.4: Ratio of zero suppressed cluster energies to non zero suppressed cluster energies as a function of the zero suppressed cluster energy for all clusters, a)for hadronic clusters and b) for electromagnetic clusters.

account the number of generated events in a given channel, the PDG value of the branching fraction of each channel, and normalising the total amount of MC to the total amount of data. We see both in figure 7.5a and 6.5b, where the 3 GeV cut is applied, that there is tension between data and MC at cluster energies below 15 GeV, this was present in the 2014 data and could be caused by insufficient cluster modelling in MC as a result of zero suppression.

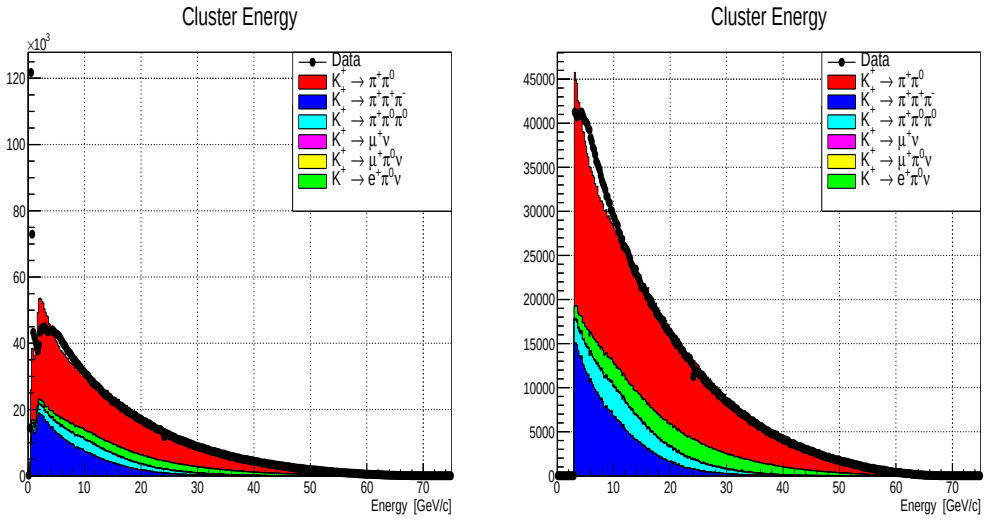

(a) (b)

Figure 7.5: a) Data-MC matching for all cluster energies for data and MC with no cuts applied. b) cluster energy matching after imposing a 3 GeV minimum cluster energy cut.

After we have pre-selected candidate clusters they are combined under the π^0 mass hypothesis as was done for 2014 to create candidate π^0s. A candidate π^0 must satisfy the following two criteria.

- Z coordinate of the decay vertex is in the fiducial decay region of [110,165]m.
- For candidate π^0s satisfying the first condition the energy of the reconstructed π^0 must lie in the region of [10,65]GeV.

Figure 7.6a shows the data-MC comparison where we compare only events which are within the decay volume of 110 to 165 m we see reasonable agreement between data and MC in this region. Figure 7.6b shows the energy of all candidate π^0s before the π^0 energy cut is applied, we see good agreement between data and MC with a slight shift between the two that is small but most likely due to any unaccounted for energy scaling. Figure 7.6c shows the number of 'good' π^0 candidates per event, here 'good' is defined as passing all selection conditions outlined in this section. It is clear from this plot that the MC has more candidate π^0s per event than the data. This was also observed in the 2014 data. The average number of in-time clusters per event in data and MC will be investigated in detail in Section 7.5.

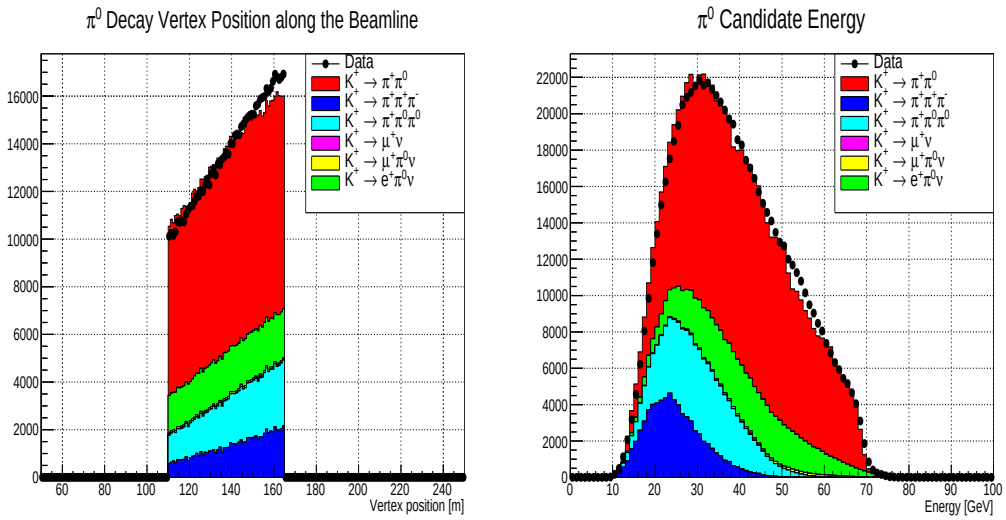

(a) (b)

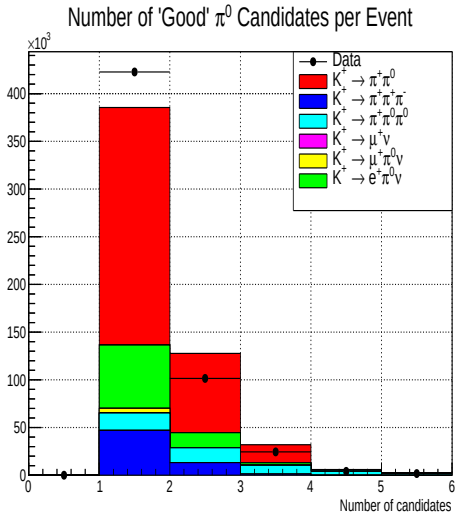

(c)

Figure 7.6: a) Reconstructed π^0 vertex position for clusters in the fiducial decay region of [110,165]m. b) π^0 candidate energy for all candidates in the fiducial decay region. c) Number of π^0 candidates per event passing all previous cuts.

7.3.5 Channel Selection

After selecting good candidate π^0s the missing mass kinematic variable was constructed for the three final states. For the $K^+ \to \pi^+\pi^0$ channel this involved selecting events with exactly one final state π^0 and subtracting the reconstructed π^0 4-momentum from the nominal K^+ 4-momentum. The resultant $(P_{K^+} - P_{\pi^0})^2$ variable is referred to as the K2π missing mass squared (MMS) variable. The K2π MMS is shown in figure 7.7a where the data-MC comparison is good across the entire region, as highlighted by the agreement when plotting on a logarithmic axis, figure 7.7b. The agreement is very similar to what was observed in 2014. We define a signal region of $0 <$ K2π MMS $< 0.04\ GeV^2/c^4$. We see in table 7.2 the values for the total amount of data for both data and scaled MC along with the MC acceptance. 191823 data events are observed in the signal region with an expected MC background of 36409 events corresponding to 18.98%. The MC signal region acceptance for K2π events is 11.65%. These values and those extracted from the Ke3 and K3π^0 signal regions will be used to compute the relative branching fractions of the three channels.

For the $K^+ \to e^+\pi^0\nu$ decay the procedure again requires exactly one candidate π^0 in the final state. We then select in the region of $0.035 < (P_{K^+} - P_{\pi^0})^2 < 0.055$ GeV^2/c^4 of the K2π MMS in order to preferentially remove K2π and K3π0 decays from the sample. If there is then exactly one additional in-time LKr cluster the e^+ 4-momentum is constructed using the position of the cluster and the reconstructed decay vertex. The Ke3 MMS variable is then constructed by subtracting the π^0 and e^+ 4-momenta from that of the nominal K^+, $(P_{K^+} - P_{\pi^0} - P_{e^+})^2$. The Ke3 MMS is shown in figure 7.8a where the data-MC comparison is good across the entire region, as highlighted by the agreement when plotting on a logarithmic axis, figure 7.8b. The agreement is very similar to what was observed in 2014. We define a signal region of -0.01 $<$ Ke3 MMS $< 0.01\ GeV^2/c^4$. We see in table 7.3 the values for the total amount of data for both data and scaled MC along with the MC acceptance. 7394 data events are observed in the signal region with an expected MC background of 2640 events corresponding to 35.70%. The MC signal region acceptance for Ke3 events is 1.54%.

The $K^+ \to \pi^+\pi^0\pi^0$ MMS variable is found by first only selecting events with exactly two final state π^0s. The 4-momenta of the two π^0s is then subtracted from the 4-momentum of the nominal K^+ to give the K3π MMS variable, $(P_{K^+} - P_{\pi^0} - P_{\pi^0})^2$. The K3$\pi$0 MMS is shown in figure 7.9a where the data-MC comparison is good across the entire region, as highlighted by the agreement when plotting on a logarithmic axis, figure 7.9b. The agreement is very similar to what was observed in 2014. We define a signal region of -0.012 $<$ K3π0 MMS $< 0.015\ GeV^2/c^4$. We see in table 7.4 the values for the total amount of data for both data and scaled MC along with the MC acceptance. 5532 data events are observed in the signal region with an expected MC background of 269 events corresponding to 4.86%. The MC signal region acceptance for K3π^0 events is 6.56%.

It should be noted at this point that for the K2π and Ke3 channels we observe rather large background MC estimates of 18.98% and 35.70% respectively. Whilst these backgrounds are large it is not possible to reduce them further using well understood cuts in a LKr only analysis. As the aim of this Chapter is to understand the over 20% discrepancy between the observed relative branching fractions and the PDG values this level of background can be tolerated.

7.3.6 Relative Branching Fractions

The relative branching fraction is calculated using the same method which was used for the 2014 data given in Chapter 6 Section 6.5. The signal region number of events, expected MC background and MC acceptance are summarised in table 7.5. The relative branching fraction calculations for cuts with nominal values and the full statistical error, as calculated for the 2014 data is given in table 7.6. This is then compared with the well established PDG value [60], table 7.6. We observe similar behaviour to what was seen in 2014, namely that the $\frac{K^+\to e^+\pi^0\nu}{K^+\to\pi^+\pi^0}$ branching ratio is much closer to the PDG value, yet both relative branching fraction involving K3π0 are over 20% below the expected PDG value. The 2015 results and 2014 results with respect to the PDG values are shown together in table 7.7. In the case of the nominal cut parameters then it would seem that the discrepancies observed in the 2014 data set persist in 2015.

Decay Mode	Data in Signal region SB_{Data}	MC Background B_{MC}	MC Acceptance (%) A
$K^+\to\pi^+\pi^0$	191823	36409	11.65
$K^+\to e^+\pi^0\nu$	7394	2640	1.54
$K^+\to\pi^+\pi^0\pi^0$	5532	269	6.56

Table 7.5: The Data and MC parameters used to calculate the relative branching fractions between the three given channels an the associated statistical error.

Decay Modes	Relative Branching Fraction	PDG Value	Variation from PDG(%)
$\frac{K^+\to e^+\pi^0\nu}{K^+\to\pi^+\pi^0}$	0.231±0.006	0.245±0.002	(-5.71±2.82)
$\frac{K^+\to\pi^+\pi^0\pi^0}{K^+\to\pi^+\pi^0}$	0.060±0.001	0.085±0.001	(-29.41±2.04)
$\frac{K^+\to\pi^+\pi^0\pi^0}{K^+\to e^+\pi^0\nu}$	0.260±0.008	0.347±0.005	(-25.07±3.40)

Table 7.6: The relative branching fractions for the three selected K^+ decay channels. Also given is the current PDG values and the difference between the two.

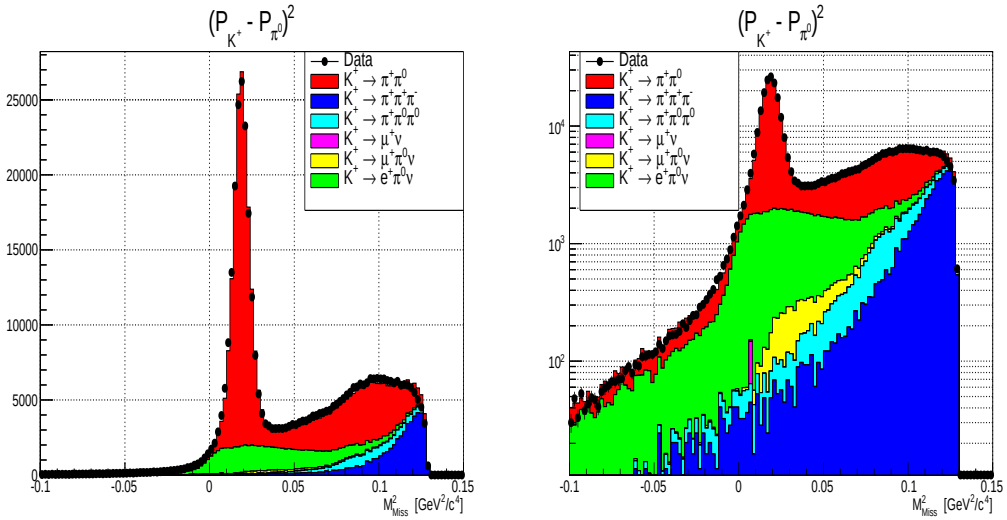

(a) (b)

Figure 7.7: Data-MC comparison of $(P_{K^+} - P_{\pi^0})^2$, on the right is the same plot on a logarithmic axis. The signal region for this distribution is chosen to be $0 <$ K2π MMS $< 0.04\ GeV^2/c^4$.

Decay Mode	Total Events	Signal Region Events	MC Acceptance %
Data	421823	191823	
$K^+ \to \pi^+\pi^0$	272823	157267	11.65
$K^+ \to e^+\pi^0\nu$	72120	32599	9.84
$K^+ \to \pi^+\pi^0\pi^0$	19951	801	0.70
$K^+ \to \mu^+\pi^0\nu$	5306	1887	0.86
$K^+ \to \pi^+\pi^+\pi^-$	51551	1039	0.28
$K^+ \to \mu^+\nu$	83	83	0.002
Total Background	149011	36409	

Table 7.2: The total number of events and number of events in the signal region $0 <$ K2π MMS $< 0.04\ GeV^2/c^4$ for the data sample and the individual MC channels where the sum of the MC channels is scaled to the total number of events in data. Also shown are the MC acceptances of events into the signal region.

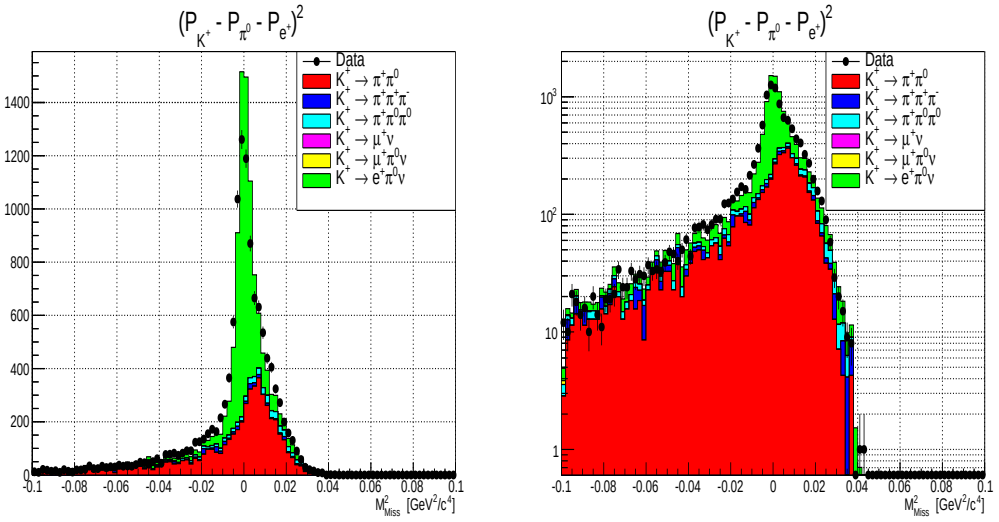

(a) (b)

Figure 7.8: Data-MC comparison of $(P_{K^+} - P_{\pi^0} - P_{e^+})^2$, on the right is the same plot on a logarithmic axis. The signal region for this distribution is chosen to be -0.01 < Ke3 MMS < 0.01 GeV^2/c^4.

Decay Mode	Total Events	Signal Region Events	MC Acceptance %
Data	12089	7394	
$K^+ \to e^+\pi^0\nu$	6107	5183	1.54
$K^+ \to \pi^+\pi^0$	5075	2363	0.17
$K^+ \to \pi^+\pi^0\pi^0$	568	181	0.16
$K^+ \to \mu^+\pi^0\nu$	5	1	0.00
$K^+ \to \pi^+\pi^+\pi^-$	334	95	0.03
$K^+ \to \mu^+\nu$	0	0	0.00
Total Background	5928	2640	

Table 7.3: The total number of events and number of events in the signal region -0.01 < Ke3 MMS < 0.01 GeV^2/c^4 for the data sample and the individual MC channels where the sum of the MC channels is scaled to the total number of events in data. Also shown are the MC acceptances of events into the signal region.

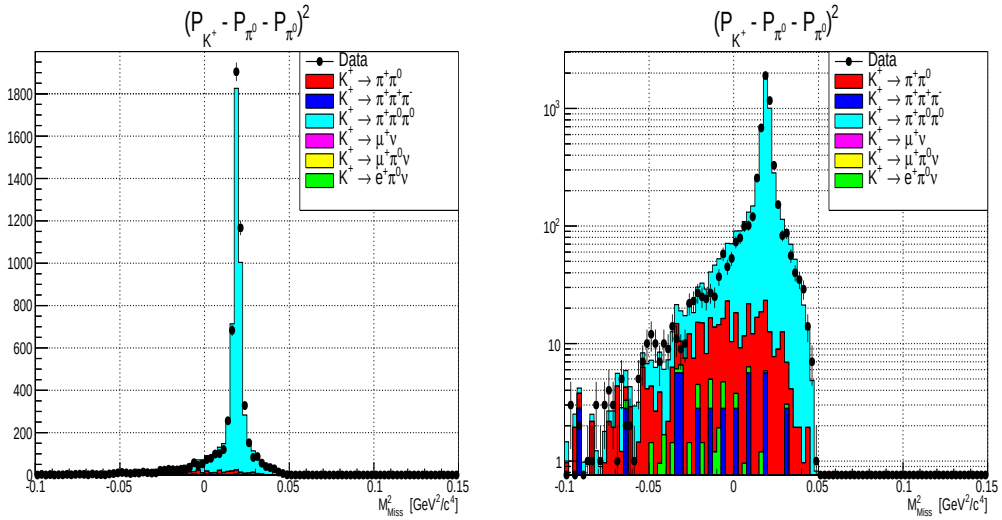

(a) (b)

Figure 7.9: Data-MC comparison of $(P_{K^+} - P_{\pi^0} - P_{\pi^0})^2$, on the right is the same plot on a logarithmic axis. The signal region for this distribution is chosen to be -0.012 < K3π0 MMS < 0.05 GeV^2/c^4.

Decay Mode	Total Events	Signal Region Events	MC Acceptance %
Data	5826	5532	
$K^+ \to \pi^+\pi^0\pi^0$	5389	5217	6.56
$K^+ \to \pi^+\pi^0$	363	237	0.025
$K^+ \to e^+\pi^0\nu$	33	12	0.005
$K^+ \to \mu^+\pi^0\nu$	0	0	0.000
$K^+ \to \pi^+\pi^+\pi^-$	42	20	0.008
$K^+ \to \mu^+\nu$	0	0	0.000
Total Background	438	269	

Table 7.4: The total number of events and number of events in the signal region -0.012 < K3π0 MMS < 0.05 GeV^2/c^4 for the data sample and the individual MC channels where the sum of the MC channels is scaled to the total number of events in data. Also shown are the MC acceptances of events into the signal region.

	Relative Branching Fraction		
Decay Modes	2014 LKr	2015 LKr	PDG Value
$\frac{K^+\to e^+\pi^0\nu}{K^+\to\pi^+\pi^0}$	0.233±0.012	0.231±0.006	0.245±0.002
$\frac{K^+\to\pi^+\pi^0\pi^0}{K^+\to\pi^+\pi^0}$	0.069±0.002	0.060±0.001	0.085±0.001
$\frac{K^+\to\pi^+\pi^0\pi^0}{K^+\to e^+\pi^0\nu}$	0.294±0.016	0.260±0.008	0.347±0.005

Table 7.7: The relative branching fractions for the three selected K^+ decay channels. Also given is the current PDG values [60] and the difference between the two.

As was the case in 2014 the cluster energy distribution differed between data and MC both with and without the minimum cluster energy cut at 3 GeV. The disagreement gets progressively better with increasing energy with no obvious differences around 15 GeV. It would be interesting then to see how the relative branching fractions change as a function of this minimum energy. Figure 7.10a shows the relative branching fraction of $\frac{K^+\to\pi^+\pi^0\pi^0}{K^+\to\pi^+\pi^0}$ as a function of energy, whilst there is some variation the relative statistical error as we go to an increased energy threshold the uncertainty becomes large as we are significantly reducing the amount of events in our sample, around 50% of all K3π0 events are removed when the minimum cut is placed at 10 GeV. Similarly the $\frac{K^+\to\pi^+\pi^0\pi^0}{K^+\to\pi^+\pi^0}$ branching ratio is shown in figure 7.10b and whilst this value is initially closer to the PDG value the agreement does improve as the threshold is increased. The significance of this however is minimal as for an increased minimum cluster energy threshold we have a significantly reduced sample size and therefore an increased the statistical error. There are tentative signs here however that show that it is possible to affect the relative branching fraction results by varying the minimum cluster energy threshold suggesting the energy response in MC is poorly modelled. Further study is required to ascertain the origin of this data-MC discrepancy. The cuts were varied and the branching ratios recalculated as was done for 2014 with similar results. Varying the cut parameters causes variation in the branching fractions no larger than 3%.

7.3.7 LKr Data Conclusions

The LKr based analysis of the 2014 data set has been repeated on the 2015 data set with the observed underestimation of relative branching fractions shown to persist. For the relative branching fraction of $\frac{K^+\to\pi^+\pi^0\pi^0}{K^+\to\pi^+\pi^0}$ the discrepancy with respect to the PDG values was shown to be (-18.82±3.13)% in 2014 and found here to be (-29.41±2.04)% for 2015 data. The analysis followed as closely as possible the 2014 analysis with the two key differences being that the MC was only generated in the signal region and the ZS algorithm changed slightly in 2015. We have seen then that an LKr only analysis of this type is not capable of producing the correct relative branching fractions. Clear evidence of a difference in the LKr response for data and MC has been observed in the cluster energy distributions

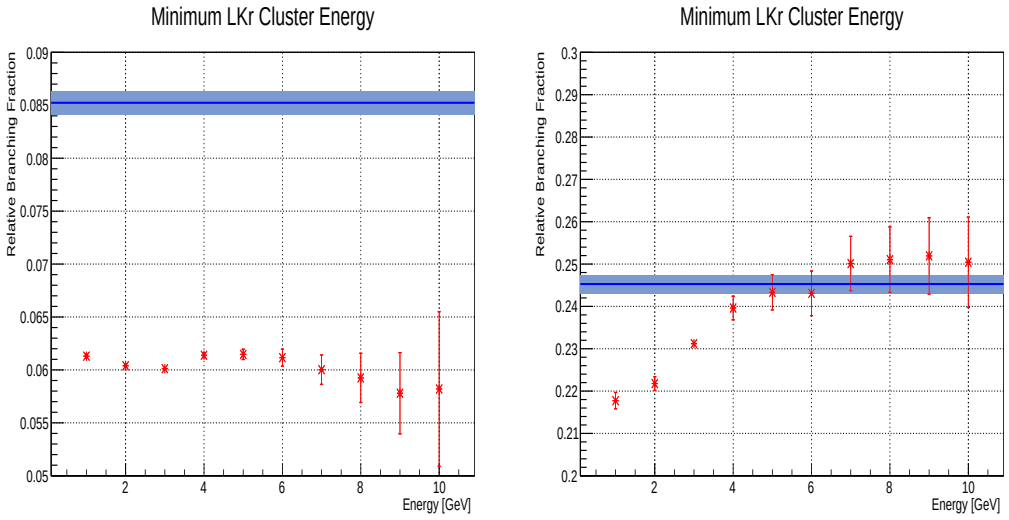

(a) (b)

Figure 7.10: Relative branching fraction of a) $\frac{K^+\to\pi^+\pi^0\pi^0}{K^+\to\pi^+\pi^0}$ b) $\frac{K^+\to e^+\pi^0\nu}{K^+\to\pi^+\pi^0}$ as a function of the minimum cluster energy threshold. The nominal value at 3 GeV has no given error and the errors are the statistical error relative to the nominal value.

and in the average number of π^0 candidates per event. We have seen also that the ZS algorithm when applied to MC does not reproduce the same behaviour in terms of reducing the energy of clusters by suppressing cells within a cluster. Different behaviour is observed with regard to zero suppression for electromagnetic and hadronic clusters. In order to see if the difference is due to the poor modelling of detector response for electromagnetic clusters, hadronic clusters, or some combination of the two a data driven study to select electromagnetic and hadronic clusters in data will be performed in Section 7.5. Before investigating further the response of the LKr it is necessary to establish that the observed discrepancy with respect to the PDG values of branching ratios is confined to the LKr and not symptomatic of the data set as a whole. To do this the next Section will contain a parallel analysis which does not use the LKr but instead uses the Straw spectrometer data to extract the relative branching fractions of $K^+ \to \pi^+\pi^0$, $K^+ \to e^+\pi^0\nu$, and $K^+ \to \pi^+\pi^0\pi^0$.

7.4 Straw based Analysis

The aim of this Section is to establish whether the discrepancies between the known PDG branching ratio values and those measured for the LKr only based analyses are confined to the LKr. This analysis uses the same data set as was used in the previous Section but selects the $K^+ \to \pi^+\pi^0$, $K^+ \to e^+\pi^0\nu$, and $K^+ \to \pi^+\pi^0\pi^0$ channels using the NA62 Straw spectrometer as the primary detector. The analysis here will show that the problems seen in Section 7.3 and Chapter 6 are confined to the LKr and not symptomatic of the larger data set.

7.4.1 The Straw Spectrometer in 2015

A detailed description of the straw spectrometer was given in Chapter 3. The Key characteristics of the straw spectrometer [37] are:

- 4 Chambers each with 16 layers of straws oriented in 4 views.
- 7166 straws total.
- 63.8mm hole in the centre of each plane to allow the beam to pass.
- 4 chambers separated by ∼10m over a 35m range.
- A dipole magnet between chambers 2 and 3 providing transverse momentum impulse of -270 MeV/c.

During the 2015 minimum bias run the spectrometer was read out in accordance with the global NA62 trigger. This was not the case in 2014 when the straws were continuously read out independently and then trigger matched at a later time. All but one of the 7166 straws was successfully read out during the run. The selection of the $K^+ \to \pi^+\pi^0$, $K^+ \to e^+\pi^0\nu$, and $K^+ \to \pi^+\pi^0\pi^0$ decays presented in this section made use of a single track analysis imposing only some basic cuts on track quality.

7.4.2 Single Charged Track Analysis

The single charged track analysis presented here uses a Q1*!MUV3 trigger applied in the same time window as was defined for the LKr analysis in Section 7.3.3. As the drift time of electrons in the spectrometer is typically around 150 ns it is not possible to time align the spectrometer tracks with the K^+ candidate, instead the spectrometer track candidates are matched to CHOD Q1 conditions and the timing is done between the CHOD candidate and the K^+ candidate allowing for the same time window which was used to define a Q1 condition in time with the KTAG. The analysis is based on selecting events with only a single reconstructed straw track and then imposing quality cuts on the track. The quality cuts placed on the straw tracks are,

- $N_{\text{Chambers}} = 4$,
- $R_{\text{Track}} > 138.8$mm,
- $\chi^2_{\text{Track}} < 5$,
- $CDA_{\text{Track}} < 20$cm,

- $105 < Z_{\text{Track}} < 165$m,
- $10 < P_{\text{Track}} < 60$ GeV,

where each of the variables is defined as follows,

- N_{Chambers} is the total number of chambers from which hits were used to form tracks.
- R_{Track} is the radial distance of the reconstructed track impact point in each chamber from the centre of each chamber, note that the chambers are centred on the upstream, undeflected beam axis (x=0,y=0) position. This relative shift in chambers has been taken into account.
- χ^2_{Track} is the χ^2 value of the fit of the track to the distribution of hits across the chambers.
- CDA_{Track} is the closest distance of approach between the reconstructed track and the nominal axis of the beam.
- Z_{Track} is the decay vertex position along the z direction. The vertex is constructed by taking the average of the spatial coordinates of the track and the nominal beam axis at the position of the CDA_{Track}.
- P_{Track} is the magnitude of the track momentum.

All the cuts listed are applied sequentially for both data and MC. All data-MC comparisons presented in this Section use the same methodology of scaling the total number of MC events to the total number of data events as was done previously for the LKr based analyses. Figure 7.11a shows that we have an increased number of tracks in data with higher track χ^2 when compared with the idealised MC case. Figure 7.11b shows the data-MC comparison of the radial distance of a tracks position in the first straw plane from the centre of the first plane. The distribution has had a cut applied at 138.8 mm and the agreement is reasonable but not perfect at this stage with differing shapes of these distributions. The 138.8 mm cut corresponds to a summation of the physical size of the hole in all straw planes of 63.8 mm along with an additional excluded region of 75 mm. Figure 7.11c shows the closest distance of approach between the track and the nominal beam axis showing good agreement between data and MC when a maximum CDA of 20 cm is applied. Figure 7.11d shows good agreement between data and MC in the fiducial decay region for $105 < Z_{\text{Track}} < 16$ 5m.

The selection criteria for this single track analysis outlined in this section and shown in figure 7.11 show reasonable agreement in MC at the current level which will be improved upon in the future by detailed work regarding alignment and efficiency of the Straw Spectrometer sub detector system.

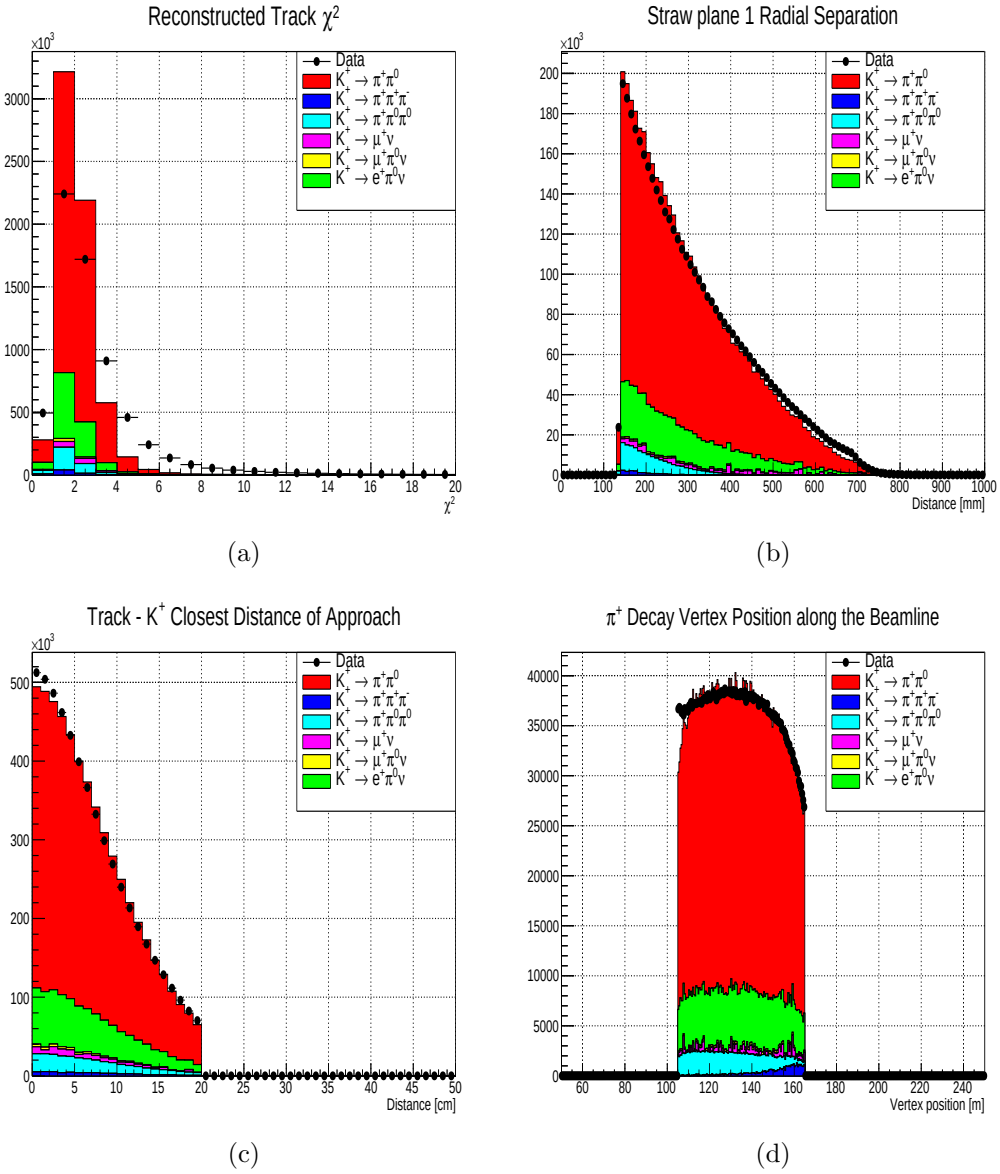

(a) (b)

(c) (d)

Figure 7.11: a) Data-MC comparison of reconstructed track χ^2. b) Data-MC comparison Straw radial separation form the track centre at the first straw plane after applying a 138.8mm cut. c) Data-MC comparison of the closest distance of approach between straw track and nominal beam axis after a maximum CDA cut of 20cm is applied. d) Data-MC comparison of reconstructed track vertex position in z for all tracks with a decay vertex in the fiducial region of 110 and 165m are applied.

Single Track Data Quality

This section of the single track analysis is concerned with performing some reasonable checks on the quality of single track data. Only data will be considered here and the restrictions placed on the vertex position of the decaying K^+ and the energy of the reconstructed track are removed in order to investigate features of the data distributions which correlate with known geometrical features of the NA62 set-up.

Figure 7.12a shows the missing mass squared variable, $(P_{K^+} - P_{Track})^2$, under the assumption that the reconstructed track is a π^+. If the reconstructed track is a π^+ we would expect to see a peak in the missing mass squared distribution at the square of the π^0 mass ($0.0182\text{GeV}^2/c^4$). Indeed as can be seen in figure 7.12a a strong peak is observed, when fitted with a Gaussian this peak is centred at $0.0187\text{GeV}^2/c^4$ with a σ value of $0.0040\text{GeV}^2/c^4$ which is consistent with π^0 mass of $0.0182\text{GeV}^2/c^4$. Figure 7.12b expands the missing mass squared variable with respect to the momentum of the reconstructed tracks. We see the π^0 peak distributed across the momentum range of 10 to 70 GeV/c with the extremities of this distribution being absent due to geometrical acceptance considerations. The most remarkable feature of this distribution is the secondary peak located at $\sim$75 GeV/c, this is understood to be a result of elastic scattering in the final GigaTracker plane, this effect is modelled and understood in the MC to the correct order of magnitude. The origin of the 75 GeV/c component is made clearer when we consult figure 7.12d where the 75 GeV/c component is located with a decay vertex before the start of the decay region at 105m strongly suggesting a scattering effect in some upstream material. The missing mass squared as a function of the z vertex position, figure 7.12c, shows the correctly identified $K^+ \to \pi^+\pi^0$ decays are distributed evenly across the decay volume as we would expect. Figure 7.12d shows the distribution of track momentum and the associated z vertex position, other than the discussed 75 GeV/c component this is distributed as expected across the decay region.

With the exception of the 75 GeV/c beam like component it would appear the the missing mass squared kinematic distribution behaves as we would expect for a single track analysis. The 75 GeV/c component has been the subject of extensive investigation by the NA62 collaboration and is believed to be as a result of scattering in the third GigaTracker plane. This effect is simulated to the correct order of magnitude in the MC.

Decay Channels

In order to compute the relative branching fractions between the $K^+ \to \pi^+\pi^0$, $K^+ \to e^+\pi^0\nu$, and $K^+ \to \pi^+\pi^0\pi^0$ decays to compare the results to both the well established PDG values and the values calculated for the previous LKr based

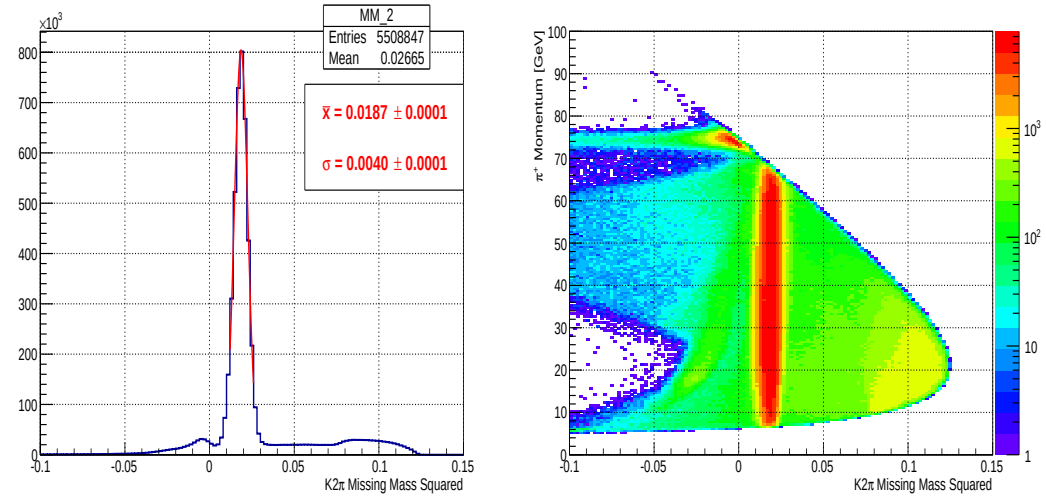

(a) (b)

(c) (d)

Figure 7.12: a) The $(P_{K^+} - P_{Track})^2$ missing mass squared spectrum assuming the track is a π^+. b) Missing mass squared as a function of reconstructed track momentum. c) Missing mass squared as a function of the reconstructed K^+ decay vertex. d) The K^+ decay vertex as a function of candidate track momentum.

analysis all three channels must be extracted and the backgrounds for each modelled in MC. In order to do this the missing mass distribution, $(P_{K^+} - P_{Track})^2$, is calculated under the assumption the reconstructed track was a π^+. The data distribution modelled alongside the MC matching where the MC is scaled to the total amount of data is shown in figure 7.13. The data MC comparison shows excellent agreement with the exception of the, negative missing mass squared values where we would expect to see Kμ2 decays. this discrepancy could be due to the modelling of the !MUV3 trigger or we may also be seeing decays from the beam like component explained in the previous section here which is underestimated in MC. In any case this disagreement is small and accounts for less than 1% of the data. There is also a discrepancy with the resolution of the $K^+ \to \pi^+\pi^0$ peak, this effect is known to the collaboration and is under investigation. For our purposes this effect can be mitigated by defining a signal region wide enough to incorporate both the data and MC peaks sufficiently. The signal region for $K^+ \to \pi^+\pi^0$ decays is defined as 0.01 to 0.03GeV$^2/c^4$ in the missing mass squared distribution. The $K^+ \to e^+\pi^0\nu$, and $K^+ \to \pi^+\pi^0\pi^0$ decays were extracted by defining signal regions of 0.035 to 0.07GeV$^2/c^4$ and 0.08 to 0.12GeV$^2/c^4$ respectively. The total amount of data in these three signal regions is detailed in tables 7.8, 7.9 and 7.10 for the $K^+ \to \pi^+\pi^0$, $K^+ \to e^+\pi^0\nu$, and $K^+ \to \pi^+\pi^0\pi^0$ decays respectively.

The scaled number of MC events for each channel in the K2π, Ke3, and K3π0 signal regions are given in tables 7.11, 7.12 and 7.13 respectively. We can select 2599600 K2π events with 66136(2.54%) expected background events, 194567 Ke3 events with 10766(5.53%) expected background events, and 233741 K3π0 events with 122725(52.5%) expected background events. These numbers will be used in the next section in order to calculate the relative branching fractions between the three channels and perform a comparison with the PDG values. It should be noted here that for the K3π0 channel the expected background is very high at 52.5% and as such has a larger uncertainty from the modelling of the background channels in MC. As we are using this single track analysis to probe a discrepancy in the relative branching fractions of over 20% in the LKr it is sufficient for this purpose.

7.4.3 Relative Branching Fractions

So far in this Section details of a single track analysis and a method for selecting the three decay channels of interest was presented alongside MC background estimations for each of the three channels. In this Section these values will be combined with MC estimations for the acceptance into the signal regions in order to extract relative branching fractions for the two channels.

The same method of calculating the branching fractions was used for the Straw analysis as was done for the LKr analysis which is detailed in Chapter 6. The number of data events in each signal region, MC background estimation of each

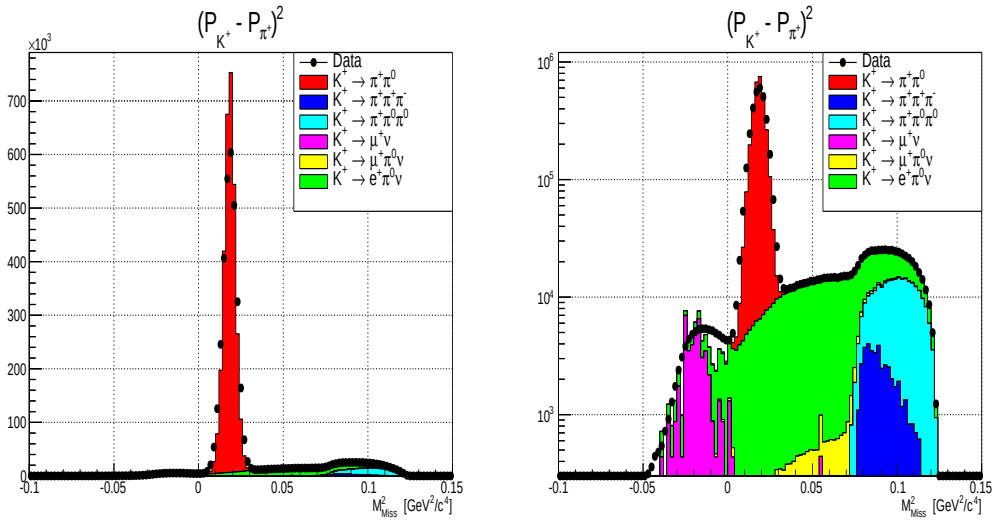

(a) (b)

Figure 7.13: a) Data-MC comparison of the missing mass squared spectrum assuming the track is a π^+. b) Logarithmic in y.

Decay Mode	Signal Region Events	MC Acceptance %
Data	2599600	
$K^+ \to \pi^+\pi^0$	2558629	36.41
$K^+ \to e^+\pi^0\nu$	63850	3.68
$K^+ \to \pi^+\pi^0\pi^0$	3	0.00
$K^+ \to \mu^+\pi^0\nu$	2283	0.20
$K^+ \to \pi^+\pi^+\pi^-$	0	0.00
$K^+ \to \mu^+\nu$	0	0.00
Total Background	66136	

Table 7.8: The total number of events and number of events in the signal region $0.01 <$ K2π MMS < 0.03 GeV^2/c^4 for the data sample and the individual MC channels where the sum of the MC channels is scaled to the total number of events in data. Also shown are the MC acceptances of events into the signal region.

Decay Mode	Signal Region Events	MC Acceptance %
Data	194567	
$K^+ \to e^+\pi^0\nu$	184536	10.85
$K^+ \to \pi^+\pi^0$	1678	0.02
$K^+ \to \pi^+\pi^0\pi^0$	125	0.02
$K^+ \to \mu^+\pi^0\nu$	8528	0.74
$K^+ \to \pi^+\pi^+\pi^-$	0	0.00
$K^+ \to \mu^+\nu$	435	0.00
Total Background	10766	

Table 7.9: The total number of events and number of events in the signal region $0.035 <$ Ke3 MMS < 0.07 GeV^2/c^4 for the data sample and the individual MC channels where the sum of the MC channels is scaled to the total number of events in data. Also shown are the MC acceptances of events into the signal region.

Decay Mode	Signal Region Events	MC Acceptance %
Data	233741	
$K^+ \to \pi^+\pi^0\pi^0$	109950	18.57
$K^+ \to e^+\pi^0\nu$	108124	6.24
$K^+ \to \pi^+\pi^0$	81	0.00
$K^+ \to \mu^+\pi^0\nu$	3432	0.30
$K^+ \to \pi^+\pi^+\pi^-$	11089	0.58
$K^+ \to \mu^+\nu$	0	0.00
Total Background	122727	

Table 7.10: The total number of events and number of events in the signal region $0.08 <$ K3π0 MMS < 0.12 GeV^2/c^4 for the data sample and the individual MC channels where the sum of the MC channels is scaled to the total number of events in data. Also shown are the MC acceptances of events into the signal region.

signal decay mode into the signal, and MC acceptance for each channel are shown in table 7.11. As was the case for the LKr analysis the MC acceptance here covers geometrical acceptance, trigger acceptance, and the acceptance probability of an event into the final signal region and is entirely based on MC simulation.

Decay Mode	Data in Signal region SB_{Data}	MC Background B_{MC}	MC Acceptance (%) A
$K^+ \to \pi^+\pi^0$	2599600	66136	36.41
$K^+ \to e^+\pi^0\nu$	194567	10766	10.85
$K^+ \to \pi^+\pi^0\pi^0$	233741	122725	18.57

Table 7.11: The number of data events in each signal region for the three decay channels alongside the MC background estimation in the signal region and the MC acceptance for each of the signal decays.

We can combine the quantities in table 7.11 to calculate the relative branching fractions of the three channels. The calculated branching fractions and full statistical error are shown in table 7.12 alongside the PDG values and the percentage difference between the two. Shown in table 7.13 are the relative branching fractions as calculated from the previous LKr based analysis in Section 7.3.

Decay Modes	Relative Branching Fraction	PDG Value	Variation from PDG(%)
$\frac{K^+\to e^+\pi^0\nu}{K^+\to\pi^+\pi^0}$	0.244±0.001	0.245±0.002	(-0.41±0.91)
$\frac{K^+\to\pi^+\pi^0\pi^0}{K^+\to\pi^+\pi^0}$	0.086±0.001	0.085±0.001	(1.18±1.65)
$\frac{K^+\to\pi^+\pi^0\pi^0}{K^+\to e^+\pi^0\nu}$	0.353±0.006	0.347±0.005	(1.73±2.23)

Table 7.12: The relative branching fractions for the three selected K^+ decay channels. Also given is the current PDG values and the difference between the two.

We can see then even for a simple one track analysis as was presented here relative branching fractions in close agreement with the PDG values are obtained. This gives strong evidence that the discrepancies observed for a primarily LKr based analysis as was done for 2014 data in Chapter 6 and 2015 data in Section 7.3 is indeed confined to the LKr and is not symptomatic of the larger data set.

Relative Branching Fractions				
Decay Modes	2014 LKr	2015 LKr	2015 Straw	PDG Value
$\frac{K^+\to e^+\pi^0\nu}{K^+\to\pi^+\pi^0}$	0.233±0.012	0.231±0.006	0.244±0.001	0.245±0.002
$\frac{K^+\to\pi^+\pi^0\pi^0}{K^+\to\pi^+\pi^0}$	0.069±0.002	0.060±0.001	0.086±0.001	0.085±0.001
$\frac{K^+\to\pi^+\pi^0\pi^0}{K^+\to e^+\pi^0\nu}$	0.294±0.016	0.260±0.008	0.353±0.006	0.347±0.005

Table 7.13: The relative branching fractions for the three selected K^+ decay channels for the three analyses performed. Also given is the current PDG values.

7.4.4 Straw Data Conclusions

The purpose of this analysis was to establish whether the discrepancies between the measured branching ratios of the $K^+ \to \pi^+\pi^0$, $K^+ \to e^+\pi^0\nu$, and $K^+ \to \pi^+\pi^0\pi^0$ using the LKr calorimeter and the PDG values persist when we compute the branching ratios with the straw spectrometer. We see that the three relative branching fractions given in table 7.13 all agree with the current PDG values within the statistical errors. This observation allows us to rule out the possibility that the discrepancy observed in Section 7.3 is due to problems with the data set as a whole and is indeed isolated to the LKr electromagnetic calorimeter. The next Section will use the Straw data in order to investigate the LKr response in data and MC and attempt to identify the origin of the discrepancy between the relative branching fractions measured using only the LKr and those calculated using the Straws which are in agreement with the PDG values.

7.5 Straw and LKr based Analysis

So far in this Chapter and in Chapter 6 we have observed the following with regard to the relative branching fractions of $\frac{K^+\to e^+\pi^0\nu}{K^+\to\pi^+\pi^0}$ and $\frac{K^+\to\pi^+\pi^0\pi^0}{K^+\to\pi^+\pi^0}$,

- For an LKr based analysis the relative branching fraction $\frac{K^+\to\pi^+\pi^0\pi^0}{K^+\to\pi^+\pi^0}$ differs with respect to the PDG value by around 20% in 2014.
- A similar level of disagreement with the PDG benchmark for the LKr based analysis of 2015 data.
- The discrepancy is not observed for a Straw spectrometer based analysis of the 2015 data suggesting the issue is isolated to the LKr.
- Differences in the cluster response between data and MC.

The observations of differing LKr cluster response are,

- Discrepancies between data and MC in the energy distribution of all clusters before and after a 3 GeV cut is applied
- A different zero suppression cluster energy correction between data and MC in both 2014 and 2015. Further analysis of the expected correction in data and MC shows discrepancies between hadronic and electromagnetic clusters.
- Data-MC comparisons of the number of reconstructed π^0s differs between data and MC. This points to a difference in the average number of candidate photon clusters between data and MC.

The first aim of this section is to establish whether the LKr environment is modelled correctly in MC with respect to data, this is done in Section 7.5.1. The definition of LKr environment here is the original detector response before clustering is applied, the number of clusters produced after applying the LKr clustering algorithm, and the typical energy response of those clusters. It is important to note here that zero suppression will be considered part of the clustering algorithm for what is presented in this Section. A non zero suppressed MC sample will be introduced in order to highlight the necessity of ZS, however without a non zero suppressed data sample it is not possible to separate out any inefficiency in the clustering algorithm from any inefficiency in the ZS algorithm. If detector response is modelled correctly we would expect to see the same average number of clusters per event in both data and MC as well as the same characteristic energy distributions of these clusters. It will be shown in Section 7.5.1 that the LKr environment is not well modelled for all clusters. Section 7.5.2 uses the Straw spectrometer single track analysis to match with LKr clusters in data and identify them as either electromagnetic or hadronic, in this way a data driven method of typical cluster response can be produced. The analysis in Section 7.5.2 shows that the poor modelling of LKr clusters is confined entirely to clusters which are hadronic in origin. Section 7.5.3 repeats the LKr based analysis shown at the beginning of this Chapter but now using the Straw Spectrometer to veto hadronic clusters from the dataset in order to test the hypothesis that it is poor modelling of hadronic cluster response which results in relative branching fractions that differ by over 20% with respect to the PDG values. Finally in Section 7.5.4 a study will be preformed to identify the hadronic cluster contamination in reconstructed single and double π^0 events where we will first select π^0s as was done for LKr only analyses and then use the straw tracking information to identify how often candidate π^0s are formed from a π^+ cluster.

7.5.1 LKr Cluster Response in Data and MC

Cluster response in the LKr is defined here as the average number of reconstructed clusters per event and the energy distribution of the clusters. Only when agreement is achieved between the two can we be confident that all LKr clusters are

being correctly modelled by the MC. Modelling here refers both to the clustering algorithm and the zero suppression algorithm. As it is not possible to directly assess these two components individually a non ZS MC sample will also be considered here alongside the ZS MC and the ZS Data. In principle the detector response will also depend on correctly modelling the LKr environment before any ZS is applied but currently there is no sufficient non ZS data sample with which to compare MC.

In all comparisons done here an in-time condition with a K^+ candidate is required, as has always been required for the analysis presented using LKr clusters. A 3 GeV minimum energy cut is also applied. This is to remove MIP energy deposits from the LKr for which there is a known discrepancy between the data and MC [74]. Figure 7.14a shows the cluster energy distributions for data, ZS MC, and Non ZS MC, where both MC samples have been individually scaled to the total amount of data. We clearly see in figure 7.14a that the cluster energy distributions all disagree specifically in the region below 10 GeV. This could be due to some unaccounted for non linear scaling or it could be that the composition of hadronic and electromagnetic events is different between data and MC such that the resultant plots containing all clusters differ. We can investigate further by looking at the total number of LKr clusters above 3 GeV as plotted for all events in figure 7.14b. We see characteristically different shapes between data and the two MC samples with data having on average fewer clusters. It should be noted at this point that the two MC samples have a much more similar average number of events compared with data. However the energy distributions in figure 7.14a showed no such agreement, this is to be understood as no zero suppression energy correction has been applied to MC which was found to be necessary for electromagnetic clusters. Typically lower energy hadronic clusters however appeared to require an energy correction but as we were not trying to actively select these clusters no correction was applied.

The LKr is an electromagnetic calorimeter and therefore it is vital to investigate further the discrepancies seen in the modelling of detector response by investigating clusters which are electromagnetic in origin from clusters which are from hadronic showers. A data driven technique using the Straw spectrometer track information was developed to this end and will be discussed in the next Section.

7.5.2 Data Driven Cluster Study

In order to study the LKr response in data and MC for electromagnetic and hadronic clusters separately a technique was developed for classifying clusters as electromagnetic or hadronic using information from the Straw spectrometer. The analysis procedure builds on that which was described in Section 7.4 as follows,

1. Select all events in the K2π missing mass squared distribution (MMS), in the

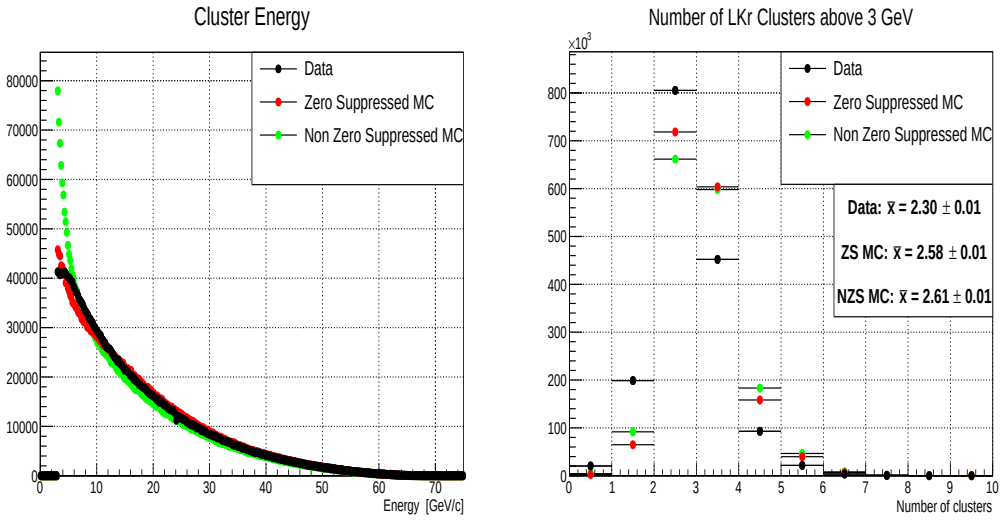

(a) (b)

Figure 7.14: a) Cluster energy response for all in-time LKr clusters above 3 GeV. d) Total number of in-time LKr clusters above 3 GeV per event with averages for the three data sets shown.

region $0.01 < \text{MMS} < 0.025$. This selects 97.5% purity K2π, as estimated using MC.

2. Propagate the reconstructed track to the LKr plane and look for the closest LKr cluster. Figure 7.15a shows the radial separation of the nearest cluster from the track impact point. A maximum separation of 50mm is imposed.

3. Any remaining K2π background decays are removed by requiring the ratio of cluster energy to the track momentum be between 0.1 and 0.9. Figure 7.15b shows this sufficiently excludes non K2π component such that the signal purity of K2π is over 99%. The matched cluster is then classified as hadronic.

4. The electromagnetic cluster definition first selects in the Straw MMS region of $0.035 < \text{MMS} < 0.07$ to select 95.4% purity Ke3 and then requires that the matched LKr cluster has the ratio of cluster energy to the track momentum be between 0.95 and 1.05. Events satisfying these conditions are classified as electromagnetic. The resulting Ke3 sample is over 99% pure, as estimated using MC.

After we have performed this selection we are left with a classification of clusters as either electromagnetic or hadronic. Figure 7.16a shows the data and MC samples scaled to the total value of data. We see excellent agreement between data and MC for electromagnetic clusters. Figure 7.16b shows the data-MC comparisons for clusters identified as hadronic. We see clear differences in the hadronic

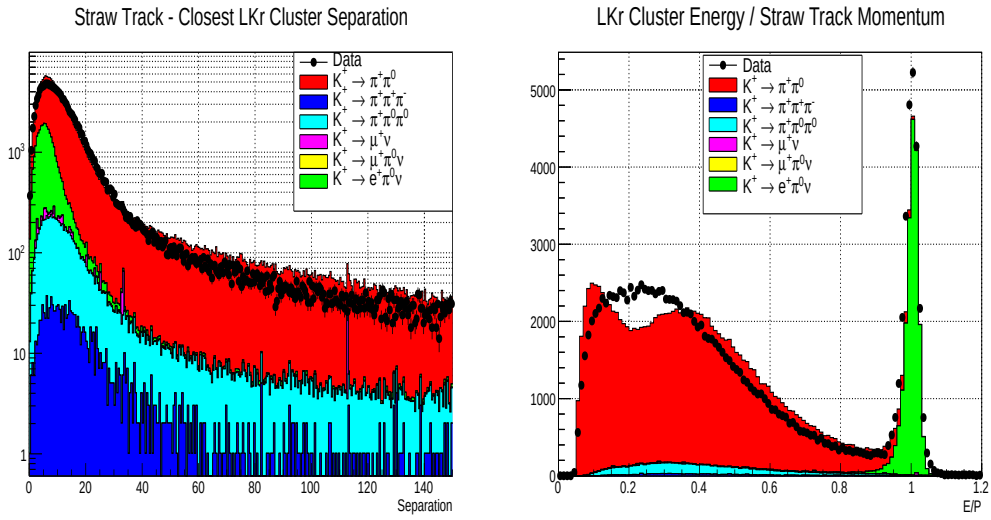

(a) (b)

Figure 7.15: a) Data-MC comparison of the separation between the Spectrometer track impact point at the LKr from all clusters. b) Ratio of cluster energy to track momentum for matched clusters.

energy response for data and MC. This is evidence that the problem is confined to the hadronic clusters but in order to complete the picture of LKr response we must also consider the response rate of the detector to an incident particle. For electromagnetic clusters this should by design be 100% provided all tracks are within the LKr geometrical acceptance. As we wish to probe the cluster response rate the ratio of cluster energy to track momentum cannot be used. The criteria for defining a track as either electromagnetic or hadronic must be relaxed to use only the tracking information. Using only the tracking information we select π^+ tracks from K2π with 97.5% purity and e^+ tracks from Ke3 with 95.4% purity. Tracks satisfying these criteria were propagated to the LKr region and a matching was required within 50 mm to associate a cluster. The percentage of all electromagnetic and hadronic tracks with an associated cluster are given in table 7.14 for data and both MC samples. It can be seen that for the electromagnetic case the rates are entirely compatible at around 84% whilst there is an almost 20% difference in the data and MC responses for hadronic clusters of around 75% and 58% respectively. The hadronic clusters will therefore have different population sizes in data and MC and consequentially differing energy spectra. The incorrect modelling of the number of hadronic clusters in the final sample will affect the LKr only analyses we have presented in this Thesis. The next Section will attempt to remove hadronic clusters from the data set by using the Straw spectrometer as a veto in an attempt to recover agreement with the PDG relative branching fractions.

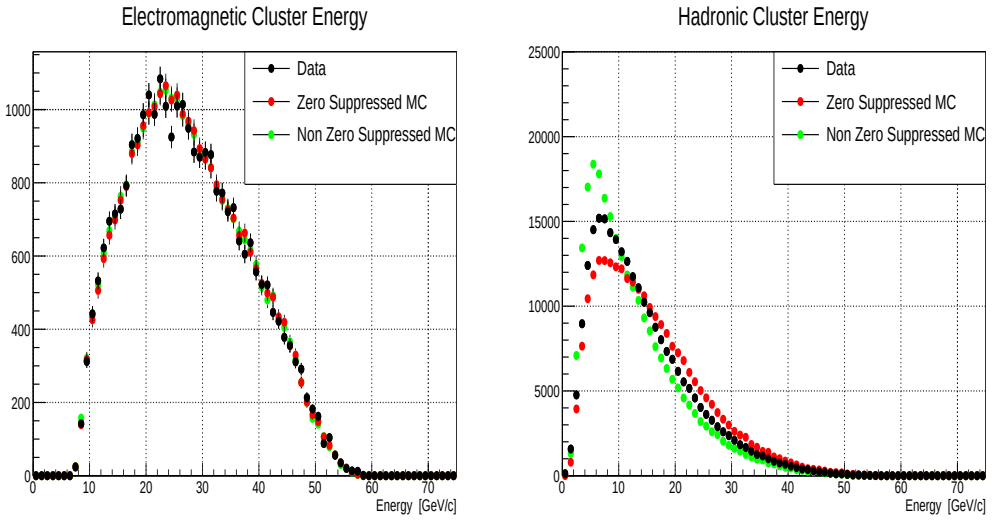

(a) (b)

Figure 7.16: Data, zero suppressed MC, and non zero suppressed MC comparisons for a) e^+ (electromagnetic) identified clusters with total MC samples scaled to total data. c) π^+ (hadronic) identified clusters with total MC samples scaled to total data.

	% of candidate straw tracks identified		
Cluster Type	Data	ZS MC	NZSMC
Electromagnetic	84.2	84.4	84.3
Hadronic	58.5	74.9	75.8

Table 7.14: Cluster Matching efficiencies for e^+(electromagnetic) and π^+(hadronic) tracks. Note than tagging efficiency is not 100% for electromagnetic clusters due to geometrical acceptance considerations.

7.5.3 Using the Straw Spectrometer to Veto Hadronic Clusters

In the previous section we concluded that electromagnetic clusters appear well simulated in both ZS and non ZS MC. This is not the case for hadronic clusters however as the energy distribution of the response differs along with the number of hadronic clusters in data and MC. In this section we will attempt to remove hadronic clusters from the sample using the Straw spectrometer tracks in order to see if we recover agreement with the PDG relative branching fraction values.

This analysis begins by selecting only events which provide one 'good' track where 'good' is defined as passing all the single track analysis cuts given in Section 7.4. The tracks are then propagated to the LKr plane. A track matching with the nearest cluster is required in order to provide a matched cluster. The separation

between the track impact point and the closest LKr cluster is shown in figure 7.15a. In order to assess what upper boundary on the track-cluster separation is required two values were chosen, 50 mm and 100 mm. For both of these cuts the energy of all non matched clusters are plotted in figure 7.17a for 50 mm separation and figure 7.17b for 100 mm separation. In the cluster energy distribution we can see that when we impose a 50 mm boundary we have significantly more background from non-matched hadronic clusters than for the 100 mm case, for this reason the 100 mm maximum separation was chosen. As described in the previous section the cluster energy distribution only addresses one aspect of the problem. We must also have the correct number of clusters per event in the detector. Figure 7.17c shows the number of non matched clusters per event for a 50 mm matching and figure 7.17b for a 100 mm matching. We can see that in both cases the data-MC comparison is much improved from when we had no cluster matching in the previous Section 7.5.1 figure 7.14b. We see the data-MC agreement improves when we go to 100 mm as we have removed more of the poorly modelled hadronic clusters than was the case for 50 mm. All clusters which are matched to a track are removed from the sample of possible π^0 photon clusters.

Once the track matched clusters have been removed from the sample the analysis proceeds in an identical manor to what was done previously for the LKr only analysis in Section 7.3. The same cut based data-MC comparisons were performed as were done in Section 7.3 and the agreement was found to be as good as if not better than 2014 in all cases. The data-MC distributions for the final three signal regions are shown in figures 7.18, 7.19, and 7.20 for $K^+ \to \pi^+\pi^0$, $K^+ \to \pi^+\pi^0\pi^0$, and $K^+ \to e^+\pi^0\nu$ respectively. Tables 7.15, 7.16, and 7.17 show the amount of data in the signal regions alongside the MC expected background and acceptances. The data-MC comparisons agree well for all three channels. As the Straw spectrometer is not providing additional background rejection we see selections with less background than was observed without using the spectrometer. For K2π we select 185257 events in data with an expected MC background of 15837 (8.55%). A combination of the reduction in K2π background and removing matched cluster events from the selection means the Ke3 has a much smaller background from K2π than for previous LKr analyses. For Ke3 we select 4485 events with 468(10.43%) expected MC background. The K3π0 signal region contains 2075 events with only 18(0.87%) expected background.

As a consistency check for this part of the analysis the difference in predicted decay vertex for the two methods is calculated. The track vertex was calculated as described in Section 7.4 and compared directly with the calculated π^0 decay vertex. We see excellent agreement between data and MC with a distribution centred on zero as expected. We can note the there is an asymmetric tail to the distribution in the positive direction suggesting that the π^0 method of vertex reconstruction is prone to finding a larger z vertex value. This is expected if the reconstructed π^0 is not formed from the correct clusters corresponding to two photons but instead contains one of the remaining few hadronic clusters which

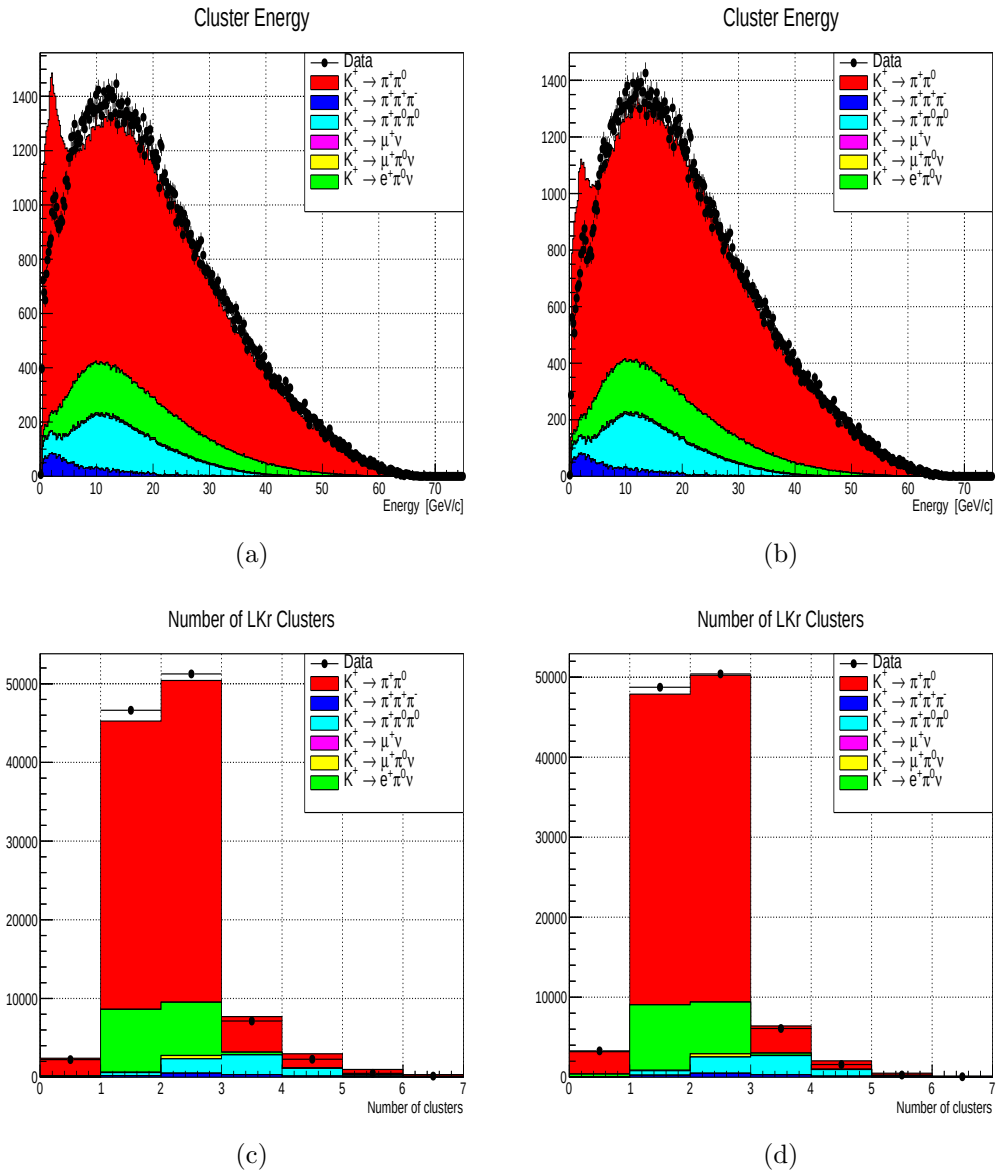

Figure 7.17: a) Energy of all in-time LKr Clusters excluding any clusters matched within 50mm of the projected Spectrometer track. b) Energy of all in-time LKr Clusters excluding any clusters matched within 50mm of the projected Spectrometer track. c) Number of in-time LKr Clusters per event excluding any clusters matched within 100mm of the projected Spectrometer track. d) Number of in-time LKr Clusters per event excluding any clusters matched within 100mm of the projected Spectrometer track.

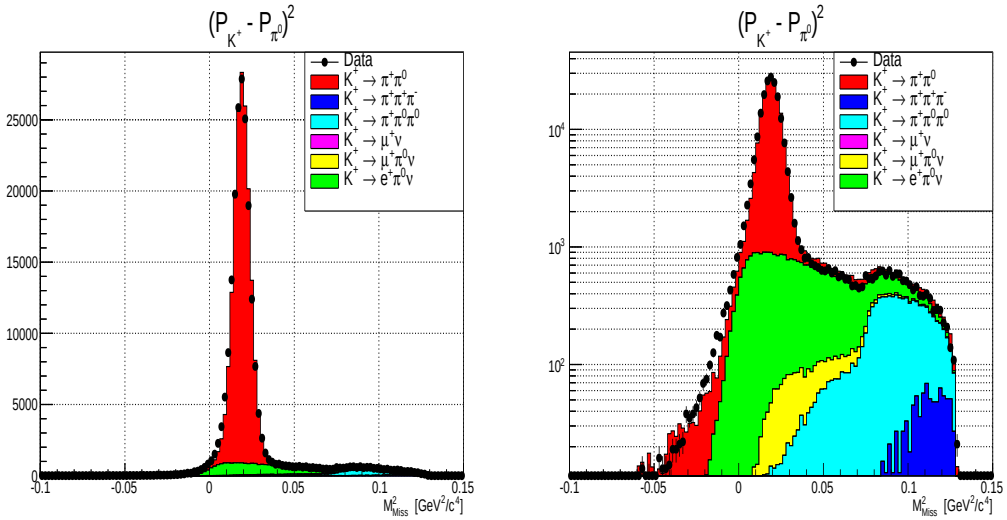

(a) (b)

Figure 7.18: Data-MC comparison of $(P_{K^+} - P_{\pi^0})^2$, on the right is the same plot on a logarithmic axis. The signal region for this distribution is chosen to be $0 <$ K2π MMS $< 0.04\ GeV^2/c^4$.

Decay Mode	Total Events	Signal Region Events	MC Acceptance %
Data	210855	185257	
$K^+ \to \pi^+\pi^0$	172237	167883	10.10
$K^+ \to e^+\pi^0\nu$	27254	15161	4.23
$K^+ \to \pi^+\pi^0\pi^0$	8807	0	0.00
$K^+ \to \mu^+\pi^0\nu$	1660	667	0.33
$K^+ \to \pi^+\pi^+\pi^-$	897	9	0.00
$K^+ \to \mu^+\nu$	0	0	0.00
Total Background	38618	15837	

Table 7.15: The total number of events and number of events in the signal region $0 <$ K2π MMS $< 0.04\ GeV^2/c^4$ for the data sample and the individual MC channels where the sum of the MC channels is scaled to the total number of events in data. Also shown are the MC acceptances of events into the signal region.

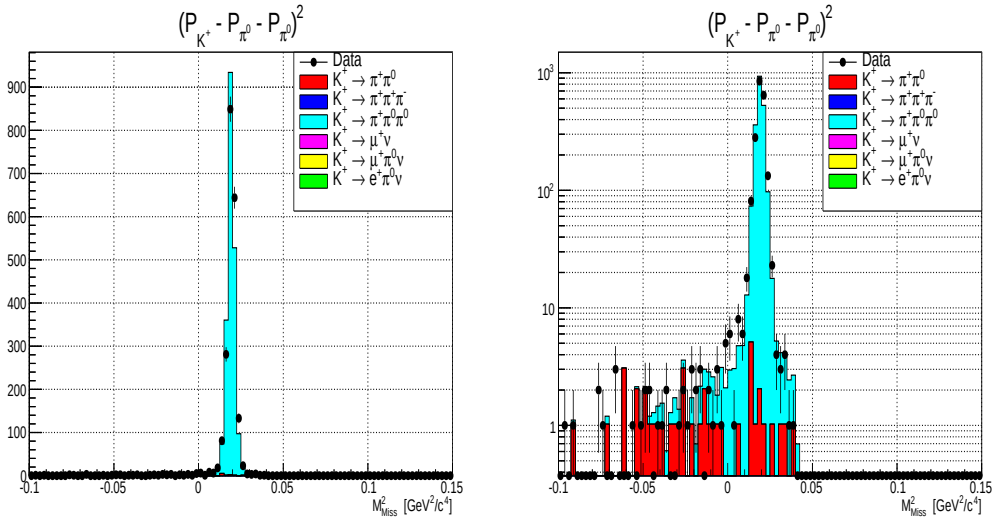

(a) (b)

Figure 7.19: Data-MC comparison of $(P_{K^+} - P_{\pi^0} - P_{\pi^0})^2$, on the right is the same plot on a logarithmic axis. The signal region for this distribution is chosen to be -0.012 < K3π0 MMS < 0.05 GeV^2/c^4.

Decay Mode	Total Events	Signal Region Events	MC Acceptance %
Data	2105	2075	
$K^+ \to \pi^+\pi^0\pi^0$	2062	2053	1.46
$K^+ \to \pi^+\pi^0$	43	18	0.00
$K^+ \to e^+\pi^0\nu$	0	0	0.00
$K^+ \to \mu^+\pi^0\nu$	0	0	0.00
$K^+ \to \pi^+\pi^+\pi^-$	0	0	0.00
$K^+ \to \mu^+\nu$	0	0	0.00
Total Background	43	18	

Table 7.16: The total number of events and number of events in the signal region -0.012 < K3π0 MMS < 0.05 GeV^2/c^4 for the data sample and the individual MC channels where the sum of the MC channels is scaled to the total number of events in data. Also shown are the MC acceptances of events into the signal region.

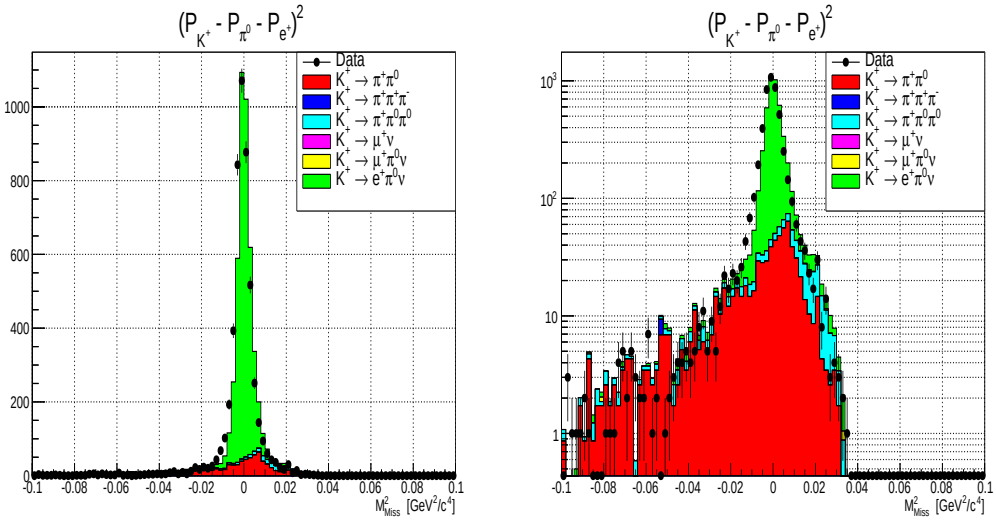

(a) (b)

Figure 7.20: Data-MC comparison of $(P_{K^+} - P_{\pi^0} - P_{e^+})^2$, on the right is the same plot on a logarithmic axis. The signal region for this distribution is chosen to be -0.01 < Ke3 MMS < 0.01 GeV^2/c^4.

Decay Mode	Total Events	Signal Region Events	MC Acceptance %
Data	5071	4485	
$K^+ \to e^+\pi^0\nu$	4074	3930	0.98
$K^+ \to \pi^+\pi^0$	763	392	0.05
$K^+ \to \pi^+\pi^0\pi^0$	230	75	0.11
$K^+ \to \mu^+\pi^0\nu$	3	1	0.00
$K^+ \to \pi^+\pi^+\pi^-$	2	0	0.00
$K^+ \to \mu^+\nu$	0	0	0.00
Total Background	998	468	

Table 7.17: The total number of events and number of events in the signal region -0.01 < Ke3 MMS < 0.01 GeV^2/c^4 for the data sample and the individual MC channels where the sum of the MC channels is scaled to the total number of events in data. Also shown are the MC acceptances of events into the signal region.

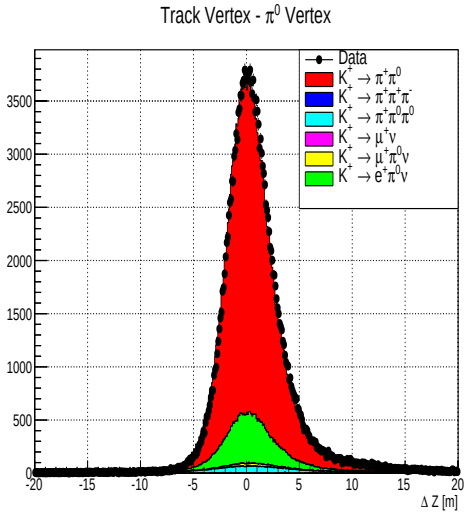

Figure 7.21: a) Data-MC comparison of the missing mass squared spectrum assuming the track is a π^+. b) Logarithmic in y.

typically have lower energy depositions.

Decay Mode	Data in Signal region SB_{Data}	MC Background B_{MC}	MC Acceptance (%) A
$K^+ \to \pi^+\pi^0$	185257	15837	10.10
$K^+ \to e^+\pi^0\nu$	4485	468	0.98
$K^+ \to \pi^+\pi^0\pi^0$	2075	18	1.46

Table 7.18: The Data and MC parameters used to calculate the relative branching fractions between the three given channels an the associated statistical error.

Decay Modes	Relative Branching Fraction	PDG Value	Variation from PDG(%)
$\frac{K^+\to e^+\pi^0\nu}{K^+\to\pi^+\pi^0}$	0.243±0.004	0.245±0.002	(-0.81±1.84)
$\frac{K^+\to\pi^+\pi^0\pi^0}{K^+\to\pi^+\pi^0}$	0.084±0.002	0.085±0.001	(-1.18±2.66)
$\frac{K^+\to\pi^+\pi^0\pi^0}{K^+\to e^+\pi^0\nu}$	0.344±0.009	0.347±0.005	(-0.86±2.99)

Table 7.19: The relative branching fractions for the three selected K^+ decay channels. Also given is the current PDG values and the difference between the two.

The result of this analysis is that we have recovered agreement with the PDG values within the statistical errors. This is strong evidence that the presence of hadronic clusters in the sample and the different rate of reconstructed π^+ clusters in data and MC is responsible for producing the incorrect branching ratios observed in Section 7.3 of this chapter and as observed in Chapter 6.

The collaboration is now aware of the inefficiency of the clustering software for hadronic clusters and indeed MIP responses in the detector. An update to the reconstruction is foreseen in the near future. It is clear that any analysis using the LKr calorimeter to reconstruct photons must contain tracking information in order to remove any uncertainty in the LKr detector response for hadronic clusters. The final section of this chapter will detail the expected rate at which we would expect hadronic contamination of π^0 candidates, this will be of interest for any subsequent analyses which must account for hadronic energy deposits without sufficient tracking information.

7.5.4 π^0 Hadronic Cluster Contamination in the Absence of Tracking

We saw in table 7.14 in Section 7.5.2 that the response for π^+ clusters is characteristically different between data and MC. Section 7.5.3 showed that removing hadronic clusters recovers agreement with the PDG relative branching fractions. The LKr based analyses presented in this Thesis were all based on reconstructing π^0s from LKr clusters. The $K^+ \to \pi^+\pi^0$ and $K^+ \to e^+\pi^0\nu$ involved finding single π^0 final states whilst the $K^+ \to \pi^+\pi^0\pi^0$ requires exactly two. The final stage of this analysis then will be concerned with quantifying the π^+ cluster contamination in single and double π^0 final states in the absence of any tracking information to veto clusters. Any discrepancy between the data and MC hadronic cluster response will affect the π^+ contamination in the single and double π^0 samples.

The first stage of the analysis reconstructs single and double π^0 final states using only the LKr in exactly the same way as was done in Section 7.3. The total number of single and double π^0 final states is outlined in table 7.20. To evaluate the rate at which clusters from π^+ go on to produce one cluster in a candidate π^0, events with a single 'good' track were selected in the Straw spectrometer, where 'good' refers to tracks which satisfy the same track quality selection cuts as were defined in Section 7.4. Tracks were then projected to the LKr plane and a matching was required of less than 100 mm to classify a cluster as matching, figure 7.20a. To distinguish whether the track and associated cluster originate from a π^+ the ratio of the cluster energy to the track momentum is required to be between 0.1 and 0.9. If the matched cluster is one of the candidate π^0 clusters then these events are considered contaminated by a hadronic π^+ cluster. The number of contaminated π^0 candidates is given in table 7.20 along with the total number of events where a π^+ cluster produced the π^0 candidate and the rate at which this occurs for both the single and double π^0 final states. We clearly see from table 7.20 that for single π^0 final state only 3.72±0.02% of clusters have a cluster positively identified as a π^+ compared with 10.21±0.08% and 12.29±0.09% for the ZS and NZS MC samples respectively. Between the single and double π^0 final states we observe an approximately 3% difference. As the two π^0 final state contains characteristically lower energy clusters than the single

π^0 state this 3% difference does not propagate in a linear fashion to the branching ratio of $\frac{K^+\to\pi^+\pi^0\pi^0}{K^+\to\pi^+\pi^0}$ relative branching fraction. We see that combining the analysis techniques developed in this Chapter that the MC candidate π^0s have typically around 7% more candidates where a cluster can be positively identified as originating from a π^+. This is a direct consequence of the poor modelling of hadronic response in the LKr calorimeter. This effect can be mitigated by using tracking information to remove π^+ clusters from the LKr sample, as we saw in Section 7.5.3. This effect may need to be addressed in future by the collaboration if the LKr detector is to be used to detect electromagnetic clusters where hadronic clusters without tracking information are a concern.

Single π^0	Total Events	π^+ cluster	π^+ cluster (%)
Data	1064380	39601	3.72±0.02
ZS MC	171846	17547	10.21±0.08
NZS MC	169054	20780	12.29±0.09

Double π^0	Total Events	π^+ cluster	π^+ cluster (%)
Data	17002	1091	6.42±0.20
ZS MC	101248	14318	14.14±0.13
NZS MC	88828	12703	14.30±0.14

table 7.20: The total number of single and double π^0 final states. Along with the number of events where a π^+ is found to be one of the π^0 clusters, defined as π^+ contaminated π^0 events.

7.6 Conclusions

In this Chapter we observed that when we attempt to compute the relative branching ratios of the $K^+ \to \pi^+\pi^0$, $K^+ \to e^+\pi^0\nu$, and $K^+ \to \pi^+\pi^0\pi^0$ decay channels we observe a disagreement with the established PDG values of around 20% for ratios including the $K^+ \to \pi^+\pi^0\pi^0$ final state decay. In order to investigate whether this behaviour is symptomatic of the data set a parallel analysis was undertaken using the Straw spectrometer to calculate the branching ratios of the same three decays. The Straw based analysis shows good agreement with the established PDG values suggesting that the problem is indeed confined to the LKr. Throughout the LKr based analysis of 2014 in Chapter 6 and 2015 in this Chapter issues were raised with the implementation of ZS in MC when compared with data. In particular ZS appeared to effect electromagnetic and hadronic clusters differently. Using the Straw spectrometer tracking information the LKr clusters could be defined as either electromagnetic (e^+) or hadronic (π^+). Electromagnetic clusters showed excellent agreement both in the cluster energy distribution and the LKr response between data and both ZS and non ZS MC. The hadronic clusters have differing cluster energy distributions for data and both ZS and non ZS MC. The MC samples we found to contain around 22% more hadronic clusters

than the data sample. The differing energy distributions between ZS and non ZS MC suggests that ZS is not sufficiently modelled in MC for hadronic clusters. The more important effect however is the 22% increased number of hadronic clusters in MC compared with data. The abundance of hadronic clusters in MC directly affects the calculated MC acceptances which are crucial to the LKr only analysis. If we use the Straw spectrometer to veto LKr clusters for which we have a matching geometrical position in the LKr detector we recover agreement between the calculated relative branching fractions and the PDG values. Finally a study was performed to assess the hadronic π^+ cluster contamination in candidate π^0s which were reconstructed using only LKr information. The result was that the π^0s reconstructed in MC contain typically 7% more π^0 candidates where one of the candidate clusters is identified as a π^+ cluster by the Straw spectrometer tracking information. A discrepancy of about 3% is observed between the single and double π^0 final state π^+ cluster contamination.

It has been established that the hadronic response of the LKr in the detector is not well modelled in MC. A well modelled LKr response is dependent on three distinct areas,

1. Correct modelling of the non zero suppressed LKr cell response.
2. Implementation of zero suppression to MC at the reconstruction phase, which mimics the zero suppression applied to data.
3. A reconstruction algorithm for making clusters from cells which is equally efficient for data and MC.

Inefficiencies in the clustering algorithm for non electromagnetic clusters are currently being understood by the collaboration and an updated version of the reconstruction is foreseen. It is hoped that this will recover the discrepancies in the number of observed hadronic clusters being around 20% larger for MC compared with data. Once an updated reconstruction is available a study of how zero suppression is implemented in MC should be undertaken starting from a new non zero suppressed data sample to validate the MC. It has been demonstrated here however that it is possible to recover sensible values for relative branching fractions if the Straw spectrometer information is used to veto hadronic clusters. The work presented here was part of a broader effort in the collaboration to understand and use the minimum bias data to produce updated measurements for relative branching fractions of the more common decays such as these.

7.6.1 Further Analysis

The investigative work done in this Chapter shows that producing a branching fraction measurement for these channels using solely the LKr electromagnetic calorimeter is not currently achievable. The uncertainty in the modelling of the

LKr environment has been noted by the collaboration and is under active investigation. It was however possible to retrieve branching fractions consistent with the PDG values. This method used upstream tracking information in order to remove clusters from consideration which could be inferred to be hadronic. This rectified the large discrepancies with the PDG values and led to the conclusion that the insufficient modelling of hadronic clusters was at fault. It must also be noted that by considering only events with one reconstructed track we have imposed additional acceptance criteria on the selection. It may be then that insufficient understanding of acceptance when using only the LKr was also contributing to the difference between the measured and PDG values of the branching fractions. If this analysis were to be taken further that would be the first area to investigate.

If this line of analysis were to be pursued further, then the first area of investigation would be to understand the acceptance of each decay into the final state signal region. In this analysis that was extracted entirely from MC. Use of the straw tracing information in a more detailed way than what was done here would be able to extract data driven estimates for the acceptance. Assuming the acceptance could be measured with the Straw spectrometer and that the hadronic modelling in MC can be validated then a branching ratio measurement that is more accurate than the current PDG value could be extracted. More data is available from 2015 and now 2016 in order to achieve this. A full systematic study must also be performed to report a measured branching fraction. This would include a full breakdown of the variation of the given cuts, touched upon for the cluster energy here. The acceptance conditions would also need to be investigated and a systematic error extracted. A systematic error due to the time dependant way in which the beam intensity is delivered per burst could also be pursued. The trigger efficiency here has also been assumed from MC. A study with a random trigger could be used to extract a data driven trigger efficiency and the associated systematic uncertainty. In reality the 2016 run is at a much more advanced level of data taking than what was the case during 2014 and 2015. As such a branching ratio measurement for the decay channels detailed in this thesis would include not only the LKr and Spectrometer but all information available to the collaboration through the multitude of additional sub detectors.

Chapter 8

Conclusions

In this Thesis two distinct pieces of analysis have been presented, the Monte Carlo driven study of the advantages and disadvantages of having hydrogen and nitrogen in the CEDAR vessel of the KTAG detector and the study of the LKr response in the first data taking runs when compared with Monte Carlo simulation. In addition to this analysis work I was also involved with the final efforts to produce the KTAG upgrade of the CEDAR differential Cherenkov detector and was part of the team which performed the mechanical installation of the detector on the beamline at CERN during 2013. During the data taking runs of 2014 and 2015 the KTAG was demonstrated to work with an efficiency for kaon tagging of over 98% and provide individual kaon timing resolution of around 70 ps resolution when using nitrogen as the Cherenkov radiator which is better than the design specifications.

A study was undertaken to identify the optimal CEDAR Chernkov gas. The conclusion drawn here, given the information from both the simulations and 2014 data analysis, was that nitrogen is the preferred Cherenkov radiator for the NA62 experiment as a whole. The increased rate on the downstream Straw spectrometer chambers from the MC simulations is less than 300 KHz (3%) on any given chamber and the increase in rate for the individual straws located closest to the beam is less than 70 KHz (15%). These results are supported indirectly from analysis of data by assessing the ratio of hits in the inner and outer straws for CEDAR filled with nitrogen and CEDAR evacuated. This analysis shows agreement between data and MC. The light loss in the KTAG detector when running with hydrogen, assuming perfect alignment, is conservatively estimated at 30% when compared with nitrogen. This translates to at least a 5% loss in efficiency for positive kaon detection. The 5% reduction in efficiency with respect to hydrogen is assuming the current 5-fold coincident octant condition can be used, in the event of a 6-fold requirement the drop in efficiency due to the 30% light loss would be closer to 15%. The benefit of running with nitrogen is evident when contrasting this modest increase in downstream rate with a light loss in the KTAG detector which impacts directly on kaon tagging efficiency that translates directly to a reduction in the size of any NA62 dataset.

The selection of the $K^+ \to \pi^+\pi^0$, $K^+ \to \pi^+\pi^0\pi^0$, and $K^+ \to e^+\pi^0\nu$ decays given in Chapters 6 and 7 used primarily the LKr electromagnetic calorimeter for the 2014 and 2015 data. It was possible to select all three decays using some simple cuts and the known kinematics of each channel. When computing the relative branching ratios of the three decays using the LKr only based selection, branching ratios involving the $K^+ \to \pi^+\pi^0\pi^0$ decay were seen to be around 20% different from the known Particle Data Group values. A hypothesis was proposed which suggested the problem was with the zero suppression implementation in Monte Carlo leading to incorrectly modelled hadronic response in the calorimeter. As the zero suppression energy correction is a non linear function of energy this will be affected by the cluster energy distributions and hence will affect the $K^+ \to \pi^+\pi^0\pi^0$ and $K^+ \to \pi^+\pi^0$ decays differently.

The 2015 data set was then analysed and the problem was shown to persist for a LKr based analysis. A parallel analysis was then performed using only the, now readily available, Straw spectrometer information. The relative branching fractions of the three channels were in agreement with the PDG values for the given statistical errors. This established that the problem was indeed with the LKr and not symptomatic of the data set as a whole. Use of the Straw Spectrometer tracking information allowed a further study of clusters to be performed in data where clusters matching tracks could be classified as either hadronic, matching a π^+ track, or electromagnetic, matching an e^+ track. This allowed detailed study of cluster types which revealed that the modelling of hadronic clusters was not sufficient in the MC whilst the electromagnetic clusters seemed to be adequately modelled as expected. The Straw spectrometer information was then used in conjunction with the LKr electromagnetic calorimeter data in order to reject hadronic clusters from the data sample and repeat the analysis. The analysis with hadronic clusters removed recovered agreement with the Particle Data Group values within statistical errors. Finally an outline was given of the observed data-Monte Carlo discrepancy for the number of hadronic clusters in the sample alongside a description of how a future data set is required before the Monte Carlo response can be fully rectified with respect to data.

Bibliography

[1] S. L. Glashow, J. Iliopoulos, and L. Maiani. Weak Interactions with Lepton-Hadron Symmetry. In: Phys. Rev. D 2 (7 1970), pp. 12851292. DOI: 10.1103/PhysRevD.2.1285.

[2] W. N. Cottingham and D. A. Greenwood. An Introduction to the Standard Model of Particle Physics. Cambridge University Press, 2007.

[3] J. H. Christenson et al. Evidence for the 2 Decay of the K2 Meson. In: Phys. Rev. Lett. 13 (4 1964), pp. 138140. DOI: 10.1103/PhysRevLett.13.138.

[4] H. Albrecht et al. Observation of B0-B0 mixing. In: Physics Letters B 192.12 (1987), pp. 245 252. DOI: http://dx.doi.org/10.1016/0370-2693(87)91177-4.

[5] M. S. Sozzi. Discrete symmetries and CP violation: From experiment to theory. 2008.

[6] K. Olive et al. Review of Particle Physics. In: Chin.Phys. C38 (2014), p. 090001. DOI: 10.1088/1674-1137/38/9/090001.

[7] J. Charles et al. CP violation and the CKM matrix: assessing the impact of the asymmetric B factories. English. In: The European Physical Journal C - Particles and Fields 41.1 (2005), pp. 1131. DOI: 10.1140/epjc/s2005-02169-1.

[8] A. Buras, S. Uhlig, and F. Schwab. Waiting for precise measurements of $K^+ \to \pi^+\nu\overline{\nu}$ and $K^0 \to \pi^0\nu\overline{\nu}$. . In: Rev. Mod. Phys. 80 (3 2008), pp. 9651007. DOI: 10.1103/RevModPhys.80.965.

[9] V Cirigliano et al. Kaon decays in the standard model. In: Rev. Mod. Phys. 84 (1 2012), pp. 399447. DOI: 10.1103/RevModPhys.84.399.

[10] D. Rein and L. M. Sehgal. Long-distance contributions to the $K^+ \to \pi^+\nu\overline{\nu}$ decay . In: Phys.Rev. D 39 (11 1989), pp. 33253329. DOI: 10.1103/PhysRevD.39.3325.

[11] J. S. Hagelin and L. S. Littenberg. Rare kaon decays. In: Progress in Particle and Nuclear Physics 23 (1989), pp. 1 40. DOI: http://dx.doi.org/10.1016/0146- 6410(89) 90007-0.

[12] M. Lu and M. B. Wise. Long distance contribution to $K^+ \to \pi^+\nu\overline{\nu}$. In: Physics Letters B 324.3 4 (1994), pp. 461 464. DOI: http://dx.doi.org/10.1016/0370-2693(94)90223-2.

[13] G. Buchalla and A. J. Buras. The rare decays $K^+ \to \pi^+\nu\overline{\nu}$ and $K_L \to \mu^+\mu^-$ beyond leading logarithms. In: Nuclear Physics B 412.12 (1994), pp. 106 142. DOI: http://dx.doi. org/10.1016/0550-3213(94)90496-0.

[14] G. Buchalla and A. J. Buras. The rare decays $K^+ \to \pi^+\nu\overline{\nu}$, $B \to X\nu\overline{\nu}$ and $B \to l^+l^-$: an update. In: Nuclear Physics B 548.13 (1999), pp. 309 327. DOI: http://dx.doi.org/ 10.1016/S0550-3213(99)00149-2.

[15] J. Brod, M. Gorbahn, and E. Stamou. Two-loop electroweak corrections for the $K^+ \to \pi^+\nu\overline{\nu}$ decays. In: Phys. Rev. D 83 (3 2011), p. 034030. DOI: 10.1103/PhysRevD.83.034030.

[16] A. J. Buras, D. Buttazzo, J. Girrbach-Noe, and R. Knegjens, JHEP 11, 033 (2015), 1503.02693

[17] A. J. Buras et al. Charm quark contribution to $K^+ \to \pi^+\nu\overline{\nu}$ at next-to-next-to-leading order. In: Journal of High Energy Physics 2006.11 (2006), p. 002.

[18] J. Brod and M. Gorbahn. Electroweak corrections to the charm quark contribution to $K^+ \to \pi^+\nu\overline{\nu}$. In: Phys. Rev. D 78 (3 2008), p. 034006. DOI: 10.1103/PhysRevD.78.034006.

[19] G. Isidori, F. Mescia, and C. Smith. Light-quark loops in $K^+ \to \pi^+\nu\overline{\nu}$ In: Nuclear Physics B 718.12 (2005), pp. 319 338. DOI: http://dx.doi.org/10.1016/j.nuclphysb. 2005.04.008.

[20] F. Mescia and C. Smith. Improved estimates of rare K decay matrix elements from K_{l3} decays." In: Phys. Rev. D 76 (3 2007), p. 034017. DOI: 10.1103/PhysRevD.76.034017.

[21] J. Bijnens and K. Ghorbani. Isospin breaking in K vector form-factors for the weak and rare decays K_{l3}, $K^+ \to \pi^+\nu\overline{\nu}$ and $K^+ \to \pi^+l^+l^-$"". In: (2007). arXiv: 0711.0148 [hep-ph].

[22] G. Buchalla and A. J. Buras. sin 2β from $K^+ \to \pi^+\nu\overline{\nu}$. In: Physics Letters B 333.12 (1994), pp. 221 227. DOI: http://dx.doi.org/10.1016/0370-2693(94)91034-0.

[23] R. Aaij et al. Measurement of C P Violation in $B \to J/\psi K^0_S$ Decays. In: Phys. Rev. Lett. 115(3 2015), p. 031601. DOI: 10.1103/PhysRevLett.115.031601.

[24] A. Artamonov et al. New Measurement of the $K^+ \to \pi^+\nu\overline{\nu}$ Branching Ratio. In: Phys. Rev. Lett. 101 (19 2008), p. 191802. DOI: 10.1103/PhysRevLett.101.191802.

[25] J. K. Ahn et al. Experimental study of the decay $K^0 \to \pi^0\nu\overline{\nu}$ In: Phys. Rev. D 81 (7 2010), p. 072004. DOI: 10.1103/PhysRevD.81.072004.

[26] G. Anelli et al. Proposal to measure the rare decay $K^+ \to \pi^+\nu\overline{\nu}$ at the CERN SPS. In: (2005).

[27] M. Togawa. Status of KOTO Experiment at J-PARC. In: Journal of Physics: Conference Series 556.1 (2014), p. 012046.

[28] U. Camerini et al. Experimental Search for Semileptonic Neutrino Neutral Currents. In: Phys. Rev. Lett. 23 (6 1969), pp. 326329. DOI: 10.1103/PhysRevLett.23.326.

[29] D. Ljung and D. Cline. Experimental Study of the Rare K + Decay Modes: , $K^+ \to \pi^+\pi^0\gamma$, $K^+ \to \mu^+\pi^0\nu\gamma$,$K^+ \to \pi^+\gamma\gamma$,$K^+ \to \pi^+\nu\overline{\nu}$, and $K^+ \to \pi^0\pi^0e^+\nu$, and $K^+ \to \pi^0\gamma e^+\nu$. In: Phys. Rev. D 8 (5 1973), pp. 13071330. DOI: 10.1103/PhysRevD.8.1307.

[30] G. Cable et al. Search for rare K^+ decays. ii. $K^+ \to \pi^+\nu\overline{\nu}$ In: Phys.Rev. D8 (1973), pp. 3807 3812. DOI: 10.1103/PhysRevD.8.3807.

[31] M. Atiya et al. A detector to search for $K^+ \to \pi^+\nu\overline{\nu}$ In: Nucl.Instrum.Meth. A321 (1992), pp. 129151. DOI: 10.1016/0168-9002(92)90382-E.

[32] Bassalleck et al. An experiment to measure the branching ratio $B(K^+ \to \pi^+\nu\overline{\nu})$ Tech. rep. BNL-67247 tri-pp-00-06. Brookhaven National Laboratory, 1999.

[33] M. Atiya et al. Search for the decays $K^+ \to \pi^+\nu\overline{\nu}$ and $K^+ \to \pi^+X^0$ for $150 < M_{X^0} < 250\ MeV/c^2$". In: Phys. Rev. D 48 (1 1993), R1R4. DOI: 10.1103/PhysRevD.48.R1.

[34] S. H. Kettell. A Search for the rare decay $K^+ \to \pi^+\nu\overline{\nu}$ In: (1996). arXiv: hep-ex/9701003 [hep-ex].

[35] S. Adler et al. Evidence for the Decay $K^+ \to \pi^+\nu\overline{\nu}$". In: Phys. Rev. Lett. 79 (12 1997), pp. 22042207. DOI: 10.1103/PhysRevLett.79.2204.

[36] S. Adler et al. Further Evidence for the Decay $K^+ \to \pi^+\nu\overline{\nu}$". In: Phys. Rev. Lett. 88 (4 2002), p. 041803. DOI: 10.1103/PhysRevLett.88.041803.

[37] NA62 Collaboration, E. Cortina et al., NA62-10-07 (2010).

[38] G. Anelli et al., CERN-SPSC-2005-013 (2005).

[39] OPAL Collaboration, K. Ahmet et al., Nucl.Instrum.Meth. A305, 275 (1991).

[40] NA62 Collaboration, A. Ceccucci et al., SPSC-M-760 (2007).

[41] NA62 Collaboration, A. Ceccucci et al., SPSC-SR-115 (2013).

[42] B. Angelucci et al., Journal of Instrumentation 9, C01055 (2014).

[43] M. Pivanti et al., Journal of Physics: Conference Series 513, 012008 (2014).

[44] C. Bovet, S. Milner, and A. Placci, IEEE Trans.Nucl.Sci. 25, 572 (1978).

[45] E. Goudzovski et al. Development of the kaon tagging system for the NA62 experiment at CERN, Nuclear Inst. and Methods in Physics Research, A (2015), pp. 86-94

[46] C. Bovet, R. Maleyran, L. Piemontese, A. Placci, and M. Placidi, (1982).

[47] A. Romano, Leptonic decays and Kaon Identification at the NA62 experiment at CERN, PhD thesis, 2012.

[48] I. Tamm, J.Phys.(USSR) 1, 439 (1939).

[49] E. Goudzovski, CEDAR Working Group Meeting 9/04/2013.

[50] http://sergiant.web.cern.ch/sergiant/NA62FW/html/index.html.

[51] Fry, J. Mechanics and Cooling. https://indico.cern.ch/conferenceDisplay.py?confId=191777.

[52] Hamamatsu, Users Data Sheet .

[53] Hamamatsu, Users Data Sheet .

[54] F. Anghinolfi et al., Nucl.Instrum.Meth. A533, 183 (2004).

[55] J. Christiansen, HPTDC High Performance Time to Digital Converter, Version 2.2 for HPTDC version 1.3, 2004.

[56] B. Angelucci et al., Journal of Instrumentation 9, C01055 (2014).

[57] E. Pedreschi, M. Sozzi, F. Spinella, NA62-10-06 (2010).

[58] G. Haefeli et al., Nucl.Instrum.Meth. A560, 494 (2006).

[59] NA62 Technical Design SPSC-SR-083

[60] J. Beringer et al. (Particle Data Group), Phys. Rev. D86, 010001 (2012)

[61] A.Dudarev, V.Kruglov, L.Kruglova, M.Nikitin, DIRAC note 08-06

[62] http://sergiant.web.cern.ch/sergiant/NA62FW/html/

[63] K.L Brown, Ch. Iselin, CERN 74-2, Geneva, 1974

[64] S. Agostinelli et al., Nucl. Instrum. Methods, A506 (2003) 250

[65] Bovet C. et al. The CEDAR counters for Particle Identification in the SPS Secondary Beams. CERN. Geneva. 1982. (CERN Yellow Report : CERN 82-13)

[66] K. Massri IOP 2013 Meeting 09/04/2013 https://indico.cern.ch/event/214998/session/11/contribution/89/material/slides/0.pdf

[67] E. Goudzovski CEDAR Working Group Meeting 09/04/2013

[68] A.Romano, "The K identification system in the NA62 experiment at CERN". Advancements in Nuclear Instrumentation Measurement Methods and their Applications (ANIMMA) April 2015.

[69] F.Newson. Kaon Identification and the Search for Heavy Neutrinos at NA62 .PhD thesis, University of Birmingham, School of Physics and Astronomy, 2015.

[70] J. Fry and L.Fulton, "The choice of Cherenkov Gas in the CEDAR Vessel". Internal note NA62-14-04, May 2014

[71] J. Fry and L.Fulton, "Experimental evidence relating to the choice of Cherenkov Gas in the CEDAR Vessel". Internal note NA62-15-04, June 2015

[72] V. Fanti et al. NIM A574, 433-471, 2007.

[73] G.Unal (NA48-98-01), NA62 Internal note NA62-15-02

[74] G. Ruggiero NA62 Weekly Meeting 23/10/2014 (https://indico.cern.ch/event/348278/contribution/2/material/slides/0.pdf)